Institut für Geodäsie und Geoinformation der Universität Bonn

Professur für Geodätische Erdsystemforschung

A likely role for stratification in present-day changes of the global ocean tides

Dissertation

zur Erlangung des akademischen Grades

Doktorin der Ingenieurwissenschaften (Dr.-Ing.)

der Agrar-, Ernährungs- und Ingenieurwissenschaftlichen Fakultät

der Rheinischen Friedrich-Wilhelms-Universität Bonn

vorgelegt von

Lana Opel

aus Hilden

Bonn 2025

Referent:	Prof. Dr.-techn. Michael Schindelegger
Korreferent:	Dr.ir. Cornelis Slobbe

Tag der mündlichen Prüfung: 08.07.2025

Angefertigt mit Genehmigung der Agrar-, Ernährungs- und Ingenieurwissenschaftlichen Fakultät der Universität Bonn.

"There is a way out of every box, a solution to every puzzle.
It's just a matter of finding it."

— *Captain Jean-Luc Picard*

Abstract

Ocean tides are a phenomenon familiar to the general society, as they are observable in almost any coastal area. The regular rise and fall of the global oceans, caused by the gravitational attraction of Sun and Moon, affects nearly all oceanographic and geodetic satellite observations. Both satellite and in situ observations of the sea surface reveal subtle changes of ocean tides on interannual to secular time scales ($\sim$1–3 cm century^{-1} in amplitude) that are unrelated to the astronomical forcing. Recent research aims to unravel and understand the physical mechanisms behind the observed tidal changes. Connections can possibly made with climate change, as it has the potential to impact tides through different physical processes. One such process is relative sea level rise, driven mainly by steric expansion of seawater and the mass input from melting ice sheets. However, sea level rise alone cannot account for observed large-scale tidal trends in the open-ocean. A second, related process is climate-induced upper ocean warming, which increases the stratification—that is, the density contrast—in the upper part of the ocean's vertical water column. The connection of tides to stratification mainly arises from the energy conversion from barotropic (depth-independent) to baroclinic (or internal) tides, when tidal currents are reflected and scattered at inclined underwater topography. The resulting internal waves of dense water are pushed upwards into lighter water, such that an oscillation is excited that depends on the strength of the stratification. As the ocean's stratification changes, tidal conversion and the energy left for propagation of the barotropic tide are modified, too. Using a three-dimensional global ocean model, I show that changes in ocean stratification are a leading cause for the interannual and long-term changes of tidal surface amplitudes observed over past decades. When analyzed from 1993 to 2020, open-ocean trends of the barotropic M_2 tide are predominantly negative (~ -0.1 mm year^{-1}), matching the trends estimated from satellite altimetry in spatial pattern and to some extent in magnitude. The tendency for decreasing barotropic M_2 amplitudes indicates enhanced energy transfer to baroclinic tides, which indeed show a positive trend in their surface amplitude over the same time span. A comparison to modeled tidal changes associated with relative sea level rise highlights the primary role of stratification in driving present-day M_2 trends in the open ocean. Toward coastal areas, where the impact of sea level rise increases, stratification still exerts controls on the tidal signal, in part overprinting the effects of sea level rise, e.g., at the US West Coast or in Northwest Australia. Analysis of year-to-year variations over 1993–2020 at individual tide gauge locations reveals that stratification also modulates tidal amplitudes on interannual time scales and with a certain regional coherence (e.g., western Pacific or Gulf of Mexico), despite the analysis being hampered by local factors. Additional simulations in decadal steps until 2100 and under a high greenhouse gas emission scenario suggest that the projected increase of ocean stratification forces future tidal changes, mostly causing decreasing M_2 amplitudes on a global scale (consistent with present-day). The decrease in M_2 amplitude does not scale linearly with time, counter to what might be expected from the projected near-monotonic increase in stratification. Alongside stratification, changes in ocean basin geometry—i.e., water depth and coastline position—affect future tides. In particular, relative sea level rise mainly drives coastal tide changes of up to $\sim$10 cm, whereas expansion of the cavities underneath melting Antarctic ice shelves mostly acts on open-ocean tides. The relative importance of three drivers (stratification, sea level rise, ice shelf melt) and the magnitude of the induced tidal changes depend both on location and the adopted climate scenario. Taken together, the findings of this work are deemed a major step toward improved understanding of the processes underlying global tidal changes on different temporal and spatial scales.

Zusammenfassung

Ozeangezeiten sind allgemein bekannt, da sie in nahezu jedem Küstengebiet zu beobachten sind. Das regelmäßige Auf- und Ab der Ozeane, verursacht durch die gravitative Anziehungskraft von Sonne und Mond, ist in fast allen ozeanographischen und geodätischen Beobachtungen enthalten. Sowohl in-situ als auch Satellitenbeobachtungen der Meeresoberfläche zeigen kleine aber messbare zwischenjährliche bis langfristige Änderungen der Ozeangezeiten ($\sim$1–3 cm Jahrhundert^{-1} in der Amplitude), die nicht durch Schwankungen der gravitativen Anziehungskraft erklärt werden können. Die Entschlüsselung der physikalischen Mechanismen hinter diesen beobachteten Gezeitenveränderungen ist Gegenstand aktueller Forschung. Ein viel diskutierter und offenkundig relevanter Prozess ist der relative Meeresspiegelanstieg, welcher hauptsächlich durch die sterische Ausdehung des Meerwassers und den Masseneintrag aufgrund schmelzende Eisschilde verursacht wird. Jedoch ist aus vergangenen Modellierungsstudien bekannt, dass der Meeresspiegelanstieg die beobachteten großräumigen Gezeitentrends im offenen Ozean nicht alleine verursachen kann. Ein zweiter Prozess ist die klimabedingte Erwärmung der Ozeane, welche die Schichtung—d.h. den vertikalen Dichtekontrast—verstärkt. Der Zusammenhang zwischen Gezeiten und der Ozeanschichtung besteht hauptsächlich in der Energieumwandlung von barotropen (tiefenunabhängigen) Gezeiten in barokline (oder interne) Wellen, wenn Gezeitenströmungen an geneigter Unterwassertopographie reflektiert und gestreut werden. Die daraus resultierenden internen Wellen aus Wasser mit hoher Dichte werden nach oben in leichteres Wasser ausgelenkt, sodass eine Oszillation erzeugt wird, die von der Stärke der Schichtung abhängt. Wenn sich die Schichtung ändert, ändert sich auch diese Form des Energietransfers und damit die Energie, die für die Ausbreitung der barotropen Gezeiten zur Verfügung steht. Anhand eines dreidimensionalen globalen numerischen Ozeanmodells wird in dieser Arbeit gezeigt, dass Veränderungen in der Ozeanschichtung maßgeblich zu den in den letzten Jahrzenten beobachteten zwischenjährlichen und langfristigen Veränderungen der Oberflächenamplituden der Gezeiten beitragen. Im Analysezeitraum von 1993 bis 2020 sind die modellierten Trends der barotropen M_2 Amplituden im offenen Ozean vorwiegend negativ (~-0.1 mm Jahr^{-1}) und decken sich in ihrer Struktur und Magnitude zu einem großen Teil mit Trends aus Satellitenaltimetrie. Die Tendenz zu abnehmenden barotropen M_2 Amplituden deutet auf eine verstärkte Energieübertragung auf barokline Gezeiten hin, welche in der Tat einen positiven Trend in ihren Oberflächenamplituden über den Zeitraum 1993–2020 aufweisen. In küstennahen Gebieten, wo der Meeresspiegelanstiegsganz wesentlich zu Gezeitentrends beiträgt, übt die Schichtung dennoch einen Einfluss auf das Gezeitensignal aus und überlagert teilweise die Auswirkungen des Meeresspieglanstiegs, z.B. an der US-Westküste oder in Nordwestaustralien. Eine Analyse der jährlichen Schwankungen zwischen 1993 und 2020 an global verteilten Gezeitenpegeln zeigt, dass die Schichtung auch die Gezeitenamplituden auf zwischenjährlichen Zeitskalen mit einer gewissen regionalen Kohärenz (z.B. im westlichen Pazifik oder im Golf von Mexiko) moduliert, obwohl diese Form der Analyse durch lokale Faktoren erschwert wird. Zusätzliche Simulationen in dekadischen Abständen bis 2100 unter einem Szenario mit hohen Treibhausgasemissionen deuten darauf hin, dass die prognostizierte Verstärkung der Ozeanschichtung auch zukünftig global abnehmende M_2 Amplituden verursachen wird. Die Abnahme skaliert dabei nicht linear mit der Zeit, obwohl dies aufgrund der prognostizierten nahezu monotonen Zunahme der Schichtung zu erwarten wäre. Neben der Schichtung, wirken sich auch Veränderungen der Geometrie der Ozeanbecken—d.h. Wassertiefe und Küstenposition—auf die künftigen Gezeiten aus. Insbesondere der relative Meeresspiegelanstieg verändert Gezeitenhöhen an der Küste bis zu $\sim$10 cm, während sich das Abschmelzen von großen Eisschelfen und damit die veräderte Beckengeometrie rund um die Antarktis hauptsächlich auf die Gezeiten im offenen Ozean auswirkt. Das Verhältnis zwischen den drei Antriebsfaktoren (Schichtung, Meeresspiegelanstieg, Rückgang der Eisschelfe) und die Größenordnung der induzierten Gezeitenveränderungen variieren räumlich und hängen stark vom angenommenen Klimaszenario ab. Zusammenfassend sind die Erkenntnisse dieser Arbeit ein wichtiger Schritt zu einem besseren Verständnis der Prozesse, welche den Veränderungen globaler Ozeangezeiten auf verschiedenen zeitlichen und räumlichen Skalen zugrunde liegen.

Acknowledgments

Writing the last parts of my thesis made me reflect the past four years. Academically, and also personally, it was a challenging journey with a lot of lessons to learn. Looking back, I can say that I am really proud of myself with the journey I made until here, and I am excited what will be next. While facing different challenges of life, I am extremely grateful for the support of a lot of people inside and outside of the scientific community. I honestly want to thank all of you, for your support, for believing in me, and for never letting me down!

Regarding this thesis, my supervisor Prof. Dr.-techn. Michael Schindelegger deserves special thanks. He already supervised my Master thesis and offered me the opportunity to join the GESS group in May 2021 as a PhD student. With my research topic being located somewhere in between geodesy and oceanography, he took the time to provide me with a comprehensive introduction to physical oceanography, and also to numerical modeling. Thank you Michael, for guiding me through my PhD journey with support, help, advice, and especially for sparking my scientific interest in tides. I learned so much within the past four years. I also would like to thank my referee Dr.ir. Cornelis Slobbe. It was a pleasure to meet and discuss the scientific field of ocean tides with you. Thank you for your expertise and taking the time to provide me with your thoughts on my thesis, which helped to strengthen my work. I am also grateful for the funding of my work, which is provided by the Deutsche Forschungsgemeinschaft (DFG, German Research Foundation), project number: 451039647 (project SCOOP). Additionally, I gratefully acknowledge the Gauss Centre for Supercomputing e.V.[1] *for funding this project by providing computing time on the GCS Supercomputer JUWELS*[2] *Moreover, I gratefully acknowledge the granted access to the Marvin cluster hosted by the University of Bonn along with the support provided by its High Performance Computing & Analytics Lab.*

A really warm thanks goes out to all my colleagues during my time at IGG, who are always open for help and provide a very nice working environment. The support from everyone of the GESS, APMG, TG, and GRV groups is deeply appreciated! Thanks for all the fun in the lunch breaks, I really enjoyed sharing my time with you. Especially, I want to thank my office partner Lara, who is always open for (non-)scientific discussions and became a close friend of mine. I am really happy to have shared the office with you for almost four years. Thanks for making me feel safe to talk about everything with you! Moreover, I want to thank all my geodetic friends who have accompanied me through the Bachelor's and Master's program in Bonn, without you I wouldn't be where I am now! Another huge thanks definitely goes out to all my non-geodetic friends! Your close friendship and support is deeply appreciated! Particularly, I want to consign heartfelt thanks to Caro, Franziska, Kaya, Krissi, Lea, Lena, Sandra, Tabea, and Vali for believing in me, supporting me, and providing me with deep talk, understanding, and fun!

I want to dedicate special and deeply felt thanks to my parents, Cornelia and Wolfgang, who support me unconditionally all my way long and always ensure me that I'm capable of much more than I think. This is also true for my sister Merle, who provides me with unlimited support and always cheers me up. I can't put into words what your support means to me. I feel so deeply happy to have a family like you!

Last but not least, I want to thank my boyfriend Jan, who became not only my partner, but also my best friend during my doctorate journey. I feel so glad to have you in my life and I want to thank you for your love and your patience with me when I am (once again) stressing myself out over every little detail, especially in the last months. Thank you for your unconditional love, support, and always being there for me!

[1] `www.gauss-centre.eu`

[2] Jülich Supercomputing Centre. (2021). JUWELS Cluster and Booster: Exascale Pathfinder with Modular Supercomputing Architecture at Juelich Supercomputing Centre. Journal of large-scale research facilities, 7, A183. `http://dx.doi.org/10.17815/jlsrf-7-183` at Jülich Supercomputing Centre (JSC).

Contents

1 Introduction

1.1 Motivation

The regular rise and fall of the Earth's oceans, known as tides, is observable for any person at the coast and determines the life of a considerable part of the world's population. Ocean tides also represent a key element of the dynamic Earth system and vary around the world's coastlines in both their periodicity and their amplitude, characterized by amplitudes greater than one meter in several coastal locations. The correlation between the tidal appearance and the movements of Sun and Moon has long been recognized and drawn scientific interest. Having started from bare observations, the scientific field of ocean tides and tidal dynamics has evolved over time, such that we are now able to explain and predict the astronomically forced water movements to high accuracy. For practical purposes, such as tidal prediction, one usually decomposes relevant observations into harmonic oscillations, also referred to as partial waves or tidal constituents. The frequencies of these constituents are defined by the tide-generating gravitational force and thus reflect the origin of the tides in the action by celestial bodies (e.g., Pugh and Woodworth, 2014; Ward et al., 2023). Our comprehensive knowledge of tides and the underlying physics notwithstanding, there are still various aspects of the global ocean tides that are puzzling and merit closer consideration.

Our empirical knowledge of ocean tides has been greatly shaped by in situ water level measurements and since the early 1990s, by satellite radar altimeter observations. Both observation techniques complement each other to some extent, as the accuracy of satellite radar altimeter observations decreases when approaching the coast, whereas this is exactly where most tide gauges are located. Together, the observations from tide gauges and satellite radar altimeters allow for a global estimation of the tidal constituent's harmonics. Additionally, complementary information is available from techniques that sense Earth's gravity field (e.g., Koch et al., 2024) or crustal deformation (e.g., Wang et al., 2024). Different aspects of oceanic variability, such as changes in the instantaneous surface elevation, and ocean mass, due to tidal dynamics, tidal energetics, or the movements of the whole vertical water column are connected dynamic processes. Therefore, globally distributed observations of the ocean's state have been leveraged both in the field of geodesy and oceanography, thus forming an interaction between these two scientific research fields (e.g., Wunsch and Stammer, 1998).

Precise observations of the ocean's state and its behavior with time have revealed unexpected and subtle changes of the global ocean tides, and respectively individual tidal constituents (see, e.g., Woodworth, 2010; Bij de Vaate et al., 2022). The causes and physical mechanisms behind these changes are unrelated to the astronomical forcing and not fully understood, thus defining an active field of research. Observational evidence for these changes extends back in time approximately 30 to 100 years, as sampled by the available satellite altimetry and tide gauge records. Overall, the changes occur from seasonal to secular time scales, with varying magnitudes in space and across constituents (see, e.g., Müller et al., 2011; Devlin et al., 2018;

Haigh et al., 2020).

Considerable effort has recently gone into unraveling the driving mechanisms behind the observed tidal changes. A key tool in this quest for causes are numerical ocean models, which represent the relevant physical processes and thus offer opportunities to study the response to particular processes and prescribed changes. Such models form a crucial tool to understand past and present tidal change. Moreover, disentangling and understanding the physical mechanisms behind present-day changes lays the groundwork for predicting and modeling the tidal evolution in the future. Given the ubiquity of ocean tides and their importance for the dynamic Earth and coastal environments, closing the knowledge gap on observed tidal changes constitutes a fundamental task to solve.

Recent efforts in identifying the physical causes behind the observed tidal changes have mostly concentrated on one specific suspected driver for tidal change, that is global and regional sea level rise, caused by present-day climate change. However, detailed numerical modeling work found sea level rise alone being unable to explain the observed large-scale open-ocean tide variability (e.g., Schindelegger et al., 2018). With the main physical causing mechanisms behind the observed tidal changes still being unknown, the question raises as to what other large-scale process could induce the observed changes. Another possible driver for tidal changes in the context of global climate change is the strengthening of the present-day ocean's vertical density structure, i.e., stratification. The strengthening occurs mainly due to climate-induced upper ocean warming (e.g., Li et al., 2020, or in the Intergovernmental Panel on Climate Change Fifth Assessment Report, IPCC-AR5), and is predicted to further increase in the future. However, the impact of increasing ocean stratification on the tides of the modern (i.e., present-day) ocean has so far not been quantified.

1.2 Relevance Statement

Knowledge of the simplest tidal dynamics, i.e., the timing of highest and lowest tide, is essential for economic harbor operations, nautical safety, and coastal risk assessments. Moreover, with the ocean covering more than 70 % of the Earth's surface, ocean tides are a key mechanism in the global ecosystem balance. In addition to the assessment of future (nuisance) flood risks, coastal characteristics like sediment flux are highly dependent on tides, and their respective changes. Moreover, tidal currents represent a source for renewable energy, e.g., via tidal power plants. In general, tidally-driven extreme sea levels may not only threaten populated coastal regions, but also may have impacts on the global ocean mixing, nutrient supply, primary production, or fisheries (e.g., Jay, 2009). Coastal ecosystems need tidal water movements to thrive, and thus allow globally important natural habitats to exist. More generally, the global ocean tides play an important role in sustaining the deep-ocean circulation, which is a key element of the global climate system (e.g., Vic et al., 2019). Thus, a socio-economic necessity arises to best accurately observe, model, and project tidal dynamics and properties into the future.

Besides socio-economic constraints, the ongoing tidal changes are also of scientific interest. The interest is not only based on the nature of curiosity, but rather than on a number of important scientific aspects. For instance, tidal changes are a relevant factor in the context of the definition of geodetic datums, general environmental considerations, or satellite missions. Accurate knowledge of ocean tides is important in the context of de-aliasing satellite altimetry and gravimetry observations (Flechtner et al., 2016; Zaron and Ray, 2018). Moreover, satellite observations with increasing accuracy nowadays, e.g., the Surface Water and Ocean Topography (SWOT) mission, are able to resolve oceanic processes at an unprecedented level (e.g., Fu et al., 2024; Qiu et al., 2024). To assess small scale ocean topography signals from satellite observations, tides are often removed in the post processing. Therefore, the community is in need of accurate ocean tide models that represent variability in space at a high level of detail, and potentially also the subtle temporal (i.e., seasonal to secular) changes of primary tidal constituents.

The consensus in literature (e.g., Haigh et al., 2020; Talke and Jay, 2020) is that there are different and possibly competing forcing factors for changes in ocean tides. In this context, the role of changing ocean stratification is presently unclear. As ocean stratification is expected to strengthen further with future climate change (e.g., Capotondi et al., 2012, IPCC-AR5, IPCC Specific Report on the Ocean and Cryosphere in a Changing Climate, SROCC), its role with regard to the dynamic system of the global tides needs to be assessed. In general, future projections of extreme sea levels often consider ocean tides to be stationary or to change with sea level rise alone (which is an important but not solely dominant factor, e.g., Schindelegger et al., 2018). Given the above outlined importance of tides at present day and their future changes, further investigation into the topic is required.

1.3 Objectives of the Thesis

The present thesis aims to clarify the effects of changes in ocean stratification on tidal variability on interannual to secular time scales with a focus on surface elevations. Such global quantification is currently lacking. The thesis therefore contributes to the understanding of the dynamic Earth system, and more specifically the behavior of the ocean, which forms a key objective in the research fields of geodesy and oceanography. In short, the central research question of this thesis is:

What is the impact of ocean stratification changes on the global surface amplitudes of the primary tidal constituents?

In order to answer this central question, I use a three-dimensional numerical modeling configuration of the *Massachusetts Institute of Technology general circulation model* (MITgcm, Marshall et al., 1997). The scope of the problem is such that it generally poses tight requirements on the three-dimensional discretization of the global model domain. The numerical simulations need to resolve tidal large-, and small-scale processes, in addition to the respective energy transfer between depth-independent (i.e., barotropic) and vertically structured (i.e., baroclinic) flow components. In the horizontal, at least a resolution of $1/10°$ is mandatory for that purpose (Arbic et al., 2018). Together with a high vertical resolution, the power of High Performance Computing (HPC) is required. With the help of supercomputers, hindcast simulations with realistic annual ocean stratification are conducted over the time period of 1993 to 2020, including the primary tidal constituents M_2, S_2, K_1, and O_1. After assessing the accuracy of the modeled tidal harmonics and comparing it to literature (e.g., Stammer et al., 2014), the MITgcm setup is also used to model future tidal changes based on projections of stratification until the end of the 21st century. Connecting to the formulated research question, the main objective of this thesis reads:

Quantification of how recent changes in ocean stratification have affected the global tidal surface amplitudes of the four primary tidal constituents M_2, S_2, K_1, and O_1.

The objective can be divided into the following major tasks

(A) Set up a three-dimensional numerical modeling configuration of the MITgcm, that yields accurate (comparable to literature, e.g., Stammer et al., 2014) estimates of the global primary barotropic and baroclinic tidal constituents M_2, S_2, K_1, and O_1.

(B) Investigate the impact of changing ocean stratification on the primary tidal constituents on interannual time scales (1993–2020) and compare against observed variability at tide gauges.

(C) Investigate the impact of changing ocean stratification on the primary tidal constituents in terms of linear trends (1993–2020) and compare against observation-based trends from tide gauges and satellite altimetry.

(D) Use the MITgcm setup from (A) to model future changes of M_2, S_2, K_1, and O_1 based on projections of basin geometry changes and future ocean stratification until the year 2100.

Parts of the work have been published, in particular the results of (C) in Opel et al. (2024) and the results of (D) in Opel et al. (2025).

1.4 Outline of the Thesis

To address the research questions of this work, the thesis is structured as follows: First, I give an overview of essential ocean physics and tidal concepts in Chapter 2. This includes a definition of ocean stratification and its implications with respect to the global oceans. Furthermore, I discuss present-day changes in ocean stratification, which are fundamental to the results of this thesis. Additionally, I describe how ocean stratification is expected to change in the future, on time scales up to the year 2100. Afterwards, I introduce ocean tidal concepts, starting from the equilibrium tidal theory, and evolving to the dynamic theory of tides. In more detail, the characteristics of the barotropic and baroclinic tidal components are described, as both are separated and analyzed individually throughout this work and form an important connection between ocean stratification and tides. This also necessitates elaborations on tidal energetics, including friction, dissipation, and tidal conversion. In the last section of Chapter 2, I present an overview of proven and potential non-astronomical driving mechanisms for long-term tidal changes.

Chapter 3 introduces the numerical ocean model used in this work. I point out the governing equations of the model, and describe important model parameters in the general context of ocean tide modeling. Moreover, the parameter settings specific to this work are summarized. A key component of Chapter 3 is the description of the representation of ocean stratification changes within the model.

In Chapter 4, methods and data essential to this thesis are laid out. Starting with the post-processing of the model output, the concept of harmonic analysis, the separation of the barotropic and baroclinic tide, and an accuracy assessment of the tidal estimation are shown. Next, observations used for validation and comparisons are introduced, including tide gauge and satellite radar altimeter observations. As a basis for Chapter 6, the estimation of linear tidal trends, including statistical significance, is introduced in Chapter 4. The chapter closes with a description of complementary simulations for other important driving factors, later used in Chapter 7 to contextualize the modeled tidal changes caused by changes in ocean stratification.

Chapter 5 presents the first results of this work, focusing on year-to-year tidal variability on interannual time scales from 1993 to 2020. The modeled tidal variability, based on annual changes in ocean stratification, is analyzed on global, regional, and local spatial scales. I conduct pointwise comparisons to amplitude time series from tide gauges, distributed globally around the world's coastlines. Furthermore, I elaborate on a possible connection between the modeled tidal amplitude variability and climate modes of the Earth.

Next, in Chapter 6, I analyze the modeled tidal amplitude changes in terms of linear trends from 1993 to 2020. Estimated trends for both the barotropic and baroclinic tidal components are discussed, with a special focus on changes in the barotropic tide at global and regional scales. Comparisons to tidal trends inferred from satellite radar altimetry and tide gauges are used as comparisons to the modeled trends. The chapter closes with the analysis of linear trends in tidal conversion, which offers key insights into the physical origin for the observed and modeled trends in the barotropic and baroclinic tides.

Chapter 7 introduces modeled tidal amplitude changes in the future, extending toward the end of the 21st century. I point out how projected future changes in stratification act onto the global tides, and set the modeled tidal changes in context to impacts by two other driving mechanisms, that is, relative sea level rise and changes in Antarctic ice shelf geometry.

Finally, the main findings of the thesis are summarized in Chapter 8. Furthermore, recommendations for extended work on using and improving the results of this work are provided.

2 Ocean Physics, Tides, and Related Quantities

Describing the physical properties of the world's ocean has been the subject of oceanographic observation, analysis, and modeling. Given the important role that the changing ocean plays in a number of global dynamic variables, accurate and realistic observations are required, which in turn provide the groundwork for realistic mathematical modeling. Given the scope of this work, the basic physical conditions of the ocean are described in this chapter. Moreover, key concepts related to oceanic motion and the associated energy exchange processes are highlighted.

2.1 A Stratified Ocean

The concept of ocean stratification, meaning the horizontal and vertical density distribution of seawater, is essential to this work and is therefore introduced at first. In the past, the global ocean tides were described mathematically using numerical models, with a single vertical layer to represent the entire ocean (*barotropic models*, depth-independent). These models are still common and important to test ideas of past and present-day tides (e.g., Sulzbach et al., 2023) or precisely model tides in shallow water (e.g., Blakely et al., 2022). Later on, tide models were, and still are being improved based on better process understanding and greater computational resources. Model resolution has been refined in the horizontal by smaller grid spacing and in the vertical by introducing multiple layers (*baroclinic models*, three-dimensional). With continued research into improving ocean tide models and growing computational power, they became successively more realistic (e.g., Arbic et al., 2004; Shriver et al., 2012; Stammer et al., 2014). This in turn requires accurate ocean stratification data (e.g., from observations or model-data synthesis) on various time scales from days to decades, which can be used as boundary conditions and validation for numerical simulations. This section provides an overview of the concept of a stratified ocean and the most relevant physical quantities.

2.1.1 Temperature, Salinity, and Pressure

The distribution of temperature and salinity within the global ocean varies horizontally and vertically. The temperature that can be directly observed is called *in-situ* temperature (T) and is characterized by the physical property of being relatively compressible. In addition to in-situ temperature, another important temperature variable is the *potential* temperature (θ). Potential temperature differs from in-situ temperature, as it describes the temperature the water would have if it were raised adiabatically (i.e., without heat exchange with the surrounding water) from ocean depth to the surface. In general, the potential ocean temperature (referred to as temperature hereafter) decreases with depth and is characterized by a steep thermocline. The decrease in temperature is considerably more rapid near the surface than in the abyssal ocean. This is due to the existence of a mixed layer in the uppermost part of the ocean. As the name

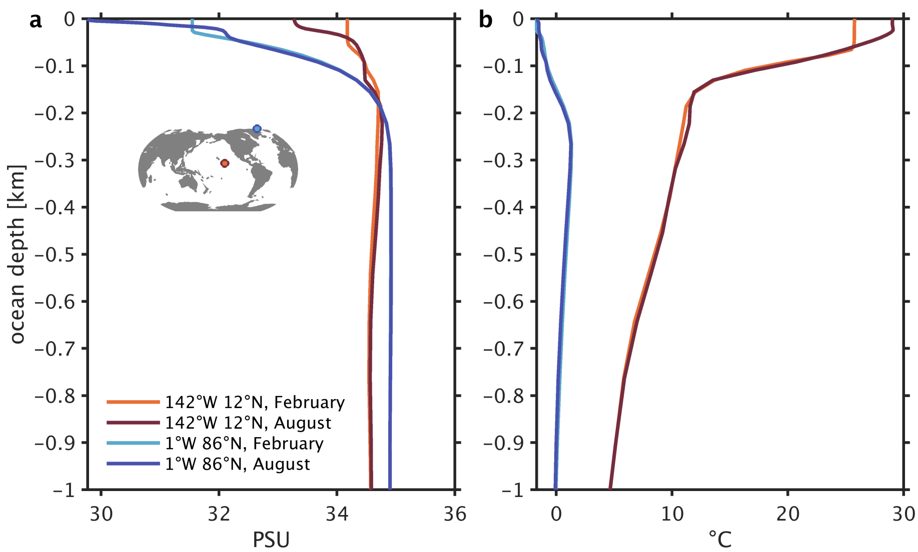

Figure 2.1: Example for salinity **a** and potential temperature **b** in the first 1000 m of the ocean. Temperature and salinity are displayed for two arbitrarily chosen locations, one in the tropics and one at high latitudes. The data is taken from monthly estimates in 2016 of GLORYS12 Version 1 ocean reanalysis (Lellouche et al., 2018). The depth of the ocean is cut at 1000 m to emphasize upper ocean changes. For both points in space, February and August are shown.

states, the mixed layer shows conditions of well mixed water, maintained by surface winds and air-sea energy exchange (Knauss and Garfield, 2016). The mixed layer also absorbs the Sun's radiation in the upper few meters, which results in heating. Below the mixed layer depth, the thermocline indicates a rapid change in temperature, which is clearly visible in a profile of depth versus temperature, indicated in Figure 2.1b. A steep decrease in temperature particularly characterizes the tropics. In contrast, the profile at high northern latitude shows a slight increase in temperature below the surface followed by a very slow decrease. The equatorial region is more affected by the Sun's radiational heating. As a consequence, the tropical ocean has a steeper thermocline than the rest of the oceans. In ocean areas below the thermocline, the temperature only changes gradually with depth. In addition, seasonal changes in temperature are present in the surface layer everywhere in the ocean. During summer, the surface parts of the ocean is heated more in comparison to winter conditions. Therefore, the upper ocean is more stratified in summer than in winter. In Figure 2.1b the two month February and August indicate the changing mixed layer depth in the tropics. In winter, here represented by February, the upper ocean is less heated and in consequence allows for a deeper mixed layer. Figure 2.2 provides a general view of the ocean's surface temperature (year 2016) highlighting in particular the typical dependence on latitude.

The salinity (S) of the ocean varies within a narrower range than the temperature, except for a few marginal seas. In numbers, 75 % of the global salinity in the ocean varies between 34.5 and 35.0 Practical Salinity Units (PSU) (Knauss and Garfield, 2016). Extremes exist in regions characterized by strong evaporation or contrary by freshwater input of estuaries or river outflows. In general, the salinity is altered by precipitation, evaporation, river runoff, melting sea ice, and oceanic transport (i.e., advection). Figure 2.3 depicts the ocean surface salinity for the year 2016. Decreased salinity is apparent in the Arctic in comparison to the rest of the Earth, which is due to freshwater input from glaciers and annually melting sea ice. Figure 2.1a shows the halocline, as evident from the salinity versus depth profile. In winter at polar latitudes, when the ice freezes and removes freshwater from the ocean, the surface water under the ice becomes

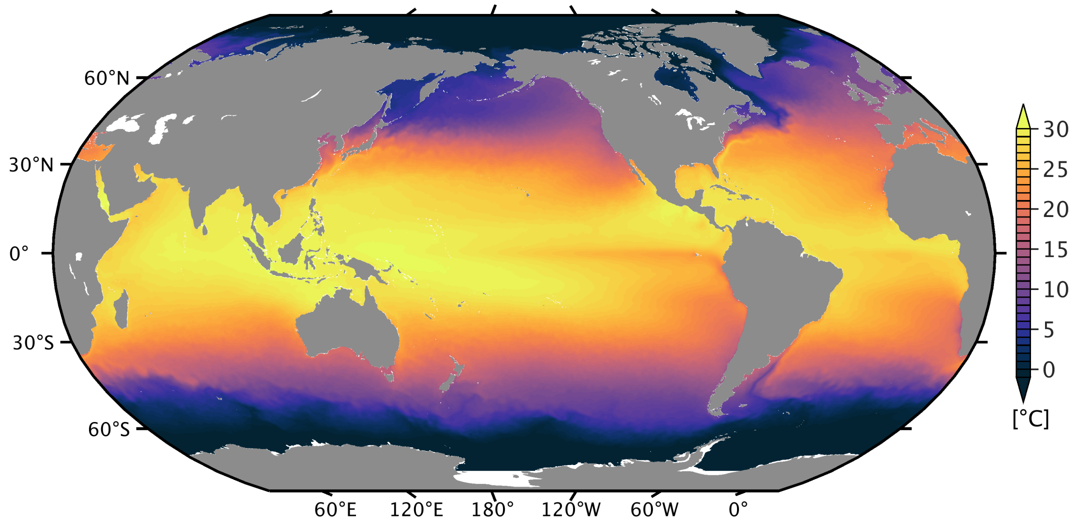

Figure 2.2: Surface sea water potential temperature for the year 2016. Monthly sea water potential temperature from the GLORYS12 Version 1 database (Lellouche et al., 2018) is annually averaged for the year 2016 and the most upper ocean layer.

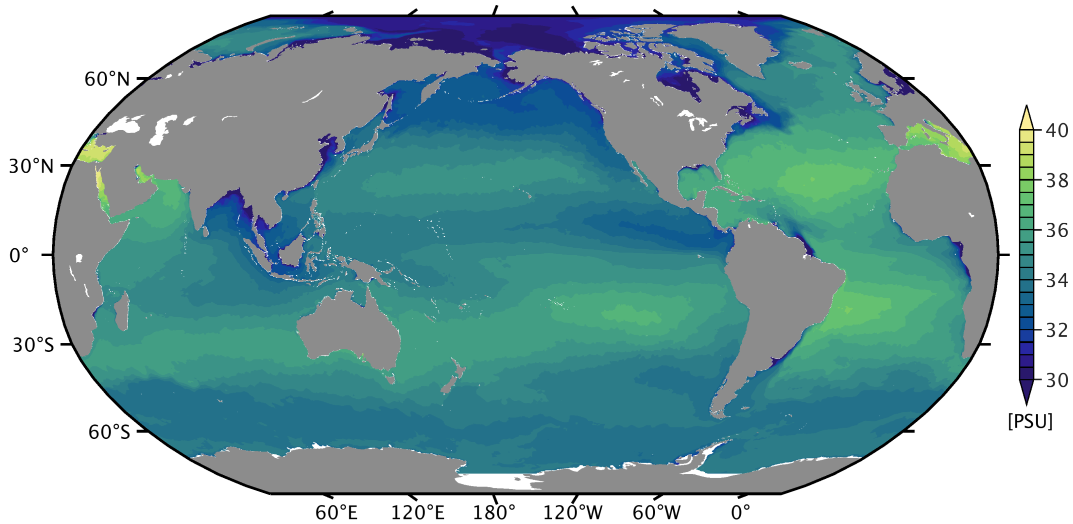

Figure 2.3: Surface sea water salinity for the year 2016. The same as Figure 2.2, but for sea water salinity.

more salty than in summer (cf. Figure 2.1a). The salinity increases with depth. In general, the surface salinity is higher in the tropics than at the poles, since more evaporation is evident due to the increased temperature. This is especially true for tropical regions located not directly at the equator. The equatorial region receives the most precipitation and therefore, the surface salinity decreases because of the freshwater input. The seasonal changes in surface salinity persisting in the tropics are mainly caused by changes in evaporation and precipitation which are associated with seasonal changes of atmospheric conditions (Liu et al., 2022a). Differences between polar regions and the tropics concern the forming and position of the halocline. A single halocline exists at about 100 m ocean depth for extratropic regions, like in Figure 2.1a for the Arctic location. However, in the tropics and subtropics a double halocline forming is possible and can be observed directly below and above the local salinity maximum (Chen et al., 2018).

Another important oceanic state variable is the hydrostatic pressure (p). It increases with depth by about 1 atmosphere, meaning the surface pressure, per 10 m ocean depth (Knauss and Garfield, 2016).

From the above elaborations it is clear that the ocean is a stratified fluid. Depending on the region, temperature, and salinity have a different amount of influence on the ocean stratification. In large parts of the ocean, temperature exerts a strong control on the stratification, especially in regions where evaporation dominates, such as the subtropics and mid-latitudes. By contrast, in the tropics and at higher latitudes, salinity has a comparable or dominant influence (Sallée et al., 2021) on how the ocean is stratified.

2.1.2 Equation of State of Seawater

The equation of state of seawater connects the main state variables of the ocean in a mathematical way. In the past, it has undergone several revisions, as it is an empirically derived equation. Therefore, as measurements improved in precision, the equation of state of seawater was revised and made more accurate. The currently used formulation is the International Thermodynamic Equation of Seawater 2010 (TEOS-10). Some of the major updates implemented in this version, including a Gibbs thermodynamic potential function and refined considerations of salinity, are described in Feistel (2003), Feistel (2008), and Millero et al. (2008).

The equation of state of seawater is necessary to compute, amongst others, the density of the ocean's water. For that purpose, values of in-situ temperature, absolute salinity and ocean depth are required to solve the 48-term equation. The ocean depth defines the amount of hydrostatic pressure in the water column. In general, density within the ocean increases with decreasing temperature, while salinity and pressure increase. A simple linearized equation of state with limited accuracy (Knauss and Garfield, 2016) takes the form

$$\rho - \rho_0 = \left[-\overline{a}(T - T_0) + \overline{b}(S - S_0) + \overline{k}p\right]. \tag{2.1}$$

Here, the overlines denote average values. Following Knauss and Garfield (2016) it is possible to calculate the in-situ density (ρ) by an accuracy of $\pm 0.5\,\mathrm{kg\,m^{-3}}$ with $\rho_0 = 1027\,\mathrm{kg\,m^{-3}}$, $T_0 = 10\,°\mathrm{C}$, $S_0 = 35\,‰$, $\overline{a} = 0.15\,\mathrm{kg\,m^{-3}}$ per degree Celsius, $\overline{b} = 0.78\,\mathrm{kg\,m^{-3}}$ per part per thousand salinity and $\overline{k} = 4.5 \times 10^{-3}\,\mathrm{kg\,m^{-3}}$ per decibar. Besides in-situ density, the concept of potential density (ρ_θ) exists, too. The definition is analogous to potential temperature, in the sense that it describes the density that the water would have if it were raised adiabatically from ocean depth to the surface.

The ocean density increases with depth, especially when the effect of compressibility is considered. However, after compressibility is removed, density with depth still increases toward deeper layers in most locations. Figure 2.4a illustrates the in-situ density in a profile versus ocean depth, for the same spatial points as Figure 2.1. Besides the seasonal differences in the upper ocean, it is clear that the density increases toward the ocean bottom. Figure 2.4b displays the Brunt-Väsälä frequency ($N^2 = -g/\rho\,(\partial\rho_\theta/\partial z)$, Knauss and Garfield, 2016), that can be considered as a stability measure for the stratification conditions (e.g., Knauss and Garfield, 2016). In general, a higher value of N^2 denotes a more stable stratified fluid. It defines the oscillation period of a water particle around its equilibrium position in the vertical water column. This quantity can especially be different for particles located at the thermocline or halocline (cf. Figure 2.1), but also for different locations in space, like deep ocean or shelf areas (Knauss and Garfield, 2016).

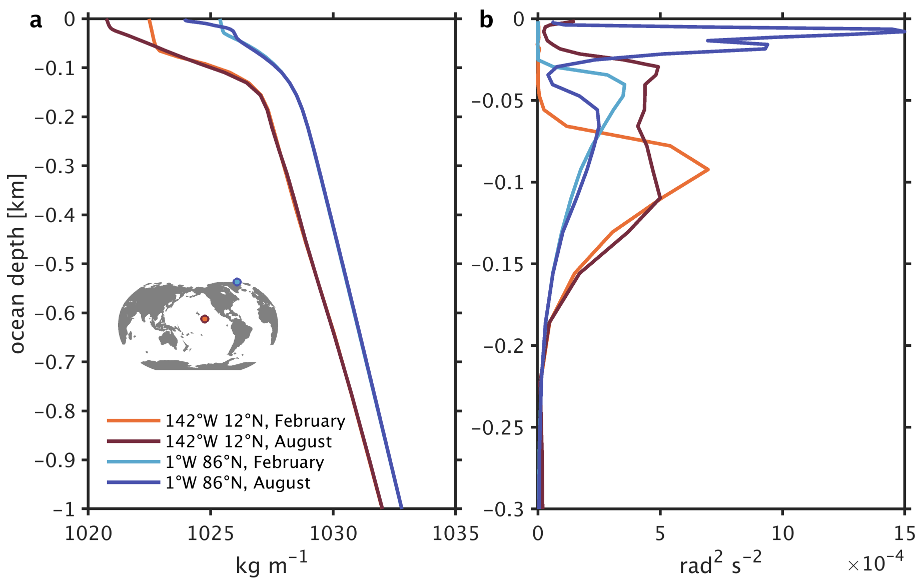

Figure 2.4: Exampled for in-situ density (ρ) **a** and Brunt-Väsälä frequency (N^2) **b** in the upper part of the ocean. Two arbitrarily chosen locations are shown, one in the tropics and one at high latitudes. The data is taken from monthly estimates in 2016 of GLORYS12 Version 1 ocean reanalysis (Lellouche et al., 2018). The depth of the ocean is cut at 1000 m for the density and at 300 m for N^2 to increase visibility of upper ocean changes. For both points in space, February and August are shown.

2.1.3 Contemporary and Future Ocean Stratification

Numerous processes in the ocean are initiated or influenced by the vertical density stratification. Horizontal and vertical mixing, though very different in magnitude, result in parts from stratification. Horizontal mixing occurs mostly along isopycnals, layers of constant density, which takes significantly less energy than across density surfaces in the vertical direction. As the stratification increases, the amount of energy needed to mix through the water column increases, too. The vertical mixing affects exchange of heat, oxygen, carbon, and nutrients (Li et al., 2020).

In general, the strength of stratification impacts the barotropic-to-baroclinic energy conversion rate (cf. Section 2.3.2), since it determines the generation and propagation of internal tides (cf. Section 2.2.4), as shown, e.g., in Müller (2012); Katavouta et al. (2016); Buijsman et al. (2017); Barbot et al. (2021). In addition, ocean stratification ultimately represents a source for kinetic energy, because the interface of the different density layers may be sloping, thereby creating a pressure gradient force. This pressure gradient is, in turn, able to induce water movement and large-scale gyres (Knauss and Garfield, 2016).

The global ocean stratification is far from being constant and undergoes substantial changes over time, see, e.g., recent studies by Yamaguchi and Suga (2019) or Li et al. (2020). The latter study found that ocean stratification has been increasing with a rate of 0.9 % per decade over the past half-century. The study argues that the upper 200 m of the ocean are mostly affected by the stratification increase, resulting mainly from temperature changes within the ocean. The upper ocean takes up both solar radiation and atmospheric heat, which is expected to increase with rising global mean temperature due to global warming. In consequence, future ocean mixing, especially in the vertical, may deviate from present-day conditions. Observing these changes remains challenging, since the measurement network of the ocean's thermohaline stratification

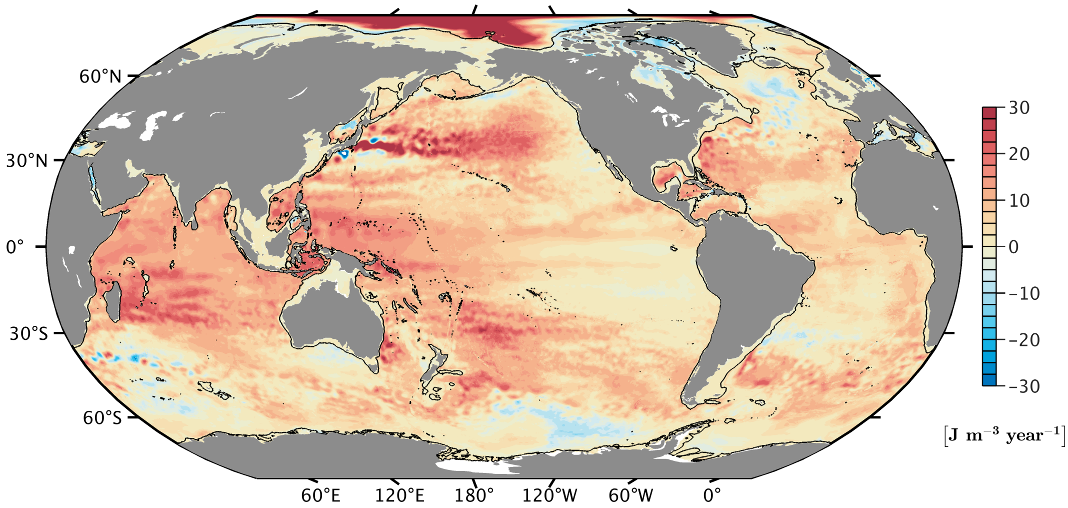

Figure 2.5: Trends in ocean stratification 1993–2020. Color shading illustrates the linear change in potential energy anomaly ϕ (J m^{-3} year^{-1}), calculated from GLORYS12 Version 1 (Lellouche et al., 2018) annual temperature and salinity profiles.

is sparse in comparison to the ocean's extent. Strengthening ocean stratification trends were found to be regional in space by Yamaguchi and Suga (2019), with a dominant contribution from the tropical ocean regions. Sallée et al. (2021) also found a global stratification increase in the upper 0–200 m, as well as in proximity to the pycnocline. They also describe regional trend patterns, with trends greater in magnitude in the tropical regions in comparison to higher latitudes. Cheng et al. (2022) found significant ocean warming of the upper 2000 m from 1958 to 2019, with a doubled rate of warming when comparing the 1960s and the 2010s. From evaluating area averages, they found the largest warming in the Atlantic Ocean and Southern ocean. The regional differences in the evolution of stratification underpin the challenges involved in observing and interpreting these changes.

The potential energy anomaly ϕ, as utilized by Simpson et al. (1981) or Yamaguchi and Suga (2019), is a measure for the amount of energy that is required to achieve a vertically homogeneous water column from a stably stratified starting condition. Analytically, we have (Simpson et al., 1981)

$$\phi = \frac{1}{H} \int_{-H}^{0} (\overline{\rho_\theta} - \rho_\theta) g z \, \mathrm{d}z. \tag{2.2}$$

Here, z denotes the vertical coordinate direction, counted positive upward and taking a value of 0 at the surface. The potential density ρ_θ is subtracted from its vertically averaged value $\overline{\rho_\theta}$, and g is the gravitational acceleration. The linear trend of the potential energy anomaly ϕ, computed from annually averaged ocean state estimates from GLORYS12 Version 1 (Lellouche et al., 2018) over the time span 1993 to 2020 is shown in Figure 2.5. Striking is the overall positive trend that is significant to 95% confidence level in several regions, especially in the Indian Ocean. This result agrees with the previously reported contemporary strengthening of ocean stratification (e.g., Li et al., 2020). In addition to the increase of stratification in the annual, it is projected that the response to global warming is amplified in summer compared to winter conditions. For example, Jo et al. (2022) suggested that the enhanced seasonal cycle of sea surface temperature is caused by increased summertime stratification in the upper ocean, combined with shoaling of the annual-mean mixed layer.

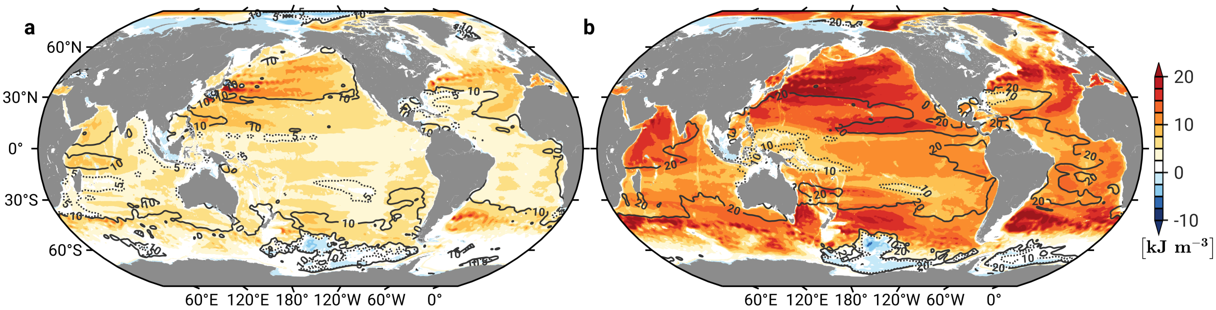

Figure 2.6: Changes of potential energy anomaly (kJ m^{-3} year^{-1}) in the years 2060 **a** and 2100 **b** relative to 2000, based on temperature and salinity fields from CMIP6. Colors indicate the change constrained to an upper-bound climate scenario with radiative forcing levels of the Representative Concentration Pathway 8.5. Contours represent the percentage changes, after smoothing to length scales of 200 km. The Figure is based on Opel et al. (2025).

The present-day trend in ocean stratification described above is expected to increase in the coming decades and beyond, as global warming and greenhouse gas emission stay high or even accelerate (e.g., Capotondi et al., 2012; Fu et al., 2016; Guo et al., 2024). The increase in stratification, as a response to enhanced upper ocean warming, is supposed to be large throughout the global ocean, with largest stratification changes in the 21st century occurring in the Arctic, the tropics, the North Atlantic, as well as in the Northeast Pacific (Capotondi et al., 2012). The relative importance of temperature versus salinity in changing the vertical density gradients can also be expected to vary from region to region. While surface temperature increase is projected to be the dominant driver in the tropics, salinity changes will mostly affect the Arctic, the North Atlantic, and the Northeast Pacific (Capotondi et al., 2012). As an example, the upper ocean stratification (averaged 0–800 m) in the Luzon Strait is estimated to increase by 26.8 % from 2015 to 2110 under high-end greenhouse gas emission, according to Guo et al. (2024). Figure 2.6 illustrates the enhanced future increase in stratification more explicitly, by showing changes in ϕ for the year 2100 relative to 2000. The estimated change in potential energy anomaly is based on temperature and salinity fields from a coupled atmosphere-ocean circulation model (detailed description in Section 3.2.2), integrated in time under a high greenhouse gas emission scenario. Additionally, the profiles of N^2 for the major ocean basins in Figure 2.7 illustrate the projected near-monotonic increase of future stratification from 2000 to 2100 under a no-policy climate scenario.

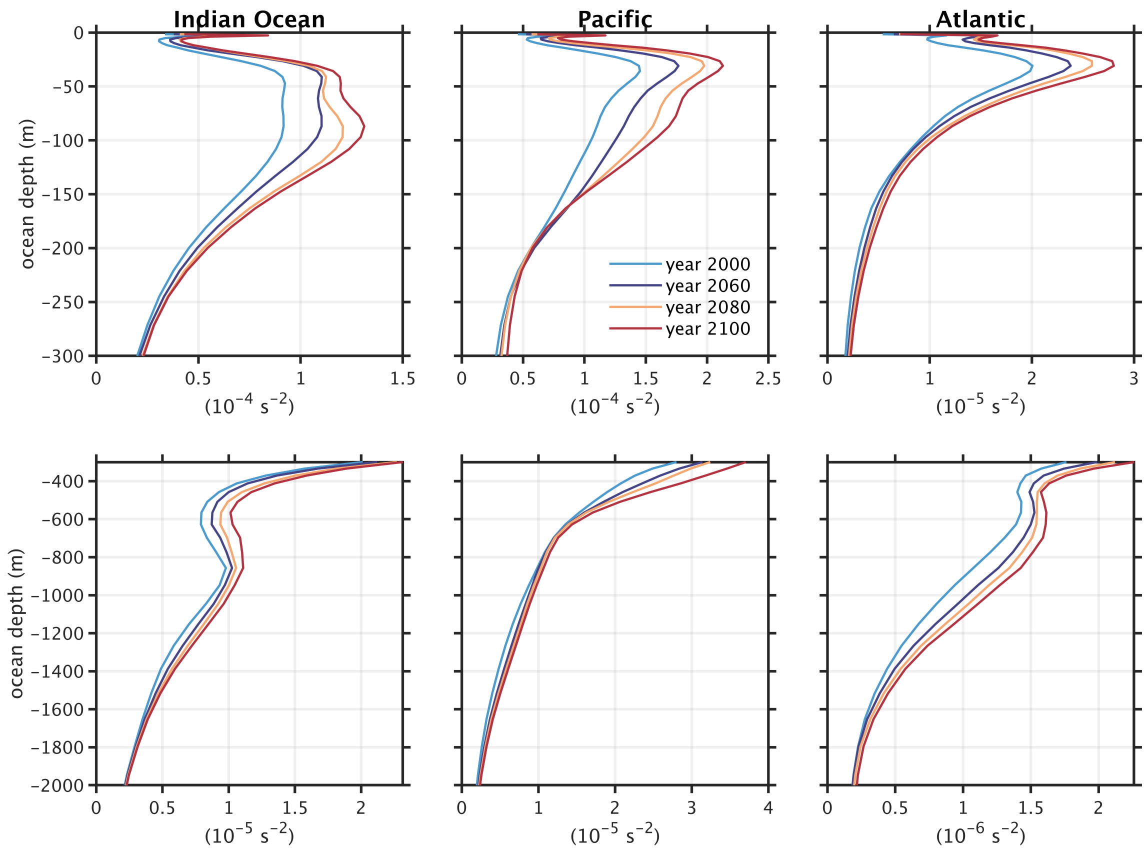

Figure 2.7: Vertical profiles of buoyancy frequency, N^2 (s^{-2}), from EC-Earth3P historical and scenario simulations at four time slices (2000, 2060, 2080, 2100). The profiles are spatial averages over the entire (left column) Indian Ocean, (middle column) Pacific Ocean, and (right column) Atlantic Ocean, split up into two depth ranges (0–300 m, 300–2000 m). Note that the climate scenario is the same as in Figure 2.6. The Figure is taken from Opel et al. (2025).

2.2 Tidal Concepts and Characteristics

The basic characteristics of the ocean tides have long been recognized, e.g., going back to the insight of Ancient Greek societies that the lunar phase and the ocean's movement are related (Ward et al., 2023). From bare observation to general concepts, the research field of ocean tides has been continuously extended over time, yielding descriptions that closer and closer agreed with reality. The first general mathematical concept of tidal forces, based on an aqua-Earth was described by Sir Isaac Newton in 1687 in the *Principia*, now known as the *Equilibrium Tidal Theory*. This achievement formed the groundwork for subsequent research, including the general response of the ocean to tidal forces presented by Daniel Bernoulli, or Leonhard Euler's finding that the horizontal component of the tide-generating force (TGF) is the actual reason for ocean tides. The dynamic theory of tides was first described by Pierre-Simon Laplace in 1799, now known as the *Laplace Tidal Equations*.

This section lays out the most relevant aspects concerning the theory of ocean tides and tidal dynamics. Starting from the TGF itself, the equilibrium tidal theory is presented. The limitations are discussed and included in a path toward the dynamic theory of tides. Selected characteristics of ocean tides are given afterwards by a description of barotropic and baroclinic tidal components.

2.2.1 Tide-Generating Force and Equilibrium Tidal Theory

A first mathematically correct concept of the TGF was described by Sir Isaac Newton, based on the simplified assumptions that the Earth is entirely covered by water and that the water reacts instantaneously to the applied forces. The concept is still of use for the description of tidal phases. But before details are given, the starting points to obtain the TGF are Newton's law of motion and Newton's law of gravitation.

Newton's first law of motion describes that a body moves on a straight path with uniform speed when unaffected by external forces. The second law states that the magnitude of the applied force is connected to the rate of change of momentum with the acceleration acting in the direction of the applied force (Pugh and Woodworth, 2014). In addition, Newton's law of gravitation is essential to the description of the TGF. It considers two masses m_1 and m_2 and describes the emerging tractive (gravitational) force acting from m_1 onto m_2 as (see, e.g., Pugh and Woodworth, 2014)

$$\text{Force} = G\frac{m_1 m_2}{r^2}. \tag{2.3}$$

Following Equation 2.3, the tractive force depends on the inverse squared distance r between the two masses, just as it is proportional to the masses themselves. G is the universal gravitational constant. In this formulation, relativistic effects are neglected, as is justified for tidal considerations (Pugh and Woodworth, 2014). When referring to the ocean tides on the Earth, the gravitational attraction of the Moon is greatest, as it is the celestial body closest to Earth. Therefore, when only considering the Earth and the Moon, m_1 and m_2 in Equation 2.3 are the masses of the Earth and the Moon, respectively. The gravitational attraction of the Moon displaces the water masses of the ocean (and also the solid Earth, but this is not of direct importance here). Consequently, a tidal 'bulge' of water forms directly beneath the Moon. The Moon's tractive force acts onto the whole Earth body and affects also the opposite side, by pulling in its direction. However, the gravitational pull is less strong on the opposite side of the Earth, since it is located farther away from the Moon.

We now allow the Moon to orbit around the Earth in one siderial period of 27.32 days (Pugh and Woodworth, 2014). Taking a closer look at the movement of the Moon around the Earth, the two celestial bodies move in fact around their common center of mass. In the case of Earth and Moon, the common center of mass lies within the Earth, which is exemplary marked in Figure 2.8a. A centrifugal acceleration thus exists in the Earth-Moon coordinate system. This centrifugal acceleration is equal everywhere on the Earth's surface (Figure 2.8a, blue arrows). The interplay between the gravitational pull and the centrifugal (fictitious) force forms the TGF. On the side of the Earth, looking away from the Moon, the centrifugal acceleration is greater than the gravitational attraction. On the Earth's side facing the Moon, the two accelerations combine. Consequently, two tidal bulges form, one directly beneath the Moon, and one on the opposite side (Figure 2.8, red arrows). Intuitively one would assume the vertical component to account for the tidal bulges forming on the Earth, but the vertical component of the force is too small in comparison to the downward directed gravitational attraction of the Earth. Hence, the horizontal (i.e., tangential) component of the TGF imparted onto the Earth's surface is the reason for tidal water movements, while the vertical component of the Moons's TGF can be neglected (Ward et al., 2023). Overall, the TGF is derived from the tide-generating potential (TGP) of a body as its gradient

$$\text{TGF} = \nabla_h \text{TGP}. \tag{2.4}$$

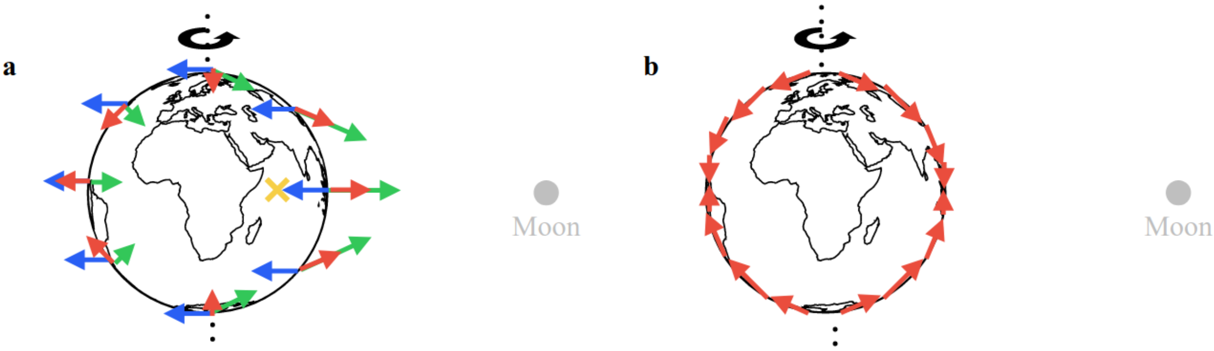

Figure 2.8: The TGF from the Moon acting onto the Earth (simplified and not to scale). Panel **a** shows the gravitational force induced by the Moon (green arrows) and the fictitious centrifugal acceleration (blue arrows). Their difference yields the TGF (red arrows). The common center of mass of the Earth-Moon system is indicated by the yellow cross. Panel **b** shows the horizontal component of the TGF. Inspired by Pugh and Woodworth (2014) and Ward et al. (2023).

As discussed above in the case of the Earth and the Moon, the horizontal gradient of the TGP forms the TGF, as illustrated in Figure 2.8b.

As the Earth is rotating around its own axis, it rotates underneath the tidal pattern generated by the Moon. For an arbitrary point on Earth, this results in a semidiurnal tide, that is the passage of two tidal highs and two tidal lows per day. One specific detail is of importance here: As the Earth performs one rotation around itself, the Moon has moved forward on its own orbit around the Earth by 1/28. An extra 50 minutes add to the 24 hours due to the time for the Earth to 'catch up' the Moon, which is 1/28 of one day (Pugh and Woodworth, 2014). Therefore, for a given location on the Earth, the two tidal highs are 12 hours and 25 minutes apart from each other. The Moon's semidiurnal tide is called M_2.

In general, a measured tidal signal can be characterized as a sum of several harmonic oscillations, the "tidal constituents". Over 600 tidal constituents can be separated, each as an individual harmonic with a fixed period (Ward et al., 2023). In 1921, the tidal potential was first mathematically decomposed into individual harmonics by Doodson (Doodson and Lamb, 1921). The theory was confirmed and improved to greater accuracy by Cartwright and Edden (1973). A limited overview of tidal constituents is given by Table 2.1. In the context of this work, especially the specified M_2, S_2, K_1, and O_1 components are important. But how come the individual tidal constituents?

In reality, the Moon's orbit is inclined with respect to the Earth's equatorial plane by 28.5°. This lunar declination varies within one full orbit of the Moon around the Earth between ±28.5° and induces modulations to the simple picture of the two bulges described above. Specifically, an arbitrary point on the Earth's surface will see an asymmetry in the tidal signal. Because of the lunar declination and its changes, locations on Earth exist where diurnal tides are observed as the major tidal signal. The diurnal tide arises from the daily tidal asymmetry, or inequality. The diurnal tide reaches its maximum when the lunar declination is also at maximum. When the Moon passes through the equator at zero declination, the diurnal amplitude is zero. In contrast, the relation between the semidiurnal amplitude and the lunar declination behaves inverse, e.g., when the lunar declination is zero, the semidiurnal amplitude is at maximum.

As a consequence of the solar declination (23.5°), solar diurnal tidal constituents are also induced.

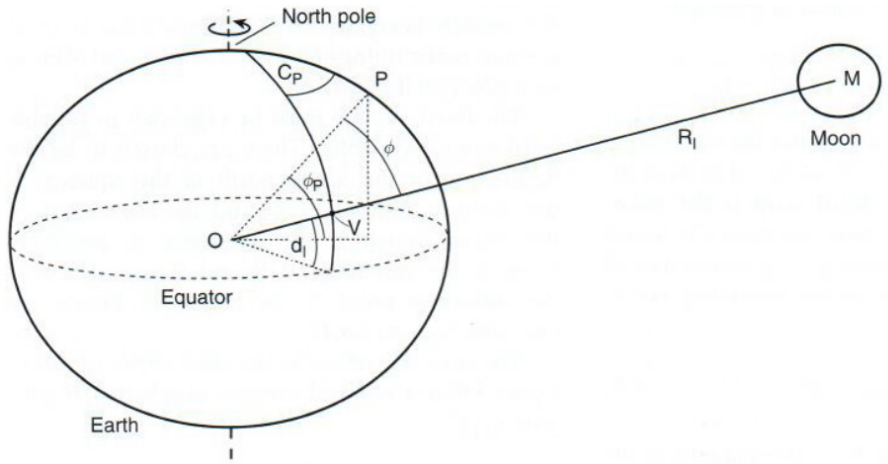

Figure 2.9: Illustration of the location of point P and variables used in Equation 2.5, taken from Pugh and Woodworth (2014) (their Figure 3.6).

The largest solar semidiurnal tides can be observed when the Sun is located directly over the equator, at the equinoxes (Ward et al., 2023).

Despite the larger mass of the Sun in comparison to that of the Moon, the huge distance between Earth and Sun induces a weaker TGF. The solar TGF is smaller by a factor ~0.46 compared to the TGF of the Moon in the equilibrium tidal theory (Ward et al., 2023). The semidiurnal amplitude S_2 acts onto the Earth with a period of half a solar day (12 hours). The semidiurnal lunar M_2 and solar S_2 tide combine in a spring-neap-cycle, which produces a fortnightly increase and decrease in the combined tidal amplitude. During spring tides, the lunar and solar TGFs combine together as Sun, Moon and Earth are in one line, whilst during neap tide they are out of phase—Sun, Moon, and Earth are in quadrature—and weaken the combined tidal amplitude (Pugh and Woodworth, 2014).

The described *equilibrium tide* can be mathematically expressed as a free surface height η_{EQ} over the sphere considering volume conservation, here taken from Pugh and Woodworth (2014), induced by the lunar (subscript $_l$) TGF, as

$$\begin{aligned}
\eta_{EQ} &= a\frac{m_l}{m_e}\left[C_0(t)\left(\frac{3}{2}\sin^2\phi_p - \frac{1}{2}\right) + C_1(t)\sin 2\phi_p + C_2(t)\cos^2\phi_p\right] \\
C_0(t) &= \left(\frac{a}{r_l}\right)^3\left(\frac{3}{2}\sin^2 d_l - \frac{1}{2}\right) \\
C_1(t) &= \left(\frac{a}{r_l}\right)^3\left(\frac{3}{4}\sin 2d_l \cos C_p\right) \\
C_2(t) &= \left(\frac{a}{r_l}\right)^3\left(\frac{3}{4}\cos^2 d_l \cos 2C_p\right).
\end{aligned} \tag{2.5}$$

Figure 2.9 illustrates the variables used in Equation 2.5. Here, C_0, C_1 and C_2 are time-dependent coefficients relative to the tidal cycle and represent, in the same order, long period tides, diurnal tides and semidiurnal tides induced by the Moon. The coefficients are dependent on the inverse cube of lunar distance r_l and on the lunar declination d_l. The involved celestial body masses are given by the lunar mass m_l and the Earth's mass m_e. Another parameter related to the Earth-Moon system is the angle ϕ_p, indicating the angle between a point directly beneath the Moon on the Earth and an arbitrary point P on the Earth's surface, so in fact, the latitude of point P.

The hour angle of P is C_p and a is the Earth's radius. The long period tides, not discussed until here, occur on time scales longer than one day (Pugh and Woodworth, 2014). The equilibrium tidal amplitudes of selected tidal constituents are displayed in Table 2.1. Equation 2.5 can be adapted for the solar TGF by replacing the mass m_l, the declination d_l, and the distance r_l by the corresponding values for the Sun instead of the Moon (Pugh and Woodworth, 2014).

In reality, several additional characteristics add to this basic concept. The tidal energy is at the same frequencies as predicted by equilibrium tidal theory, but the produced amplitudes are too small and the tidal phases attain spatially heterogeneous patterns. This is due to the neglect of the effects of Earth rotation, landmasses (even islands) that interrupt the propagation of the tidal signal, and the finite water depth of the oceans, amongst other factors. Nevertheless, the equilibrium tidal theory is useful as a reference for observed harmonics in tidal analysis (Pugh and Woodworth, 2014).

Table 2.1: Selected tidal constituents. Adapted from Ward et al. (2023).

	Name		η_{EQ} (cm)^a	Rel. Amp.^{b}	ω ($10^{-4}\,\mathrm{s}^{-1}$)^c	Period (h)
Semidiurnal	Principle lunar	M_2	24	1.0000	1.405 189	12.42
	Principle solar	S_2	11	0.4656	1.454 441	12.00
Diurnal	Principle lunar	K_1	14	0.5842	0.729 211 7	23.93
	Principle solar	O_1	10	0.4148	0.675 977 4	25.82
Long period	Fortnightly	Mf	4	0.1722	0.053 234	327.85
	Monthly	Mm	2	0.0909	0.026 392	661.31

^{a,c}Arbic et al. (2004), ^{b}Amplitudes expressed relative to M_2, ^{c}Angular frequency

2.2.2 Dynamic Theory of Tides

The tides of the actual ocean do not behave as equilibrium tides, as indicated at the end of Section 2.2.1. Due to friction and slow wave speed, the equilibrium tides cannot keep up with the Earth's rotation. The important characteristic of ocean tides, absent from the equilibrium tidal theory, is their propagation as so-called shallow water waves. Per definition, ocean tides are waves with a very long forced period, and thus wavelength. The period of the tidal wave equals the period of the forcing. In addition, the magnitude of the forcing determines the height of the waves. This is due to the relation of increasing energy (from forcing) in shallow water waves with the squared wave height (Ward et al., 2023). The distinction between shallow water waves and deep water waves is defined by the ratio between wavelength and the depth of the medium they propagate through. Deep water waves are defined to propagate in water that is deeper than 1/2 wavelength (Ward et al., 2023). This is not the case for ocean tides, since the world's ocean have an average depth of 4000 m, which is smaller than twice the tidal wavelength (Ward et al., 2023).

Equilibrium tidal theory further neglects the existence of underwater topography. The interaction with the seafloor in turn leads to friction between the tidal wave and the bathymetry, which makes it impossible for the ocean tides to exactly follow the Earth's rotation. This can be verified with the formula for the propagation speed, c, of a surface shallow water wave (Ward et al., 2023),

$$c = \sqrt{gH}. \tag{2.6}$$

Here, g is the gravitational acceleration and H is the water depth. This relation indicates that the tide is not able to maintain an equilibrium with the forcing, since the speed is limited by the water depth (Ward et al., 2023). Along with the propagation speed, also the wavelength L depends on gravity and water depth,

$$L = cT, \tag{2.7}$$

with T being the wave's period that is inherited by the tidal forcing. The maximum current speed u_{max} of a shallow water wave is

$$u_{max} = \eta\sqrt{\frac{g}{H}}, \tag{2.8}$$

where η is the tidal amplitude (Ward et al., 2023). The currents under the wave crests flow in the direction of propagation, while the ones under the troughs behave in the opposite way. A mathematical description of ocean tides as shallow water waves is given by the *Shallow water equations*. The partial differential equations are derived from the general *Navier-Stokes equations*, that describe a fluid in motion, through the prescription of boundary conditions and integration. The Navier-Stokes equations originate from the equation of continuity (Equation 3.3), and the momentum equation that describes the conservation of linear momentum, see Section 3.1.

In addition, landmasses in north-south direction avoid undisturbed east-west propagation and cause resonance responses due to natural modes of oscillation (Blackledge et al., 2020). Besides different local resonance characteristics, basin wide resonances such as in the North Atlantic occur, too. The global ocean tidal behavior can be characterized as a coupled-oscillator model (Arbic and Garrett, 2010). Therefore, the large ocean basins can be resonant to individual frequencies. This can be achieved if the natural period of an ocean basin (spatial size and depth) correspond to half a wavelength of the propagating tidal wave (Arbic et al., 2009a; Green, 2010). The semidiurnal tidal frequencies nearly correspond to the natural resonance of the world's ocean basins, resulting in larger semidiurnal tidal amplitudes compared to the equilibrium tide (Pugh and Woodworth, 2014; Arbic et al., 2009a). The amplitudes and phase lags for M_2 and K_1 are illustrated in Figure 2.10, showing larger amplitudes of the semidiurnal tide in contrast to the diurnal tide. Not only do resonances amplify the tidal amplitude, but a resonant ocean basin or shelf geometry can affect, respectively, the ocean or shelf tides through backeffects (Arbic and Garrett, 2010). The elastic response of the solid Earth to tidal forcing is another factor for more complicated tidal behavior and can be characterized with Love numbers (Munk and MacDonald, 1960; Hendershott, 1972).

Furthermore, equilibrium tidal theory neglects the Coriolis acceleration. When the Earth's rotation around its own axis is regarded in an Earth-fixed coordinate system, it induces an acceleration that deflects moving objects from a straight path. The deflection of the moving object occurs to the right/clockwise (left/counterclockwise) for the Northern (Southern) hemisphere (Ward et al., 2023) and is also proportional to the speed of the moving object (Knauss and Garfield, 2016). This is called Coriolis acceleration and acts as a fictitious (i.e., pseudo) force, since it only acts on moving objects within a rotating coordinate system (like the centrifugal acceleration). Tidal currents are moving relative to the Earth and are therefore altered by Coriolis acceleration. In general, the deflection of the tidal currents (hereafter: Northern hemisphere) leads to accumulation of water at the right boundary of the ocean basin. This results in an inclination of the sea surface and produces a pressure gradient force. The inclination of the surface reaches equilibrium by balancing the Earth's rotation, which is called geostrophic force

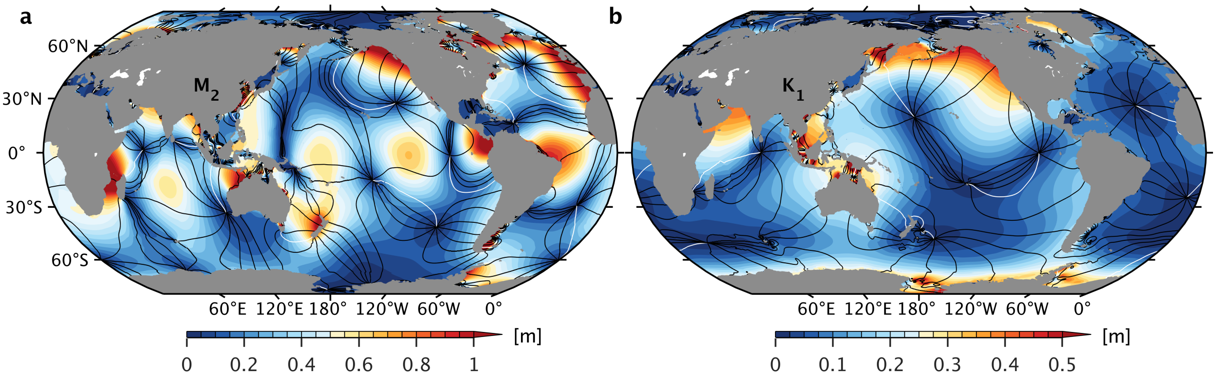

Figure 2.10: Co-tidal charts of M_2 **a** and K_1 **b**, with data from TPXO9-atlas (updated version of Egbert and Erofeeva, 2002). Colors represent the amplitude and black lines show the phase lag every 30°, with phase lags of 0° indicated in white.

(Pugh and Woodworth, 2014).

Through this acceleration, different types of waves form, all characterized as long waves with periods exceeding several hours, e.g., *Kelvin waves*, *inertia gravity (Poincaré) waves*, or *Rossby waves* (Knauss and Garfield, 2016). Kelvin waves, illustrated in Figure 2.11, are important in the consideration of tidal dynamics. They originate from a propagating long wave and are deflected by the Coriolis acceleration on their path. The accumulation of water on the right side (Northern Hemisphere) leads to an altered wave movement. Kelvin waves travel parallel to coastal boundaries. In the Northern (Southern) Hemisphere, the water deflection to the right (left) side leads to an counterclockwise (clockwise) movement of the wave along the coastline, with the maximum amplitude directly at the boundary (Knauss and Garfield, 2016). The waves are deflected westward (eastward) when meeting either lateral coastlines or, due to the latitude dependence of the Coriolis acceleration, the equator. Kelvin waves and Poincaré waves consider constant Coriolis acceleration (no latitude dependence). Poincaré waves are dispersive, meaning their speed depends on their wave frequency. While the wave frequency is greater than the Coriolis parameter, an elliptical water movement is induced (Knauss and Garfield, 2016). Otherwise, the wave frequency becomes too small to be affected by the Coriolis acceleration. In contrast, the dispersive Rossby waves include the latitude dependence of the Coriolis acceleration. Due to a change in latitude of a water particle and consequently a change in Coriolis acceleration, a change in potential vorticity is evoked. The potential vorticity is proportional to the change in latitude (Knauss and Garfield, 2016).

The dynamic theory of tides improves the equilibrium tidal theory by including several of the afore-mentioned physical properties, particularly the effects of currents and tidal motion. The theory originates from the *Laplace tidal equations* found in 1799 by Pierre-Simon Laplace. It includes the hydrodynamic equations of continuity and momentum, considering a fluid within a rotating Earth-fixed coordinate system (Pugh and Woodworth, 2014). Assumptions made are a spherical Earth body that induces a gravitational force from a geocentric point. This results in the TGF being homogeneous in both horizontal and vertical direction. One major finding of the theory is the dependence of tides on water depth (Pugh and Woodworth, 2014).

Defined on a sphere, the Laplace tidal equations represent a linear version of the general Navier-Stokes equations, which describe a fluid in motion (Vreugdenhil, 2013). Mathematically, the Laplace tidal equations can be written as an interplay between the Coriolis acceleration, the pressure gradient force, and the horizontal TGF (Ward et al., 2023). Spatial and temporal

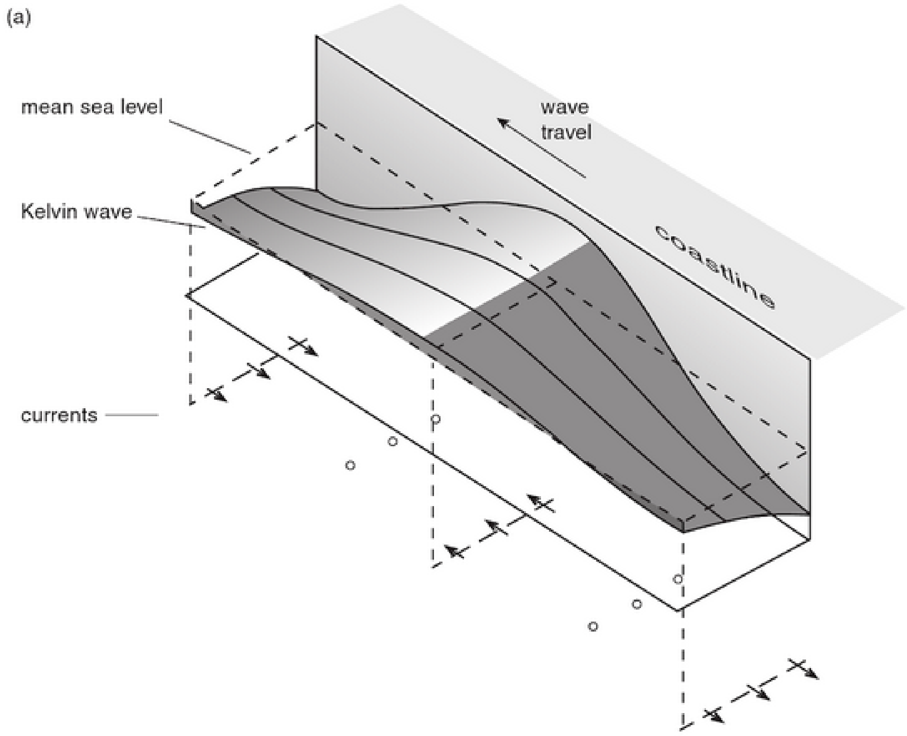

Figure 2.11: Kelvin wave dynamics, taken from Pugh and Woodworth (2014) (their Figure 3.6a). The three-dimensional elevation and the currents are illustrated, running parallel to a coast (northern hemisphere).

variations are present. Equation 2.9 shows the hydrodynamic relation in vectorized form (for Cartesian coordinates see Ward et al., 2023), depth-integrated, and for a motion of unit mass of water

$$\begin{aligned}&\frac{\mathrm{D}\mathbf{u}}{\mathrm{D}t} + f \times \mathbf{u} = -g\nabla_h \eta + \mathbf{F}_h \\ &\partial_t \eta + H(\nabla_h \cdot \mathbf{u}) = 0.\end{aligned} \tag{2.9}$$

In general, x, y, z are the Cartesian coordinate directions in a local coordinate system with the three axes pointing to the East (x), North (y), and local zenith (z), while $\mathbf{U}$ describes the flow velocities in all three coordinate directions. In Equation 2.9, the depth-averaged velocity $\mathbf{u} = \begin{bmatrix} u & v \end{bmatrix}^T$ is along the x/y direction and the Lagrangian acceleration, i.e. the total derivative with respect to space and time, is included as ${}^{\mathrm{D}\mathbf{u}}/_{\mathrm{D}t}$. Vertical velocities are assumed to be negligible. The Coriolis parameter is included through f and varies with latitude. ∇_h denotes again the horizontal gradient operator and ∂_t is the partial derivative in time. The surface amplitude is given by η and the horizontal tidal forcing by $\mathbf{F}_h = \begin{bmatrix} F_x & F_y \end{bmatrix}^T$. Conservation of momentum is encapsulated by the first equation, while the second equation ensures conservation of mass. For the horizontal components, local and advective accelerations are included (through ${}^{\mathrm{D}\mathbf{u}}/_{\mathrm{D}t}$), as well as the Coriolis acceleration, the geostrophic force, and the TGF. By solving the Equations 2.9 for oscillating tidal forcing, a series of waves is obtained (Ward et al., 2023). Note, however, that the Laplace tidal equations neglect frictional forces, which remove energy from the global tidal oscillations.

An important form of tidal waves are standing wave systems. When an incoming wave is compressed at the continental shelf and reflected at the coastline, the incoming and reflected wave interact. If the shelf has spatial properties that fit to the wavelength, it can cause the two waves to form a standing wave (Ward et al., 2023). The described forces and water movements cause amphidromic systems of the ocean tides, which can be predicted by the dynamic theory of tides. Amphidromic points have zero tidal range and strong, rotating tidal currents (Ward et al., 2023). They are caused by a Kelvin wave that is deflected at the coastline and travels along it. The tidal amplitude rises with distance from the amphidromic point toward the coast where it is maximum.

2.2.3 Deformation and Gravitation Effects

A secondary force that already Pierre-Simon Laplace was aware of, is the self-attraction and loading (SAL) effect resulting from a yielding solid Earth and surface loads, meaning the redistribution of water masses and their self-gravitational potential in the global ocean's due to tides. Thus, the Laplace tidal equations need a modification to allow for an elastically deforming Earth body and the effects caused by the changing weight of the water column in the ocean, as described in Hendershott (1972).

On one hand, not only the oceans, but also the solid Earth body responds directly to the TGF. Including the tidal deformation of the solid Earth within the tide-raising potential allows for more accurate prediction of long-term tides (Thomson, 1863). The *body tide* is a latitude dependent, vertical, and elastically deformation with an amplitude of ~10 cm (Lau and Schindelegger, 2023). The perturbation effect of the body tide deformation on the gravitational potential can be mathematically described through a scale factor $(1 + k_2 - h_2)$, including the Love numbers k_2 and h_2 (e.g., Hendershott, 1972; Arbic et al., 2004), and is considered for η_{EQ} in Table 2.1. The scale factor differs for the individual tidal constituents, and is, e.g., 0.693 for M_2 and 0.736 for K_1 (Arbic et al., 2004).

On the other hand, redistribution of the ocean's water masses due to tides changes the weight of the water column, thus yielding the solid Earth and causing again a deformation of the body. A horizontal force arises, that is the *self-attraction and loading* (SAL), which is composed of three effects (e.g., Stepanov and Hughes, 2004) and is illustrated in Figure 2.12 for M_2 and K_1. First, the weight of the water column acts on the seafloor and generates a local depression in combination with an uplift of the seafloor further away from the load, causing a horizontal force directed in the direction of the depression. Second, the rearranged mass of the Earth results in a change of the gravitational field. Third, the anomalous mass of water induces a gravitational attraction of the surrounding water.

In general, the SAL tide reaches $\sim 1/10$ of the astronomical TGF (Hendershott, 1972), but is spatially more complex than the equilibrium tide. As evident from Equation 2.5, the gravitational potential (or η_{EQ}) is usually expressed in terms of low-degree spherical harmonics. By contrast, the SAL tide includes spatial scales of higher spherical harmonics depending on the instantaneous distribution of ocean masses (Hendershott, 1972). Therefore, the SAL tide has to be integrated into numerical ocean models using a convolution of instantaneous water levels over the global Earth's surface through numerical Green's function (e.g., Hendershott, 1972) or a quasi-spectral formulation based on spherical harmonics (Schindelegger et al., 2018). When using spherical harmonics, the advantage is that the costly convolution becomes a multiplication. A mathematical formulation following Ray (1998), who highlighted the importance of including

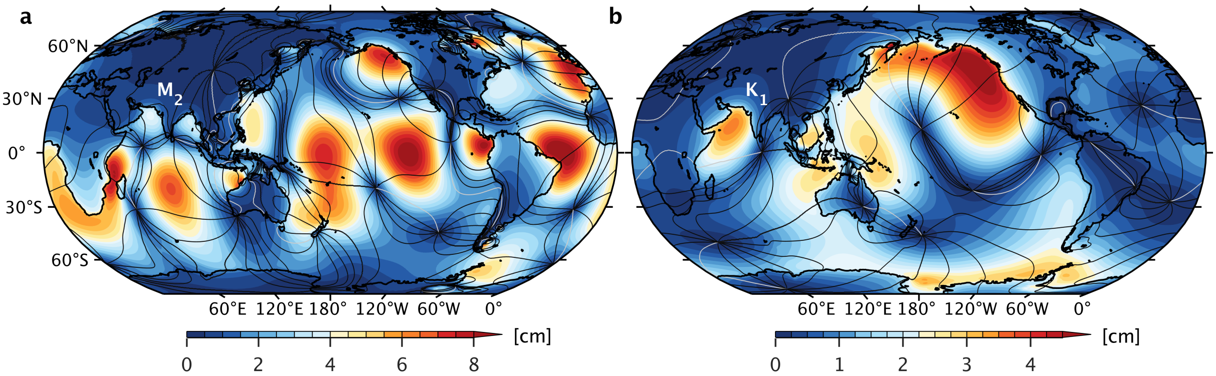

Figure 2.12: Co-tidal charts of the SAL tide of M_2 **a** and K_1 **b**, based on the application of a spherical harmonic formulation (Ray, 1998) to the individual tidal constituents's in-phase and quadrature components from the TPXO9-atlas (updated version of Egbert and Erofeeva, 2002). Colors represent the amplitude and dark gray lines show the phase lag every 30°, with phase lags of 0° indicated in light gray.

SAL terms for accurate numerical ocean modeling, is

$$\eta_{SAL,nm} = \frac{3\rho_w\,(1 + k'_n - h'_n)}{\rho_e\,(2n+1)}\eta_{nm}. \tag{2.10}$$

Here, n, m are the degree and order of the spherical harmonics, ρ_w, ρ_e are mean densities of seawater and Earth's body, whilst η_{nm} is the instantaneous tidal elevation expanded in spherical harmonics. The load Love numbers are k'_n, accounting for the gravitational effect of the deformed Earth, and h'_n, accounting for the deformation of the Earth due to loading (Munk and MacDonald, 1960).

2.2.4 Barotropic and Baroclinic Tide

The periodic tidal water movements, forced directly by the Sun and the Moon, can be characterized as depth-independent and 2D. This condition is referred to as the *barotropic tide*. The gravitational forces cause a given water column of the ocean to harmonically oscillate in the same direction (Ward et al., 2023). The currents coming with this oscillation, meaning both their speed and direction, are vertically invariant. In such a barotropic fluid, the density is solely determined by the pressure. Therefore, the isopycnals (surfaces of constant density) and isobars (surfaces of constant pressure) do not cross each other (Knauss and Garfield, 2016). A fluid with constant density throughout the water column is homogeneous. If a barotropic fluid is stratified and the density changes with depth, the isopycnals and isobars are parallel. The associated barotropic currents cause a vertically uniform, non-divergent and incompressible flow (Ward et al., 2023). Figure 2.13 shows an exemplary pattern of the semidiurnal M_2 barotropic tidal component oscillating around Madagascar in the South Indian Ocean. The tidal amplitude variations in the range of ± 1 m are clearly visible, which repeat themselves every $\sim$12 h and 25 min.

Besides the 2D barotropic tide, that is coherent with the astronomical forcing, a second type of tidal flow exists within the stratified ocean: the *baroclinic tide*. In baroclinic conditions, isobars and isopycnals are not parallel to each other and the isobars are also not parallel to themselves (Knauss and Garfield, 2016). Therefore, baroclinic flows are 3D and depth-dependent. The

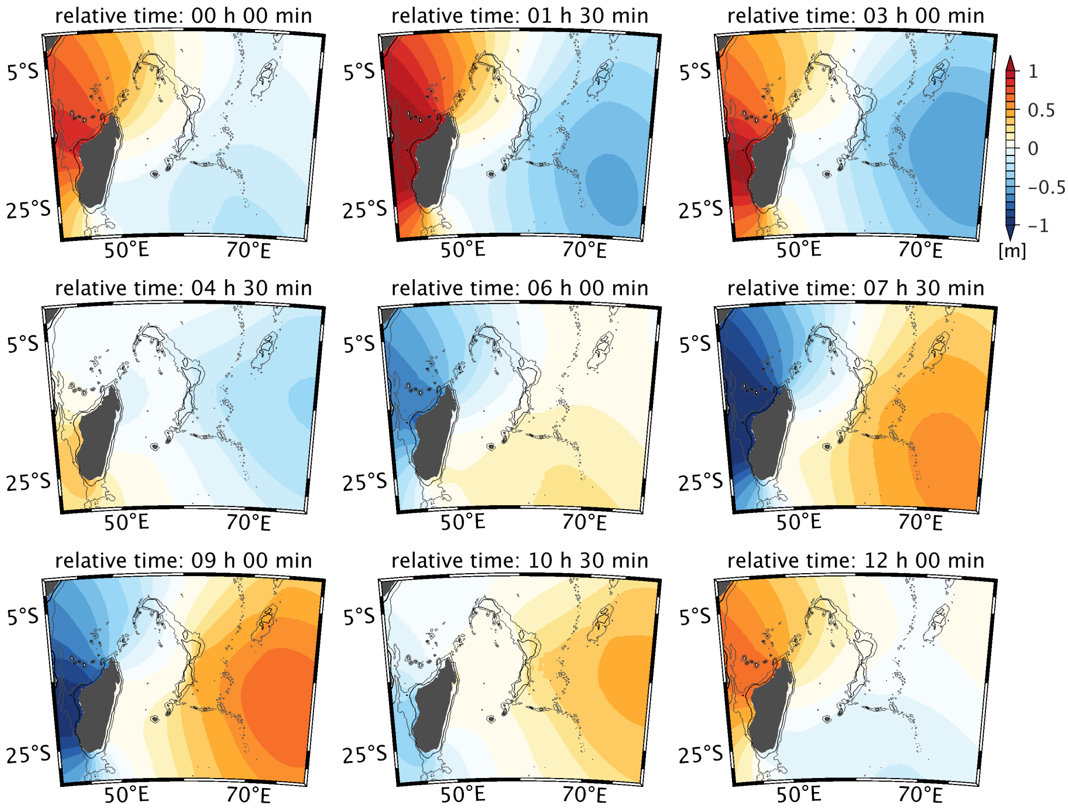

Figure 2.13: Barotropic M_2 oscillation in the South Indian Ocean. The contour lines connect points at the seafloor at depths of 500 m and 2500 m.

density of the fluid varies horizontally and vertically, which causes the current velocity to be a function of ocean depth (Ward et al., 2023). In fact, the ocean is a highly baroclinic fluid (Knauss and Garfield, 2016). Often, baroclinic tides are also referred to as *internal tides*, which reflects the definition as internal gravity waves at tidal frequencies (Garrett, 2003).

The generation of the baroclinic tide requires two factors, which are a stratified fluid and underwater topography meeting the flow direction. As the ocean is a stratified fluid, layers of different density are separated, forming internal interfaces. The baroclinic tide is generated by flow of the barotropic tide over steep or rough underwater topography (Wunsch, 1975; Munk, 1981; Baines, 1982). The ocean bottom topography forces the parallel density layers to move vertically upward the topographic feature and also again downward on its other side. This deflection in the vertical induces oscillations of the distinct internal interfaces, since the denser and heavier water, that has been deflected upward into lighter water conditions then moves down due to action of gravity. This causes high-frequency fluctuations in the density distribution of the ocean (Arbic et al., 2018). The wave like, vertical oscillation is greatest in amplitude near the generation site. The amplitudes can reach 50 m within the ocean, but are typically only a few centimeter at the surface. The corresponding currents are large in comparison, reaching velocities greater than $2\,\mathrm{m\,s^{-1}}$ (Arbic et al., 2012). The internal waves propagate away from the generation site with typical speeds of $\sim 1\,\mathrm{m\,s^{-1}}$ (Arbic et al., 2012), much slower than the barotropic tide. Due to their low speed, these waves can take days to propagate through an ocean basin. Generally, they travel long distances up to thousands of kilometers (Ray and Mitchum, 1996, 1997; Dushaw et al., 1995). On their propagating path, the phase of the currents is modified by irregular (e.g., wind-driven) currents, eddies, or density variations before they decay, break, or interact with similar waves from other generation sites (Pugh and Woodworth, 2014; Arbic et al., 2012). In general, generation sites can be deep ocean ridges, seamounts, continental shelf edges, or islands.

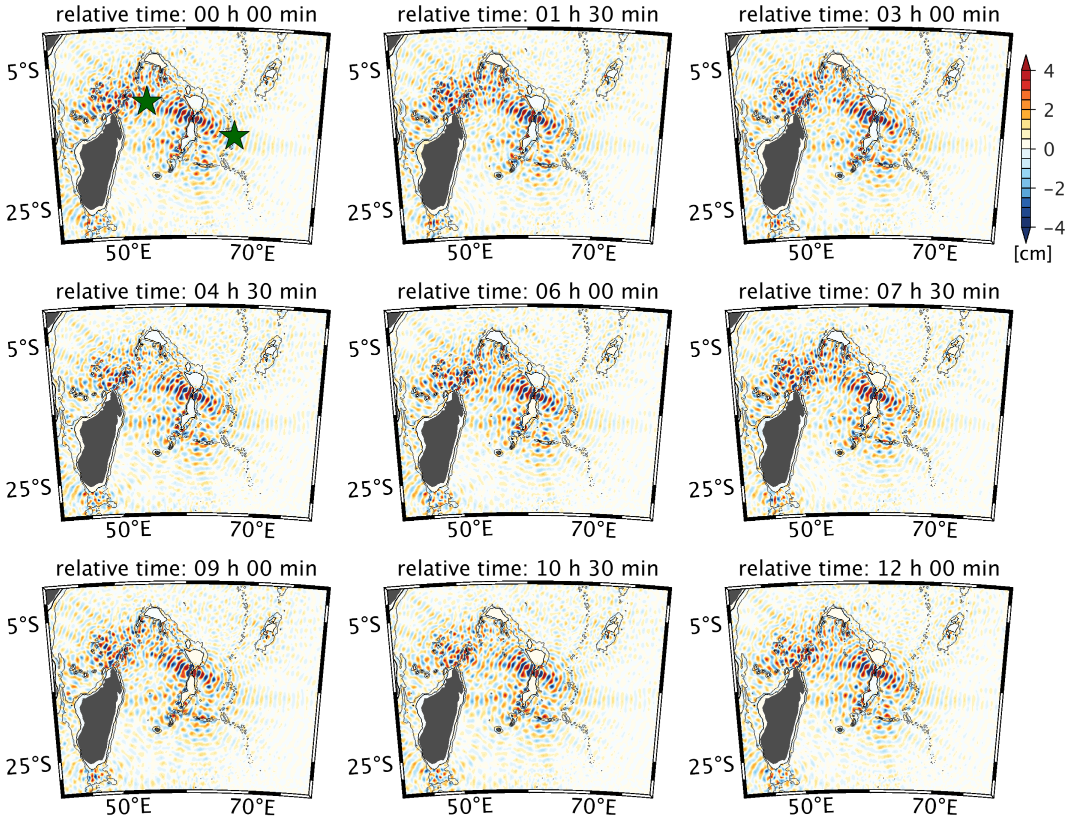

Figure 2.14: Baroclinic M_2 oscillation in the South Indian Ocean. Same as in Figure 2.13, but for the baroclinic tidal component. The green stars mark the endpoints of the transect of Figure 2.15.

Figure 2.14 displays the baroclinic tidal component corresponding to the barotropic tide in Figure 2.13. Surface manifestations of the internal tides on the order of a few centimeters can be observed, centered around the Mascarene Ridge. They propagate away from the location of generation with decreasing amplitude. The ratio of surface displacement and the counterpart within the ocean between distinct levels of density is highlighted in Figure 2.15. The isopycnal displacement, computed as in Gerkema and van Haren (2007), shows the large magnitude of the oscillations within the ocean's interior, in contrast to their small size at the surface.

Internal tides are incoherent—i.e., not phase-locked—with the astronomical forcing (Arbic et al., 2012). Nevertheless, their generation depends on the barotropic tide forced by Moon and Sun. Therefore, the internal tides and associated currents are strongest during spring tides. In addition, the density of seawater varies with the seasons (cf. Section 2.1.1), which in turn influences the generation of internal tides (Pugh and Woodworth, 2014). Theoretically, progressive internal waves are unable to propagate through their frequency-dependent *critical latitude*, that is determined by the ratio of Coriolis acceleration and the wave's frequency (Rainville and Pinkel, 2006; Zhao et al., 2012). For the M_2 tide, the critical latitude is 74° and for K_1 it is 30°. Nevertheless, observations of semidiurnal bottom-trapped internal tides have been made poleward of 74° (Albrecht et al., 2006).

The TGF inputs a significant amount of mechanical energy into the Earth system, particularly to the barotropic tide. The transfer of energy from the barotropic to the baroclinic tide is discussed in Section 2.3. Overall, the small-scale processes of generation, propagation, and dissipation of

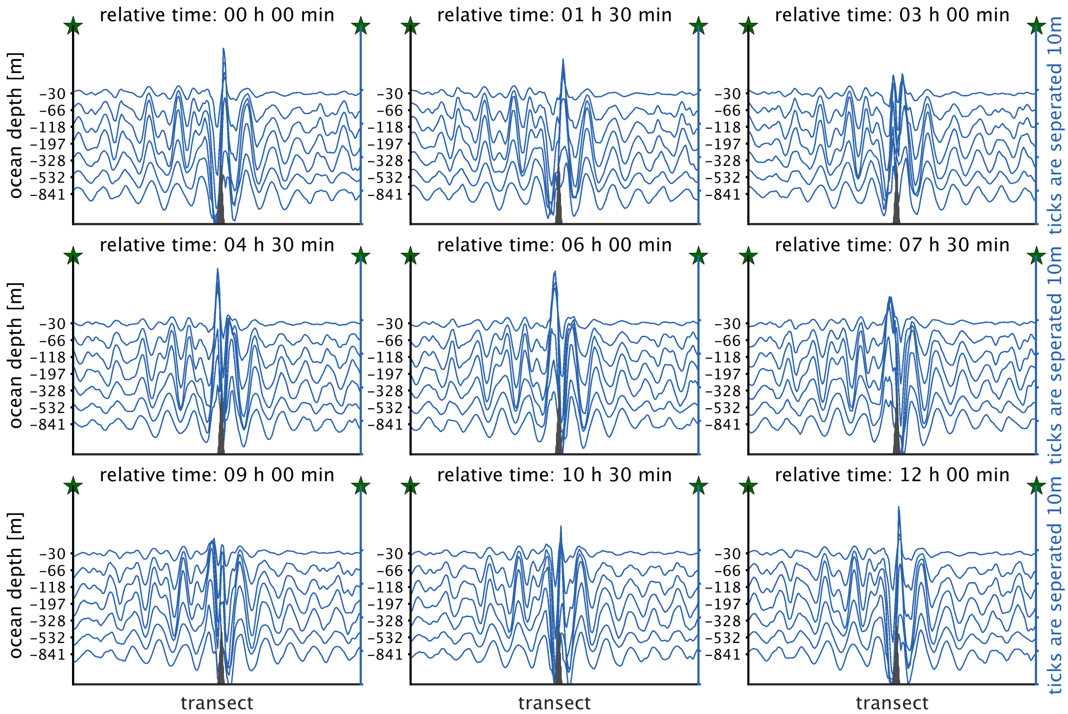

Figure 2.15: Isopycnal displacement of M_2 at the Mascarene Ridge. Corresponding to Figures 2.13 and 2.14 along one transect. The endpoints of the transect are shown in Figure 2.14.

internal tides is of major importance for oceanic diapycnal mixing. Vertical mixing, in turn, is thought to be an essential process for maintaining the deep-ocean circulation (Vic et al., 2019). Therefore, tides assume an important role when discussing the large-scale, low-frequency ocean circulation and thus the climate controls of the Earth (Munk, 1966; Wunsch and Ferrari, 2004).

2.3 Tidal Energetics

This sections highlights salient aspects of tidal energetics. The TGF and the resulting ocean tides represent a huge energy input into the global ocean system. The way that energy is drained from the system will be described below.

2.3.1 Friction and Dissipation

The Earth's rotation around its own axis is slowed down by the TGF through *tidal friction*, slightly increasing the length of day. The deceleration of Earth's rotation transfers part of the angular momentum from the Earth to the Moon. This transfer can be observed with lunar laser ranging as the rate of the Moon's increasing orbit by $3.82 \pm 0.07\,\mathrm{cm\,year^{-1}}$ (Munk and Wunsch, 1998). That secular recession of the Moon is directly proportional to the global tidal dissipation rate (e.g., Farhat et al., 2022). Following Egbert and Ray (2001), the ocean tides account for a rate of approximately 3.5 TW energy loss, making up most of the total planetary energy loss of about 3.7 TW. The remaining 0.2 TW are lost in processes of friction from atmospheric and solid Earth tides (Platzman, 1984).

In general, the dissipation rate (D) of tidal energy, taken either at a location or as a global sum, can be assessed through different mathematical approaches. One approach estimates D locally as the difference of work done by the TGF (W) and the net input flux of tidal energy ($\mathbf{P}$). Following Egbert and Ray (2000), the general formulation of local balances is

$$D = W - \nabla_h \cdot \mathbf{P}. \tag{2.11}$$

Here, W and $\mathbf{P}$ are time averaged quantities, as indicated by $\langle\rangle$, reading

$$\begin{aligned} \mathbf{P} &= \overline{\rho_0} g \Big\langle \mathbf{V}\zeta \Big\rangle \\ W &= \overline{\rho_0} g \Big\langle \mathbf{V} \cdot \nabla_h \left(\eta_{EQ} + \eta_{SAL}\right) \Big\rangle \end{aligned} \tag{2.12}$$

where $\overline{\rho_0}$ is a mean seawater density, g represents the gravitational acceleration, $\mathbf{V}$ denotes the volume transport, and the surface amplitude is composed of the equilibrium and SAL tide.

A second approach evaluates friction, as well as viscosity terms directly within the model to estimate D again as 2D field. This method can be fairly intricate and depends on the details of the chosen frictional closures and parameterizations. The third approach makes use of global integration of the rate of working of tidal forces on the ocean tide (Platzman, 1984; Egbert and Ray, 2001). The global dissipation rate at semidiurnal frequencies is estimated as follows

$$D = (24\pi/5)^{1/2}\, G\, m_e\, \tilde{\eta}\, \overline{\rho_0} \left(1 + k_2'\right) \omega\, D_{22}^{+} \sin\psi_{22}^{+} \quad [\mathrm{W}] \tag{2.13}$$

where ω represents the frequency, G the gravitational constant and m_e the Earth's mass. $\tilde{\eta}$ is the tidal constituent's potential amplitude (e.g., Cartwright and Edden, 1973, in length units), k_2' is the degree-2 load Love number, and $\left(D_{22}^{+}, \psi_{22}^{+}\right)$ denote the amplitudes and phase lags of the degree-2, order-2 prograde components of the ocean tide. The expression for diurnal constituents is identical to Equation 2.13 but require degree-2, order-1 spherical harmonics $\left(D_{21}^{+}, \psi_{21}^{+}\right)$ and the factor $(6\pi/5)^{1/2}$ instead of $(24\pi/5)^{1/2}$.

A major sink for the tidal energy in the world's ocean is *bottom friction*, typically parameterized in models as $\mathcal{F}_b = (\mathrm{C}_d||\mathbf{U}||/H)\,\mathbf{V}$ (e.g., Egbert et al., 2004). The non-dimensional bottom drag coefficient C_d is typically chosen as $\sim$0.003 in literature (e.g., Arbic et al., 2009b). The implied frictional force is quadratic, as it increases with the squared speed of flow (Ward et al., 2023). Especially in shallow seas, where tidal currents are fast, boundary layer friction drains a substantial amount of energy from the flow. The energy gets lost in turbulence and is able to alter stratification conditions in shallow water (Pugh and Woodworth, 2014). Dissipation through bottom friction is mainly concentrated in basin areas that are resonant with the global ocean tides (Taylor, 1920; Egbert and Ray, 2001). Several regions are known to contribute more than others, comprising, e.g., the southwestern Indian Ocean or the Mid Atlantic Ridge (Pugh and Woodworth, 2014). On a local level, tidal friction is known to shift the position of amphidromic points, since a reflected, outgoing Kelvin wave will lose energy in comparison to the incoming wave in a semi-enclosed basin (Rienecker and Teubner, 1980; Opel et al., 2025). For a long time, bottom friction was believed to be the only sink for tidal energy. However, with the aid of satellite altimeter observations, dissipation through generation of internal tides in the deep ocean was found to be another important energy sink (cf. the following Section 2.3.2). For the semidiurnal tides, the ratio of energy dissipation in shallow regions versus the deep ocean is approximately 3:1, while for diurnal tides, shallow regions account for $\sim$90 % of the global energy dissipation (Egbert and Ray, 2001), as shown in Figure 2.16.

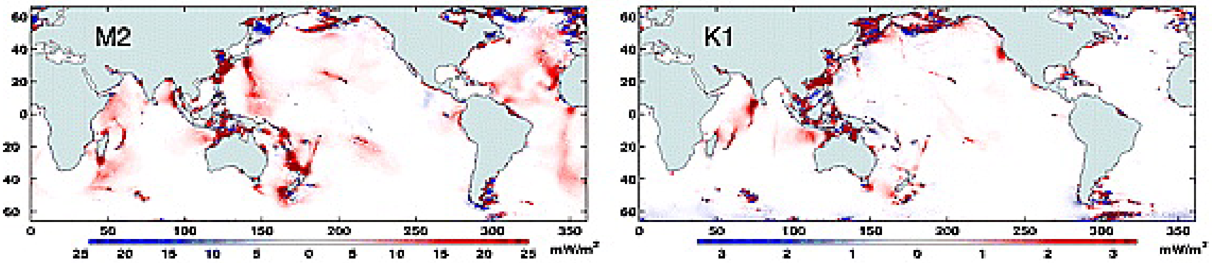

Figure 2.16: Dissipation maps of M_2 and K_1, taken form Egbert and Ray (2003) (their Figure 1).

2.3.2 Tidal Conversion

Substantial energy transfer occurs between the barotropic and baroclinic tidal component. In contrast to the small amplitude of internal tides at the surface, their amplitude is much greater within the ocean (cf. Section 2.2.4). Moreover, they contain a substantial amount of mechanical energy that is substantial for vertical ocean mixing which partly maintains the global meridional overturning circulation (e.g., Wunsch and Ferrari, 2004). This energy is extracted from the barotropic tide during the generation of internal tides over sloping ocean bottom topography (cf. Section 2.2.4). Hence, the barotropic tide loses energy that is transferred to the baroclinic tide, which is referred to as *tidal conversion* (Nycander, 2005; Vic et al., 2018). Therefore, changes in the barotropic tides may go along with changes in the baroclinic tide, which are themselves linked to the ocean's density distribution.

Part of the barotropic tidal energy is already dissipated through bed friction within the process of tidal conversion directly at the generation sites. The rest of energy is transferred to the internal tides and transported up to thousands of kilometers through the ocean basins on the propagation path. While energy losses can also occur along the path itself, the baroclinic tides propagate until they break or dissipate their energy, which can occur far away from the actual generation site (Alford, 2003; Zhao et al., 2016).

To quantify the barotropic-to-baroclinic energy converison, one first evaluates the barotropic velocity $\mathbf{u} = (u, v)$, computed as follows

$$\mathbf{u}(z,t) = \frac{1}{H}\int_{-H}^{0} \mathbf{U}(z,t)\mathrm{d}z\,, \tag{2.14}$$

where H is the resting water depth. The second relevant quantity is the baroclinic bottom pressure anomaly $p'_\mathrm{b}(t) = p'(z = -H, t)$ at the ocean bottom (described in detail in Section 4.1.2). The combination of $\mathbf{u}(z,t)$ and $p'_b(t)$ yields the depth integrated barotropic-to-baroclinic energy conversion rate C (e.g., Buijsman et al., 2012)

$$C \approx -\Big\langle \nabla_h H \cdot \mathbf{u}(t) p'_\mathrm{b}(t) \Big\rangle\,. \tag{2.15}$$

As apparent from this expression, the gradients of the bathymetry ∇H affect the amount of energy conversion. The globally integrated conversion rate for the deep ocean is estimated to be approximately 1 TW (Egbert and Ray, 2001), providing about one third of the total amount of energy of barotropic tide that is dissipated in the oceans.

Figure 2.17 presents the global spatial distribution of tidal conversion for the M_2 constituent, estimated from 3D model output of this work. Since energy conversion appears at underwater topography and rough bottom topography, the locations in Figure 2.17 with high conversion estimates, are regions known for complex bathymetry and topographic gradients (cf. Figure 3.4). Especially the West Pacific is a familiar hot-spot for tidal conversion, in particular Luzon Strait (e.g., Jan et al., 2007; Buijsman et al., 2012; Kerry et al., 2014; Wang et al., 2016). Besides others, the Mascarene Ridge, the Amazon Shelf break (Tchilibou et al., 2022) or the Northern Mid-Atlantic Ridge (Vic et al., 2018) are important generation sites. Modeled conversion estimates themselves are quite complex to verify, since in-situ observations for validation are sparse (Wang et al., 2016). Additionally, changes in background circulation or the impact of remotely generated internal tides may also impact the process of tidal conversion (Kerry et al., 2014). Nevertheless, dedicated processing of satellite altimetry observations can provide a global picture of observed tidal conversion for validation of modeled estimates (Vic et al., 2019). Figure 2.17 highlights that most of the energy conversion appears from the barotropic to the baroclinic tide (positive tidal conversion). Nevertheless, there is also evidence for negative conversion in some locations, indicating energy transfer from the baroclinic to the barotropic tide. Such sinks form due to a special geometric constellation between the phases of the density perturbation and the barotropic vertical velocity, in detail when the phase difference exceeds 90° (Zilberman et al., 2009; Carter et al., 2012).

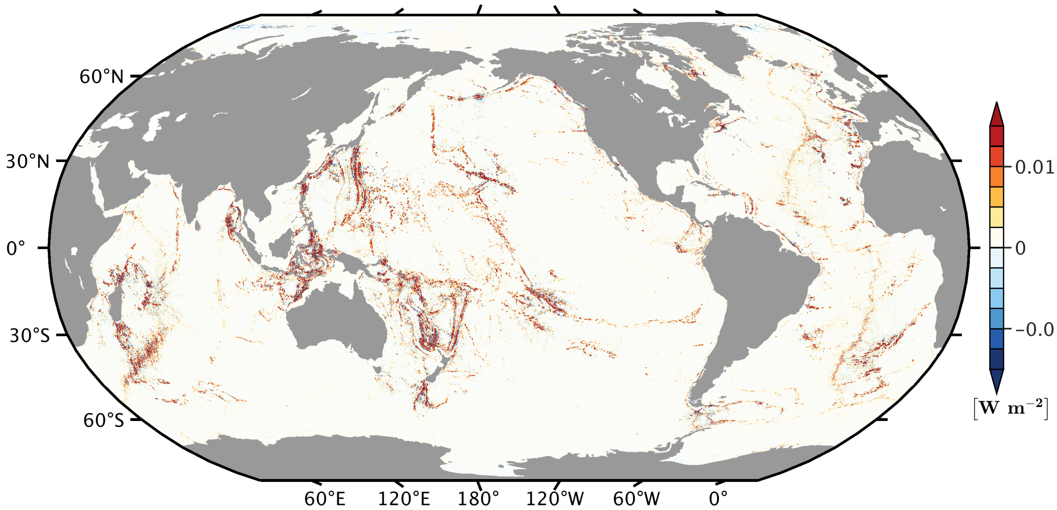

Figure 2.17: M_2 conversion for the year 2006 from numerical simulations of this work ($\mathrm{W\,m^{-2}}$).

2.4 Non-Astronomical Driving Mechanisms for Long-Term Tidal Changes

The TGP is a very stable and regular phenomenon on short geological time scales, such as in this study, e.g., 30–100 years of analysis. Changes in the tide-raising astronomic potential are well understood and allow for predictions far into the future (Pugh and Woodworth, 2014; Cartwright, 1999). However, present-day tides are subject to subtle changes, which have been explored in a number of studies with different approaches and varying regional foci. Observations of these subtle changes in ocean tides serve as the starting point for further analysis and research on the underlying processes. The objective of this chapter is to provide a concise overview of contemporary observed variability and long-term changes in ocean tides and their potential driving mechanisms, which are currently understood or considered to be relevant.

Changes of tidal constituents, both at semidiurnal and diurnal frequencies, have been detected through the analysis of long-time tide gauge records, and recently also by satellite altimetry. Tides are significantly changing along many coastlines, exhibiting both positive and negative amplitude trends. M_2 is observed to change at rates of 1–10 cm century^{-1} in absolute terms, as described by, e.g., Woodworth (2010) and Haigh et al. (2020). Woodworth (2010) found tidal changes that are not necessarily of large spatial extent, but possibly regionally coherent. However, the changes in some regions are restricted to smaller areas, e.g., in Europe or the Far East. Since the inhomogeneous network of tide gauge stations limits the ability to detect spatially coherent variations, conclusions remain speculative for some regions. Besides long-term changes, seasonal (Kang et al., 2002; Müller et al., 2014; Devlin et al., 2018; Bij de Vaate et al., 2021) and interannual (e.g., Colosi and Munk, 2006; Santamaria-Aguilar et al., 2017; Ray and Talke, 2019) variability were also reported and examined in the literature.

On the subject of trends, significant secular tidal changes in the M_2 constituent (Ray, 2006; Schindelegger et al., 2022), as well as the S_2 constituent (Ray, 2009) were observed in the Gulf of Maine. The semidiurnal tide is not only observed to change at the Gulf of Maine, but on a larger scale at the North Atlantic coasts. Pineau-Guillou et al. (2021) estimated that the changes have started long before the 20th century and that they are not necessarily linear. The authors also found mostly spatially consistent M_2 variations in the North-East Atlantic, with positive trends since 1910, but changing sign around 1990. Müller et al. (2011) detected tidal trends in amplitude and phase over large spatial scales with tide gauge analysis, mainly in the Northern Atlantic and Pacific. Tide gauges in the East Pacific have also revealed spatially coherent increasing M_2 and K_1 amplitudes (excluding the Gulf of Panama) (Jay, 2009). Based on the analysis of open-ocean tide gauge stations across the Pacific, Zaron and Jay (2014) estimated the M_2 amplitude to increase with a statistically significant trend. In that study, K_1 amplitudes showed a mix of positive and negative variations. The authors identified a region in the western Pacific where changes are coherent (stations: Malakal, Yap, Saipan, Kapingamarangi, and Pohnpei). However, the individual water level records cover different time periods, possibly limiting the inference about spatial coherence. At the coasts of China, especially in the Yellow Sea, trends up to 4–7 mm year^{-1} between 1954 and 2012 were observed by Feng et al. (2015).

Another emerging possibility to detect tidal trends is through satellite radar altimeter analysis, as demonstrated first by Bij de Vaate et al. (2022) at satellite groundtrack crossover locations. Given the nature of satellite observations, such approach allows for a quasi-global estimation of tidal trends, thus complementing tide gauge observations, which are restricted to the coast. Bij de Vaate et al. (2022) detected linear trends in the amplitudes of four primary tidal constituents M_2, S_2, K_1, and O_1, up to 0.1–1.0 mm year^{-1}. Some of the pointwise trends of the individual tidal constituents are coherent over wider scales, e.g., at the lunar semidiurnal frequency in regions located on the Northwest European Shelf. For M_2, Bij de Vaate et al. (2022) found predominantly negative amplitude trends across the ocean. The tidal amplitude trends observed with tide gauges and satellite altimetry indicate similar regional coherence for some coastal locations. Regional coherence is also observed and holds for tidal high water, low water and tidal range observations at tide gauge stations (Woodworth et al., 1991; Flick et al., 2003; Mawdsley et al., 2014, 2015; Jänicke et al., 2021).

Tidal changes are suspected to be caused by diverse non-astronomic factors of both natural and anthropogenic origin (Talke and Jay, 2020). Many of the potential natural driving mechanisms (Figure 2.18) may occur at once or even interact, making it challenging to identify one driver and

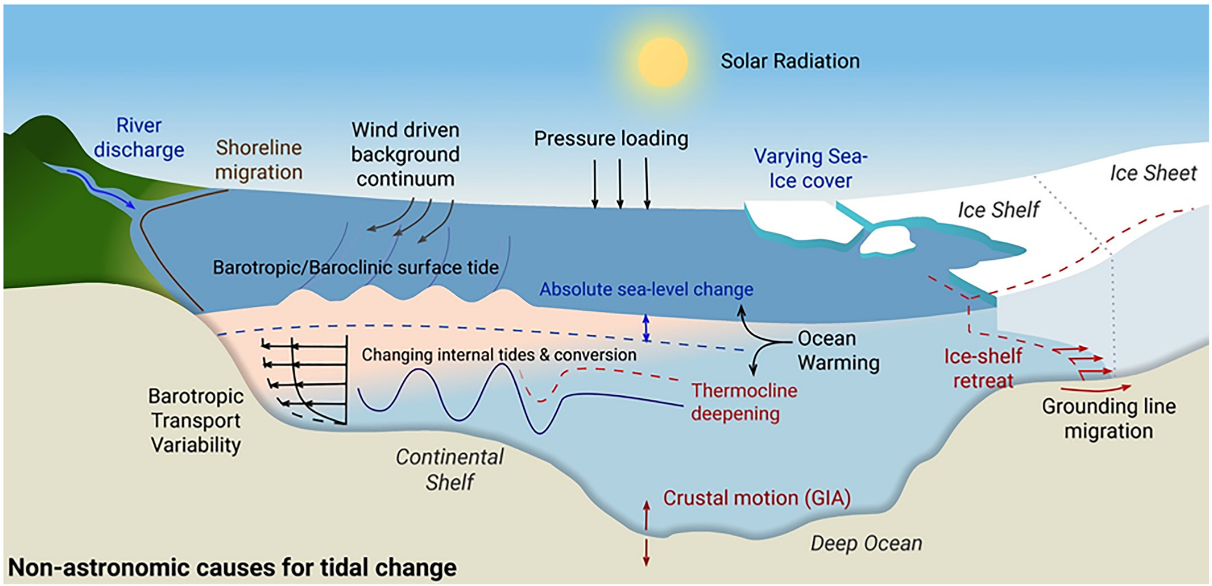

Figure 2.18: Schematic overview of possible driving mechanisms for long-term secular tidal changes, taken from Haigh et al. (2020) (their Figure 3).

its individual influence on the tidal regime. A review of non-astronomical driving mechanisms for secular tidal changes is given in Haigh et al. (2020) and briefly reflected below. Haigh et al. (2020) differentiate spatially between local and regional/global effects. For the scope of analyzing the global tidal signal in this work, the focus will be on the natural driving mechanisms of regional or global extent.

Water depth in combination with the shapes of the ocean basins impacts the tidal amplitudes through resonance conditions (Arbic et al., 2009a). The parameters are set by the configuration of tectonic plates and can be altered, both on geological and shorter time scales, by changes in shoreline position or grounding line migration (Haigh et al., 2020, e.g., shoreline migration, cf. Figure 2.18). As the determining factors of the resonance properties change, the tidal amplitude is modulated as well. This is especially true for tidal regimes that are near to resonance, such as in the Bay of Fundy for the semidiurnal tide (Pugh and Woodworth, 2014). While changes in ocean basins occur on geological time scales due to natural processes, shoreline migration is often related to anthropogenic activity on local scales, e.g., harbor modification or land reclamation (Su et al., 2015; Haigh et al., 2020).

Both boundary layers of the ocean are able to impact the propagation of tidal waves. On the upper boundary, the ice extent influences the tides through different physical processes (Figure 2.18), linked to the thinning of ice shelves and their retreat, which leads to grounding line migration and an expansion of the sub-shelf cavity. While ice shelf melt is estimated to play a minor role for present-day tidal changes, it is speculated to gain in importance in the future. The assumption is based on sensitivity experiments by Rosier et al. (2014) and Wilmes et al. (2017). In general, friction underneath the ice dissipates energy, while melting can alter the geometric configurations of resonance, as well as reflection properties (Haigh et al., 2020). Especially in the future, the thinning and retreat of large Antarctic ice shelves might result in geometry changes and altered dissipative behavior of the cavities. As a result, back-effects on the open-ocean tides could be evoked (Arbic et al., 2009a; Arbic and Garrett, 2010; Wilmes and Green, 2014). Due to the shallow and open ocean behaving like a coupled oscillator, such back-effects are greatest when the deep and shallow ocean regions are near to tidal resonance, which is true for the

Atlantic ocean and the Filchner-Ronne Ice Shelf (Arbic and Garrett, 2010). Additionally to the above described physical mechanisms, frictional effects associated with varying sea ice cover are known to induce appreciable seasonal variations of the tides (Müller et al., 2014; Bij de Vaate et al., 2021).

Another (though unlikely) driver for tidal change at the upper ocean boundary is the radiational forcing by diurnally heated atmosphere, which contributes to the solar tidal constituents S_1 and S_2. The origin of the radiational part lies in variations of air pressure that load the ocean and excite similar normal modes as their gravitational counterparts. Especially for S_1, the radiational part dominates the gravitational part by a factor of $\sim$5 within the global ocean (Ray and Egbert, 2004; Schindelegger et al., 2016). For the S_2 component which is several times larger than S_1, the gravitational part exceeds the radiational part by a factor of $\sim$7 (Arbic, 2005). Long-term changes in atmospheric pressure tides have been suggested to cause the anomalous S_2 ocean tide trends over 1935–2005 along the US East coast (Ray, 2009), but the meteorological record has so far remained inconclusive.

On the lower ocean boundary, changes in sea bed roughness can evoke changes in bottom friction, reflecting back on the tidal signal. Within the ocean's interior, nonlinear interactions can take place between tidal constituents, as well as between tides and non-tidal processes (Arns et al., 2020). As an example, Devlin et al. (2014) suggested energy transfer through resonant triad interactions in the western Pacific between M_2, K_1, and O_1. Several of the nonlinear interacting mechanisms are described in Haigh et al. (2020) and the references within, but generally remain hard to quantify.

Much of the discussion of drivers for tidal trends has hitherto focused on water depth changes on regional and global scales. Variations in the extent of the vertical water column are a direct result of sea level rise (SLR). Besides SLR, glacial isostatic adjustment (GIA) of the Earth's crust also modifies the ocean's water depth (Tamisiea and Mitrovica, 2011). Both physical processes are represented in Figure 2.18 through absolute sea level change (caused, e.g., by ocean warming) and crustal motion. In this context, literature has focused on high tides and increased flood risk in coastal areas (e.g., Arns et al., 2015; Greenberg et al., 2012; Kemp et al., 2017) and changes in ocean tidal constituents (e.g., Müller et al., 2011; Pelling et al., 2013; Pickering et al., 2017; Ross et al., 2017; Schindelegger et al., 2018; Rose et al., 2022). Since tides propagate as shallow water waves through the oceans, they are directly affected by the water depth. For one thing, greater water depths lead to altered resonance conditions, while the modified tidal wave's propagation speed also results in a possible shift of amphidromic points (Pickering et al., 2012; Idier et al., 2017). Müller et al. (2011) found that $\sim$1 m change in global mean sea level can evoke changes in tidal amplitude of $\sim$1 % and in tidal phase of $\sim$1°. Moreover, Müller et al. (2011) attempted to find some correspondence between observed and modeled tidal changes in relation to SLR, but this turned out to be challenging. Schindelegger et al. (2018) conducted numerical experiments and could indeed highlight a link between SLR and changing tides, but nevertheless stressed that the trend in mean sea level alone is insufficient to explain the observed trends in tidal constituents around the world (e.g., European Shelf or Gulf of Maine). More specifically, Figures 5 and 6 of Schindelegger et al. (2018) revealed coherent signals at the coasts of Australia, Europe, and the US, characterized by mostly alternating patterns of positive and negative M_2 amplitude trends. Comparisons with tide gauges (as, e.g., along the US coast in Figure 2.19) suggest that the model results, reflecting the effect of SLR, capture most of the observed M_2 trends in sign, but not in magnitude. Thus, SLR appears to be part of the puzzle, but not the sole cause for present-day trends in the ocean tides.

The impact of changing stratification on the global tides has not been explored, thus far. Yet, regional studies present evidence for a likely influence of stratification on tides, e.g., Kang et al. (2002); Müller (2012); Katavouta et al. (2016); Barbot et al. (2021); Tchilibou et al. (2022) on seasonal time scales, or Colosi and Munk (2006) on secular time scales. Generally, there are three physical mechanisms, through which stratification is able to impact tidal characteristics. As a first mechanisms, stratification alters the vertical eddy viscosity and hence the turbulent dissipation. In consequence, the barotropic tidal transport is changed, as elaborated in Müller (2012) (Figure 2.18, barotropic transport variability). Kang et al. (2002) also presented seasonally induced baroclinic effects by winter/summer stratification conditions in the Yellow and East China Seas. In detail, they found that the current shear, the frictional dissipation, and the barotropic energy flux are modified. As a second mechanism, changes in the density structure evoke changes in the surface expression of internal tides, particularly their phase speeds (see, e.g., Colosi and Munk, 2006, for the tide at Honolulu) (Figure 2.18, Baroclinic surface tide). As a third mechanism, stronger stratification causes the tidal energy conversion rate to increase near steep (upper-ocean) underwater topography (Figure 2.18, changing internal tides and conversion). Changes in the baroclinic tide and the tidal conversion rate in turn imply changes in the barotropic tide (Schindelegger et al., 2022). Generally, the varying energy transfer from barotropic currents to baroclinic modes is the subject of current research, especially in regions that are known generation sites of internal tides, e.g., Kerry et al. (2014) (Philippine Sea), Jithin et al. (2020b) (Bay of Bengal), Tchilibou et al. (2022) (Amazon Shelf) or Vic et al. (2018) (Mid-Atlantic Ridge). An analysis of baroclinic energy by Buijsman et al. (2017) revealed that stratification variability is an important effect for internal tide coherence in the equatorial Pacific. The connection between stratification and internal tides is also supported by Yadidya and Rao (2022), who found that the Indian Ocean Dipole influences the circulation and in turn the density stratification on interannual time scales, which leads to modified internal wave generation and propagation, local dissipation, and diapycnal mixing. Moreover, the altimetry-based analysis of Zhao (2023) suggested that internal tides at the M_2 frequency have significantly strengthened in the past 30 years.

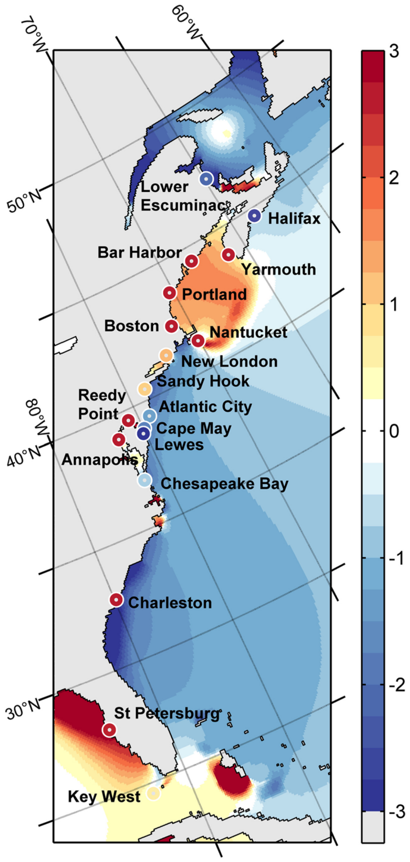

Figure 2.19: Observed and modeled M_2 tidal amplitude change (cm) along the North American East Coast to a 0.5 m increase in nonuniform global mean sea level (with GIA), taken from Schindelegger et al. (2018) (their Figure 5).

The working hypothesis of the present thesis is that changing ocean stratification conditions play a—probably important—role in the contemporary changes of ocean tides. The assumption is based on both physical arguments and previous modeling results at regional scales. Yet, a rigorous, global quantification of the effects of this specific driver is still lacking. As a strengthening ocean stratification is clearly detected in observations (cf. Section 2.1.3), the question remains as to what impact it has on the global tidal constituents. Realistic 3D simulations, with a global high-resolution numerical model, are needed to address the question and map the response of barotropic and baroclinic surface tides to changes in stratification, both on interannual and multi-decadal time scales.

3 Numerical Ocean Model

The numerical model used to conduct the tidal simulations in this study is the *Massachusetts Institute of Technology general circulation model* (MITgcm), described in Marshall et al. (1997). It can be adapted to regional or global, as well as two-dimensional (2D) or three-dimensional (3D) ocean modeling problems (e.g., Gerkema et al., 2006; Buijsman et al., 2012; Ponte and Cornuelle, 2013; Rocha et al., 2016; Savage et al., 2017; Arbic et al., 2018; Zeng et al., 2021; Schindelegger et al., 2022; Dushaw and Menemenlis, 2023). It allows for efficient parallelization across different HPC platforms. It consists of a hydrodynamic kernel that exploits mathematical isomorphisms in the fluid equations, allowing for use both as an atmosphere and ocean model.

3.1 Governing Equations

Here, the model is configured as a 3D global ocean model. It solves the 3D primitive equations, including the hydrostatic and Boussinesq approximation. The Boussinesq approximation consists of two assumptions. On the one hand, incompressibility of the ocean's flow is assumed, and on the other hand, density variations due to dynamics are assumed to be significantly smaller than the reference density (Knauss and Garfield, 2016). The hydrostatic balance in the vertical

$$\partial_z p = -g\rho \tag{3.1}$$

results in vertical pressure that solely changes with the density distribution. The equation contains the individual part $\partial_z p$ which is the pressure gradient in the vertical direction, as $x/y/z$ represent again the Cartesian coordinate directions. g denotes the gravitational acceleration and ρ is the ocean's density. Together, all mentioned assumptions prevent instantaneous vertical velocity changes.

The governing equations describe the dynamics and thermodynamics of the ocean and contain several forces and acceleration terms. The momentum equations in the local (x,y,z) coordinate system introduced near Equation 2.9

$$\frac{\mathrm{D}\mathbf{u}}{\mathrm{D}t} + f \times \mathbf{u} + \frac{1}{\rho}\nabla_h p - \nabla_h \cdot A_h \nabla_h \mathbf{u} - \partial_z A_z \partial_z \mathbf{u} = \begin{cases} \mathcal{F}_h & \text{(surface)} \\ 0 & \text{(interior)} \end{cases} \tag{3.2}$$

are a part of the governing equations and are valid for zonal and meridional flow (Equation 3.2). Here, from left to right of the equations, the derivative $\mathrm{D}\mathbf{u}/\mathrm{D}t$ represents the full Lagrangian acceleration, including the depth-independent barotropic velocity $\mathbf{u} = (u, v)$. The Coriolis parameter is f, and the term $1/\rho \nabla_h p$ describes the pressure gradient. The expressions including the divergence operator represent one possible form of dissipation of momentum in the horizontal direction, followed (as the last term on the left hand side) by the dissipation of horizontal momentum in the vertical direction (e.g., due to frictional effects between layers), with A_h and

A_z being horizontal and vertical viscosity coefficients. On the right hand side of Equation 3.2, $\mathcal{F}_h$ denotes a forcing term for momentum (e.g., wind stress) in the particular direction. In general, conservation relations exist for ocean water and its properties like salinity or heat. In Knauss and Garfield (2016) it is demonstrated that the incompressible and homogeneous flow in all directions leads to the equation of continuity for mass in the differential form through derivations with an rectangular imaginary control volume. Here, the continuity equation reads

$$\partial_t \eta + \nabla_h \cdot \mathbf{u} = 0\,, \tag{3.3}$$

implying that time variations of the surface η are tied to the spatial variability of the horizontal flow. Due to the Boussinesq approximation (e.g., Knauss and Garfield, 2016) that is underlying Equation 3.3, the continuity equation is a statement of volume conservation (and not mass conservation). Moreover, the thermodynamic balance equations for temperature and salinity are considered

$$\frac{\mathrm{D}\theta}{\mathrm{D}t} - \nabla_h \cdot \mathcal{K}_h \nabla_h \theta - \frac{\partial}{\partial z}\Gamma(\mathcal{K}_z)\frac{\partial \theta}{\partial z} = \begin{cases} \mathcal{F}_\theta & \text{(surface)} \\ 0 & \text{(interior)} \end{cases} \tag{3.4}$$

$$\frac{\mathrm{D}S}{\mathrm{D}t} - \nabla_h \cdot \mathcal{K}_h \nabla_h S - \frac{\partial}{\partial z}\Gamma(\mathcal{K}_z)\frac{\partial S}{\partial z} = \begin{cases} \mathcal{F}_S & \text{(surface)} \\ 0 & \text{(interior)} \end{cases}\,. \tag{3.5}$$

$\mathcal{K}_h$ indicates the horizontal eddy diffusion coefficient, while $\mathcal{K}_v$ is its vertical counterpart (both in $\mathrm{m}^2\,\mathrm{s}^{-1}$). These two equations describe the transport of potential temperature θ (°C) and salt S ($\mathrm{g\,kg}^{-1}$)—i.e., two possible tracers—by advection and diffusion. The forcing term $\mathcal{F}_\theta$ stands for the temperature change, in particular the net heat flux into the ocean. The forcing term $\mathcal{F}_S$ represents the surface salinity change, which can be altered by e.g., continental runoff or the net surface freshwater flux (evaporation minus precipitation).

The governing equations are discretized in time and space for the purpose of a simulation (Marshall et al., 1997). The time-stepping is split for the dynamics and the thermodynamics. The dynamics, including a time discrete form of the momentum equations, can be evaluated with different approaches, e.g., the implicit Crank-Nicolson (Crank and Nicolson, 1947) approach or the explicit Adams-Bashforth approach (Durran, 1991). For calculating the pressure field in one time step, a discretized version of the above mentioned momentum equations is substituted into the continuity equation, which results, for a hydrostatic model, in a 2D elliptic equation. This mathematical approach is necessary because the Navier-Stokes equations do not contain an explicit equation for pressure. A conjugate-gradient iteration gives the hydrostatic pressure at any level. It is derived from the weight of the water above. The thermodynamics, like temperature and salinity, are propagated with the so-called tracer equations. They are integrated with a staggered algorithm and half a time step before the variables of the flow. The discretization in space is conducted with a finite-volume approach (Marshall et al., 1997).

In the horizontal, the components of the flow are arranged with an Arakawa-C-grid (first introduced in Arakawa and Lamb, 1977). Special care needs to be taken with regard to the cell boundaries of different model variables. The cells are slightly shifted in their middle points, and therefore also their boundaries. The four different discretizations are schematically illustrated in Figure 3.1a, consisting of tracer cells (meaning a continuity cell), vorticity cells, u cells (western flow) and v cells (southern flow). A Lorenz grid is used concerning the vertical discetization of the model domain. Generally, it is possible to choose between height and pressure coordinates. Here, the focus will be on height coordinates. The uppermost vertical layer can have a non-linear free surface and in consequence be time-dependent. In general, the 3D domain decomposition

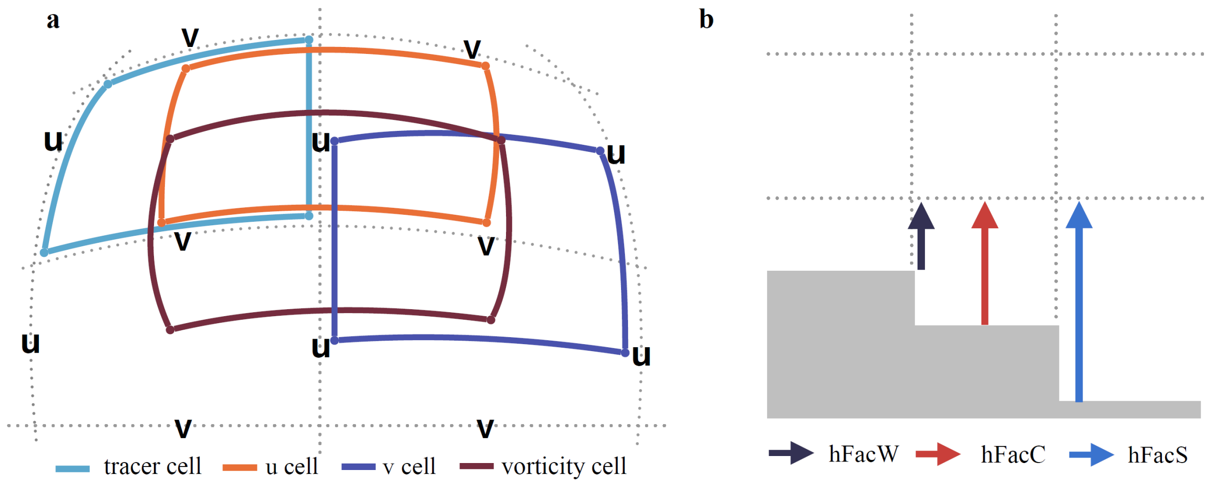

Figure 3.1: Schematic illustration (simplified) of important grid elements in the **a** horizontal and **b** vertical direction. The figures are based on Figure 2.8 (Section 2.11.4 Horizontal grid) and Figure 2.10 (Section 2.11.6 Topography: partially filled cells) of the MITgcm's user manual (Adcroft et al., 2024).

is realized through finite volumes. The tracer points are either specified at the cells center (default) or at the cell interfaces. The fluxes are defined in the normal direction to the volume's faces. The boundaries, particularly the ocean bottom, are represented as so-called lopped or shaved cells, which allows for the representation of more complex geometries by considering details of the boundaries within a given vertical layer (Adcroft et al., 1997). The discretization of the ocean bottom is carried out with so-called hFacs, where three of them are necessary to describe one bottom cell. Schematically, the three hFacs (hFacW, hFacC, hFacS) are shown in Figure 3.1b. Additionally, the viscosities need to be specified for every model run, because they influence momentum transfer, friction, mixing, and turbulent dissipation at small scales (e.g., of internal tides). They need to be set individually for horizontal and vertical direction and can be both, fixed or variable with a mixing scheme.

3.2 Model Configuration

The model setup in this work is a global 3D configuration of the MITgcm, of which the specific model settings and parameters are outlined below. The communalities of all runs are summarized first, followed by a description of the differences in the input data.

3.2.1 Model Parameters

The scope of this work requires to model both the barotropic and the baroclinic tide, and their corresponding transfer of tidal energy. Therefore, the global model configuration needs to resolve large-scale, as well as small-sscale oceanic processes and energy exchanges in the horizontal and vertical direction. Arbic et al. (2018) stated that at least a horizontal resolution of $1/10°$ is needed to fully resolve a low–mode internal tide field. The wavelength of M_2 mode-1 internal tides amounts to ~130 km globally (Zhao, 2018), while the K_1 mode-1 wavelength is larger with

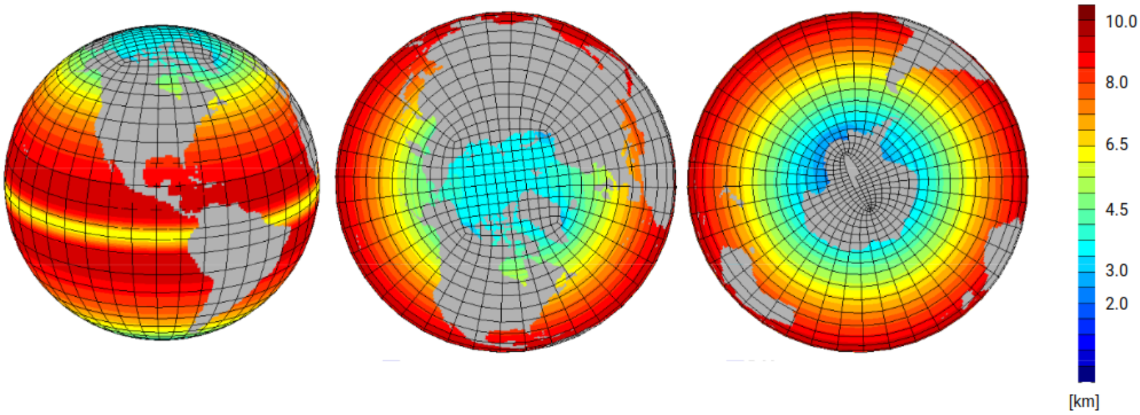

Figure 3.2: Characteristics of the LLC1080 grid, adapted from Forget et al. (2015). Colours represent the average grid spacing (km), computed as the square root of the grid cell area.

a range between 200–400 km (Li et al., 2017). In comparison to the M_2 mode-1 internal tide, the wavelength of the S_2 mode-1 internal tide is slightly shorter (Zhao, 2017). Overall, the chosen model resolution is a trade off between the ability to resolve small-scale processes and being computationally feasible. The grid used in the horizontal domain originates from the Latitude–Longitude–polar–Cap–Grid (LLC) family. The individual realizations within the LLC family are derived from a global parent grid, the LLC4320 with a nominal resolution of $1/48°$. Here, the realization LLC1080 is chosen, which corresponds to a nominal resolution of $1/12°$, as illustrated in Figure 3.2. The grid name's suffix (here: 1080) represents the discretized number of points along one-quarter of the Earth's circumference at the equator (Forget et al., 2015). The LLC grids are realized as curvilinear coordinate systems. The meridional spacing telescopes to a factor of about 3 finer in the tropics, to capture the zonal currents in the equatorial region. In the Northern hemisphere at latitudes higher than 57°N, a so-called Arctic cap is used to discretize the polar model domain. The Arctic cap is designed for spherical geometry and consists of a 2D conforming mapping algorithm (Forget et al., 2015).

Choosing the vertical discretization in general circulation models is generally a matter of some delicacy, as, e.g., throughout the whole water column, topographic gradients or changes in the vertical eddy viscosity need to be represented accurately to obtain realistic simulation output. Especially toward the ocean bottom, the vertical resolution becomes important for accurate representation of shallow water processes and correct mapping of the energy exchange between barotropic and baroclinic tide, which strongly depends on the bottom topography. In this work, a set of 59 vertical levels is used. The layer thickness increases with depth and ranges from 6 m at the ocean's surface to 484 m in the deep ocean at the deepest level of 7130 m. The distribution of layer thickness is shown in Figure 3.3 and displayed in detail in Table B.1. The ocean's bottom is mathematically described with a partial cell approach (Adcroft et al., 1997), which allows for a more flexible adaption to the bathymetry. The ocean's surface is represented by a linear free surface, within the framework of classical height (z) coordinates. This simplified approach is well suited to maintain stratification throughout the simulation and avoid model crashes. Another treatment of the vertical coordinate, the more flexible z^* (rescaled height) formulation, including a non-linear surface, can improve model performance, but also erodes the stratification near topographic features (Adcroft and Campin, 2004). Such stratification changes would be detrimental to this study. On the other hand, tidal simulations typically contain surface oscillations of the free surface in the range of several meters. For a linear surface formulation (z), this can have an effect on the accuracy of the simulated surface tide in very shallow water (Section 4.1.3).

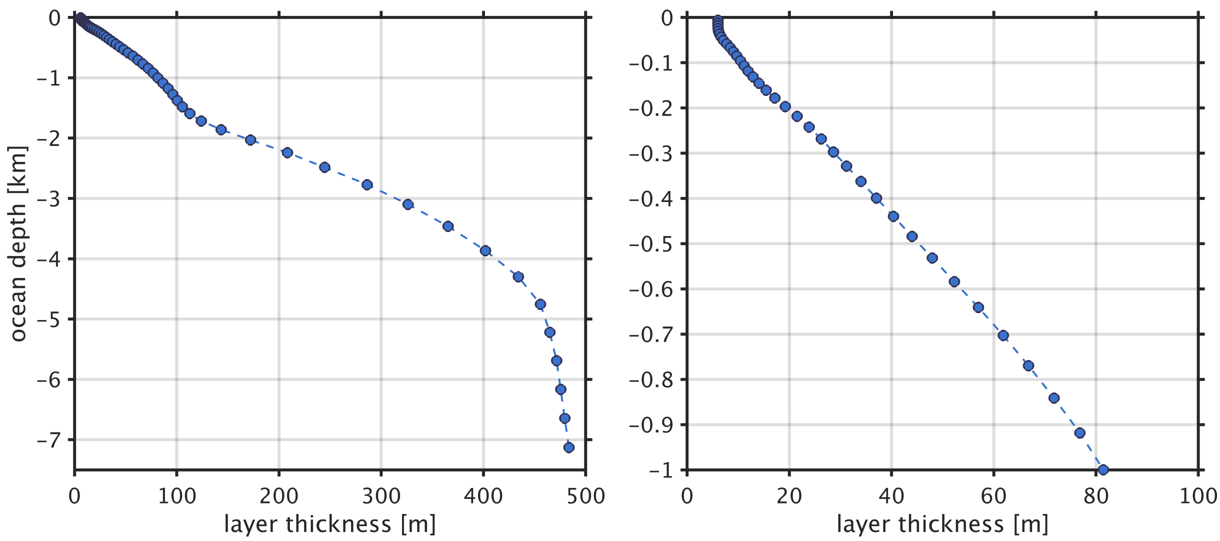

Figure 3.3: Vertical model domain discretization, consisting of 59 vertical layers with increasing thickness toward the ocean bottom. The surface layer thickness is 6 m and the bottom layer thickness is 484 m. The right panel is zoomed in and shows the first 1000 m of the ocean.

Along with the discretization in space, the choice of time discretization also influences the stability of the model integration. The time integration of the equation of motion follows a staggered time-step approach, here including an explicit 3^{rd} order Adams-Bashforth (AB) scheme (Durran, 1991). Here, the parameters for the time-stepping are: $\alpha_{AB} = 0.5$ and $\beta_{AB} = 0.281105$. It is used for advection and Coriolis forward integration. The dissipation terms are kept outside of the AB integration, since the 3^{rd} order AB scheme reduces the stability limits for damping problems, like diffusion (Durran, 1991), which has an impact on the time step. The dissipation is integrated in time with a simple forward time-stepping. With this methodical settings for time-stepping it is possible to set the time discretization to a time step of 75 seconds for momentum and tracer equations. Sensitivity tests with larger time steps mostly resulted in model crashes, while 75 seconds worked well for this specific model configuration.

Another crucial component of the setup is the forcing. In this work, the forcing is simplified in contrast to other numerical ocean modeling studies (e.g., Weis et al., 2008). Since the overall goal is to quantify the influence of ocean density changes on the global ocean tides, the forcing must be exactly the same for all simulations, excluding an explicit dependence on absolute time (i) nodal variations, and (ii) atmospheric forcing. Only gravitational tidal forcing is used, which is included through the MITgcm's capabilities to prescribe pressure loading. As the tidal forcing acts in the opposite direction to the pressure loading on the ocean, it is applied as inverse pressure loading. All simulations are started from rest and the forcing is linearly ramped up over a model time span of 3 days to ensure model stability. The tidal forcing consists of four primary partial tides, two semi-diurnals M_2 and S_2, and two diurnals K_1 and O_1. Their equilibrium tidal forcing (η_{EQ}) and their SAL tidal forcing (η_{SAL}) are both included. The SAL tide is computed externally beforehand through a spherical harmonic formulation, described in Ray (1998) (cf. Section 2.2.3), for each partial waves's in-phase and quadrature components from the TPXO9-atlas (an updated version of Egbert and Erofeeva, 2002).

The forcing imparts energy to the model, which also must be dissipated. Since energy dissipation in the ocean eventually occurs at the scale of molecules (Wunsch and Ferrari, 2004), no modern model, no matter how fine in discretization, is able to fully capture this process. Therefore, it is necessary to set model parameters to mimic this dissipative behavior. Much work has been

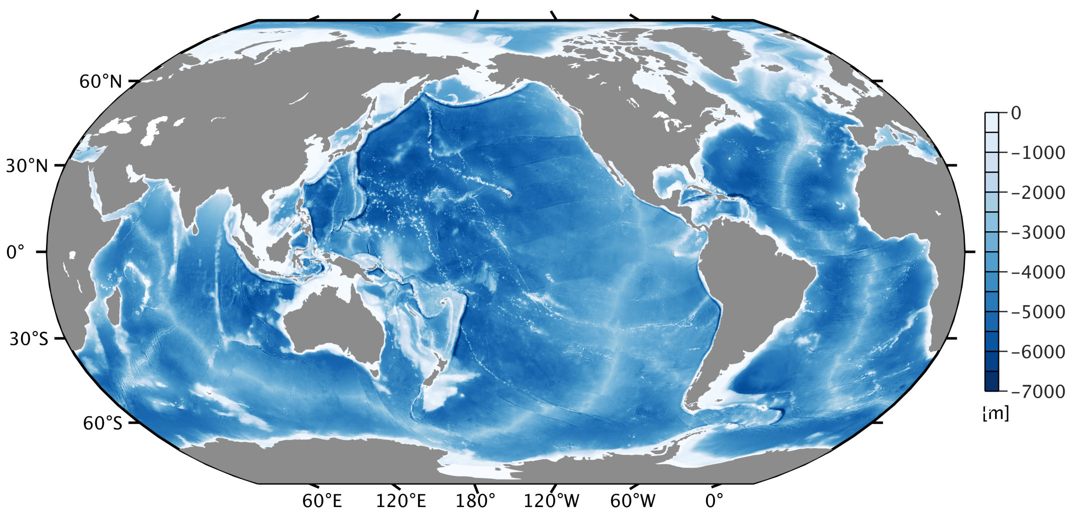

Figure 3.4: Model ocean bottom topography (bathymetry), based on Schaffer et al. (2016).

invested to tune model parameters to realistic values (e.g., parameterization of internal wave drag, Egbert et al., 2004; Arbic et al., 2010; Buijsman et al., 2015). Arbic et al. (2010) argue for an additional wave drag parameterization in 3D models, because the internal tides may be too strong (in their case for the model HYCOM). In this work, an additional wave drag parameterization is not included, since the surface tidal elevations with the encoded dissipation mechanisms are already sufficiently accurate (cf. Section 4.1.3). Yet, the choice of parameter values is dependent on the model and the application. Here, the horizontal viscosity and diffusivity is parameterized with a modified Leith-scheme following Leith (1996). In the vertical, viscosity and diffusivity are computed with a K-Profile-Parameterization (KPP) as described in Large et al. (1994). The background viscosity of the KPP scheme is set to a standard value of $5 \times 10^{-5}\,\mathrm{m^2s^{-1}}$ and accounts for mixing effects of unresolved breaking internal waves in the momentum equation, since the model is only able to partly resolve the barotropic-to-baroclinic energy conversion. The bottom friction is parameterized by standard quadratic law, as common in literature (e.g., Arbic et al., 2009b), with a dimensionless drag coefficient of 0.003.

The bottom topography of the model is based on the RTopo-2 dataset (Schaffer et al., 2016) and shown in Figure 3.4. For stability reasons, the minimum ocean depth is assumed to be 10 m, therefore all data points of the model bathymetry below this threshold are set to 10 m. As described above, the bathymetry is implemented with a partial cell approach (Adcroft et al., 1997). The partial cells are parameterized through three hFacs, illustrated in Figure 3.1b. The appearance of the hFacs can be fairly crucial, since the discretization of the bathymetry can result in supercritical slopes. Supercritical slopes are able to suppress tidal conversion in the model, since the internal tide field is dominated by higher modes when generated at supercritical slopes (Liu et al., 2022b), resulting in shorter wavelength that the model is unable to resolve.

The MITgcm gives a user flexibility in configuring the model through its various packages, which can be switched on/off for each simulation. In all simulations described in this thesis, the sea ice, as well as the shelf ice packages are excluded. This is necessary since both processes could result in tidal changes caused by frictional effects at the ice base. These changes due to variable sea/shelf ice would be unrelated to the direct stratification impact on the tides (e.g., Müller et al., 2014; Bij de Vaate et al., 2021).

Results in this thesis are obtained from *time slice simulations*. It is important to highlight that one individual time slice simulation is run for each time stamp of analysis (e.g., a specific year or decade). This procedure avoids the need for a costly spin-up simulation and subsequent multi-decadal integrations. Each time slice simulation is started from rest, as described above, and integrated forward for 40 days. As an example, the annual analysis time span of 1993 to 2020 would consist of 28 individual time slice simulations. For each of these annual runs, their corresponding averaged density structure over the whole year is used as input data. Details concerning the density structure of each run are given below.

3.2.2 Representing Present-day and Future Stratification Changes

To represent stratification changes across the simulations, each run's density structure is strongly constrained to the initial, time-invariant annual mean temperature and salinity fields. For this purpose, the restoring boundary condition package (RBCS) of the MITgcm is used for nudging to prevent unwanted erosion of the (initial) background stratification. The restoration (or relaxation) time scale is set to 3 days. The choice is based on experiments in a regional MITgcm setup (Schindelegger et al., 2022) and global simulations without a nudging scheme, which resulted in changes of the density structure through, e.g., advection processes in geostrophic currents. The use of a relaxation scheme allows for a longer integration that still maintains the desired initial density structure. Relaxation approaches are for example used in literature in the context of tidal prediction (Kodaira et al., 2019) or in studies of generation and propagation of internal tides (Barbot et al., 2022). The integration time of 40 days represents a period that the model's mean sea level η_0 needs to converge, since it is affected by changes due to steric expansion or unsuppressed mass transfer that is not captured by the nudging. Nevertheless, the remaining impact of changing mean sea level and steric effects amongst the annual simulations needs to be corrected a posteriori (see Section 4.3.2 for details).

Estimates for the ocean's density structure are taken from the Global Ocean Physics Reanalysis Version 1[1] described in Lellouche et al. (2018). This eddy resolving ocean reanalysis assimilates observations into a numerical model through a reduced-order Kalman filter. The observations consist of different sources, like satellite altimeter observations, satellite sea surface temperature observations, or observations from in situ buoys including vertical temperature and salinity profiles. The GLORYS12V1 fields have proven their quality in various studies with different objectives, e.g., Verezemskaya et al. (2021); Lellouche et al. (2021); Jutras et al. (2023). The global, monthly 3D potential temperature and absolute salinity fields are used. They are given on an $1/12°$ grid with 50 vertical levels. The monthly data are averaged horizontally and vertically for each period of analysis. Afterwards, the mean fields are linearly interpolated to the 3D LLC1080 model grid. The linear trend of the GLORYS ocean's density structure from 1993 to 2020 is displayed in Figure 2.5 in terms of potential energy anomaly, indicating a present-day strengthening of ocean stratification.

As another data source, future temperature (sea water potential temperature, *thetao*) and salinity (sea water salinity, *so*) fields are obtained from the Coupled Model Intercomparison Project Phase 6 (CMIP6) (Eyring et al., 2016; Haarsma et al., 2016). In detail, monthly output from the ocean component of the High Resolution Model Intercomparison Project (HighResMIP) are used. In particular, the *EC-Earth-3P-HR* (called Earth-3P hereafter) protocol is used, provided on an $1/4°$ horizontal grid ($\sim$25 km) and 75 vertical levels (Haarsma et al., 2020). A time span until December 2099 is covered, and this is the only contribution to the HighResMIP that ex-

[1]GLORYS12V1, DOI: 10.48670/moi-00021, product ID: GLOBAL_MULTIYEAR_PHY_001_030

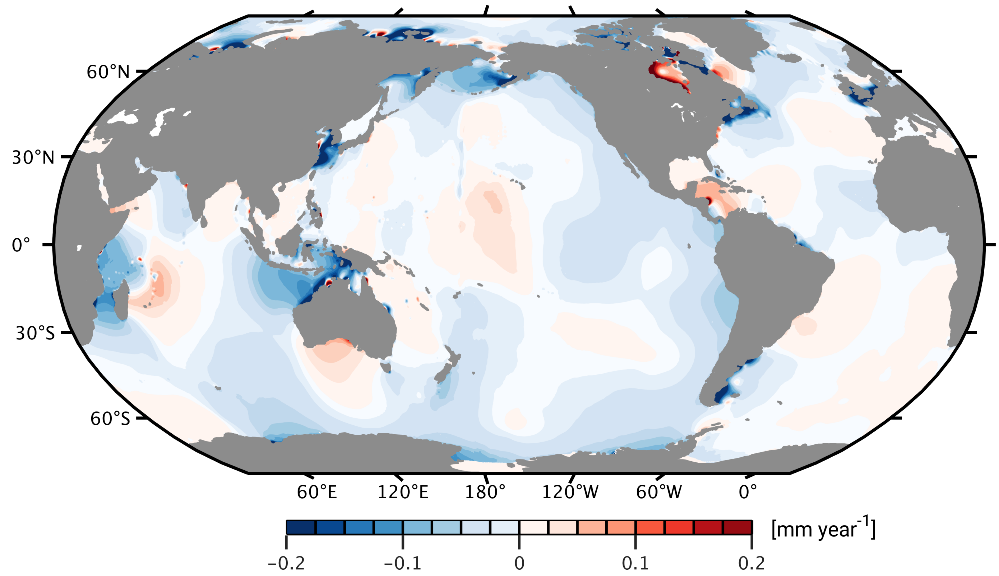

Figure 3.5: Present-day M_2 amplitude trend simulated with Earth3P stratification (1997–2017).

tends beyond 2050. The assumed Representative Concentration Pathways (RCP) are diversified in CMIP6 using Shared Socioeconomic Pathways (SSPs, O'Neill et al., 2016). The temperature and salinity fields used and described here, are constrained to SSP5-8.5, representing a high-end scenario based on expanded fossil fuel-driven development. SSP5-8.5 is called RCP8.5 hereafter for simplicity. To consider a second, more moderate greenhouse gas emission scenario, the simulated results under RCP8.5 are scaled to RCP4.5, because no high resolution stratification exists for RCP4.5 up to the year 2100. The scaling is performed through global mean (air) temperature curves that underlie the two RCP scenarios (O'Neill et al., 2016). The global mean temperature constrained to RCP4.5 stabilizes in a range between 2040 and 2060 regarding RCP8.5. Consequently, the year 2050 of RCP8.5 is assumed to represent the year 2100 in RCP4.5 in this work.

The temperature and salinity fields are interpolated vertically and horizontally to the LLC1080 model grid without performing a drift correction. In the context of analysis of CMIP-output, estimation of a drift-correction based on output from a control run with pre-industrial forcing is standard (Sen Gupta et al., 2013). Here, the decision to refrain from a drift correction is based on the realization that a large temperature anomaly ($\sim$0.05 °C decade^{-1}) exists in the Earth-3P control run between approximately 500 and 1400 m ocean depth (which are critical in the context of tidal conversion). Additional tidal simulations with the control run fields used for correcting the Earth3P future stratification have indeed shown some questionable future M_2 changes. To get further insight, present-day simulations with Earth-3P data (1997–2017) are conducted. The result without a drift correction matches the observed (and modeled) present-day trends from Opel et al. (2024) sufficiently well. Figure 3.5 shows the present-day M_2 amplitude trend obtained with the uncorrected Earth-3P density data. Both the magnitude of the M_2 changes and the tendency for predominantly negative open-ocean trends are consistent with Opel et al. (2024).

Generally, the monthly future density structure is merged to five-year-averages. For example, the data for the year 2050 consist of the average from 2047–2051, the year 2060 of the average from 2057–2061, and so on. The only exception is the year 2100, since data is only available until December 2099, therefore, the average consists of three years (2097–2099). The reference time for all future simulations is the year 2000 (1997–2001). The evolution of future stratification is shown in Figure 2.6 for the years 2060 and 2100, in terms of potential energy anomaly ϕ. A clear increase of the potential energy anomaly due to future upper ocean warming, based on RCP8.5, is evident (Capotondi et al., 2012). The increase reaches 15–20 $\mathrm{kJ\,m^{-3}}$ in regions of western boundary currents, the North Pacific, or the Arabian Sea (~20 %) in 2100.

4 Methods and Data

4.1 Post Processing of Model Output

The model output is created with the MITgcm diagnostics package and comprises hourly dumps of 2D surface height anomaly (η, m) and bottom pressure potential anomaly (p/ρ, $\mathrm{m}^2\,\mathrm{s}^{-2}$). Additionally, 3D output of the zonal (UVEL) and meridional (VVEL) velocity components ($\mathrm{m}\,\mathrm{s}^{-1}$), as well as potential temperature (THETA, °C) and salinity (SALT, $\mathrm{g}\,\mathrm{kg}^{-1}$) is enabled. The 3D output is especially useful for the separation of barotropic and baroclinic tides. The fields for each variable are harmonically analyzed, over the last 15 days of model time. The first days of the simulation are needed to ramp up the forcing and allow the ocean to adjust to the forcing and equilibrate. The last 15 days, one complete spring-neap cycle (i.e., the beat period between M_2 and S_2), of the 40 simulated days are necessary to isolate the individual partial tides (Pugh and Woodworth, 2014).

4.1.1 Harmonic Analysis

The tides themselves are periodic oscillations and the individual harmonic constants of the partial tides can be extracted with harmonic analysis of the model output. Here, the harmonic analysis is mainly split into two parts. First, the 2D surface height and bottom pressure are analyzed. They provide the tidal amplitude and Greenwich phase lag for the four main partial tides M_2, S_2, K_1, and O_1. Second, the 3D diagnostics are analyzed to compute the tidal contributions to the ocean's density, the baroclinic bottom pressure and barotropic velocities in zonal and meridional direction.

The harmonic constants from the 2D diagnostics are estimated with a least-squares adjustment (Koch, 1999, see Appendix A for a brief description). The mean surface amplitude and a linear trend are also estimated. The functional relation is given by a finite sum of harmonic oscillations for several tidal constituents, each consisting of cosine and sine oscillations, including the partial tidal amplitude and frequency. Equation 4.1 shows the harmonic composition for M_2 at any time tag t

$$x_{M_2}(t) = \eta_{COS_{M_2}} \cos(\omega_{M_2} t + \Phi_{EQ_{M_2}}) + \eta_{SIN_{M_2}} \sin(\omega_{M_2} t + \Phi_{EQ_{M_2}}). \tag{4.1}$$

The amplitudes $\eta_{COS_{M_2}}$ (cosine) and $\eta_{SIN_{M_2}}$ (sine) are estimated for the four tidal constituents M_2, S_2, K_1, and O_1. The equilibrium tidal phase Φ_{EQ} and the angular frequency ω are required. The former can be computed through the formalism of equilibrium tidal theory or from catalogues of the TGP, e.g.. HW95 (Hartmann and Wenzel, 1995). The angular frequency is taken as a constant for each partial tide and shown in Table 2.1 (e.g., Arbic et al., 2004). Within the functional relation, the tidal constants of several compound tides and shallow water tides are also included. The tidal spectrum of the model results is tested with the UTide software package

(Codiga, 2011) and gives the basis for the chosen additional tidal constituents. Included are M_4, MS_4, S_4, M_6, MSF, MS_6, and M_3. The tidal amplitude ζ and the tidal phase lag relative to the equilibrium tidal phase at the Greenwich meridian Φ (hereafter called *tidal phase*) can be computed as follows

$$\eta_{M_2} = \sqrt{\eta^2_{COS_{M_2}} + \eta^2_{SIN_{M_2}}}, \quad \Phi_{M_2} = \tan^{-1}(-\eta_{SIN_{M_2}}, \eta_{COS_{M_2}}). \tag{4.2}$$

The harmonic analysis of the 3D diagnostics mainly serves the computation of the 3D internal tides, which in turn gives the possibility to separate the barotropic and baroclinic tidal signal. Hence, it is explained in detail below (Section 4.1.2), along with the general separation of barotropic and baroclinic tides.

4.1.2 Separation of Barotropic and Baroclinic Tide

The tidal harmonics, as deduced with the least-squares adjustment described in Section 4.1.1, are a combination of the barotropic and the baroclinic tidal component. To analyze the variations of the tides in more detail, the two components need to be separated. Therefore, the 3D diagnostic model output is analyzed. As a first step, the ocean's density ρ is computed. The baroclinic bottom pressure anomaly (Nash et al., 2005; Wang et al., 2016) is derived afterwards and computed as follows

$$p'_b(z,t) = -\frac{1}{H}\int_{-H}^{0}\int_{z}^{0} g\rho'(\hat{z},t)\mathrm{d}\hat{z}\mathrm{d}z + \int_{z}^{0} g\rho'(\hat{z},t)\mathrm{d}\hat{z}\,. \tag{4.3}$$

Here, g is the gravitational acceleration, and H is again the resting water depth. ρ' denotes the density perturbation, meaning that the tidal period mean of the vertical density profile is subtracted from the in-situ density profile. The surface signal of the internal tides (η') can be deduced from the baroclinic tidal bottom pressure anomaly

$$\eta'(t) = \eta(t) - \frac{p_\mathrm{b}(t) - p'_\mathrm{b}(t)}{\rho_0\ g}. \tag{4.4}$$

including the surface amplitude η, the bottom pressure p_b and the constant reference density ρ_0 that is used for the model simulations. p_b is corrected from harmonic contributions of the tidal forcing, which consists of equilibrium and SAL tide. The derived internal tide can be subtracted from the full tide. This step results in the barotropic tide, allowing for a separation of the tidal components. Figure 4.1 shows a global estimate of the surface M_2 cosine amplitude ($\zeta_{C_{M_2}}$) from the year 2006, split into barotropic and baroclinic components. The differences are clearly visible, especially in magnitude and the spatial scales. The baroclinic tide in Figure 4.1b is present at locations near rough bottom topography, characterized by radiation paths away from the generation sites.

The described approach relies on the 3D information from the model output. As an alternative, one can also adopt the following, a more approximate but still feasible method. For annual time slice simulations, the yearly changes of the barotropic surface tide should be extracted. Since the mean of the full tide remains the same, the tidal anomalies contain the interannual information. Hence, the yearly full tide, split into in-phase and quadrature component, is reduced by the corresponding mean tide of the analysis period (e.g., 1993–2020). The subtraction also reduces parts of the baroclinic tidal signal, especially its stationary (coherent) long wavelength features.

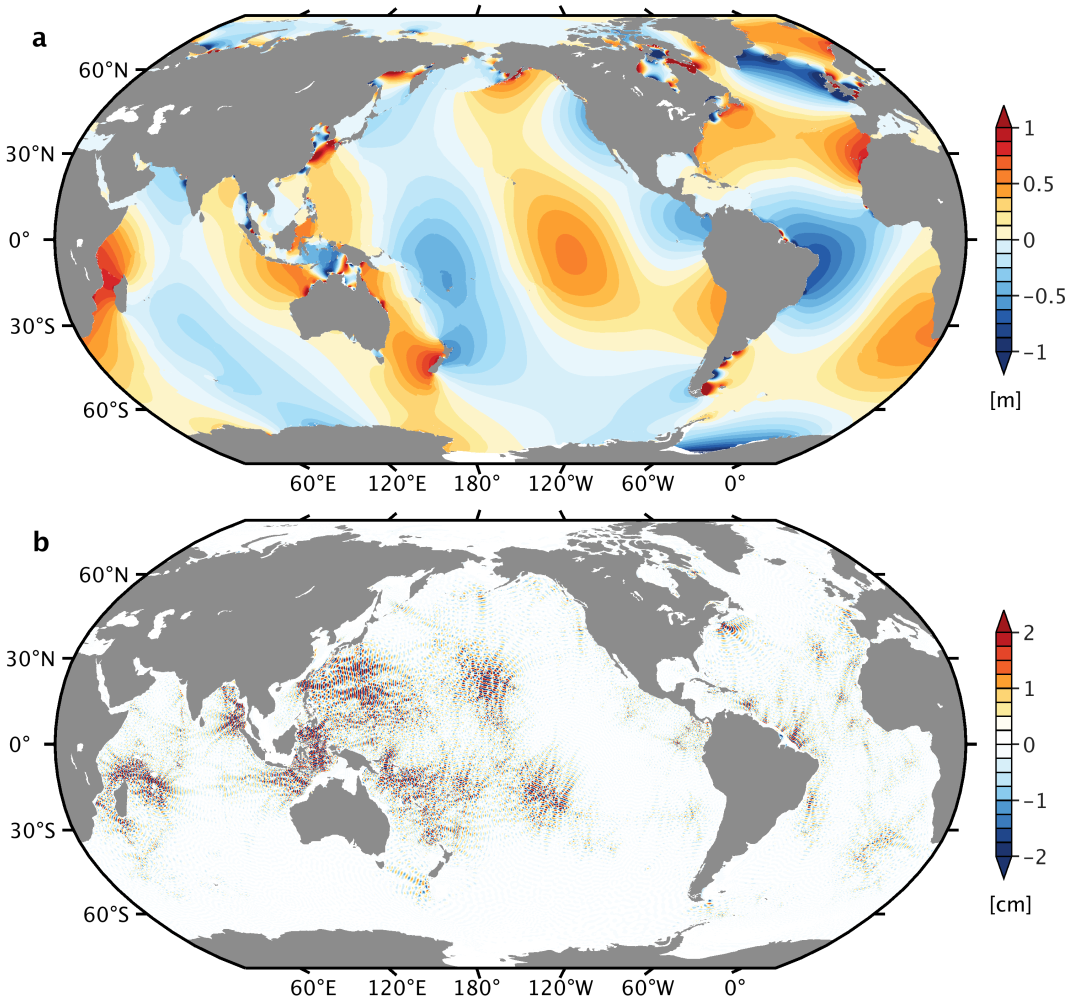

Figure 4.1: M_2 cosine amplitude (2006). The harmonics were deduced from a simulation with density structure for the year 2006 (GLORYS12 V1, Lellouche et al., 2018). The full surface tide is separated into its **a** barotropic and **b** baroclinic components.

Afterwards, the residuals are low-pass filtered in space. For the semi–diurnal tides, a Hamming window with a cutoff wavelength of 390 km in deep water ($\geq$500 m) and 100 km in shallow water is deemed appropriate. The cutoff wavelength for the diurnal constituents is 440 km in deep water and 210 km in shallow water. The filtering suppresses the remaining part of the baroclinic tide and yields estimates of the barotropic tide.

4.1.3 Accuracy Assessment of Modeled Barotropic and Baroclinic Tide

The realism of the modeled barotropic and baroclinic tide is evaluated by computing the spatially averaged root mean square (RMS) ($\overline{\Delta\eta}$) and the percentage of variance explained (PVE) relative to the TPXO9 atlas (updated version of Egbert and Erofeeva, 2002). The respective formulae read

$$\overline{\Delta\eta} = \left[\frac{\int\int |\hat{\eta} - \hat{\eta}_R|^2 \mathrm{d}A}{2\int\int \mathrm{d}A}\right]^{1/2} \tag{4.5}$$

$$\mathrm{PVE} = 100 \cdot \left[1 - \left(\frac{\overline{\Delta\eta}}{S}\right)^2\right] \tag{4.6}$$

where $\hat{\eta}$ denotes the simulated tide (in complex notation), $\hat{\eta}_R$ is the reference tide from TPXO9, dA represents the surface element of the considered ocean domain, and the signal S is defined as

$$S = \left[\frac{\int\int \eta^2 \mathrm{d}A}{2\int\int \mathrm{d}A}\right]^{1/2} \quad . \tag{4.7}$$

Additionally, a comparison to seafloor gauges (Ray, 2013), as well as a network of pelagic tide gauges is performed. Moreover, a comparison to an internal tide model (Zaron, 2019) is presented. The calculations are carried out without area weighting.

Table 4.1 illustrates, the quality of the M_2, S_2, K_1, and O_1 barotropic surface tide solutions in terms of a spatially-averaged RMS error and PVE relative to TPXO9. As is standard, these metrics are evaluated in latitudes equatorward of 66 °. The evaluation is split into ocean areas deeper and shallower than 1000 m. The M_2 solution has a relatively low RMS amplitude error in deep water (4.9 cm, PVE = 96.6 %), made up in approximately equal measure by amplitude (3.2 cm) and phase (3.8 cm) contributions. For comparison, the RMS difference with M_2 ground truth estimates from 151 deep-ocean bottom pressure recorders (Ray, 2013) is 5.4 cm. These values are smaller than published deep-ocean RMS errors of other baroclinic forward models (e.g., Stammer et al., 2014; Jeon et al., 2019) and suggest no need for a parameterized topographic wave drag in the model, as advocated for in, e.g., Arbic et al. (2010). Statistics for S_2, K_1, and O_1 in Table 4.1 further underline the realism of the simulation in the deep ocean. The comparatively low variance captured in the case of S_2 (PVE = 90.8 %) is not surprising, given that barometric pressure loading by the semi-diurnal solar atmospheric tide is omitted in the forcing data (Arbic, 2005).

In shallow water, where tidal amplitudes tend to be larger than in the deep ocean, the M_2 RMS error grows to 23.0 cm relative to TPXO9 (PVE = 78.5 %) and to 32.5 cm if the M_2 harmonics at the coastal tide gauges (Section 4.2.1) are taken as reference. Similar increases in error are evident for S_2 and the diurnal constituents. Reduced fidelity over shelf seas and at the coast is common in the context of baroclinic tidal simulations (Stammer et al., 2014), especially when compared to the skill of carefully tuned barotropic models in the same areas (e.g., Blakely et al., 2022). As an example, the LLC1080 simulation produces an M_2 amplitude of 273 cm at Boston (USA), twice as large as the observed value. Accordingly, one can expect the modeled year-to-year M_2 changes in the Gulf of Maine to be a factor of ∼2 higher than the changes reported in Schindelegger et al. (2022) for the same region.

Continuing the validation with the baroclinic tidal regime, area-averaged amplitudes in specific regions, which are known to be energetic (Shriver et al., 2012), are calculated. The regions differ for diurnal and semidiurnal internal tides. The exact bounds are given in Table 4.1 and are illustrated in Figure 4.2. The values in Table 4.1 correspond to one year of simulation (here:

Table 4.1: Validation of modeled barotropic and baroclinic surface tides (from Opel et al., 2024).

	M_2	S_2	K_1	O_1
Comparison with TPXO9[a], RMS misfit $\overline{\Delta\eta}$ (cm) and PVE (%)				
> 1000 m	4.9 (96.6)	3.2 (90.8)	1.9 (96.1)	1.7 (93.0)
< 1000 m	23.0 (78.5)	10.2 (69.9)	8.8 (78.0)	6.6 (76.4)
Comparison with in-situ data, RMS misfit $\overline{\Delta\eta}$ (cm)				
Deep-ocean seafloor gauges[b]	5.4	3.7	1.5	1.8
Coastal tide gauges, this study	32.5	19.2	4.9	3.9
Area-averaged amplitudes (cm) of internal tides[c]				
North Pacific	1.02 (0.98)	0.45 (0.38)	–	–
South Pacific	0.90 (0.85)	0.29 (0.19)	–	–
Madagascar	1.02 (0.76)	0.53 (0.30)	–	–
Philippines	–	–	0.79 (0.56)	0.60 (0.49)
Central Indian Ocean	–	–	0.38 (0.23)	0.24 (0.11)

[a]Statistics are for the spatially smoothed surface tide solutions of the year 2006 in latitudes lower than 66°; PVE values are given in parentheses.
[b]151 deep-ocean seafloor gauges are from ref. Ray (2013).
[c]Stationary baroclinic tidal signals are compared to the altimetry-based estimates of Zaron (2019) (in parentheses) over five rectangular domains, as marked out in Figure 4.2

2006). Sensitivity tests reveal that the choice of the analysis year influences the resulting area-averaged internal tide amplitudes only at the sub-mm level. Therefore, the impact of the choice of year is insignificant for this comparison. The values for validation are computed from the internal tide model of Zaron (2019), which includes no explicit along-track filtering of satellite altimetry tracks.

For diurnal tides, two regions are chosen for validation, one around the Philippines, and one located in the central Indian Ocean. Overall, the diurnal internal tides are higher in terms of the area-averaged mean amplitude than those from the model of Zaron (2019). Despite the overestimation, their propagation direction still seems plausible. The regions for the semidiurnal tides represent the North Pacific, the South Pacific, and a region around Madagascar. Again, the simulated estimates are overestimated in comparison to those from Zaron (2019). This is especially true for the internal tides near Madagascar. The reason might originate from the altimetry processing, from the MITgcm including both the representation of topography and stratification, or a combination of several of these factors. Within the altimetry processing of Zaron (2019), spatial smoothing is involved and the extraction of internal tides is generally rather challenging. Moreover, within the model, wave breaking and dissipation may not be represented accurately enough on small spatial scales. In addition, there could be too little interaction of internal tides with the general circulation, since the latter might be too weak in the absence of atmospheric forcing. It is worth noting, that the conducted 40 days of integration produce an internal tide field which is probably not fully developed. The distance traveled by low mode internal tides in 40 days is about 10 000 km, assuming an average phase speed of $3\,\mathrm{m\,s^{-1}}$, keeping in mind that the phase speed in the real ocean is actually variable and depends, e.g., on the latitude. Here it is important to note that the model is integrated forward from a cold start, thus the spin-up is also contained within these 40 days of integration. Considering K_1, the traveled distance of internal tides is higher than for M_2, but has a strong limitation depending on latitude. These assumptions are based on phase speed estimates and considerations from literature (e.g., Zhao, 2014; Zaron, 2019; Li et al., 2017).

In general, the results described above are consistent with estimates that are observed from satellite altimetry by, e.g., Shriver et al. (2012). Altogether, the internal tide field is fairly accurate and features familiar regions of internal tide generation, described previously in the literature. The global barotropic tides are also realistic, especially in the open ocean. Especially, high accuracy is achieved in the deep ocean. The shallow areas show reduced accuracy in comparison to the deep ocean, but this is common among baroclinic tide models (Stammer et al., 2014; Jeon et al., 2019). Overall, the simulations with the MITgcm setup produce sufficiently accurate estimates of the four major tidal constituents.

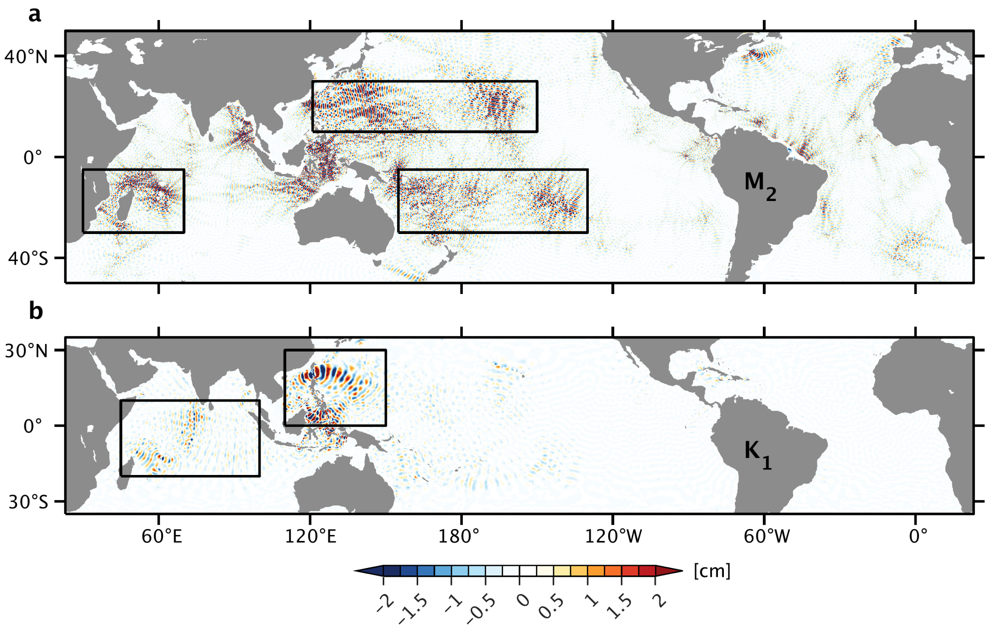

Figure 4.2: In-phase component of the stationary **a** M_2 and **b** K_1 internal tide in surface amplitude from one simulation (year 2006). Black boxes denote the regions used to compute the area-averaged internal tide amplitudes in Table 4.1.

4.1.4 Sensitivity Experiments

The vertical domain discretization is typically a critical component of general circulation models. Here it possibly limits the realism of the model in shallow water, but also in the deep ocean, where barotropic-to-baroclinic energy conversion is taking place. The 59-layer setup represents a trade off between computational costs and a stable model that can handle tidal surface oscillations in the meter range. Additional experiments with surface layers of 1 m were conducted, but resulted in model crashes for many of the test simulations. For the purpose of this thesis, which is mainly the analysis of the global ocean tides, the 6 m vertical layer thickness is sufficient. It also allows for ∼3–4 layers in very shallow regions to represent, e.g., the impacts of vertical eddy viscosity changes on tidal currents and surface elevations (Müller et al., 2014).

Energy exchanges between the barotropic and baroclinic tide (cf. Section 2.3.2) shift the focus from the surface vertical resolution to the deeper ocean vertical resolution. Experiments were

Table 4.2: Comparison of different vertical model configurations.

	RMS[a] M_2 (cm)			$\overline{C}$ (TW)		
	all	shallow[b]	deep[c]	all	sources	sinks
original	8.7	24.9	5.1	0.50	0.66	−0.16
66 layers (cf. Figure 4.3)	8.7	24.9	5.1	0.50	0.66	−0.16
66 layers, modified parameters[d]	8.8	25.1	5.1	0.35	0.47	−0.12

[a]RMS relative to TPXO9 (Egbert and Erofeeva, 2002), [b]ocean regions shallower than 1000 m, [c]ocean regions deeper than 1000 m, [d]Leith viscosity & bottom drag modified

conducted with refinements in the vertical resolution between 3000 m and 5500 m ocean depth. Figure 4.3 shows the comparison of the original vertical setup (Figure 3.3) to a refined test setup. Here, a sensitivity test was performed with 66 layers in the vertical. The resulting harmonic tidal solution, as well as the tidal conversion estimates, were essentially unchanged from the 59-layer simulation and showed no significant improvements. As the increase in layer number results in a longer model runtime, the original setup of 59 layers was chosen. The exact differences between the setups can be read in Table 4.2. Here, additionally a test with 66 layers and altered Leith viscosity (from 2 to 1.5) and bottom drag (from 0.003 to 0.002) was performed. This setting slightly degraded the RMS and reduced the globally integrated conversion estimate. The performed sensitivity tests testify to a stable model setup, since neither the vertical spacing nor the frictional closures seem to exert major control on the simulation results for surface elevations.

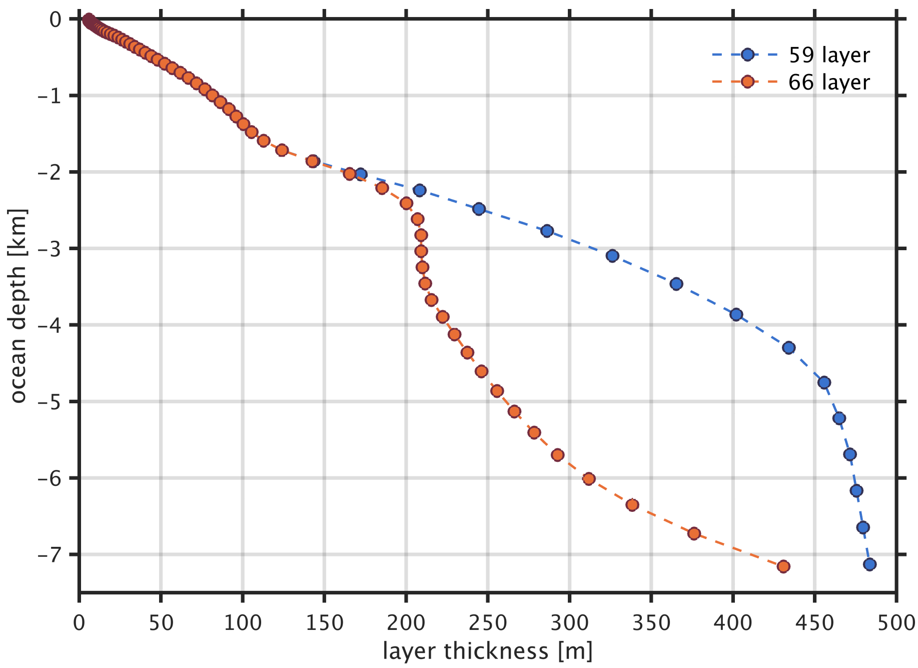

Figure 4.3: Visual comparison of two vertical layer discretizations.

4.2 Observations

Observations of the sea level have a long history, as they are important for many reasons, such as nautical safety, coastline management, or economics. Globally distributed tide gauge measurements of instantaneous water levels form an important observational basis (e.g., Woodworth, 2010; Haigh et al., 2020). Since tide gauge measurements are restricted to the coast, observation of the offshore oceanic sea level are also appreciated to better map oceanic variability and understand the underlying processes. Global observation of the ocean's surface is achieved with satellite altimetry. Many different missions are in orbit and continuously contribute to a globally evolving observational network since the first altimeter satellite missions in the 1970s (Ray and Egbert, 2017). Tide gauges and satellite altimeter observations complement each other to some extent, since altimeter observations become more uncertain toward the coast (e.g., Ray and Mitchum, 1997).

A water height observation of a specific point in time contains a sum of different physical parts. It is composed of the mean sea level, the tidal level and a residual sea level (Pugh and Woodworth, 2014). These components change on different time and spatial scales. Both observational sources, tide gauges and satellite altimetry, yield on one hand the mean tide, which can be used as an accuracy assessment basis. On the other hand, they also contain information on tidal changes. In this work, altimetry observations are used to estimate tidal trends, while tide gauges are used to quantify both trends and the year-to-year changes.

4.2.1 Tide Gauges

Tide gauge observations form an important part of validation measure for the simulated harmonic tidal constituents in this work. Harmonic constants are estimated from a network of 201 globally distributed tide gauge stations, illustrated in Figure 4.4. The network is extracted from the GESLA-3 database (Global Extreme Sea level Analysis Version 3, Haigh et al., 2022; Woodworth et al., 2016; Caldwell et al., 2015).

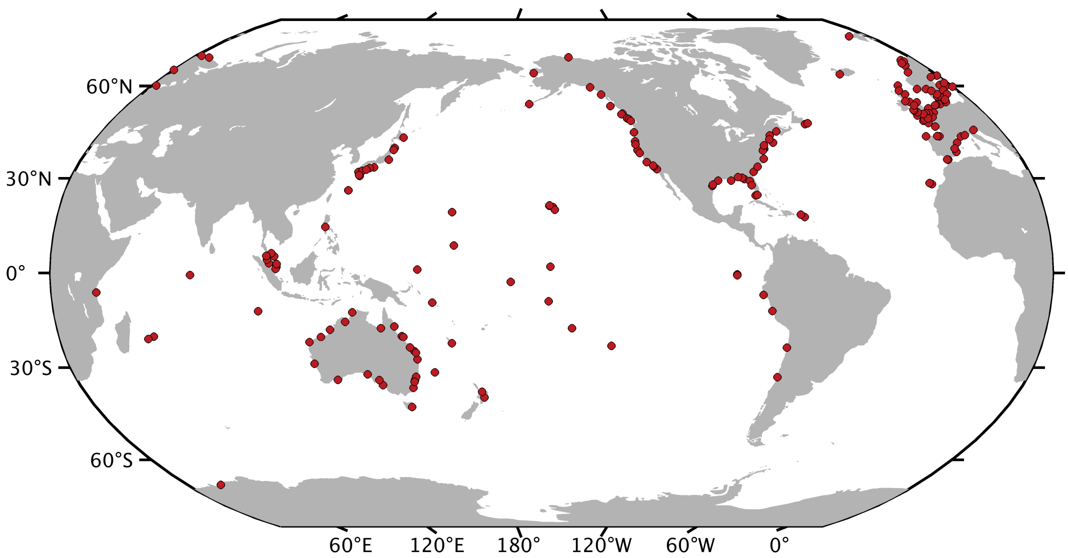

Figure 4.4: Locations of the 201 tide gauges used in this study.

The choice of stations is based on an automatic throughput of all stations with different quality checks. The conditions that have to be met for one station to be included in the harmonic analysis are:

- Hourly sampling rate
- Minimum temporal coverage of 28 years (Mawdsley et al., 2015)
- Minimum of 15 calendar years of data
- No data gaps longer than 20 years
- Within one year of data: only data gaps $<$ 20 days (otherwise: calendar year skipped)

Additionally, the estimated individual amplitude and phase time series of the stations are visually inspected. The stations that pass these quality checks are harmonically analyzed with respect to their tidal constituents by the UTide software package (Codiga, 2011). The harmonic analysis includes 67 tidal constituents that are annually estimated with an ordinary least-squares analysis. The associated formal uncertainties are obtained simultaneously by a spectral approach. The nodal cycle of 18.61 years (e.g., Pugh and Woodworth, 2014) is reduced from the yearly tidal constants over the whole record length. Afterwards, the time series of tidal harmonics is cut to the desired analysis window of 1993–2020 to validate the modeled estimates at every station. Note also that most stations are relatively open to the sea. For example, stations that are directly influenced by an estuary or an inland waterway are skipped, since the tidal characteristics, including their temporal evolution, are likely affected by a number of local factors that complicate the analysis (Haigh et al., 2020).

Within this work, mainly two metrics are used to evaluate the agreement between modeled and observed tidal interannual estimates (cf. Chapter 5). When comparing two time series, the Pearson correlation coefficient R and the PVE are computed to assess the spatiotemporal agreement. Additionally, the Kling-Gupta efficiency (KGE, Gupta et al., 2009) is used as another metric to evaluate the model performance in comparison to observed time series of tide gauges. Corresponding visualizations of the KGE, analogous to Figures 5.4–5.6, are provided in the Appendix (Figures D.5–D.7). The metric does not provide additional insights compared to R and PVE, rather it stresses the difficulties in the comparison of the modeled and observed time series. The KGE is sensitive to the relative variability in terms of the ratio of modeled and observed standard deviation in combination with the ratio of the averages of observed and modeled timeseries, which results here mostly in negative KGE values (cf. Figures D.5–D.7), indicating bad agreement between model and observations. This could arise due to overestimation of the model or more generally, its decreased performance in shallow waters.

4.2.2 Satellite Altimetry

Observations from satellite radar altimetry are widely used to map changes, especially in terms of geometry of various Earth system components, including land topography or the height of ice sheets. They also form a powerful tool for validating ocean model output and studying oceanic phenomena in general (e.g., Wunsch and Stammer, 1998; Stammer et al., 2014; Ray and Egbert, 2017; Carrère et al., 2021; Morrow et al., 2023). In contrast to pointwise tide gauge observations that are restricted to coastal areas, satellite observations are capable of a continuous global coverage. Precise observations are particularly available for the open ocean, several tenths of kilometers from the shore, whereas the uncertainty of altimetric sea levels increases toward the coast. Recently, considerable effort has been devoted to estimate also trends in the ocean tide from satellite altimetry. The undertaking is quite challenging, since a main limitation persists in the temporal sampling of the satellite altimetry data. Additionally, the variability of the individual partial tides can be rather subtle in comparison to the overall observed sea level variability, while data noise and systematic errors can also be implicated. Bij de Vaate et al. (2022) estimated tidal trends of M_2, S_2, K_1, and O_1 tides at specific crossovers of satellite ground-tracks. The involved satellite mission are T/P and Jason satellites. The 30-year trends reveal novel insights into tidal trends in the open ocean.

With regard to this work, satellite altimetry is used to validate the modeled tidal trends on a global scale for each partial tide's amplitude and phase lag. The description of the most relevant processing steps below and in Section 4.3.3 is a summary of the methods described in Opel et al. (2024) and further expanded on in Ray and Schindelegger (2025). The estimated tidal trends from satellite altimetry are, as clarified in the author contributions of Opel et al. (2024), conducted by Richard Ray[1]. Given that the estimates form an important point of comparison in this work, the analysis of the data, as well as sources of uncertainties, are summarized below. Limitations mainly persist in the common latitude restriction of ±66° and larger uncertainty toward shallow and marginal seas.

The data source is the *Radar Altimeter Database System* (RADS) (Scharroo et al., 2013). Within the analysis period of 1993–2020, data from Topex/Poseidon (T/P), Jason-1, Jason-2, and Jason-3 satellites are used. To remain consistent, only data that are restricted to a primary T/P ground-track are considered. The methodology for processing the altimetry data is chosen differently to Bij de Vaate et al. (2022). The approach builds on Schrama and Ray (1994), by creating overlapping bins of tidal residuals, which offers the advantage of suppressing noise through optimization of the bin size. Another benefit is that the averaging of data within sufficiently wide bins will remove residual signals by internal tides. The bin size is variable, depending on latitude, water depth and the distance to the coast. In the deep ocean of low latitudes, the bin size is approximately 1.5° times 6°, which is chosen to include at least two ascending and two descending ground-tracks. Within each bin, the individual satellite tracks are counted as independent data (and not every data point itself), to account for serial correlation among observations within one pass.

The corrections applied to the altimeter data include default and standard corrections of RADS (e.g., for barotropic ocean tides as stationary phenomena). Additionally, gridded sea surface heights (Taburet et al., 2019) are used to remove non-tidal and especially mesoscale variability, which generally results in lower noise levels in the subsequent analysis. Moreover, stationary internal tide signals are removed with the harmonics of Zaron (2019). As the estimated tidal trends are of small magnitude, they can be affected by subtle systematic errors, as mentioned in Opel et al. (2024) and discussed more broadly in Ray and Schindelegger (2025). One such error is included in the standard altimeter dealiasing (dynamic atmospheric) correction (DAC) (Carrère and Lyard, 2003). The DAC correction accounts for the wind-, and pressure-driven dynamic ocean variability on time scales <20 days, comprising also sub-daily variability and thus the atmosphere-driven component of the M_2 tide. As evident from Figure 4.5, the M_2 harmonic in the DAC fields has a small unexpected trend. This artificial trend in the DAC correction

[1]Geodesy & Geophysics Laboratory, NASA Goddard Space Flight Center, Greenbelt, MD, USA

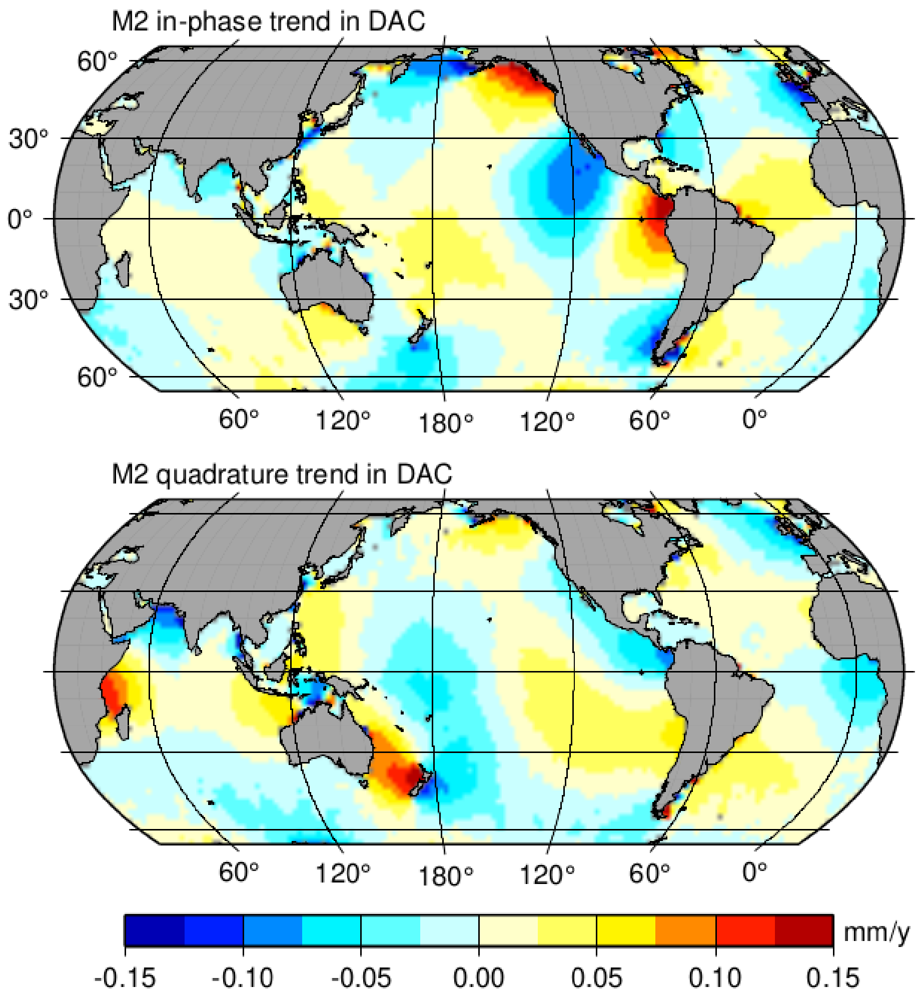

Figure 4.5: In-phase and quadrature trends in M_2 extracted from the DAC elevations taken from Ray and Schindelegger (2025) (1993–2022). The DAC trends used in this work are based on a slightly shorter time span (1993–2020) for consistency with the model simulations. Addition of two years of DAC data barely changes the trend values.

appears to be caused by temporal changes of the lunar semidiurnal air pressure tide that is contained within the DAC forcing fields (Ray and Schindelegger, 2025). The trend accounts for a substantial fraction of the total altimetric M_2 trend in several locations and must therefore be corrected. Upon extracting the trend from the DAC fields, its in-phase and quadrature components (Figure 4.5) are readily added to the total altimetric M_2 trend, thus eliminating spurious contributions from the DAC (Opel et al., 2024).

Secondly, coherent errors in satellite ephemerides possibly affect the small estimated trend signals. This holds also for inconsistencies in geocenter models due to annual geocenter motion (Desai and Ray, 2014), or inconsistencies in the RADS processing. Approximate estimates for orbit errors affecting M_2 trends are in the order of magnitude of the associated standard errors, and similar statements hold for other tidal constituents (Ray and Schindelegger, 2025). These quantifications are based on comparing different satellite ephemerides products, which serves as a stand-in as long as the true tidal orbit errors are unknown.

Thirdly, the correction for non-tidal sea surface height variability (Taburet et al., 2019) contains small errors from aliased tidal variability (Zaron and Ray, 2018). This is a known issue, but it remains unclear how and to which extent the estimated tidal trends are affected. If the tidal leakage would change over time, it would affect the small estimated tidal trends. Investigations by Ray and Schindelegger (2025) reveal that the impact on M_2 trends is expected to be within uncertainties for the open ocean. In coastal areas and marginal seas, the impact is considerably larger, but the altimetry trends are in any case uncertain there. In addition, imperfect tropospheric and ionospheric path delay corrections induce no appreciable systematic error for the lunar semidiurnal tide, while the matter is thought to be considerably different for solar tidal constituents (Ray and Schindelegger, 2025).

4.3 Estimation and Statistical Significance of Tidal Trends

Time series of modeled and observed tidal amplitudes are used in this work to derive linear trends with related formal uncertainties of M_2, S_2, K_1, and O_1 in the analysis period of 1993–2020. The methodology of the trend estimation differs based on the source of the tidal amplitude time series. The trend estimation of tidal amplitude time series from tide gauges and from simulations of this work, both consisting of annual amplitude estimates, is carried out in the same way, as described below in Section 4.3.1. The trend estimation of satellite altimetry observations requires a different approach, described in Section 4.3.3.

4.3.1 From Interannual Time Series to Linear Trends

Each constituent's time series of yearly amplitudes and phases, either modeled or based on observations at a tide gauge, is used to estimate a linear trend between 1993 and 2020. The trend estimation is based on the amplitude time series alone, or expressed in in-phase/quadrature time series that also include the tidal phases (cf. Equation 4.2). The trend estimation is conducted with least-squares adjustment (cf. Appendix A for a brief overview, otherwise Koch, 1999, for more details), including a mean value, a linear trend, and a lag one-year autocorrelation of the residual terms to account for serial correlation within each time series (cf. Opel et al., 2024). The associated estimation of formal uncertainties is carried out based on the stochastic model of the least-squares fit. As described in Opel et al. (2024), the t-values for the two-sided tests at α-levels of 0.05 and 0.32 are typically 2.101 and 1.023 (increasing with decreasing degrees of freedom of the time series). The location-dependent t-values are multiplied with the formal standard errors of the stochastic model to obtain the individual 95 % and 68 % confidence intervals.

The processing and estimation of formal uncertainties of the annually modeled tidal amplitudes and phases is conducted at every grid point, resulting in global maps of the modeled linear tidal trends. Formal uncertainties are also estimated based on the stochastic model of the least-squares adjustment as described above. Whenever trends are used to compute a derived quantity (e.g., a spatially averaged trend), the corresponding uncertainties are estimated via variance propagation.

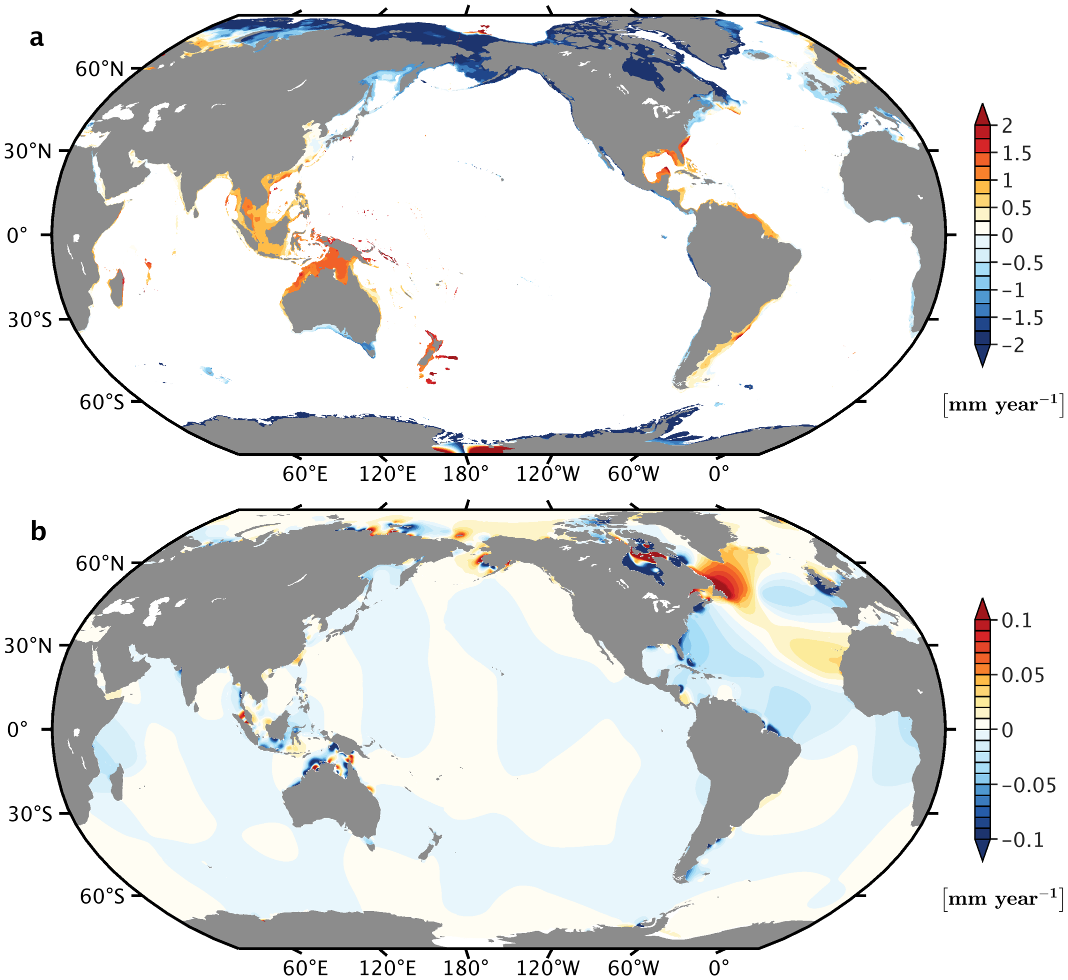

Figure 4.6: **a** Trend in the MITgcm's mean free surface height across the 28 simulations and **b** the corresponding M_2 amplitude response (in mm year^{-1}), as deduced from two endpoint simulations with perturbed and unperturbed water depths. Values at deep ocean grid points (> 500 m) are clipped in **a** to emphasize shallow regions were the tide is sensitive to water depth changes.

4.3.2 Indirect Effects of Residual Sea Level Changes in the Model

The MITgcm uses the Boussinesq approximation, which results in an inability to represent the effect of steric expansion and contraction in the momentum equations. However, steric expansion is included in the equation of state (Greatbatch, 1994). This expansion effect leads to a trend in the free surface of the MITgcm simulations across the 28 yearly simulations, as shown in Figure 4.6a for water depth shallower than 500 m. Especially in coastal regions and shallow waters with depth below 200 m, the tide is sensitive to water depth changes (Müller et al., 2011). These regions reveal trends of the mean free surface up to ± 2 mm year^{-1}.

The question thus arises by which amount the trend in model sea level is able to alter the tidal harmonic solutions. To quantify the effect, one additional simulation is performed. This simulation gives the possibility for an *a-posteriori* correction of the estimated tidal trends. Beforehand, the correlation between the year-to-year changes in the mean free surface η_0 and the M_2 amplitude changes is tested. No obvious correlation can be found, supporting the approach of correcting the impact of residual sea level changes on M_2 through a single simulation.

Specifically, the trend from Figure 4.6a is multiplied by the overall analysis time span that is, 27 years between the mid-years of the first and last simulations. Hence, a multiplication by 27 gives the total change in water depth associated with the ocean's steric expansion in the analysis period. Afterwards, this total value is subtracted from the model bathymetry.

The so-perturbed bathymetry is used as input for the additional simulation of one specific year of stratification. Here, the year 2006 is chosen (again) somewhat arbitrarily. The direct comparison of the harmonics of the original unperturbed run of 2006 and the perturbed run of 2006 reveals the impact of the trend in model sea level on the tidal estimations. The difference is scaled by the time span ($^1/_{27}$) and represents the correction that is subtracted from the original M_2 trends. The correction is shown in Figure 4.6b and indicates large trends at the US East coast, on the Amazon shelf, on the North Australian continental shelves, and in the Celtic and Irish Seas.

4.3.3 Trends from Satellite Altimetry

The trend analysis of the satellite altimetry data is conducted within bins of tidal residuals, as described in Section 4.2.2 (Opel et al., 2024). For each bin, the mean in-phase and quadrature component of a partial tide (main focus on M_2) are estimated relative to the RADS prior, as well as the linear trend. Allowance is made for corrections to the two nodal sidelines of M_2, since in some locations the trend estimation could be affected by the 18.6-year nodal cycle (Feng et al., 2015). The estimated in-phase and quadrature trend maps are smoothed with boxcar averaging. The empirically tested, and again somewhat arbitrarily chosen filter settings are $10° \times 10°$ in waters deeper than 500 m, whereas for shallow water the settings are $1.5° \times 1.5°$. Moreover, the in-phase and quadrature trends are converted to amplitude trends, as illustrated in Figure 4.7a for M_2. The associated formal standard errors of the unsmoothed trend estimate are displayed in Figure 4.7b. The formal errors are valid for the amplitude trend, as well as the in-phase and quadrature trends. To transfer the displayed error to the smoothed estimate (Figure 4.7a), the trend map is smoothed with the same boxcar filter as the trends themselves, and additionally scaled by $\sqrt{n_1/n_2}$, with n_1 being the number of altimeter tracks crossing the original analysis bin and n_2 being the number of altimeter tracks crossing the wider filter bin (Opel et al., 2024).

4.4 Complementary Simulations

As mentioned in the beginning of Chapter 2, modeling the global ocean with only one vertical layer was, and still is, quite common to address certain research questions in ocean science. These so-called barotropic (constant-density or shallow-water) models are depth-independent. In the context of this work, the estimated impact of stratification on tides is compared to another, frequently discussed driver for tidal changes, viz., relative sea level rise (cf. Chapter 2.4). The model configuration to evaluate the impact of sea level rise on tides, is described in detail in Schindelegger et al. (2018) and also used in Opel et al. (2024). The model is originally based on codes from Einšpigel and Martinec (2017). Below I include a brief description for completeness, as the modeling results are important to this thesis for context and comparisons.

The barotropic model solves the shallow water equations on a quasi-global finite difference grid. The model's resolution is $^1/_{12}°$ in the horizontal (86°S–84°N). The forcing consists of the

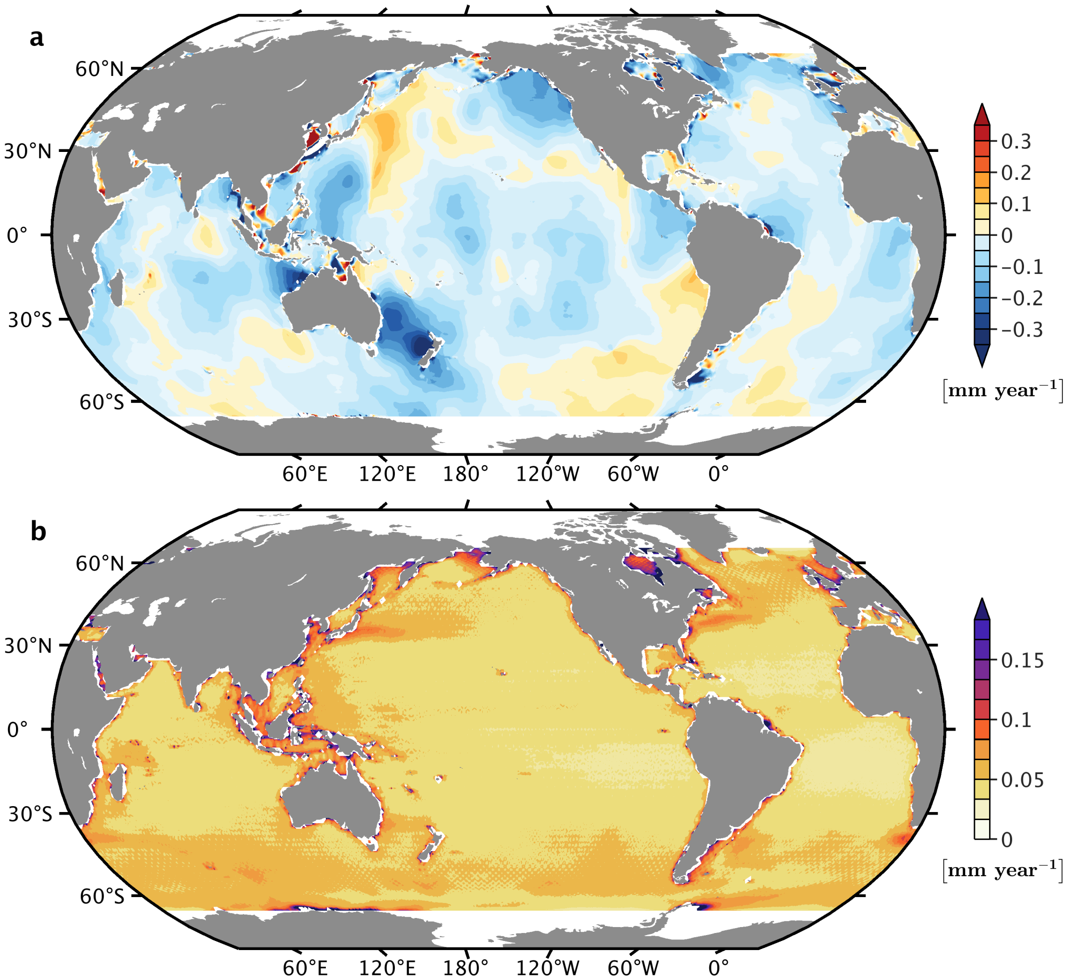

Figure 4.7: **a** Smoothed altimetry-based M_2 amplitude trends (1993–2022) and **b** the associated onefold (68 %) standard error for the original unsmoothed M_2 amplitude trend, based on Opel et al. (2024).

equilibrium (η_{EQ}), as well as the SAL (η_{SAL}, computed inline) tide, including the four primary tidal constituents M_2, S_2, K_1, and O_1. Changes in relative sea level are induced as perturbations to the local water depth. The model includes a parameterization for internal wave drag, which is carefully chosen as it directly impacts the realism of the model-based tidal estimations in comparison to altimetric tide observations (Schindelegger et al., 2018). The simulations are conducted with an annual time slice approach, as above for the 3D MITgcm simulations. The integration time span is 27 days, whereof the last 15 days are used for the harmonic analysis. The modeled tidal harmonics, that reflect the impact of sea level rise on the global tides, are used for comparison in Chapters 5 and 6.

Additionally, relative sea level rise is estimated as future projections and included in Chapter 7 to simulate its impact on tides toward the end of the 21st century. Therefore, an aggregated projection of the main components of future sea level rise is compiled for any location at time t (Jackson and Jevrejeva, 2016; Kopp et al., 2019), yielding

$$\eta_{rsl} = \overline{\eta}_{steric} + \eta_{steric}^{melt} + \eta_{dyn} + \eta_{GIA} + \eta_{ice} + \eta_{glacier} \quad . \tag{4.8}$$

The individual components are the globally averaged steric expansion $\overline{\eta}_{steric}$, spatially varying steric expansion due to ice sheet freshwater discharge into the ocean η_{steric}^{melt} (Golledge et al., 2019), the ocean's dynamic response to atmospheric and buoyancy forces η_{dyn}, glacial isostatic adjustment η_{GIA}, and sea level fluctuations due to ice sheet η_{ice} and glacier $\eta_{glacier}$ mass fluxes. In general, the terms $\overline{\eta}_{steric}$ and η_{dyn} depict ensemble means of climate models. The contributions of η_{ice} and $\eta_{glacier}$ originate from sea level fingerprints computed from model projections of glacier and ice sheet mass loss. For more details on the sea level projection and numerical model setup, the reader is referred to Opel et al. (2025). Table 4.3 highlights the most important model parameters as a comparison for the three drivers of 21st-century changes in ocean tides (based on Opel et al., 2025).

Table 4.3: Details related to the representation of the three drivers of 21st-century changes in ocean tides

	Ice shelf melt	Sea level rise[a]	Stratification change
Numerical model	2D shallow water model	2D shallow water model	3D MITgcm
Grid spacing	1/12°	1/12°	∼1/12°
Perturbed component	Water depths under ice shelves	Water depths of all wet points	Model initial hydrography
Data source	Antarctic ice sheet simulation (Golledge et al., 2019)	CMIP5 output, simulated land ice changes (Golledge et al., 2019; Huss and Hock, 2015), GIA model	EC-Earth-3P-HR as part of CMIP6 HighResMIP (Haarsma et al., 2020)
Scenarios	RCP4.5, RCP8.5	RCP4.5, RCP8.5	SSP5-8.5
Nominal averaging period	5 years (2046–2050, 2056–2060, etc.)	5 years as for the other drivers, 20 years for $\overline{\eta}_{steric}+\eta_{dyn}$ (2040–2059, 2050–2069, etc.)	5 years (2046–2050, 2056–2060, etc.)
Average for last time slice	2096–2100	2100	2096–2099
Baseline period	1996–2000	1996–2000 and 1986–2005 for $\overline{\eta}_{steric}+\eta_{dyn}$	1996–2000

[a]See Eq. 4.8 for the individual terms in the sea level model.

5 Tidal Variability

In this chapter, I assess the low-frequency—i.e., interannual—variations over approximately three decades in the detrended modeled tidal harmonics and set it into context to observed tidal variability at tide gauges. Thereby, the impact of stratification changes on the overall tidal signal is determined at several globally distributed locations.

5.1 Low-Frequency Variability

Tidal variability in the 3D simulations arises from the prescribed and changing ocean density structure. To assess the interannual tidal variability of each constituent's amplitude, a linear trend is first removed from the amplitude time series (1993–2020) for every point in space. This is true for all data presented in this section, except for the regional time series of Figure 5.3.

The standard deviation at each grid point is computed over the 28-year analysis window for the whole globe. This analysis is conducted separately for the barotropic and baroclinic tidal component. The standard deviation can be taken as a measure of the interannual variability. For the M_2 tidal amplitude, the standard deviations of the barotropic and baroclinic tide are shown in Figures 5.1a and c. Comparing the deep and shallow ocean of the barotropic variability, changing stratification clearly induces a higher standard deviation in shallow and coastal waters. This spatial variability is especially visible in the Indonesian Seas, which are known to host very complex tidal patterns, due to highly variable land-sea distribution and bottom topography, as well as narrow straits through which tidal regimes of both the Indian Ocean and the Pacific Ocean come together (Ray et al., 2005). Other striking regions are the North Australian coast (cf. White et al., 2014), the Northwest European Shelf (e.g., Woodworth et al., 1991; Jänicke et al., 2021, for the North Sea), Baffin Bay, the Patagonian Shelf, the Gulf of Maine (cf. Ray, 2006; Katavouta et al., 2016; Schindelegger et al., 2022) and the Yellow and East China Seas (cf. Kang et al., 2002; Feng et al., 2015). Particularly the Celebes Sea and the Strait of Makassar reach spatially homogeneous peak variability of ~6 mm and ~7 mm in the period of 1993 to 2020 in the barotropic M_2 amplitude.

In contrast, the latter two regions also stand out in the barotropic S_2 component (Figure 5.1c) with spatially homogeneous (peak) amplitude variability of ~4.5 mm and ~6 mm. Other shallow regions with enhanced S_2 variability in Figure 5.1c are mainly the Patagonian Shelf, the Northwest European Shelf, the Northern coasts of Australia, and regions around the Arctic Northwest passage. The open ocean variability of the barotropic S_2 tide is <1 mm. For both S_2 and M_2, the tidal variability in shallow regions, can be caused by the ocean stratification acting onto the eddy viscosity profile, which regulates part of the tidal dissipation and thus the surface tidal amplitude (Kang et al., 2002; Müller, 2012; Katavouta et al., 2016).

The barotropic interannual variability of the diurnal tidal constituents is mainly concentrated in

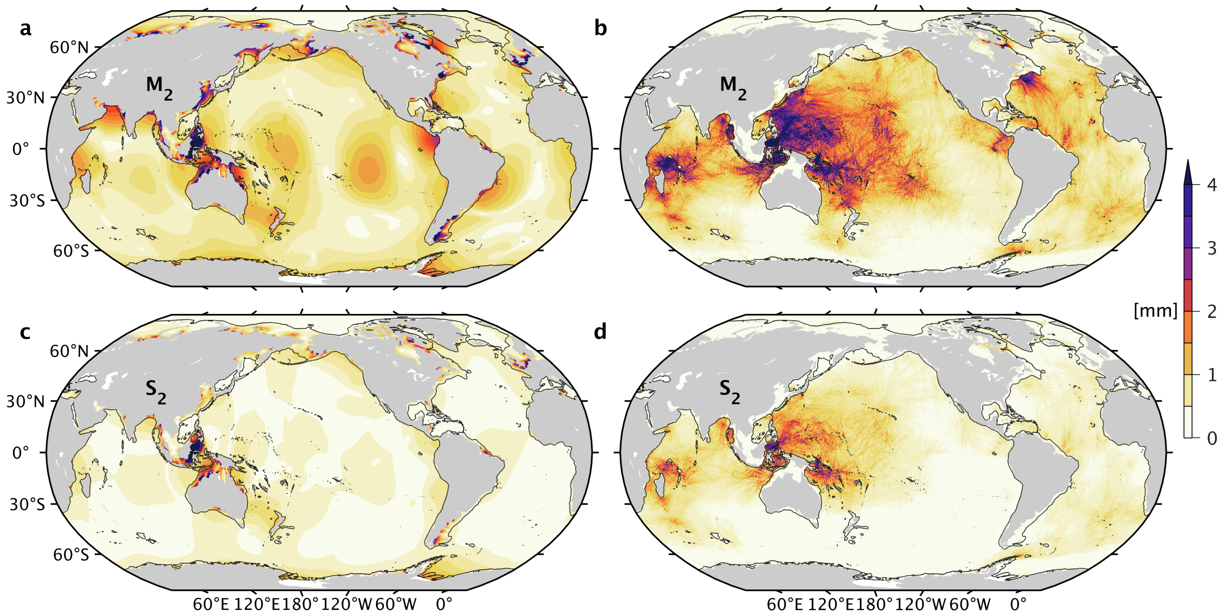

Figure 5.1: Standard deviation (mm) of the simulated M_2 and S_2 amplitude for the barotropic tide (M_2 **a**, S_2 **c**) and the baroclinic tide (M_2 **b**, S_2 **d**) (1993–2020). A linear trend has been removed beforehand from the yearly estimates. The black solid line marks the 500 m bathymetry level.

shallow and coastal regions, too. This is shown in Figures 5.2a and c. For K_1, values exceeding 2 mm are reached in the seas southwest of Papua-Neuguinea, around Indonesia, in the Gulf of Thailand, the South China Sea, the Yellow and East China Sea and in the Sea of Okhotsk. Interannual variability of ~1 mm in magnitude is present on the Northwest European Shelf, the Gulf of Saint-Lawrence, and in Baffin Bay. The barotropic O_1 tide shows interannual variability in similar regions as K_1. Figure 5.2c reveals smaller and more localized peak variability for O_1 than for K_1, evident especially along coastlines in the Indonesian Seas. For both diurnal constituents, largest sensitivity to stratification is found in the Sulu Sea with magnitudes of ~2.5 mm (K_1) and ~2 mm (O_1). Different to K_1, interannual changes in the barotropic O_1 component appear to be absent in the Yellow and East China Seas.

In contrast to the barotropic tide, the simulated baroclinic tide shows increased variability in regions of the open ocean. Shallow waters remain unaffected, given that internal tides are per physical definition unable to propagate in only one, well-mixed layer. This leads to the assumption that changing observations at tide gauge stations on continental shelves remain mainly unaffected by internal tides, whereas pelagic tide gauge stations, that are located mainly on smaller islands in the open ocean, can contain signals from internal tides. One such known case is the tide gauge of Honolulu (Colosi and Munk, 2006). These authors found modulations of the internal tide impacting the observed surface tide. They identified the time-variable density structure as the reason for the internal tide modulation, which in turn alters the measured tidal harmonics on secular and interannual time scales. They specifically found a modulation of the tidal phase speed, and thus phase angle, of the baroclinic component approaching the Honolulu tide gauge station.

Areas that indicate higher standard deviations of the baroclinic M_2 tide in Figure 5.1b coincide with regions of enhanced tidal conversion from barotropic to baroclinic modes (Zaron, 2019; Zhao et al., 2016). Particularly conspicuous in Figure 5.1b is the tropical western Pacific, including several known active regions of tidal conversion (e.g., Ray et al., 2005; Robertson and Ffield,

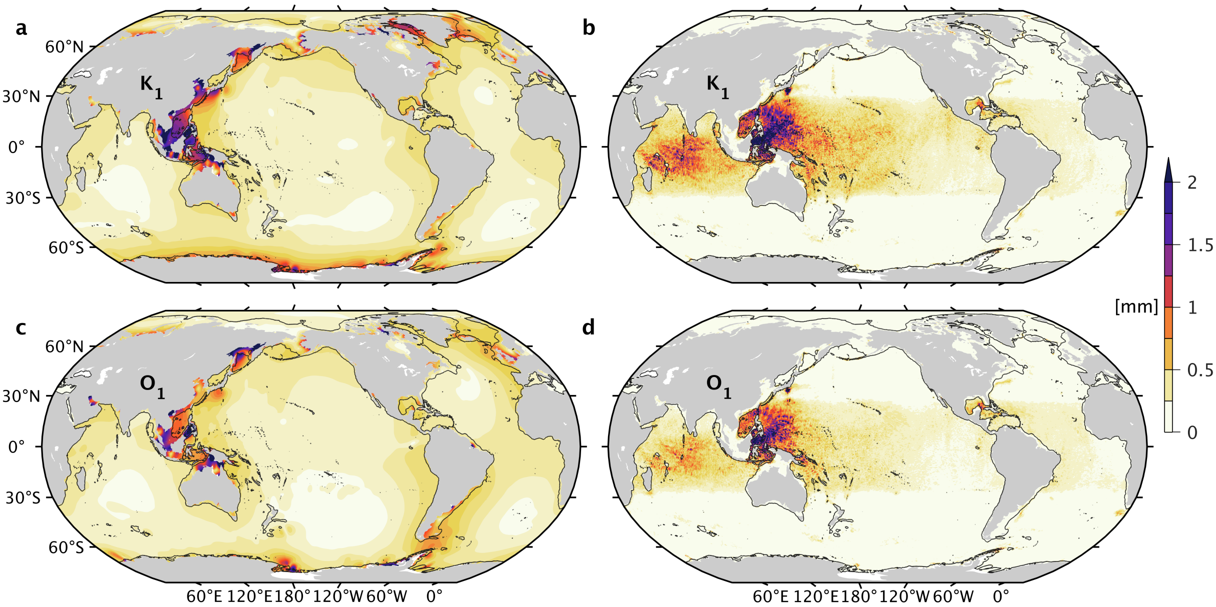

Figure 5.2: Standard deviation (mm) of the simulated K_1 and O_1 amplitude for the barotropic tide (K_1 **a**, O_1 **c**) and the baroclinic tide (K_1 **b**, O_1 **d**) (1993–2020). A linear trend is removed beforehand from the yearly estimates. The black solid line marks the 500 m bathymetry level.

2008; Müller, 2013). The Celebes Sea reaches magnitudes of ∼4 mm to 10 mm. Other regions that feature enhanced interannual variability of the baroclinic M_2 tide in the model are the Hawaiian Ridge (cf. Ray and Mitchum, 1996; Zaron and Egbert, 2014; Colosi and Munk, 2006), north and northwest of Madagascar (cf. Zhang et al., 2023), the northeastern Indian Ocean (Bay of Bengal and Andaman Sea, cf. Jithin et al., 2020a; Yadidya and Rao, 2022), the Amazon Shelf (cf. Tchilibou et al., 2022) and the Gulf of Maine (cf. Schindelegger et al., 2022). The baroclinic S_2 component in Figure 5.1d has weaker variability than the M_2 counterpart. Here, the interannual variability is concentrated north of Madagascar and in the tropical western Pacific. The magnitude and the spatial extent of the signal is considerably smaller than for M_2. In general, within the interannual variability, the modulations along the propagation paths of the internal tides are visible.

The critical latitude for the semidiurnal constituents is ∼74°, while for the diurnal constituents it is ∼30°, easily detectable in Figures 5.2b and d. Beyond these latitudes, internal tides are physically unable to propagate. Hence, the interannual variability of the diurnal constituents is limited to the equatorial region bounded by ±30° in latitude. For both diurnal constituents, largest variability is apparent in the north-western Pacific; see, e.g., Wang et al. (2023) for observed internal tides in the region. The Celebes Sea again reaches maximum values above 2 mm. Additionally, the Luzon Strait is known as a hot spot of generating diurnal internal tides (e.g., Jan et al., 2007; Zhao, 2014; Zhang et al., 2021). For K_1, the Indian Ocean also contains interannual variability of ∼1 mm.

Figure 5.3 reveals the area-averaged interannual variability of the barotropic M_2 component in four selected regions. Here, the tidal estimates are not detrended. No area-average is shown for the seas around Indonesia, since the region contains several local features and large variability due to the complex geometry of the region. Therefore, general averaging of a larger area would merge localized tidal features, which is unwanted here. The highest correlation R with the globally averaged barotropic M_2 amplitude changes, shown as reference in the background of Figure 5.3, is achieved for the New Zealand time series ($R = 0.92$), closely followed by the

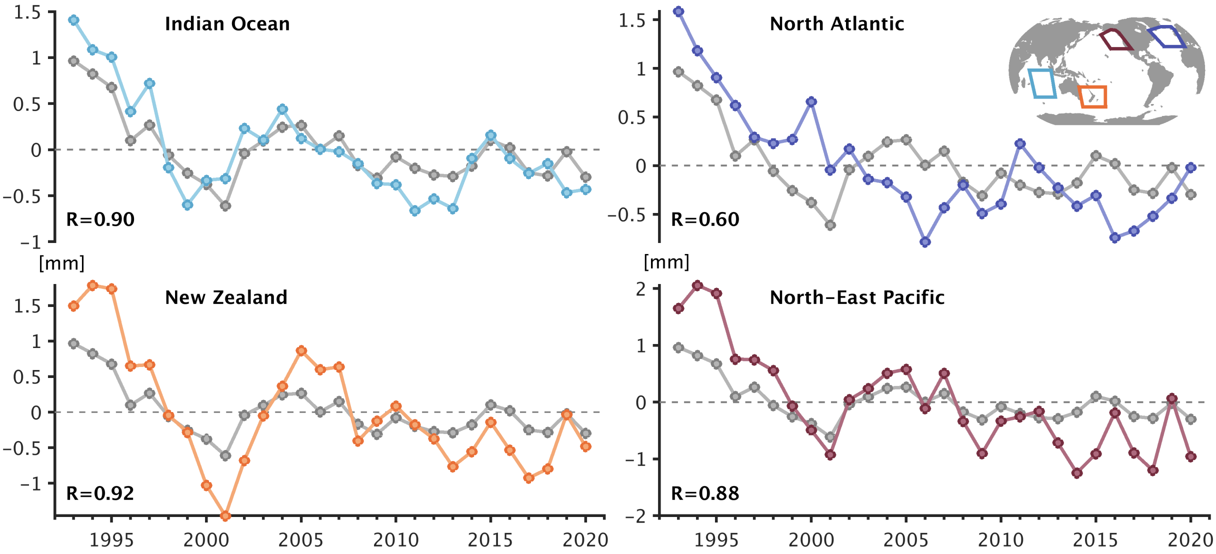

Figure 5.3: Area-averaged annual barotropic M_2 amplitude anomalies (cm) from MITgcm simulations in four regions (shown as polygons on the map, top right corner). The grey amplitude anomalies indicate the globally area-averaged barotropic M_2 tide. Corresponding trend estimates for every region are given in Table 6.1.

Indian Ocean ($R = 0.90$). Northeast Pacific and North Atlantic attain correlations of $R = 0.88$ and $R = 0.60$, respectively. All four selected regions show a decrease in M_2 amplitude, which is further discussed in Chapter 6. The correlation gives a tentative idea of how each region contributes to the globally changing barotropic M_2 amplitude in the period of 1993 to 2020. In addition, it illustrates the amount of interannual variability that is contained within the time series of individual regions in comparison to a global mean time series.

Corresponding time series for S_2, K_1, and O_1 tide are provided in Figures D.1, D.2, and D.3. The major difference to the M_2 estimates is the reduced magnitude of the interannual variations. From a few millimeters for M_2, it is in the order of 10^{-3} mm for the other three tidal constituents. The region of highest correlation varies across the three partial tides. The interannual S_2 variations are strongly correlated with the central Indian Ocean ($R = 0.85$), followed by the North Atlantic. A negative correlation is found for the Northeast Pacific. The K_1 tide shows relatively low correlation for all regions, with a maximum of $R = 0.5$ for the box around New Zealand. For O_1, the North Atlantic stands out with $R = 0.76$, followed by the Indian Ocean ($R = 0.65$). The Northeast Pacific seems to exert no control on the interannual O_1 variability, with a correlation of -0.1. Note that the four selected regions are designed to encompass important structures of M_2, and may be less suited for the analysis of other tidal constituents, in particular diurnal tides.

Figures 5.4, 5.5, and 5.6 show for three regions the correlation and PVE between the full (i.e., barotropic plus baroclinic) modeled and observed M_2 amplitude changes at tide gauges, as well as between the modeled and observed baroclinic M_2 amplitude. This analysis is of pointwise character and necessarily limited by sparse data coverage. Such pointwise approach brings difficulties for interpretations, since for each station local effects—such as changes in the environment at the tide gauge or the instrumentation itself—can be involved (Haigh et al., 2020; Ray et al., 2023). This can hamper the identification of spatially coherent signals. Local and large-scale effects may also occur at once and cause superimposed signals (Jänicke et al., 2021), which in the case of sparsely distributed observing stations can be difficult to disentangle. Therefore,

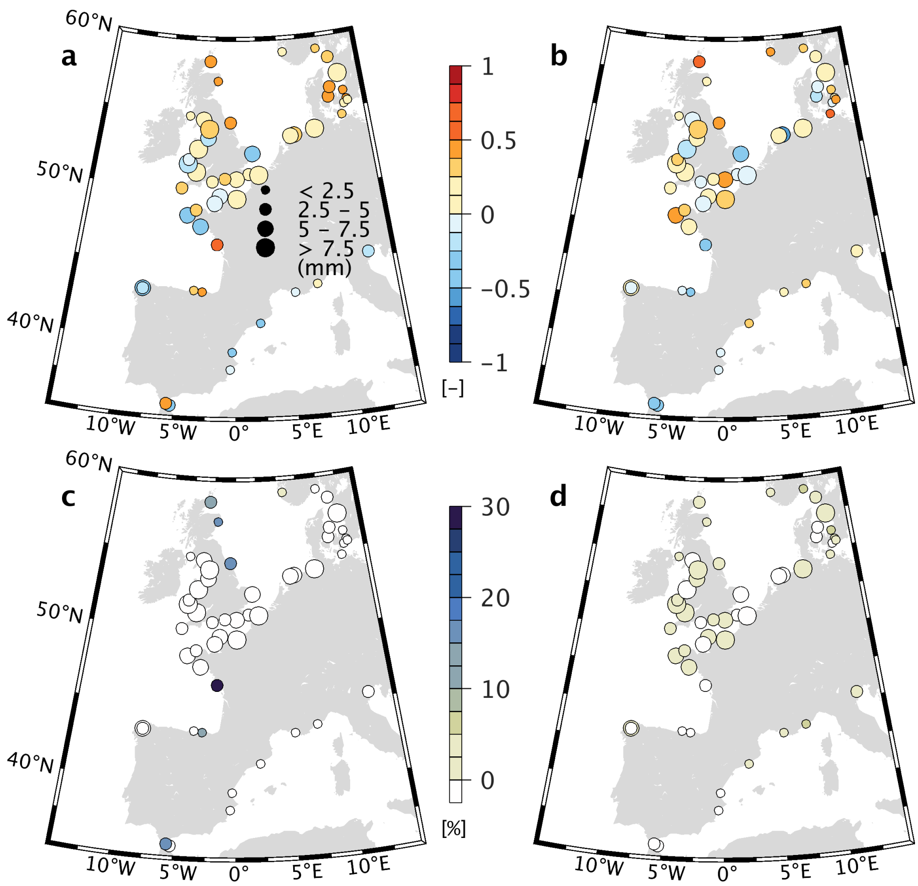

Figure 5.4: Observed and simulated M_2 amplitude changes in Europe (1993–2020, linear trend removed) compared using (**a**,**b**) correlation coefficient (dimensionless) and (**c**,**d**) PVE (%). Panels (**a**,**c**) are based on the full surface tide (sum of barotropic and baroclinic tide) and (**b**,**d**) are based on the baroclinic tide. The marker size is related to the standard deviation (mm) of tide gauge observations as explained in the legend in panel **a**.

the identification of local influence poses a challenge. By contrast, the model gives similar tidal harmonics for adjacent locations, since the model geometry is invariant. However, the model has a reduced fidelity at the coast, since the vertical discretization limits the model's ability to accurately represent all processes in shallow water (cf. Section 4.1.4). These limitations mostly result in overestimated tidal amplitudes at the coast.

Overall, the full tide has higher correlations and PVE, since the full signal is the counterpart to the observed signal at the tide gauge stations. The comparison between the observed and the modeled internal tide should enable a comparison between open ocean and the coast. This can reveal areas of influence of internal tides, as well as the fraction of the tidal signal they account for at the individual stations.

The model's shortcomings in representing shallow water processes are a possible reason for the low correlation of the M_2 tide on the European Shelf, especially in the English Channel, the North Sea, and at the Scandinavian coasts, visible in Figure 5.4 with values < 0.5. Three stations along the North-East coast of the UK show PVE values of $\sim 15\,\%$ and correlations slightly around 0.4, indicating a possible spatially coherent signal present in both the simulations and the observations. Otherwise, the correlation shows a mixed picture of positive and negative correlations. The station with the highest PVE $> 30\,\%$ and correlation on the European Shelf (lessablesdolonne_60minute-les-fra-cmems, cf. Figure D.8 for M_2) is located at the coast of France, in the Bay of Biscay. A number of stations show a negative PVE, graphically displayed in white. Accordingly, the remaining variance of the difference between the detrended observed and modeled tidal amplitude is greater than the originally detrended variance of the observations alone. This mismatch can be mostly attributed to the general overestimation of the simulated tidal amplitudes in shallow oceanic regions. To gain further insight, the modeled M_2 amplitude changes are scaled by the ratio of

$$\frac{\text{observed total } M_2 \text{ amplitude}}{\text{simulated total } M_2 \text{ amplitude}}, \tag{5.1}$$

and the PVE computation is repeated, yielding results illustrated in Figure D.4. In comparison to Figures 5.4c, 5.5c, and 5.6c, a few tide gauges indicate a higher amount of agreement to the observed time series after scaling, even stations with previously negative PVE values. As an example, the station Kapingamarangi in the western Pacific (north of Honiara, $R \sim 0.55$) is characterized by a negative PVE, changing to $\sim$17 % after scaling. Moreover, for instance, the PVE of Port Hedland improves from $\sim$7 % to $\sim$16 %. The overall picture on the European Shelf still remains difficult to interpret (Figures 5.4c and D.4b). Only the coastlines of Denmark show consistently positive PVE values after scaling.

Regarding North America (Figures 5.6c and D.4c), e.g., Cedar Key ($R \sim 0.35$) and Saint Petersburg ($R \sim 0.5$) depict PVE values of $\sim$12 % and $\sim$22 % after scaling. The amount of agreement between modeled and observed tidal changes in the Gulf of Mexico, indicates a link between the altered density stratification and tidal changes in this region.

The internal tide shows widespread low PVE on the European Shelf, indicating that the baroclinic tide here does not explain the observed tidal variations. At a few stations, the correlation is higher for the baroclinic tide than it is for the full counterpart. However, this result should not be mistaken as an indication for a dominant contribution of internal tides, given the noted problems for the simulated barotropic component, the possibility of spurious correlation between two time series and slight imperfections in separating barotropic and baroclinic tides with a spatial filter. Therefore, the two statistical measures of correlation and PVE should always be interpreted in conjunction.

The Australian coasts (Figure 5.5) reveal some spatial connectivity in the analyzed statistics. The Australian Northeast coast shows consistent negative correlation, while three stations at the Northwest coast are correlated positively with the model solution (stations: Broome, Port Hedland, Exmouth). The Southeast of Australia is also characterized by positive correlation above 0.5, except for one station with a high standard deviation over the analysis period and a slightly negative correlation. The tide gauge station in Tasmania (spring_bay-61170-aus-bom, cf. Figure D.8) shows a high correlation of $\sim R = 0.7$ and PVE > 30 %. Additional regions that exhibit positive correlations are the West coast of Malaysia and mostly the Japanese coast.

Concerning the internal tide, a few stations that are open to the ocean can be used for analysis. Since internal tides are characterized by very small scales, similarity in the statistics between neighboring sites is not expected. Nevertheless, a sequence of small positive correlations is obtained along the Northeast coast of Australia. At the coast of Japan, four neighboring stations feature positive correlations with the simulated variability of the internal tide, indicating a possible area of influence of internal tides on the surface tidal signal. At individual deep ocean stations that are located on smaller islands with no extended shelf area, the influence of internal tides would be expected. Despite negative correlations at a few open ocean stations, a high

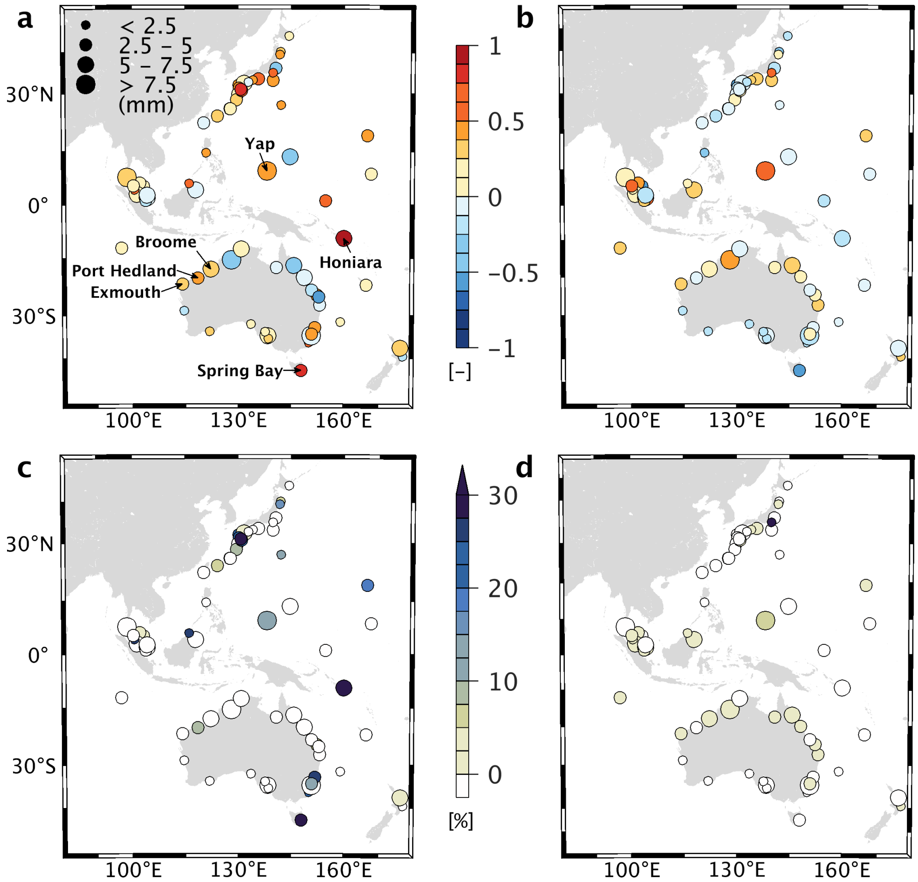

Figure 5.5: As Figure 5.4, but for the equatorial region of Australia and the Western Pacific.

correlation of $R > 0.5$ is present at the station Yap, which lies in the vicinity of tidally baroclinic active regions (cf. Figure 5.7b). The PVE for Yap is below 10 %, but still implies that the internal surface tide accounts for an appreciable fraction of the full M_2 surface tide. Moreover, a correlation with the full tide of $R > 0.5$ and PVE > 20 % is found at Brunei Darussalam, a tide gauge time series characterized by a low M_2 standard deviation. The highest correlation in Figure 5.5 is apparent at the station Honiara, located in the western equatorial Pacific, with a correlation of nearly 0.9 and a PVE of ~70 %.

Both the western and eastern coasts of North America show largely positive correlations with the full modeled tide, except for a few stations that have a slightly negative correlation. In Figure 5.6, we see some smaller regions where coherent correlations of $R \sim 0.5$ between neighboring stations exist, e.g., in the Gulf of Maine or at the western coast of Florida (eastern Gulf of Mexico). The Mid Atlantic Bight connects the two regions, but shows lower correlations. The consistent positive correlation likely reflects a connection between altered density stratification of the ocean and coastal tidal changes (here for M_2). The link between changing stratification and the changes in tidal harmonics at the Gulf of Maine have indeed been addressed in the literature (e.g., Katavouta et al., 2016; Ray and Talke, 2019; Schindelegger et al., 2022). With the scaling experiment of Equation 5.1, the previously negative PVE values of Boston and Portland, located in the Gulf of Maine, improve to ~14 % and ~12 % (Figure D.4c). Moreover, noticeable are one station in the northwestern Gulf of Mexico and two stations on the North American West coast (Los Angeles and Arena Cove) with PVE above 30 % and correlations $R > 0.5$. Winter Harbor, also on the US West coast, shows PVE slightly below 15 % and correlation of $R \sim 0.4$. Regarding the internal tide, we have a very inconsistent picture on both North American coasts

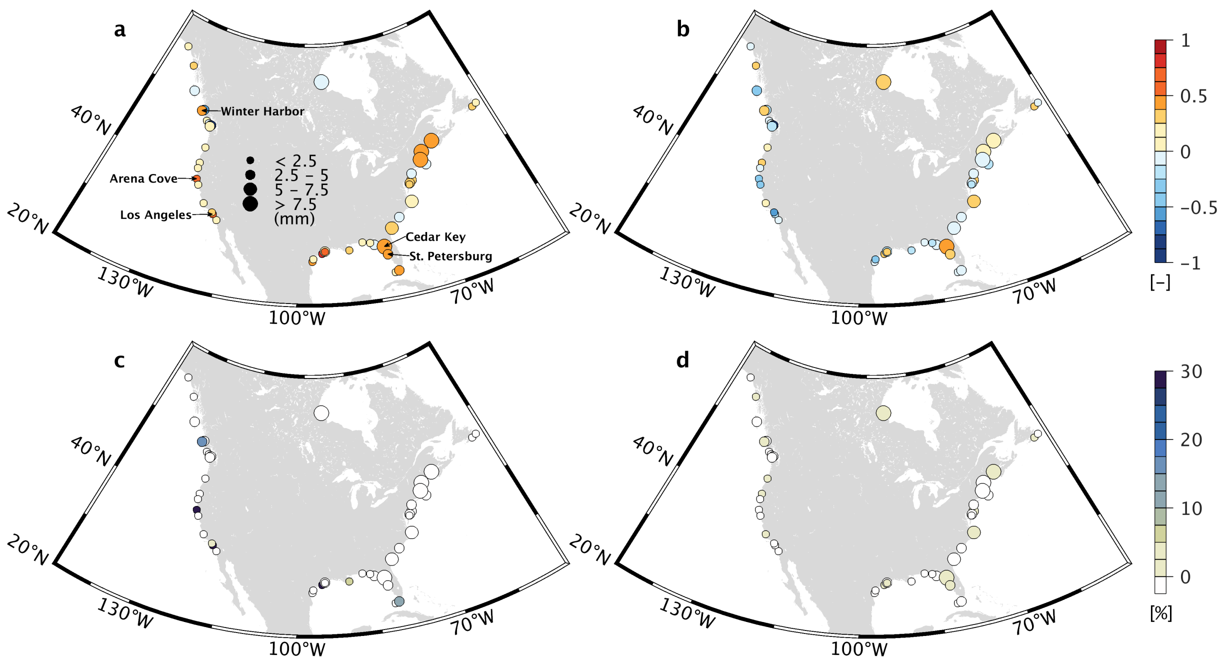

Figure 5.6: As Figure 5.4, but for both North American coasts.

(Figure 5.6b) with mostly negative correlations. The strongest correlation is observed for Cedar Key on the West Florida Shelf ($R \sim 0.4$). The PVE is below 5 % everywhere in the region.

When viewed globally, 15 % of the analyzed tide gauges exceed a positive correlation of 0.4. Despite this being a small fraction, the documented correlations and PVE values between the observed and the full modeled tidal solution indicate that the stratification is a factor to consider when exploring the causative mechanisms for the observed tidal changes. Evidently on interannual time scales, the influence of local factors on tide gauge observations complicates the direct comparison to the modeled tidal solution. This complication becomes particularly apparent when viewing statistics for neighboring stations, which often change erratically due to local and transient anomalies in the tide gauge time series.

To analyze the model-data agreement in more detail, a few stations are chosen that stand out in Figures 5.4, 5.5, and 5.6. The observed and modeled time series for M_2 between 1993 and 2020 are shown in Figures 5.7 and D.8. The Section is completed by similar analysis of the partial tides S_2 (Figure D.9), K_1 (Figure 5.8) and O_1 (Figure D.10). As mentioned above, the comparison between observed and modeled time series of annual tidal amplitudes can be clouded up by local changes at or in the vicinity of the tide gauges. In most cases, these local changes (e.g., dredging) are not known or communicated. In addition, several competing processes and non-linear effects may exist in reality (Arns et al., 2013; Challis et al., 2023), which are not or only partly represented in the model. Nevertheless, a tide gauge analysis constitutes an important validation of the model results.

Figure 5.7 involves tide gauge locations along wider stretches of coastline (c,d,f–h), as well as locations on islands that classify as pelagic tide gauges (a,b,e). The latter may feature propagating internal tides since they are located relatively open to the deep ocean. For Honolulu and Honiara (Solomon Islands), the measured and modeled time series closely resemble each other in appearance. Honiara reaches, as mentioned above, a correlation of nearly $R = 0.9$ and a PVE of $\sim$70 %. In both cases, the annually varying stratification can therefore be identified as

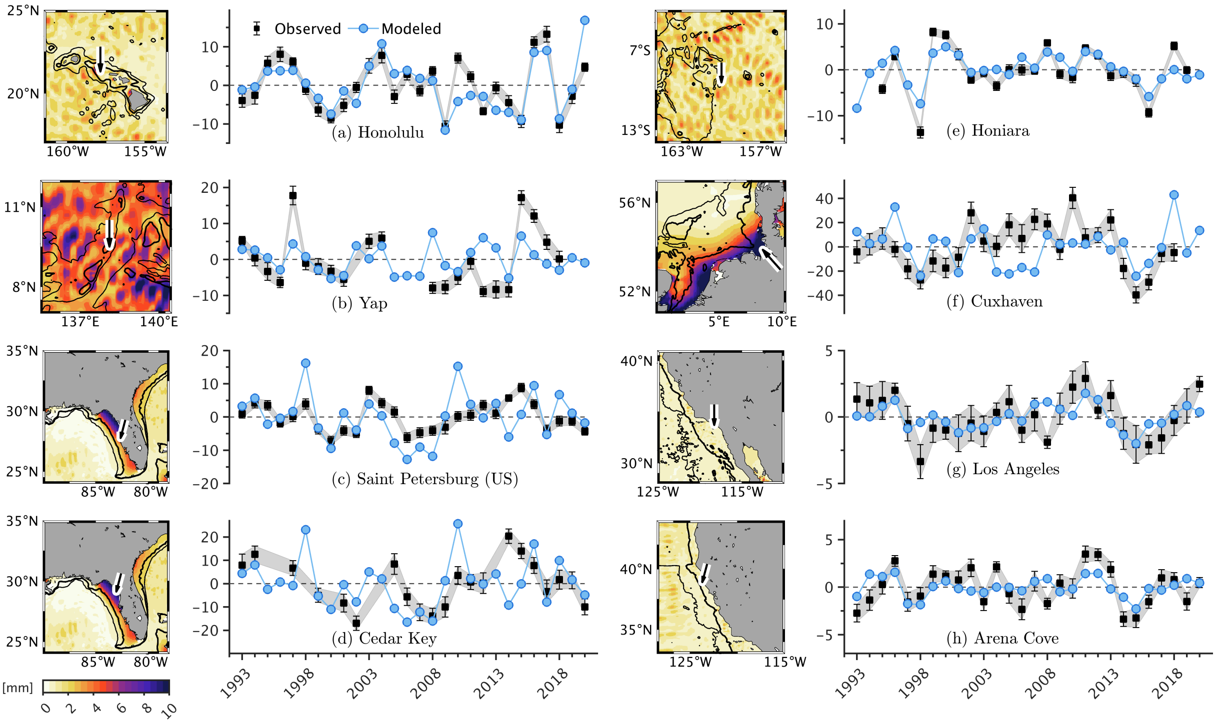

Figure 5.7: Annual M_2 amplitude changes (mm) from 1993 to 2020 at eight locations that are pinpointed with an arrow in the spatial maps on the left. Panels with time series provide a comparison of the M_2 surface tide anomalies in time (simulations results in blue, tide gauge results with standard errors in black), while boxes show close-ups of the full M_2 surface tide standard deviations. Isobaths are marked as black contours, with thicker lines for shallower water drawn at (**a**,**b**,**d**,**e**,**g**) 2000 m and (**c**,**d**,**f**) 30 m. Lines correspond to the (**a**,**b**,**d**,**e**,**g**) 4000 m and (**c**,**d**,**f**) 50 m isobaths.

a major contributor to the observed year-to-year variations in the M_2 amplitude and associated modulations of propagating internal tides.

As regards to the exact mechanisms, Devlin et al. (2014) pointed to the possibility of triad interactions at Honiara between the barotropic M_2 tide with first mode K_1 internal tides and O_1 components. For Honolulu, Colosi and Munk (2006) found that the changing density structure alters the phase speed of the internal tide, which impacts the measured surface tide at he coast. Especially the changes in sign seen for M_2 at Honolulu and Honiara are reproduced by the simulations.

Concerning S_2, the observed and modeled amplitudes are generally smaller than for M_2, as evident from Figure D.9. For Honiara, the magnitude and timing of the S_2 amplitude changes are still very much consistent between simulations and observations. For Honolulu, the picture is somewhat more involved, since the sign of the changes is mostly correctly reflected in the model, but the magnitude is underestimated. Between 2004 and 2008, the two time series differ, as the model shows almost no variability. Generally, Devlin et al. (2014) related the tidal changes of M_2 and S_2 at Honiara to variations in thermocline depth. In the case of Honiara, such variations can arise due to El Niño Southern Oscillation events (McPhaden, 2015), such as the strong El-Niños in 1997/1998 or 2015/2016, visible clearly as an amplitude minimum for both semidiurnal constituents, which is also found by Pan et al. (2025) from observations. As is clear from Figures 5.7 and D.9, the simulations with observation-constrained density fields can reproduce these minima in 1997/1998 and 2015/1016, as well as the subsequent transitioning into positive M_2 amplitude anomalies during La Niña conditions.

Another pelagic tide gauge is Yap (Figure 5.7b, Federated States of Micronesia), an island surrounded by much larger M_2 interannual variability than Honolulu and Honiara. Both the standard deviation map and the comparison with the observations make a strong case for an impact of stratification, also at this site. In detail, a decrease in the M_2 amplitude is present just at the beginning of the analysis period between 1993 and 1996. The amplitude drop is apparent in both the observed and modeled time series. Following an isolated peak in 1997, both observed and modeled time series show another consistent decline through to 2001. The tide gauge time series contains a gap between 2004 and 2008. After the gap, the observed and modeled time series match less well for reasons unknown. From the plain time series, its impossible to quantify if something changed during the observational gap, either regarding the instrumentation itself or modifications of the surrounding area. Theoretically, it is also possible that the driving mechanisms of the tidal regime changed, which is also not quantifiable with the available information. Ray et al. (2023) described that during the data gap, adjustments to the instrumentation were made in form of a sensor change, primary to discrepancies in the recorded time stamps. With their method of validation using satellite altimeter data, they find that the records at Yap are subject to an offset in comparison before and after the data gap. As they estimate the offset for Yap as only a small fraction ($< 2\,\mathrm{cm}$, Ray et al., 2023), it should not affect the results shown here much, but could slightly falsify the detrending of the time series. Nevertheless, the observed decline in the M_2 amplitude from 2015 to 2019 is also evident in the simulations, indicating that changes in the density structure still play an important role in later years. Similar inferences can be made for S_2 (Figure D.9), especially as the two maxima in 1997 and 2015 appear in the modeled tidal estimate. Both semidurnal tides at Yap appear to be affected by ENSO, here visible as amplitude maxima in 1997 and 2015.

Shifting the focus more to tide gauges along continental boundaries, the analysis and interpretation are complicated by the model's decreased accuracy, especially over shallow continental shelves (cf. Section 4.1.4). The tide gauges of Cuxhaven and Saint Petersburg (Figure 5.7f and c), as well as Cedar Key (Figure 5.7d), represent areas of high interannual variability in the M_2 surface tide, indicated by the standard deviation in the spatial maps. For Cuxhaven, in particular the two minima of M_2 amplitude around 1998 and 2015 are reproduced by the model. Note that Cuxhaven is located in the German Bight, which is part of the shallow Wadden Sea. The characteristics of this unique area regarding, e.g., water depth changes due to bed load transport, are especially challenging to model with a global setup. In addition, Cuxhaven is located in the estuary of the Elbe, which could possibly add further complications to the observation of the sea level (Pineau-Guillou et al., 2021).

At Saint Petersburg, the first half of the analysis period features good agreement between the model and observations, while the second half of the time series is characterized by overestimation of the simulated amplitude (cf. Section 4.1.4). The overestimation of tidal amplitude changes is also apparent in the time series of Cedar Key. Both Saint Petersburg and Cedar Key are located on the western coast of Florida within the Gulf of Mexico, characterized by a semidiurnal tidal regime (e.g., He and Weisberg, 2002). All four time series (modeled and observed for both locations) indicate maxima around 2003 and 2015, pointing to a possible influence of stratification changes. The modeled time series for both locations are far more consistent than their observed counterparts are amongst each other, suggesting that the latter contain a number of local signals. In any event, the sign of the interannual changes are often comparable between observations and model. Thus, stratification seems to drive part of the tidal amplitude changes even if the connection is somewhat more obscured.

Los Angeles (Figure 5.7g) represents an onshore tide gauge in a region of low interannual variability in shallow water (± 5 mm) in M_2 amplitude. The station reaches a correlation of $R \sim 0.5$ and a PVE $> 30\,\%$. Here, no overestimation of the modeled amplitude is present. The range in magnitude is reflected by the model, as well as most of the multi-year increases and decreases. Particularly, the amplitude maximum in 1996, as well as the change in sign from 2001 to 2007 and the major amplitude decrease from 2011 to 2015, are captured by the model. The decrease from 2011 to 2015 is also present in the time series of Arena Cove (Figure 5.7h), located north of San Francisco. In both cases, the minimum is followed by an increase. The agreement is a strong indicator for a regional influence of the changing density structure on the tidal harmonics.

M_2 amplitude time series at a few more interesting stations are also included. The tide gauge of Spring Bay (Figure D.8c), located in Tasmania, attains a correlation of $R \sim 0.7$ and a PVE $> 30\,\%$. The modeled and observed time series are in very close agreement until 2002, clearly highlighting the impact of the oceanic density on the tide. Results for tide gauges on the European Shelf are very mixed (cf. Figure 5.4), since the shallower water processes on the continental shelf are difficult to depict for the model. Selected examples for stations Les Sables-d'Olonne and Whitby (Figure D.8a and d) point to an underestimation, rather than an overestimation by the model. Les Sables-d'Olonne on the French coast reaches the highest correlation and PVE among the stations on the European Shelf. The second half of the analysis period mostly reflects the correct change in sign, with exceptions like the year 2016. For Whitby the model estimates follow the observations within calculated uncertainties at the beginning and end of the analysis period. Here again, stratification seems to exert some control on the tidal harmonics, but the influence is reduced by the middle part of the time series. Certainly, the large variations and gaps in the observed time series raise the question if changes to the local environment or the tide gauge itself occurred. It is hard to say if physical processes or adaptions/outages of the tide gauge are the cause here. Figure D.8b represents the tide gauge of Boston, that was already subject to analysis in, e.g., Schindelegger et al. (2022), where changes in stratification were revealed to exert major control on the observed tides. The impact of stratification is also evident in Figure D.8b, especially from 1994 to 2001 and from 2012 to 2019.

Modeled and observed K_1 amplitude changes are compared for six tide gauges in Figure 5.8. The station of Port Kembla is located on the southeastern coast of Australia and characterized by low interannual K_1 variability. The model solutions partly reflect the amplitude minimum between 1994 and 1996, as well as the amplitude increase from 1998 to 2002 and the following decrease. The second half of the analysis period shows essentially no agreement between model and observations, with the modeled interannual variability being very close to zero. The interannual variations at Port Kembla for O_1 (Figure D.10a) are similar to those of K_1, albeit with a slightly diminished magnitude. Furthermore, the agreement between observations and model is comparable, with the same tendency to underestimated variations by the model. White et al. (2014) found smallest interannual variability of the relative mean sea level in South and East Australia, compared to the North and West. They suggest a close relation to Pacific Ocean climate variability (e.g., SOI or PDO), which supports the connection to changing stratification as a major driver for tidal change, since the stratification includes such climate signatures.

Underestimation of the interannual variability by the model is also present at Kwajalein (Figure 5.8c, Marshall Islands) and Saint Petersburg (Figure 5.8f, West coast of Florida). For Kwajalein, the first half of the analysis period is more consistent, especially from 1997 to 2002. The discrepancies over other periods may inidcate that at this particular location, the ocean's

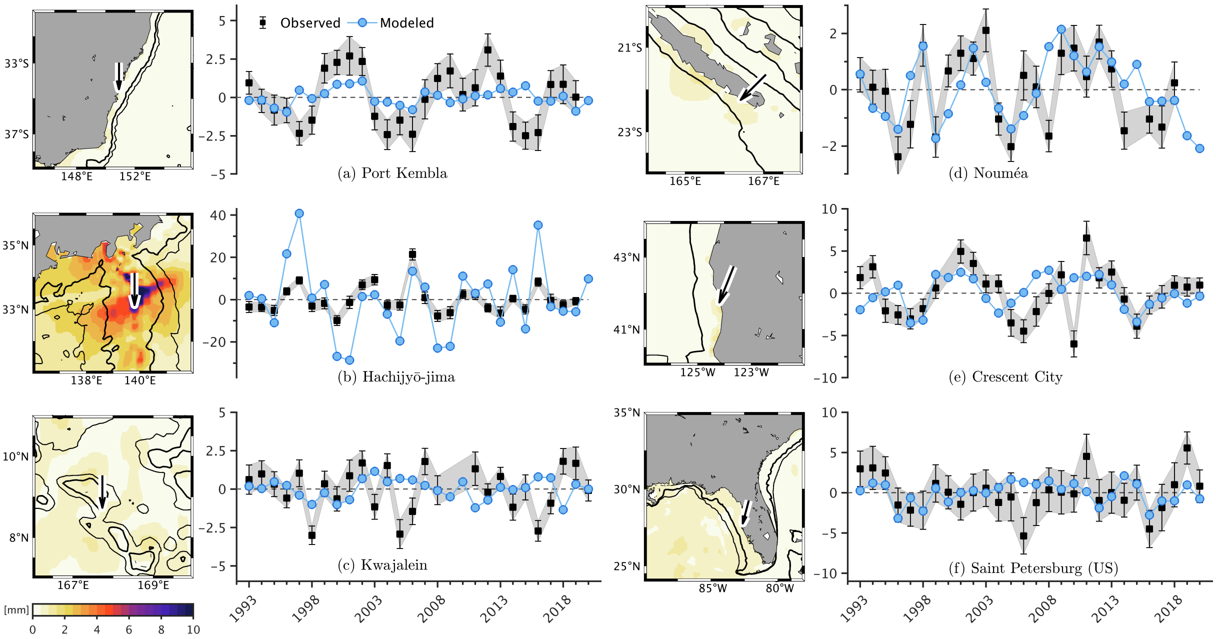

Figure 5.8: Annual K_1 amplitude changes (mm) from 1993 to 2020 at six locations that are pinpointed with an arrow in the spatial maps on the left. Panels with time series provide a comparison of the K_1 surface tide anomalies in time (simulations results in blue, tide gauge results with standard errors in black), while boxes show close-ups of the full K_1 surface tide standard deviations. Isobaths are marked as black contours, with thicker lines for shallower water drawn at (**a**–**d**) 2000 m and (**f**) 30 m. Lines correspond to the (**a**–**d**) 4000 m and (**f**) 50 m isobaths.

density exerts little control on the tide. Moreover, the tide gauge of Kwajalein is located on an atoll, specifically within the partially enclosed lagoon of the atoll (Zaron and Jay, 2014). This can lead to differences between the observed and modeled tidal signal, since small scale processes may be present within the lagoon. The tide gauge of Saint Petersburg seems to observe K_1 changes induced by the ocean's changing density structure, since the changes in sign of the tidal amplitude is mostly reflected by the model. This holds especially for the beginning and end of the analysis period, where the modeled K_1 amplitude is largely within the observation's uncertainties. Concerning O_1 (Figure D.10), the modeled interannual variability is mostly underestimated compared to the observations. For Saint Petersburg, two of three minima are not reproduced by the simulations, but apart from that, the modeled variations are within the uncertainties of the observed estimates (Figure D.10f).

In contrast to above tide gauges, Hachijyō-jima (Figure 5.8b) southeast of Japan is subject to overestimated K_1 amplitude variability, often in the order of a few centimeters. Generally, the standard deviation is high in that region for the modeled K_1 amplitude, likely pointing to a localized peculiarity in the generation and propagation of internal tides or their interaction with bottom topography or the Kuroshio current. The observed interannual variability reaches also up to 2 cm for the year 2006, which is present in both the observations and simulations. The increases and decreases are mostly reflected well, but with magnitudes often greater than twice the observed variability. Despite the model's overestimation, changing stratification seems to be an important factor for the K_1 amplitude changes at Hachijyō-jima. A similar conclusion can be drawn for O_1, disregarding the two peaks in the modeled estimate in 1996/1997 and 2016 (that are apparent in the K_1 estimate).

In the cases of Nouméa (Figure 5.8d, New Caledonia) and Crescent City (Figure 5.8e, US West coast), simulations and observations agree fairly well in terms of the timing and magnitude of the K_1 amplitude anomalies. Nouméa is located in the world's largest lagoon surrounding New Caledonia and is characterized by K_1 amplitude variability ± 2 mm, but with erratic amplitude changes from year to year. Most of these changes are also apparent in the modeled tide (e.g., until 2013 except for 2007–2009). In contrast, the model-data agreement is low at Nouméa in the case of O_1. This is also partly true for Crescent City, where the O_1 amplitude seems to be underestimated by the model. Nevertheless, the changing sign is generally correctly reflected, e.g., for the amplitude maximum during 1999–2001 and the minimum during 2014–2016. Observed and modeled interannual K_1 variations at Crescent City are in large parts very consistent. Amongst the discrepancies, an observed minimum is evident in 2006 that is two years earlier in the modeled time series. In 2006, a tsunami caused by an earthquake at the Kuril Islands damaged the harbor structures of Crescent City (e.g., Dengler and Uslu, 2011), which could have temporarily affected the tide gauge instrumentation. The observed minimum in 2010 and maximum in 2011 are not present in the model, raising the question if the causes are real physical signals of the ocean's surface. Apart from the named differences, the stratification seems to cause tidal changes here as well.

Altogether, the above comparisons of annual observed and modeled amplitude changes reveals that changing stratification conditions affect the tidal harmonics. The changing barotropic tide has a larger and more widespread influence on the analyzed tide gauges than the baroclinic tide. This is in part due to and also biased by the coastal locations of the tide gauges. It is important to bear in mind that each individual tide gauge time series is possibly affected by rather local factors such as dredging or harbor modifications. Therefore, it is important to base conclusions on the agreement of neighboring tide gauges, rather than on one single tide gauge (White et al., 2014). Some examples of fairly consistent time series at tide gauges in vicinity to each other were given, e.g., in the western Pacific, at the coasts of Northwest Australia, or in the Gulf of Mexico (e.g., Cedar Key and Saint Petersburg). In general, the ocean's changing density structure seems well capable of modulating tides. The connection is evident for all four partial tides considered, although the exact variability differs from location to location. The findings are especially important in the context of analyzing satellite observations, e.g., in the de-aliasing of satellite gravimetry observations (Flechtner et al., 2016). In addition to gravimetry, ocean tides are crucial in the analysis of satellite altimetry observations, particularly for recent missions like SWOT, which observes the Earth with an unprecedented horizontal resolution. Tides, especially the baroclinic component, are a subject of analysis in some studies (Tchilibou et al., 2024; Zhao, 2024), but otherwise need to be accurately removed in order to assess non-tidal signals of smaller scales (Arbic et al., 2015; Zaron, 2017). In such applications, ocean tides are often removed through given amplitude and phase maps of tidal surface expressions, that are assumed to be constant over time. The findings of this thesis clearly indicate that such an approach can afflict small errors, given that both the barotropic and baroclinic tides are changing with time.

5.2 A Tidal Connection to Climate Modes?

As noted above, some tide gauges observations contain signals induced by climate phenomena like *El Niño Southern Oscillation (ENSO)*, the largest natural oscillation of the climate system on interannual time scales (McPhaden, 2015). Climate modes have characteristic, time-evolving spatial patterns that have been identified in observations of the atmosphere, oceans, terrestrial

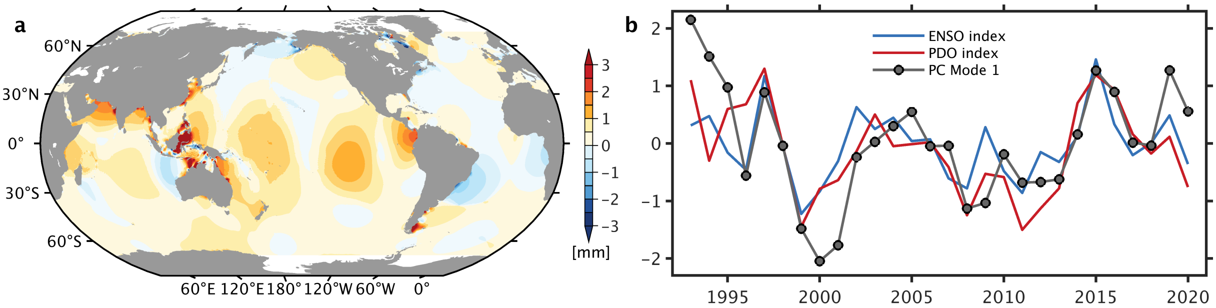

Figure 5.9: EOF of mode 1 **a** computed from the barotropic M_2 amplitude anomalies over 1993–2020 (mm) that capture ∼45 % of the total variance on interannual time scales. Additionally, the corresponding PC time series of mode 1 **b** is shown. Pattern **b** also contains the PDO and ENSO index.

hydrology, and even cryosphere on different spatial and temporal scales. Besides their highly non-uniform appearance, they also interact amongst each other, often impeding their individual observation (Wang and Schimel, 2003). In addition, they can affect the climate system globally, despite of their regionally limited appearance in the first place. Important climate modes are, amongst others, the ENSO, the *Pacific Decadal Oscillation (PDO)*, the *North Atlantic Oscillation (NAO)*, the *Atlantic Multidecadal Oscillation (AMO)* and the *Arctic/Antarctic Oscillation (annular modes)*. Fingerprints of climate modes in water height records and ocean tides have been a recent subject of analysis, e.g., in White et al. (2014); Deepa and Gnanaseelan (2021); Viola et al. (2024); Pan et al. (2025); Devlin et al. (2025).

Here, the interannual variability of the barotropic M_2 component is further analyzed by a principal component (PC) analysis of the tidal residuals to provide indications for possible connections to climate modes. The spatial pattern (i.e., the empirical orthogonal function, EOF) associated with mode 1 is shown in Figure 5.9a and closely resembles in structure the previously mapped M_2 standard deviations (Figure 5.1). This mode explains approximately 46 % variability of the barotropic M_2 anomalies, raising the question as to the physical causes behind the mode. To tackle this question, the corresponding time series of mode 1 (i.e., PC1) is presented in Figure 5.9b, along with the PDO and ENSO indices over the period 1993–2020. The annual PDO index data is computed by Japan Meteorological Agency (2024) and the ENSO index is provided by NOAA (2024a). In general, both ENSO and the PDO indices are determined from Sea Surface Temperature (SST) anomalies of the Pacific Ocean. For ENSO, the tropical Pacific is considered, with values published as three-month rolling means. For the comparison here, annual averages are computed. As the term ‘decadal’ in PDO indicates, it seesaws between decades. The climate mode resembles ENSO, but differs by its longer timescales (Mantua et al., 1997). The PDO index shown in Figure 5.9b is estimated by a projection of pre-processed mean SST anomalies onto the corresponding EOF. Pre-processing includes, e.g., removal of global warming signatures. The region is defined as the North Pacific north of 20°N.

A recent study by Devlin et al. (2025) highlighted a significant impact of climate modes, especially the PDO, on the M_2 tide at Honolulu. In this work, the two time series of PC1 and PDO in Figure 5.9b reach a correlation of $R = 0.69$, also pointing to a possibly tight physical connection. The signature of the climate mode is contained within the changing oceanic density structure, since the modeled interannual tidal variability originate solely from the annually changing stratification within the global oceans. The corresponding correlation coefficient of the ENSO index with PC1 is slightly lower ($R = 0.67$). The high correlation in both cases strongly suggests that Pacific climate modes play an important role within the global interannual tidal variability of the barotropic M_2 tide. Subsequent modes from the EOF analysis explain ∼11 %, and ∼8 %, respectively. Both are not further examined here, since the amount of variance captured is low.

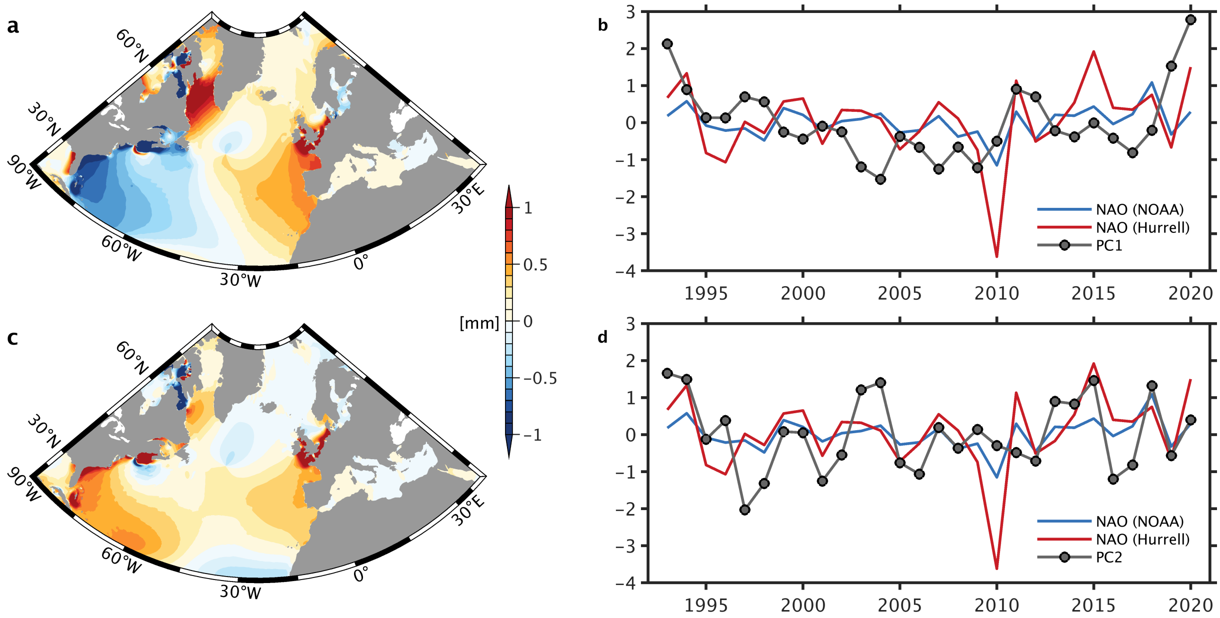

Figure 5.10: EOF of mode 1 **a** and mode 2 **c** computed from the barotropic M_2 amplitude anomalies from 1993–2020 (mm) that capture ∼51 % (mode 1, **a**) and ∼21 % (mode 2, **c**) of the total variance on interannual scales. Additionally, the corresponding PC time series of mode 1 **b** and mode 2 **d** are shown. The time series also contain the NAO index from two different sources, described in the text.

The North Atlantic is also an interesting region for analysis of potential climate impacts on tidal harmonics. In this region, Müller (2011) found spatially coherent tidal amplitude variations for M_2 and S_2. In detail, they report a significant change (essentially an amplitude decline) of the tides since the early 1980's. They attribute the changes to global warming, which can entail different physical processes in the ocean and atmosphere. Since the analysis period of this thesis starts in 1993, the 1980's amplitude evolution cannot be explored here. Nevertheless, Figure 5.3 shows clearly a decrease in M_2 amplitude form 1993 to approximately 2006 for the averaged area of the North Atlantic, in keeping with the findings of Müller (2011) and also Pineau-Guillou et al. (2021), who analyzed M_2 variations in the North-East Atlantic. Both studies, especially Pineau-Guillou et al. (2021), suggested a connection to the NAO. The climate mode NAO is defined as a large-scale atmospheric circulation pattern with the related NAO index derived as the principal component time series from an EOF of the sea level pressure anomalies in the North Atlantic (Hurrell et al., 2003). It shifts with displacements of the Icelandic low and the Azores high. Hurrell et al. (2003) mention large-amplitude anomalies in the NAO index since the early 1980's, which agrees in terms of timing with the changing tidal signal found by Müller (2011).

Building on this tentative evidence, Figure 5.10 shows the results from an EOF analysis of the M_2 barotropic amplitude residuals in the North Atlantic. For better comparison, the barotropic M_2 anomalies are cut to the region which underlies the NAO index computation (20°–80°N, 90°W–40°E) prior the the EOF analysis. The time series of the PCs of Mode 1 and 2 are compared to the annual estimates of the North Atlantic Oscillation index. Since climate mode indices cannot be defined exactly, two possible NAO index realizations are depicted. The first is from Hurrell et al. (2018), while the second time series is provided by NOAA (2024b) as monthly estimates, which are annually averaged for comparison here. The difference between the two

NAO index time series is clearly evident in Figures 5.10b and d. The EOF mode 1, estimated from the simulations, explains ~51 % of variance, while the second mode captures ~21 % of variance. Both modes differ particularly regarding the signal structure along the US East coast. The time series of PC1 is quite different from both NAO indices, reaching only a correlation coefficient of $R = 0.06$ (NOAA) and $R = 0.24$ (Hurrell). In comparison, PC2 exhibits higher correlation with the NAO index time series, with $R = 0.57$ (NOAA) and $R = 0.37$ (Hurrell). The analysis results prohibit a definite conclusion on the connection between the simulated tidal changes and the NAO, but the correlation of PC2 and the NAO index could be seen as a hint for such a connection. In addition, it is possible that some of the mode's imprint on M_2 is absorbed by the linear trend over 1993–2020 (Figure 5.3), which has been removed from tidal amplitude changes in the EOF analysis.

The above described findings indicate a close link between the modeled tidal harmonic variability, that is solely driven by variations in ocean stratification, and different climate modes. The PDO in particular seems to dictate large parts of the year-to-year variability of the global barotropic M_2 tide. Since climate modes are reflected in the ocean's stratification through modified temperature and salinity conditions, they are also able to drive tidal changes through processes that will be discussed in more detail in the context of trend-like changes in the next chapter. These changes are not only present in the modeled tidal harmonics, but are also reported in a few recent studies in literature (see above). In particular, detection of the modeled spatial patterns with tide gauges could strengthen the analysis. However, identification of common, spatially coherent modes of interannual variability is difficult with the available tide gauge network, due to sparsity, data gaps, or local effects. In any event, ocean stratification appears to be capable capable of changing tidal harmonics, both on global and regional scales, and in the open ocean as well as at the coast.

6 Present-Day Trends

In this chapter, I estimate the impact of long-term changes in ocean stratification (cf. Section 2.1.3) on the global tides from 1993 to 2020. To that end, linear tidal trends are computed from the annually modeled tidal harmonics. The trend estimates are corrected for steric effects, see Section 4.3.2. Formal uncertainties are derived as described in Section 4.3.1. Validation is conducted with tidal trends computed from satellite altimetry (cf. Section 4.2.2) and from tide gauge time series (cf. Section 4.2.1). The discussion is complemented by a comparison to the effects of water depth changes induced by relative sea level rise and glacial isostatic adjustment. Throughout this chapter, findings, and figures, build upon the work published in Opel et al. (2024).

6.1 Barotropic Tide

6.1.1 Global Synthesis

The annually modeled barotropic tidal estimates are used to compute linear tidal trends for the individual tidal constituents M_2, S_2, K_1, and O_1 in the period from 1993 to 2020 (cf. Section 4.3.1). The analysis of the barotropic trend estimates reveals present-day large scale trends in the major ocean basins, presented in Figures 6.3 and 6.1. Particularly for the M_2 amplitude trend in Figure 6.1a, the spatial patterns with larger signals are statistically significant at the 95 % confidence level, for example in the tropical Indian Ocean ($\sim -0.06\,\mathrm{mm\,year^{-1}}$) or in the region off the western coast of South America ($\sim 0.1\,\mathrm{mm\,year^{-1}}$). The strongest statistically significant decreasing M_2 amplitudes are seen in the Indonesian Seas with local rates up to $-1\,\mathrm{mm\,year^{-1}}$, around New Zealand ($\sim -0.1\,\mathrm{mm\,year^{-1}}$), at the US West coast ($\sim -0.14\,\mathrm{mm\,year^{-1}}$) and in the Labrador Sea ($\sim -0.18\,\mathrm{mm\,year^{-1}}$). Although most regions show decreases, evidence exists also for strengthening M_2 amplitudes in a few regions. Such increases are revealed at the western coast off South America and in the Gulf of Maine. Within the Gulf of Maine, the M_2 amplitude seems to strengthen by $\sim 0.2\,\mathrm{mm\,year^{-1}}$, attributable to a weaker stratification over the close-by continental shelf (Schindelegger et al., 2022).

Generally, the amplitude trends of S_2 (Figure 6.1b), K_1 (Figure 6.1c) and O_1 (Figure 6.1d) reveal smaller magnitudes than M_2. The S_2 tide is characterized by amplitude trends significantly negative north of Australia up to $-0.3\,\mathrm{mm\,year^{-1}}$ and in the Indonesian Seas locally up to $-0.6\,\mathrm{mm\,year^{-1}}$, adding to the negative M_2 trends in this location. However, a slight increase ($< 0.1\,\mathrm{mm\,year^{-1}}$) is evident in the Yellow and East China Seas. Additionally, as for the M_2 amplitude, the S_2 amplitude trend is also negative in the Indian Ocean and west of Madagascar. At the US West coast, S_2 has a slightly positive amplitude trend, contrary to M_2. Tidal trends of the diurnal constituents K_1 and O_1 also show mostly decreases of the amplitude, but restricted to a few regions. For O_1, the decrease is highest in the South China Sea ($\sim -0.1\,\mathrm{mm\,year^{-1}}$), with local rates up to $-0.4\,\mathrm{mm\,year^{-1}}$ in the Gulf of Tonkin and up to $-0.2\,\mathrm{mm\,year^{-1}}$ in the Gulf of Thailand. The K_1 amplitude trend only shows very localized signals in the regions around Indonesia, albeit statistically insignificant in most cases. The very shallow Sea of Okhotsk reveals significant K_1 decrease, but should be treated with caution, since the region involves pronounced non-linear effects and is thus challenging to model.

The simulated M_2 amplitude trends are partially consistent with the point-wise satellite-based tidal trend estimates of Bij de Vaate et al. (2022). Figure 6.2 depicts a comparison of the modeled M_2 amplitude trend to the altimetry-based trend estimate from Bij de Vaate et al. (2022) and trend estimates by Schindelegger et al. (2018) based on relative sea level rise. A general consistency in magnitude, and partly in the spatial pattern, is evident. The magnitude of the tidal trend from this work is more comparable to the observed trends than the trends caused by relative sea level rise. Despite the European Shelf being a challenge for tide modeling, agreement between Figures 6.2a and b persists, e.g., around Southwest England. Across the North Sea, the model suggests only a very small trend, which can be attributed to real-world processes being absent in the model (e.g., coastline development or bedload transport), or to limitations of the model's vertical discretization in very shallow water. Literature does indeed suggest a relatively strong sensitivity of tides to stratification changes in the North Sea (Müller et al., 2014; Jänicke et al., 2021).

More spatially coherent observed and modeled signals are illustrated in Figures 6.2d and e, especially toward the open ocean, visible in the western Pacific. In terms of structure, the observed and modeled patterns also agree around the coastlines of Australia and New Zealand, both showing decreasing M_2 amplitudes. The latter two regions highlight the predominant impact of stratification on the tides, compared to the impact of relative sea level rise. Elsewhere, in the Yellow and East China seas, the observed strong trends are not present in the simulations, implying a different underlying cause. Indeed, the studies of Su et al. (2015) and Jiang et al. (2022) suggested large-scale tidal flat reclamation (at the Jiangsu coast, north of Shanghai) as a major mechanism for changes in wave propagation characteristics, resulting in an increased M_2 amplitude in the Yellow Sea, and a decreased M_2 amplitude in the East China Sea.

Figure 6.3 depicts a global validation of the modeled in-phase and quadrature trends of the barotropic M_2 tide against an independent, gridded estimate from satellite altimetry (cf. Section 4.2.2 this work and Opel et al., 2024). Generally, Figures 6.3a–b and 6.3d–e reveal that the modeled present-day M_2 trends reproduce many of the satellite-based M_2 changes in terms of structure and sign. Despite the agreement of the independent estimates, the magnitude of the modeled estimates is smaller than the satellite-based trends by a factor of approximately 1.5 to 1.75. The discrepancy may be attributed to limitations of the model setup or subtle errors in the altimetry analysis, but most likely it reflects imperfections in the adopted 3D density distribution, especially at depths critical for the energetics of M_2 (e.g., the continental slope and mid-ocean ridges). Despite this issue, the broad consistency of spatial structure and sign indicates that the large-scale M_2 trends are in large parts caused by changes in the ocean's density structure. Good agreement for both in-phase and quadrature trends between modeled and observed M_2 trends is seen for example in the tropical Indian Ocean, at the US West coast, at the western coast of South America, in the region around New Zealand, and more generally in the equatorial Pacific. A region that reveals discrepancies is the North Atlantic including the European Shelf (cf. also Figure 6.2a). The large continental shelf of Europe challenges global 3D models to correctly depict the physical processes that are acting and also interacting (e.g., Jeon et al., 2019).

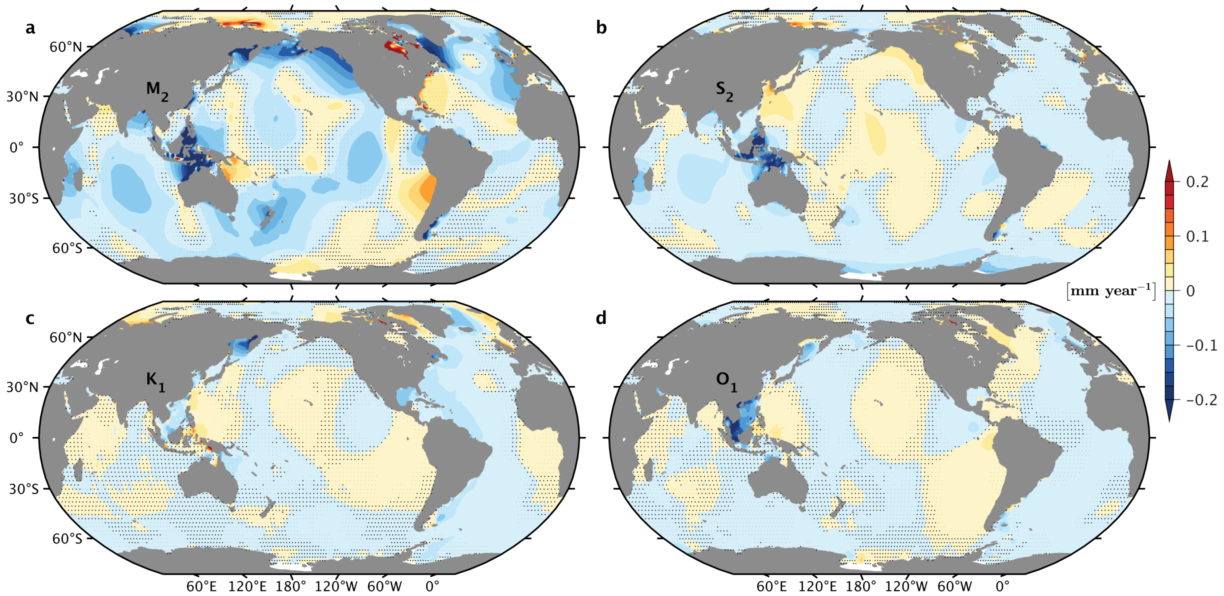

Figure 6.1: Modeled barotropic tidal amplitude trends (in mm year^{-1}) of **a** M_2, **b** S_2, **c** K_1 and **d** O_1 (1993–2020). Heavy (or light) black dots identify regions where values do not pass the 68 % (or 95 %) threshold for statistical significance. All trends are based on estimates of Opel et al. (2024).

Additionally, the altimetric and stratification-induced M_2 trends are compared to similarly computed trends from time slice simulations with a 2D shallow water model, representing the effects of sea level rise (Schindelegger et al., 2018; Opel et al., 2024). Sea level rise, or more generic, water depth changes, are a frequently discussed driver in the context of changing tidal harmonics (e.g., Müller et al., 2011; Pelling et al., 2013; Pickering et al., 2017; Ross et al., 2017; Schindelegger et al., 2018; Rose et al., 2022). The tidal trends, shown in Figure 6.3c and f, are adapted for the same time span (1993–2020) and illustrate the response of the M_2 tide to present-day sea level rise in a long-term sense. As is clear from visual interpretation, the tidal sensitivity to sea level rise is mostly confined to shallow water. Water depth is an essential variable for the propagation of tides in shallow or resonant areas, for example in the Indonesian Seas, or in the Gulf of Maine. In contrast, Figure 6.3c and f reveal only minor trend signals in the deep ocean. The spatial patterns in the open ocean neither match the observed spatial structure, nor the observed sign. These results clearly highlight the major impact of changing stratification on the tides, especially in the open ocean.

A quantification in terms of area-averaged M_2 amplitude trends in the same regions as in Figure 5.3 is presented in Table 6.1. Modeled trends associated with stratification are shown along with trends from satellite altimetry and the 2D tide model representing the effect of sea level rise over 1993–2020. The M_2 amplitudes from altimetry decrease at rates between −0.06 and −0.14 mm year^{-1} in the selected regions. As discussed above, the 3D model produces trends that are smaller in magnitude, but agree in sign with their observed counterparts. One region where the modeled trend is considerably lower than the observed one is around the Tasman Sea. The strong negative trend indicated by satellite altimetry would be desirable to validate with independent observation, but unfortunately the network of tide gauges is sparse in that region. The time series corresponding to the analyzed regions (Figure 5.3) all show a trough around 1997 and 2004. This common feature could indicate a connection to a climate mode, which is reflected in all regions (cf. Section 5.2). However, this link is difficult to verify and remains speculative. The comparison to the regional averaged trends from the 2D simulations

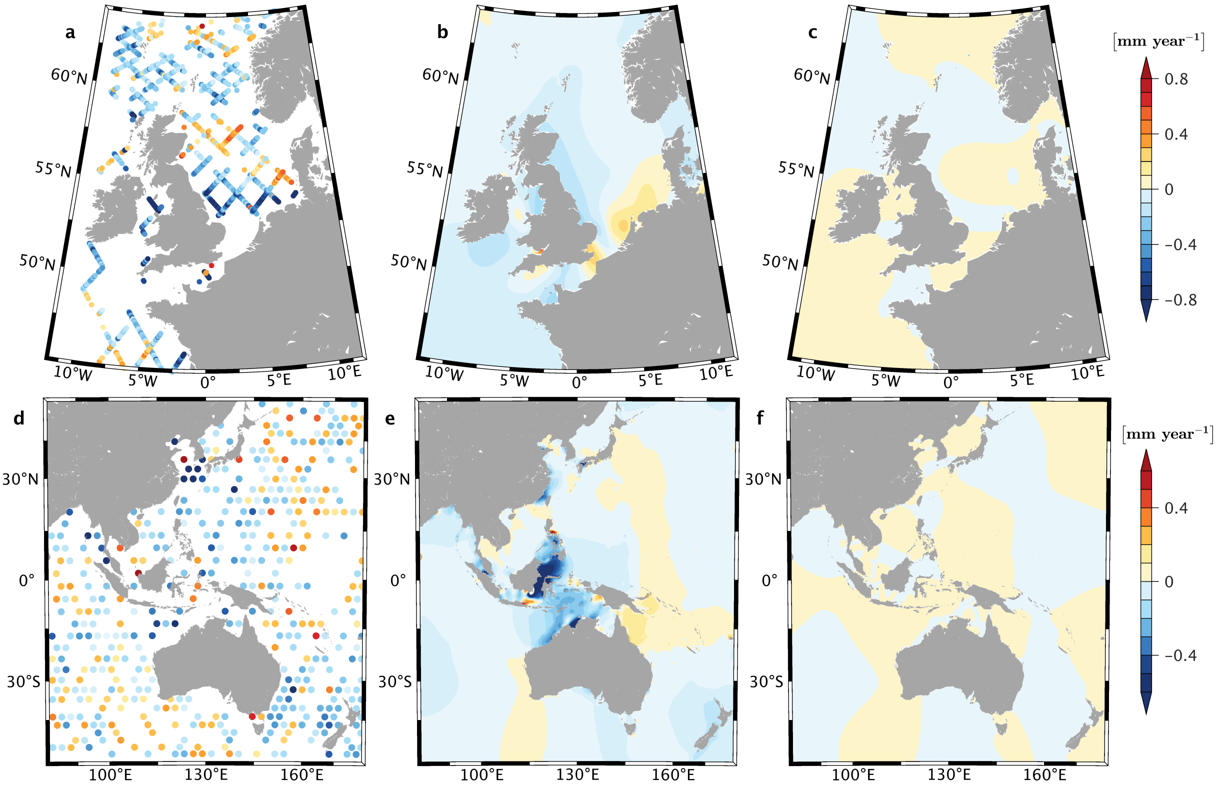

Figure 6.2: M_2 amplitude trend (in mm year^{-1}, 1993–2020) deduced from **a, d** TOPEX-Jason along track altimetry observations at crossover locations from Bij de Vaate et al. (2022), **b, e** from the 3D model of this work considering the effect of ocean stratification changes (Opel et al., 2024), and **c, f** from barotropic tide modeling considering the effect of relative sea level rise from Schindelegger et al. (2018).

in Table 6.1 again stresses the minute impact of sea level rise at large scales in the open ocean.

The above described findings show the effect of changing ocean stratification from 1993 to 2020 onto the main tidal constituents M_2, S_2, K_1, and O_1. The increased ocean stratification, attributed in part to present-day climate change and subsequent upper ocean warming, evokes mainly a decrease in the barotropic surface amplitudes, that is in agreement with the increasing ocean stratification over the same time span (cf. Figure 2.5). The two processes (i.e., stratification and tidal dynamics) are connected in the way that sharper vertical density gradients naturally enhance the generation of internal tides, and thus also enhance the energy transfer from the barotropic to the baroclinic tide. This results in a decrease of the barotropic surface amplitude, since less energy is left for the barotropic tide to propagate. This phenomenon can be local to regional in character, but yet reveals large scale tidal trends in the major ocean basins, particularly for M_2.

6.1.2 Regional Foci

As implied by Figure 6.3, changes of the individual tidal constituents are often regional or local in character. To further investigate the changes of M_2, emphasize is placed on a few coastal regions that contain a tide gauge network which is dense enough to allow for a validation of the modeled trend estimates. In contrast to the open ocean, where satellite altimetry provides

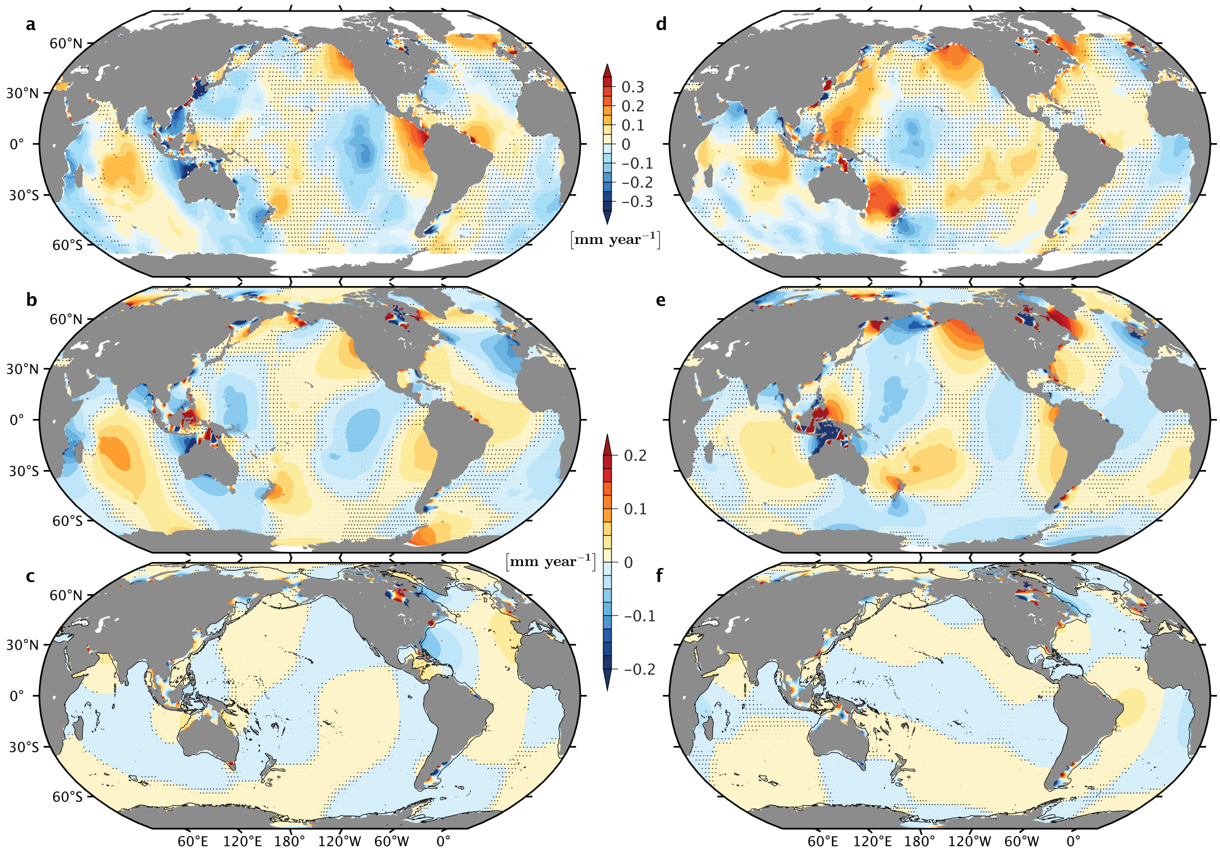

Figure 6.3: Observed and modeled barotropic M_2 trends (1993–2020) in-phase (**a**–**c**) and quadrature (**d**–**f**) component from satellite altimetry and numerical ocean models. Shown are smoothed trends from satellite altimetry (**a**, **d**), along with simulated M_2 trends due to stratification changes (**b**, **e**) and relative sea level rise (**c**, **f**). Note that the color axis in **a** and **d** extends to $\pm 0.35\,\mathrm{mm\,year^{-1}}$, a factor of 1.75 higher than in **b**, **c**, **e**, **f**. Heavy (or light) black dots identify regions where values do not pass the 68 % (or 95 %) threshold for statistical significance. All trends are based on estimates of Opel et al. (2024).

a solid point of comparison, altimetry-derived tidal trends in shallow and coastal regions have larger uncertainties (cf. Figure 4.7) and low spatial resolution. Hence, tide gauge observations are the preferred means of validation as one approaches the coast.

The regional trend maps of Figures 6.4, 6.5 and 6.6 emphasize the coastal aspects of the tidal changes. Since at the coast the tides respond appreciably to changes in water depth, the modeled trend estimates now contain the sum of the modeled responses to stratification and sea level rise to better compare to observations. Since the barotropic tide is the center of focus here, tide gauge locations where surface signatures of internal tides likely alter the observed tidal signal are discarded in the analysis. This is necessary at, e.g., stations on small islands in the western Pacific or around the Ryukyu Arc between Japan and Taiwan.

In general, tidal trends from tide gauges are difficult to compare across the literature (e.g., Jay, 2009; Woodworth, 2010; Müller et al., 2011; Zaron and Jay, 2014; Schindelegger et al., 2018; Bij de Vaate et al., 2022), since the trends themselves are quite sensitive to the analysis window, which tends to vary from study to study. In the extreme cases, different time spans can lead to changes in the sign of the trend for the same station. Additionally, neighboring tide gauges are sometimes inconsistent with respect to the observed changes, pointing to the presence of

Table 6.1: Area-averaged M_2 amplitude trends ($\mathrm{mm\,year^{-1}}$) between 1993 and 2020 in four selected regions from Opel et al. (2024).

	Altimetry	3D model (STR)	2D model (SLR)
Tropical Indian Ocean	-0.06 ± 0.00	-0.04 ± 0.01	0.00 ± 0.00
Tasman Sea/New Zealand waters	-0.14 ± 0.00	-0.05 ± 0.01	0.00 ± 0.00
Northeast Pacific	-0.13 ± 0.01	-0.08 ± 0.01	0.01 ± 0.00
Northeast Atlantic	-0.08 ± 0.01	-0.05 ± 0.01	0.01 ± 0.00

Barotropic M_2 amplitude trends, averaged within regions in Figure 5.3, from satellite altimetry and model simulations with time-varying stratification. 68 % confidence intervals are provided. All estimates are statistically significant at the 99 % level. STR = stratification, SLR = sea level rise

localized factors. Therefore, a dense network is necessary to reveal spatially more extended changes in tidal constituents. Inconsistencies of neighboring stations are, for instance, present at the Japanese coast, visible in Figure 6.4. In this special case, the modeled estimate is also insignificant at 68 % confidence and is therefore not amenable to interpretation.

The coasts of Australia (Figure 6.4a) feature an adequate network of tide gauges. In general, the models and observations agree well in terms of the sign of M_2 amplitude trends. For the northwest coast of Australia, also the magnitude of the negative trend is consistent. The time series of the tide gauge station Broome in northwest Australia (Figure 6.7) illustrates the consistency between the modeled and observed M_2 amplitude trend in the time span of 1993 to 2020. Additionally, the averaged M_2 amplitude trend of the four tide gauges in the region is consistent between observations ($-0.86 \pm 0.18\,\mathrm{mm\,year^{-1}}$) and model ($-0.53 \pm 0.19\,\mathrm{mm\,year^{-1}}$), as shown in Figure 6.6. For Northwest Australia, modeled trends are almost solely driven by stratification changes, cf. pie chart in Figure 6.6. In contrast to the negative trend in Northwest Australia, the northeast coast shows an overall positive M_2 amplitude trend. The observations suggest much more pronounced changes than the sum of the two model trends, with the disparity in magnitude being about 5:1 (Figure 6.6). The region's complex geometry and seabed topography (e.g., around the Great Barrier Reef) may limit the model's realism in this tidally active region.

In the seas surrounding Indonesia and at the coastline of China and Vietnam however, the tide gauge network is very sparse. In comparison to earlier studies that analyze water level series pre-dating the era, some correspondence can be established for example in the Yellow and Bohai Sea. Feng et al. (2015) found significant increases particularly in M_2, while a large fraction of the Yellow Sea shows an insignificant M_2 amplitude trend, in the simulations the Bohai Sea contains a robust increase in the M_2 amplitude, similar to the trend of Feng et al. (2015) at the tide gauge of Dalian. However, the observed trend from Feng et al. (2015) for Dalian ($3.6 \pm 0.8\,\mathrm{mm\,year^{-1}}$) is given for the period of 1980 to before 2000. Therefore, a direct comparison to the modeled estimate of $\sim 0.2\,\mathrm{mm\,year^{-1}}$ is formally incorrect. Nevertheless, greater observed trends are also present in the global amplitude trends of M_2 for the trend from satellite altimetry (cf. Figure 4.7a). In comparison, the modeled trend is much smaller. This indicates that other driving mechanisms for tidal changes are at work and that stratification is of secondary importance.

Elsewhere in Figure 6.4, the East and the West coast of Malaysia reveal an interesting trend pattern. The East coast is characterized by positive M_2 trends, while the West coast is consistently negative. This asymmetry is found both in the observed and modeled trend estimates. The tight agreement (within formal errors) between the observed ($\sim -0.39 \pm 0.13\,\mathrm{mm\,year^{-1}}$) and

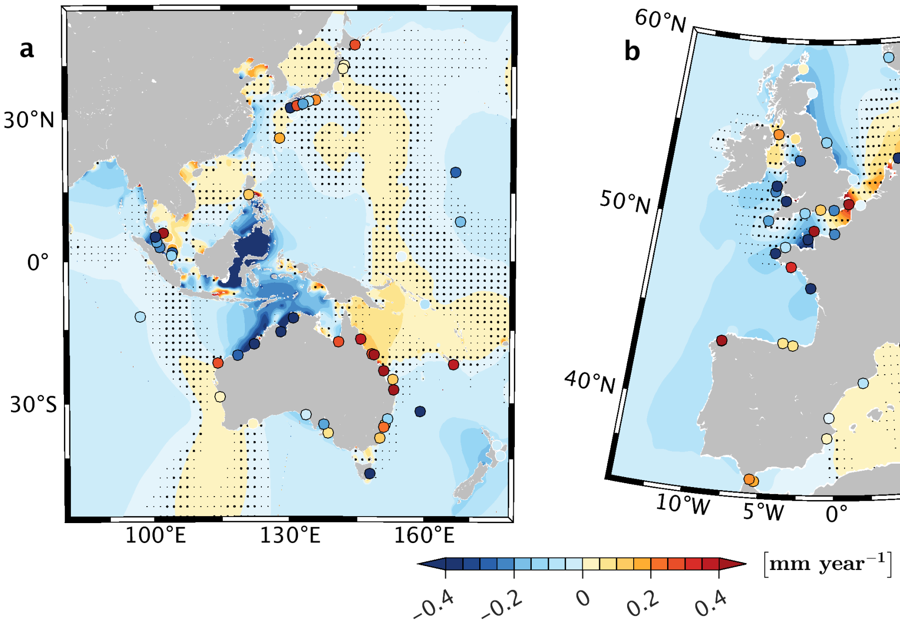

Figure 6.4: M_2 amplitude trends around Australia/Southeast Asia and Europe, 1993–2020. Colored markers represent measured M_2 trends (mm year^{-1}) in **a** Australia and Southeast Asia, and **b** Europe. Markers are highlighted with black (or respectively white) outlines wherever fitted rates are statistically significant (insignificant) at 68 % confidence. Color shading indicates modeled amplitude trends, representing the combined response of the barotropic M_2 tide to stratification changes (this work) and relative sea level rise. Heavy (or light) black dots identify regions where values do not pass the 68 % (or 95 %) threshold for statistical significance. All trends are based on estimates of Opel et al. (2024).

modeled ($\sim -0.36 \pm 0.07$ mm year^{-1}) trend is also highlighted in Figure 6.6. Here, three available tide gauges on the Malaysian West coast at the Strait of Malacca are used for averaging the local trends. As evident from the pie chart included in Figure 6.6, stratification is the primary driver for these changes.

Another region with complex tidal patterns is the European Shelf. Given its shallow bathymetry, the European Shelf poses a challenge for baroclinic tide models, particularly in the Wadden Sea. Figure 6.4b depicts the trends of M_2 amplitude around Europe. Even for the signals observed by the tide gauges, the small spatial extent and largely incoherent nature of the trends become apparent. Nevertheless, in regions like the Irish Sea and in the English Channel, the simulations largely reproduce the sign of the observed trends. However, model estimates are insignificant in many locations of the European Shelf, since the stratification based trends are highly sensitive to the a posteriori correction of residual steric effects (cf. Section 4.3.2). The pointwise comparison of observed and modeled M_2 amplitude time series of Newlyn in Figure 6.7c yields a negative linear rate in both cases, but the magnitude of the modeled trend is lower and paired with a relatively high uncertainty. Pineau-Guillou et al. (2021) also found a negative M_2 trend at Newlyn from 1990 to 2016 of -0.28 ± 0.49 mm year^{-1}. The general high model uncertainty in the region of the Northwest European Shelf is also reflected in the spatial averages in Figure 6.6, where the mean of 13 locations shows an observed ($\sim -0.29 \pm 0.04$ mm year^{-1}) and modeled ($\sim -0.14 \pm 0.07$ mm year^{-1}) decrease in M_2 amplitude. Here again, the large formal errors of the model estimate only allow for a tentative conclusion as to the underlying physical processes. Certainly, Figure 6.6 indicates a dominant role for stratification, rather than sea level rise.

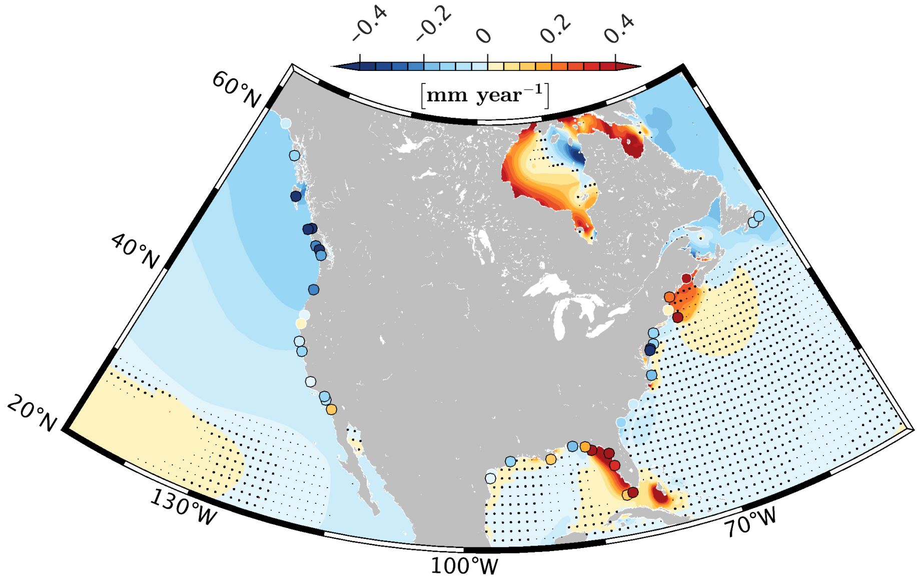

Figure 6.5: M_2 amplitude trends around North America, 1993–2020. Same as in Figure 6.4. All trends are based on estimates of Opel et al. (2024).

Even higher uncertainties are present in the German Bight. Figure 6.6 clearly indicates that the model and the observations are highly disparate in that region. While the observed trend is strongly negative, the modeled estimate points to an increase of M_2 amplitude, but again with very large formal errors. The difficulty to model the Wadden Sea, in particular with a global modeling approach, is underlined in Figure 6.7d based on the time series for Cuxhaven. The amplitude decrease from 1996 to 1999 are the only points in the analysis time span where observation and model are close together. Especially in the second half of the analysis period, the time series have very little in common. As revealed by Figure 6.6, within the German Bight, sea level rise appears to be a more potent driver for tidal changes than changing stratification conditions. The observed negative trend is generally consistent with increased tidal dissipation in the shallow southern part of the North Sea (Pelling et al., 2013; Schindelegger et al., 2018). The increased dissipation may be related to changes in morphology of the Wadden Sea that superimpose the effects of the background sea level rise or stratification (e.g., Benninghoff and Winter, 2019). The time series of Cuxhaven in Figure 6.7d additionally illustrates a recently increasing amplitude from 2015 to 2019, which does not follow the negative trend from 1993 to 2020. This contrast highlights the sensitivity of trend estimates to the analyzed time span. A similar caveat has been put forth by Pineau-Guillou et al. (2021), who found for Cuxhaven a positive M_2 trend from 1910 to 2018, but in contrast, a negative trend from 1990 to 2018. Besides the difficulties to model the German Bight, particularly the Wadden Sea, to a realistic extent, diverse physical processes might be acting here in this complex environment. The processes may even change over time, causing a possible reversal in the sign of the tidal trend.

The East and West coast of North America both contain quite a dense network of tide gauge stations. At the East coast, the modeled M_2 trend is widely insignificant, impeding conclusions about the driving mechanisms. Nevertheless, the Gulf of Maine is characterized by M_2 increases between 1993 and 2020, caused by to changing tidal conversion at the mouth of the Gulf (Schindelegger et al., 2022). The modeled estimate, despite lacking statistical significance, correctly reflects the strong and local increase of the M_2 amplitude in the Gulf of Maine. The M_2 trends at Eastport, Portland and Boston are all found to intensify when comparing trends from 1910–2018 to trends from 1990–2018 (Pineau-Guillou et al., 2021). This condition possibly indicates that a physical process might strengthen over time in or at the entry of the gulf, and

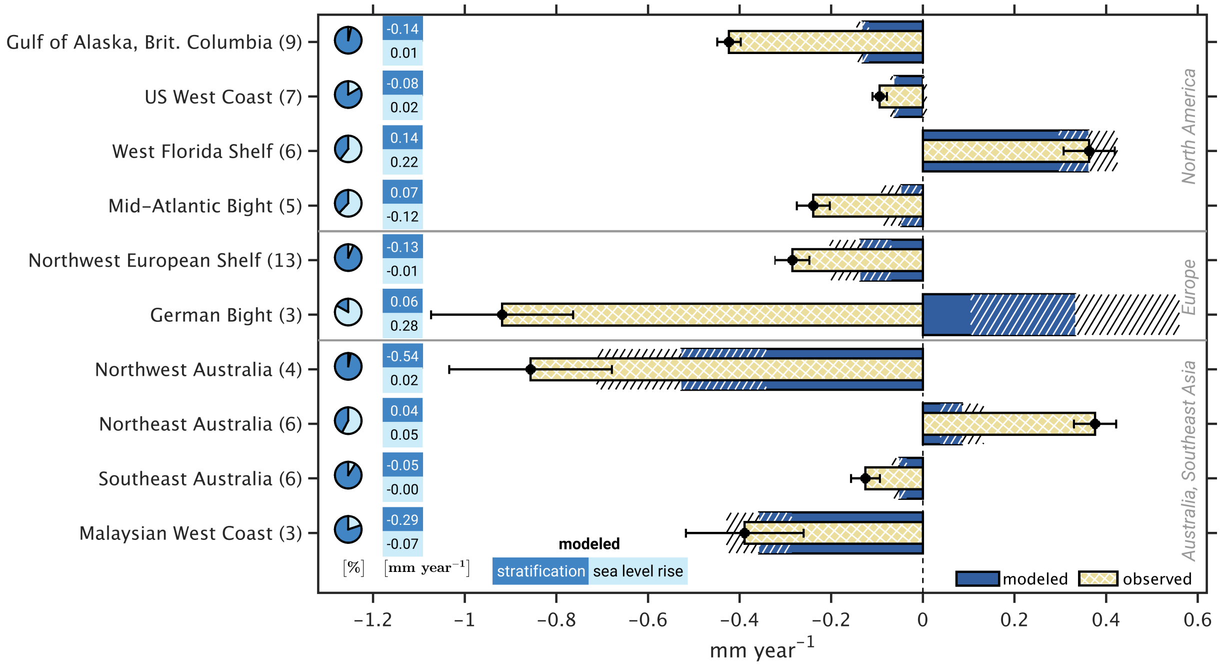

Figure 6.6: Budget of contemporary M_2 amplitude trends in selected coastal regions. Shown are spatial averages of M_2 amplitude trends (mm year^{-1}) at tide gauge locations in 10 regions, deduced from water level observations (cross-hatched creme bars) and numerical modeling results that account for the combined effect of stratification and sea level changes over 1993–2020 (dark blue bars). Black error bars and the hatched extension of the modeled M_2 trends represent the respective 68 % confidence limits. Only tide gauges with observed trends being "likely" significant (68 % level) are considered. Numbers in parentheses on the vertical axis show the total count of tide gauges per average. Pie charts on the left indicate the relative contributions of the two different driving processes to the modeled M_2 amplitude trend in each region. The region referred to as "Northwest European Shelf" comprises the Celtic and Irish seas, and the English Channel (see Figure D.11). The Figure is taken from Opel et al. (2024).

that this change is part of a long-term process.

The West Florida Shelf is another region that is subject to a strong and regional M_2 amplitude increase. The trend estimate is overall positive, both in the observations and the model solution. Six tide gauge stations are assembled to form an averaged trend estimate for the West Florida Shelf in Figure 6.6. The comparison of modeled and observed trend indicates a relatively tight agreement. Both considered processes, stratification changes and sea level rise, induce an increase in the amplitude. The different effects add up and form a robust M_2 amplitude increase of 0.36 ± 0.06 mm year^{-1}, matching to what is inferred at tide gauges (0.36 ± 0.06 mm year^{-1}). In the Mid Atlantic Bight, the statistical insignificance of the modeled trend is due to the approximate cancellation of trends from stratification changes (positive) and sea level rise (negative M_2 trend). This circumstance causes the modeled trend to be smaller by a factor of $\sim$5 than the observed trend (Figure 6.6).

The West coast of North America is consistently characterized by a decrease of M_2 amplitude. Figure 6.6 divides the coastline in two regions, the US West coast and the Gulf of Alaska/British Columbia. The US West coast averages of observed and modeled trends are almost matching within uncertainties. Here stratification acts as the dominant driver for long-term tidal changes, and is even more so in the Gulf of Alaska and British Columbia. The observed trend has

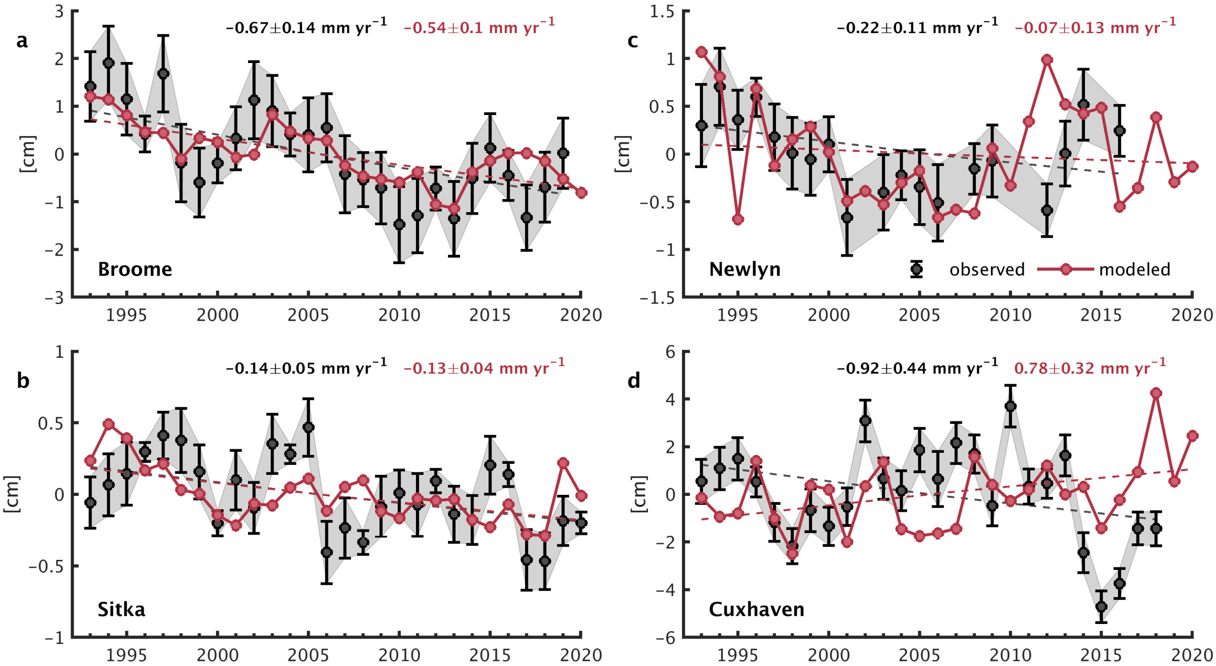

Figure 6.7: Annual M_2 amplitude changes (cm), 1993–2020, at tide gauges **a** Broome, Australia, **b** Sitka, Canada, **c** Newlyn, United Kingdom, and **d** Cuxhaven, Germany, from observations (black markers, with standard errors) and simulations (magenta markers). Respective trend estimates and 68% confidence intervals are included in the top right corner. The simulation results represent the sum of sea level rise and stratification effects on the barotropic M_2 tide. Tide gauge locations are highlighted in Figures D.11 and D.12.

a higher magnitude with -0.42 ± 0.03 mm year^{-1} than the modeled counterpart with -0.13 ± 0.01 mm year^{-1}. The disparity is partly caused by the tide gauge at Queen Charlotte on Graham Island, whose trend estimate is much more negative than that of the surrounding stations (Opel et al., 2024). The neighboring station Sitka in the north of Queen Charlotte indicates a negative trend too, but much smaller in magnitude, as shown in Figure 6.7b. Here, the observed and modeled M_2 changes are consistent.

Overall, the above analysis shows how numerical modeling, considering both the effects of modeled sum of tidal trends from stratification changes and sea level rise, allows one to explore and also partly explain along the world's coastlines. The role of stratification is thereby dependent on the region. In fact, there is no analyzed region where the present-day changes in stratification do not add to the representation of observed trends, whereas sea level rise plays a minor role in some locations. In particular at the West coast of North America or at the northwest Australian coast, stratification is the single most important forcing factor for present-day tidal trends.

6.2 Baroclinic Tide

The surface manifestations of the baroclinic tidal amplitudes are subject to significant linear trends between 1993 and 2020, too. Figure 6.8a presents the linear trend of the M_2 baroclinic surface amplitude that exceeds the 68 % confidence level. Regions that are known to host patterns of enhanced tidal conversion stand out with an increase in the tidal amplitude, that is estimated to be ∼20 % of the mean surface amplitude of the baroclinic tide itself. This finding is

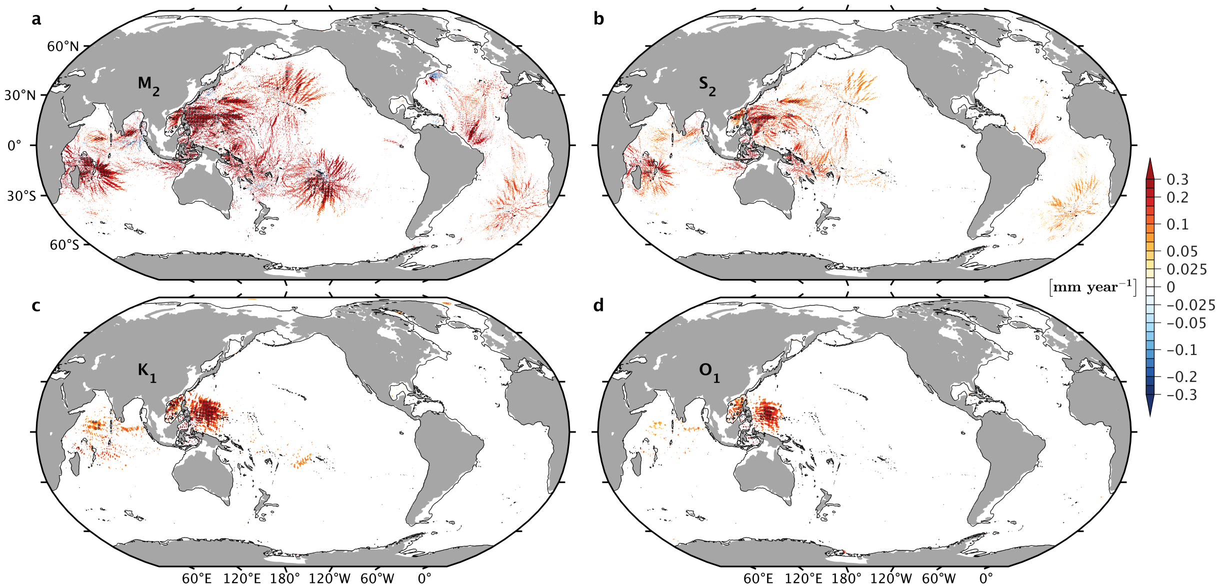

Figure 6.8: Modeled trends of the **a** M_2, **b** S_2, **c** K_1 and **d** O_1 internal tide surface amplitude, 1993–2020, in mm year^{-1}. Grid points with statistically insignificant trends (at the 68 % confidence level) and areas shallower than 500 m are masked. Black boxes are drawn for $2° \times 2°$ cells where trend values are significant at 95 % confidence for at least a third of the contained grid points. The figure of M_2 corresponds to Figure 4 from Opel et al. (2024). Note the non-linear color scale.

consistent with a recent study by Zhao (2023), who found a globally averaged strengthening of the mode-1 M_2 internal tide kinetic energy in the averaged period of 2010–2019 in comparison to 1995–2009. The author indicated the dominance within this estimate of a few contributing regions around the world, which are, amongst others, the Mascarene Ridge, the Luzon Strait and the western Pacific. All of these regions also feature increased baroclinic M_2 amplitudes in Figure 6.8a. In the analysis period from 1993 to 2020, the region around the Mascarene Ridge yields peak trends up to 0.6 mm year^{-1}, the Luzon Strait up to $\sim$0.5 mm year^{-1} and the western Pacific localized peak values up to 0.8 mm year^{-1}. All of these estimates are significant at the 95 % confidence level. Moreover, regions near the Amazon Shelf and French Polynesia reveal strengthening rates of $\sim$0.3 mm year^{-1}, which are also significant at the 95 % confidence level. The trends are strongest near familiar generation sites for internal tides, and decrease with the propagation path of the baroclinic tides away from the generation sites.

Besides M_2, the surface amplitudes of the tidal constituents S_2, K_1, and O_1 are also subject to mostly positive trends of average $\pm$0.2 mm year^{-1} (Figure 6.8b, c, d). In contrast to the baroclinic M_2 trend, the magnitude is lower. Nevertheless, the three tidal constituents all contain trends of the baroclinic amplitude that are significant at the 95 % confidence level. The S_2 trend patterns bear some resemblance to those of M_2. Despite the smaller magnitude of the trends, 95 % confidence is achieved east of Madagascar around the Mascarene Ridge, in the western Pacific in the regions of the Philippine Sea, as well as east and west of the Luzon Strait with trends up to 0.3 mm year^{-1}. Contrary to M_2, the regions around French Polynesia, at the mouth of Gulf of Maine, and off the Amazon Shelf show no significant increase of the baroclinic amplitude. The trend patterns of K_1 and O_1 reveal statistically significant trends (95 % confidence) up to 0.4 mm year^{-1} (K_1) and 0.3 mm year^{-1} (O_1) in the Philippine Sea. For K_1, 95 % confidence level is also achieved in the central Indian Ocean for a few locations with trends < 0.1 mm year^{-1}.

The above described findings are potentially important in the context of deep-ocean mixing and in sustaining the meridional overturning circulation, since baroclinic tides play an essential role for both of these processes, e.g., Vic et al. (2019); Dematteis et al. (2024). However, the intensified amplitudes of the surface signatures of internal tides in Figure 6.8 are mainly generated near shelf breaks or at the continental slope. After generation, they propagate along their characteristic beams, which, when generated in shallow ocean regions, are found to exhibit little downward propagation of tidal energy into the abyssal ocean (de Lavergne et al., 2020). Therefore, the overall positive tidal trends from 1993 to 2020 shown in Figure 6.8 are unlikely to directly reflect into the deep ocean mixing (Yang et al., 2024). Nevertheless the contribution of internal tides generated in shallow ocean regions is not negligible, because they still contribute to the energy budget of the abyssal ocean with a fraction of the energy they carry through the oceans.

6.3 Evolving Tidal Conversion

Barotropic-to-baroclinic conversion has long been suspected to contribute to the ocean's dynamics and tidal energy dissipation, but most considerations were of theoretical nature (Munk, 1981; Munk and Wunsch, 1998). From the time on that numerical models were able to resolve the generation of internal tides, tidal conversion has been subject to several, mainly regional, modeling studies (e.g., Müller, 2013; Falahat et al., 2014; Schindelegger et al., 2022; Liu et al., 2022b). Nowadays it is possible to observe the surface signatures of baroclinic tides globally with satellite observations (e.g., Ray and Mitchum, 1997; Zhao et al., 2012; Zaron, 2019), and the topic of energy transfer from barotropic to baroclinic tide is still in the focus of recent research. The global tidal energy conversion is connected to both the barotropic and the baroclinic tide, since the tidal conversion rate represents the amount of energy that is extracted from the barotropic tide and transferred to the baroclinic tide over underwater topography, e.g., at submarine ridges, seamounts, continental shelf breaks, or generally rough bottom topography. Figure 2.17 describes the global point-wise conversion together with the spatial distribution of the important energy component of the oceans. From regional studies, evidence exists that seasonal changes in stratification impact the amount of tidal conversion (e.g., Müller et al., 2012; Wang et al., 2016). Therefore, it is natural to suggest that a changing stratification in a long-term sense also acts upon the tidal conversion rate. This connection is examined below.

It is common in literature to compute area-integrated estimates of conversion rates C (cf. Equation 2.15) in global and regional domains. To analyze the annual tidal conversion in this work, globally-integrated barotropic-to-baroclinic energy conversion rates ($\overline{C}$) are computed for every analysis year per tidal constituent. The global integral $\overline{C}_{1993-2020}$, summed for the four primary tidal constituents used in this work and averaged over all 28 modeled years, yields an estimate of $\overline{C}_{1993-2020}$ ~0.7 TW. Egbert and Ray (2001) suggested ~1 TW for all tidal constituents. As is evident from observations by, e.g., Egbert and Ray (2003), M_2 dominates $\overline{C}$ over the contribution of other tidal constituents, in this work with $\overline{C}^{\mathrm{M}_2}_{1993-2020}$ ~0.5 TW (with ~0.66 TW contributions from sources and ~−0.16 TW from sinks). In comparison to values from literature by Egbert and Ray (2001), who observed the globally integrated conversion rate for M_2 to ~0.7 TW for the deep ocean, the model-based estimate of the present work is lower in magnitude. In additional experiments, evidence was found that this discrepancy is mainly associated with inaccuracies in the adopted density distribution and to some extent also the vertical model discretization.

Following Müller (2013), 32 % of tidal conversion takes place in ocean areas shallower than

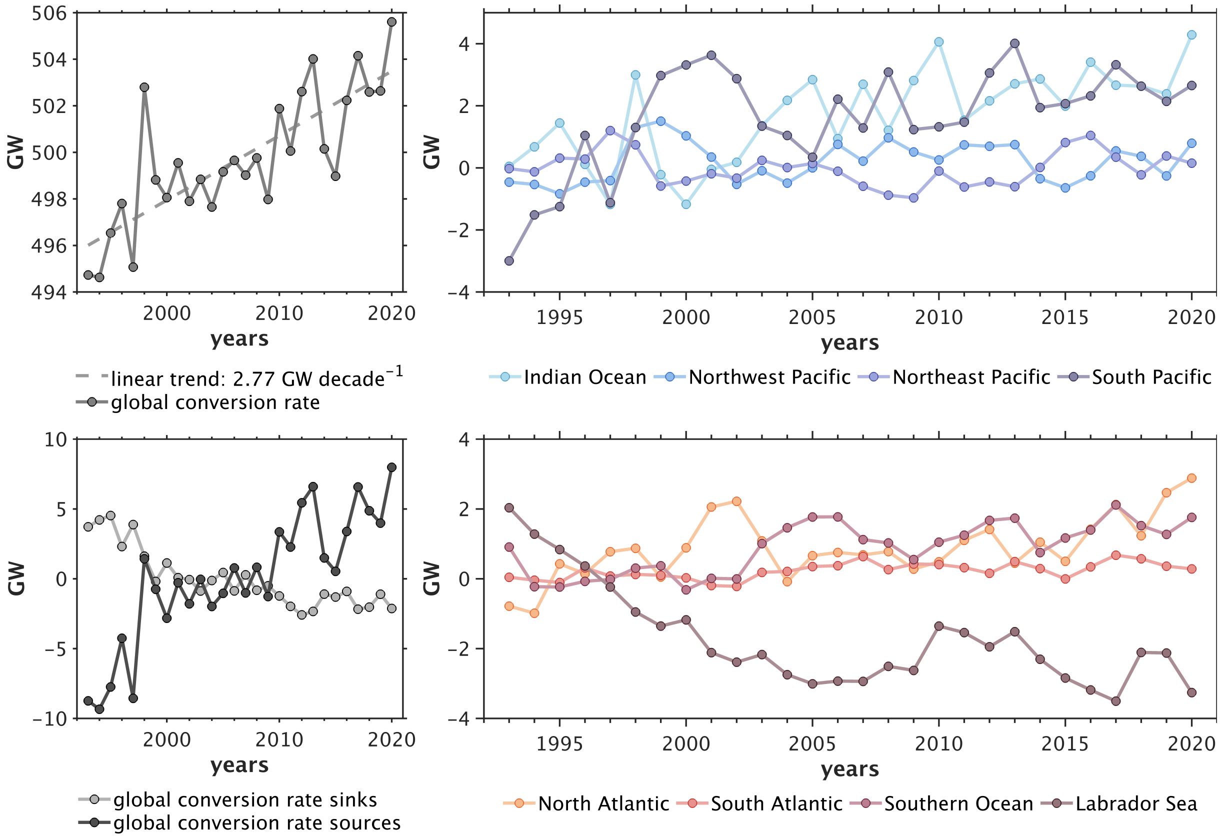

Figure 6.9: Changes in the modeled M_2 conversion rate, integrated globally (left panels) and regionally (right panels) corresponding approximately to basins from Müller (2013). The left panels illustrate both the contributions form sources and sinks (mean reduced), along twith the total conversion rate and a straight line fit to that time series. Linear trend estimates for the regional time series are displayed in Table 6.2.

1000 m, while extending the depth to 2000 m yields 50 %. Similar values are estimated in this work for M_2, namely, 27 % conversion in the upper 1000 m of the ocean and 52 % for the upper 2000 m. Additionally, it is estimated that the upper 500 m of the ocean contribute 12 % to the total conversion.

The global area-integrated conversion estimates for each year between 1993 and 2020 are characterized by interannual variability, visible in Figure 6.9 for M_2. The global interannual variability is superimposed on a significant positive linear trend of 2.77 ± 0.41 GW decade^{-1} between 1993 and 2020. The global increase of M_2 conversion leads to the assumption that more energy is transferred to the baroclinic tide during the analysis period. This is indeed confirmed by the overall positive trend of the baroclinic surface tide (cf. Section 6.2). Furthermore, the increasing global conversion rate provides a physical explanation for the predominantly negative barotropic amplitude trends (cf. Section 6.1), which loose more energy to the baroclinic tide. The enhanced energy transfer is a combination of increasing conversion from sources, and decreasing conversion from sinks (Figure 6.9).

As Figure 2.17 implies, conversion is a quite local, or regional phenomenon. Therefore, major contributions to the global conversion rate originate from a few regions alone. Figure 6.9 represents, besides the global area-integration, the annual time series of different regional basins following those used in Müller (2013). For all time series, interannual variability is present,

Table 6.2: Linear trend of time series from regionally integrated M_2 tidal conversion estimates between 1993 and 2020, corresponding to Figure 6.9.

	$\dot{\overline{C}}$ (GW decade^{-1})
Global	2.77 ± 0.41
Global — sources	4.93 ± 0.54
Global — sinks	-2.16 ± 0.25
Indian Ocean	1.26 ± 0.24
Northwest Pacific	0.15 ± 0.15
Northeast Pacific	-0.01 ± 0.13
South Pacific	1.21 ± 0.32
North Atlantic	0.66 ± 0.17
South Atlantic	0.17 ± 0.04
Southern Ocean	0.67 ± 0.12
Labrador Sea	-1.28 ± 0.23

but it is fairly small for some regions, e.g., the South Atlantic. The corresponding linear trend estimates are provided in Table 6.2. Clearly, the highest contributions to the modeled global increase in M_2 conversion originate from the Indian Ocean and the South Pacific, which is also visible in Figure 6.10. In Müller (2013), the absolute conversion is estimated and the regions with the highest conversion are in fact the South Pacific (> 300 GW) and the Indian Ocean (> 200 GW), which show also the highest trend estimates here. Despite lower trend estimates, the regions of South and North Atlantic, as well as the Southern ocean, also contribute to the global conversion increase. The Northeast and Northwest Pacific show no significant trend of tidal conversion from 1993 to 2020, although the mean conversion rate in that region is considerable (> 100 GW) and supported by several hot spots such as Luzon Strait (e.g., Buijsman et al., 2012; Kerry et al., 2014; Wang et al., 2016). The Labrador Sea denotes a significant negative trend, as the only one of the eight regions. The negative trend of the region may be affected by uncertainties in the 3D GLORYS12V1 density fields due to sparse data coverage in the high latitudes.

The recent evolution of the tidal conversion rate, as simulated by the model, highlights the importance of regarding tides as variable phenomena, since internal tides act as a primary source of mechanical energy in the deep ocean, maintaining the meridional overturning circulation (e.g., Wang et al., 2016). With a changing conversion rate, the amount and strength of internal tides is altered, too. Although the magnitude of the globally integrated tidal conversion rate in this study is somewhat ($\sim$30 %) too low compared to literature, the linear trend estimates, covering the time period from 1993 to 2020, reveal a significant increase of tidal conversion. This result complements recent altimetry-based insights into internal tide energetics (Zhao, 2023). The findings are also in agreement with studies that conduct seasonal analysis of tidal conversion, showing higher conversion during summertime where the stratification is strengthened compared to winter months (e.g., Wang et al., 2016). Importantly, the enhanced conversion rate from 1993 to 2020 unveil the physical cause for the positive trend of the surface amplitudes of the baroclinic tide, as well as for the predominantly negative trend in barotropic tidal amplitude, that is induced through changing ocean stratification.

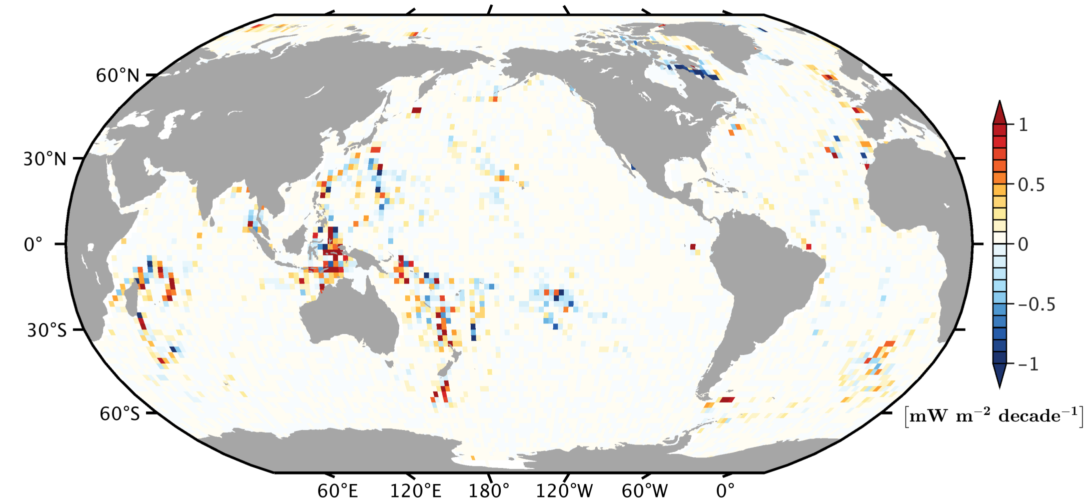

Figure 6.10: Modeled area-averaged (2°×2°) linear trends of M_2 barotropic-to-baroclinic conversion rates $\dot{C}_{1993-2020}$ ($\mathrm{mW\,m^{-2}\,decade^{-1}}$).

7 Future Tides — A Model-based Glance to the End of the 21st Century

The above material has revealed a connection between present-day variations in tides and the ocean's evolving density structure. The 3D simulations with the MITgcm reproduce considerable fractions of the observed trends, and therefore, as a further step, I use the validated MITgcm setup for simulations with stratification of the future, extending to the end of the 21st century. The projection of the ocean's future density stratification is taken from the CMIP6 database, as described to more detail in Section 3.2.2. Effects of residual sea level changes amongst the time slice simulations are corrected analogously to present-day, as described in Section 4.3.2. The findings and figures within this chapter, especially in Section 7.2, build upon the work published in Opel et al. (2025).

7.1 Tidal Response to Future Stratification Changes

Figures 7.1 and 7.2 illustrate future barotropic amplitude changes of M_2, S_2, K_1, and O_1 with respect to the year 2000 in response to strengthened ocean stratification, as depicted in Figures 2.6 and 2.7. Constrained to the high greenhouse gas emission scenario SSP5-8.5 (here named RCP8.5 for simplicity), Figure 7.1a reveals a predominantly decreasing global barotropic M_2 amplitude, consistent with the associated present-day trends of this work and Opel et al. (2024). The spatial patterns of the M_2 amplitude changes in 2100 (Figure 7.2a) largely agree with those of 2060, indicating that the same normal modes near the M_2 frequency are damped in both cases (Platzman et al., 1981). Despite the consistently decreasing M_2 amplitude in 2060 and 2100, it is evident from the modeled M_2 amplitude changes, that the magnitude of the surface amplitude response does not adhere to a linear scaling with time, or respectively with the change of potential energy anomaly (which is $\sim$10–20 % for 2100, cf. Figure 2.6). Individual (mainly coastal) regions are indeed affected by intensified decrease from 2060 to 2100 of rates almost up to doubling (e.g., Patagonian Shelf, Northwest Australia, Bay of Bengal, or regions around New Zealand), but the characteristic basin scale decrease is somewhat less pronounced in 2100 than in 2060, e.g., in the central Pacific, at the US West coast, or in the open Atlantic. In general, decadal variability ($\pm$5 cm) is present within the simulated M_2 amplitude changes in a few shelf regions (cf. Figure D.13, e.g., Gulf of Maine, Yellow Sea, parts of Northwest European Shelf). This variability suggests that the response of M_2 to future stratification changes is a fairly complex process, depending on various factors, like, e.g., bottom topography in connection to the ocean's density surfaces, or the influence of climate modes.

In comparison to M_2, the future barotropic S_2 amplitude changes are mainly restricted to a few coastal regions, that show a decrease in amplitude, as visible in Figures 7.1b and 7.2b. Little pronounced changes on basin scales are apparent. The regions characterized by a decreasing S_2 amplitude are the Mozambique Channel, Northwest Australia, the European Shelf, the Labrador

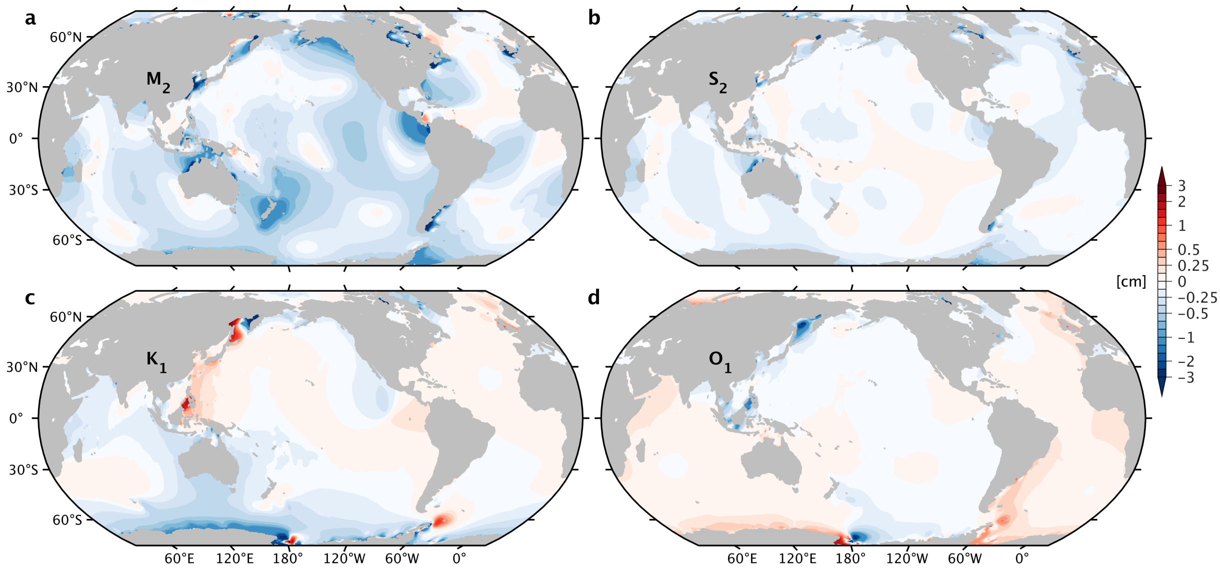

Figure 7.1: Barotropic amplitudes of M_2 **a**, S_2 **b**, K_1 **c**, and O_1 **d** in 2060 relative to 2000, under RCP8.5 assumption.

Sea, and the Patagonian Shelf. The spatial structures are similar for 2060 and 2100 (cf. Figures 7.1b and 7.2b), with the decreases being stronger in 2100 compared to 2060. The future amplitude changes of both diurnal tides are characterized by increases (e.g., north of Antarctica Peninsula for both tidal constituents), as well as decreases (cf. Figures 7.1c–d and 7.2c–d). For K_1, positive amplitude anomalies are present in 2060 in the Sulu Sea, but seem to vanish in 2100. In contrast, a K_1 increase of ∼0.8 cm emerges in the Yellow and East China Sea in 2100, which is not yet present in 2060. Similarly, a decrease of the K_1 amplitude in North Australia in 2100 is not yet visible in 2060. Consistent for both time stamps, a K_1 decrease off East Antarctica is evident, pointing to an effective dampening of the tide's main normal mode in form of a Kelvin wave (Cartwright and Ray, 1991; Ray and Egbert, 2004). Concerning O_1, the modeled amplitudes seem to decrease consistently over time in the Indonesian Seas. In 2060, an increase in O_1 amplitude located around the United Kingdom is evident, but becomes less apparent in 2100, again suggesting the presence of decadal variability.

The globally area-integrated conversion rate of M_2 increases from 0.519 TW in the year 2000 to 0.584 TW in the year 2100 (based on RCP8.5), equivalent to a relative change of ∼12.5 % (see Figure 7.4 for global, spatially area-integrated conversion differences relative to 2000). The increase in future barotropic-to-baroclinic energy conversion directly impacts the baroclinic tides. Figure 7.3 illustrates the baroclinic surface amplitude differences for M_2, S_2, K_1, and O_1 in the year 2100 with respect to 2000, constrained to RCP8.5. Changes in the baroclinic surface amplitudes are mainly present at known locations of enhanced tidal conversion for all four tidal constituents. Since the signal is computed as the difference of two global baroclinic surface amplitude patterns of specific years, the alternating patterns of amplitude increases and decreases partly indicate phase shifts between the two years, and not necessarily a pure change in magnitude. A recent study by Gong et al. (2025) found a significant, global-scale accelerating trend of internal tide speed, stemming from the projected intensification of upper-ocean stratification. This result highlights the sensitivity of internal tides to a warming climate, as evident also from Figure 7.3. The general tendency for decreasing barotropic M_2 amplitudes in combination with a globally increasing energy conversion rate (and thus increasing surface amplitudes of internal tides) is qualitatively consistent with the tidal changes in present day (cf. Chapter 6). However, the barotropic decrease does not scale linearly with time or with the respective change in

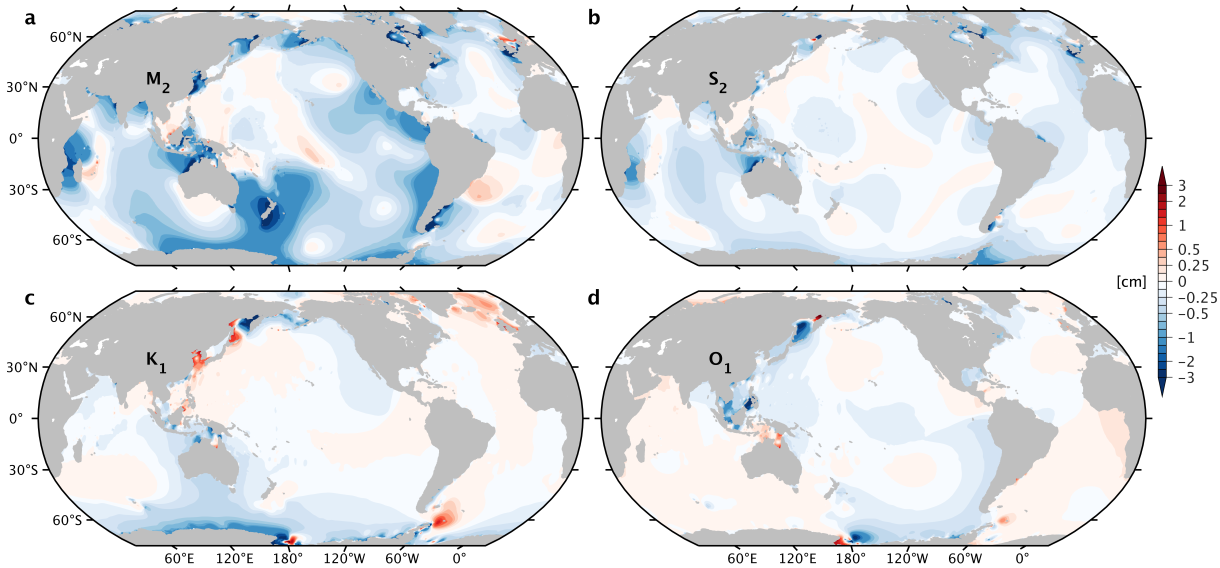

Figure 7.2: Barotropic amplitudes of M_2 **a**, S_2 **b**, K_1 **c**, and O_1 **d** in 2100 relative to 2000, under RCP8.5 assumption.

potential energy anomaly ϕ.

In detail, we have a stratification increase of ∼20 % in 2100, an increase of M_2 tidal conversion of ∼12.5 %, and barotropic M_2 amplitude changes of ∼2 % with respect to the mean amplitude (all values with RCP8.5 assumed). These numbers appear to be somewhat contradictory. However, the disparity between the change in conversion rate and tidal surface amplitude can be physically explained (cf. Opel et al., 2025). First, dissipation based on tidal conversion is quadratic in velocity (e.g., Green and Nycander, 2013), while the connection of tidal velocity and tidal amplitude can be approximated to be linear. Second, because of increased conversion in deep ocean regions, dissipation is enhanced, too. Consequently, the tides that are approaching continental shelves are less energetic, since more energy is lost to dissipation. In shallow waters, bed friction dominates the dissipation, which is cubic in velocity (Taylor, 1920). Thus, the tidal change in shallow waters are larger than those in the deep ocean and can re-arrange dissipation on the shelf, which would again feed back on the tides in the deep ocean. Ultimately, shelf and deep-ocean tides are pushed to a new state of coupled resonance, which is different in the distribution of dissipation but not necessarily in surface amplitude.

7.2 Comparing Three Drivers of Future Tidal Changes

In the decades to come, not only stratification changes, but also other non-astronomical processes are assumed to impact the global tides. Of particular interest in this regard are stratification changes, relative sea level rise, and ice shelf cavity geometry changes, i.e., defining elements within the warming climate system (cf. Fox-Kemper et al., 2021). The latter driver, resulting from ice shelf thinning and retreat, impacts the global tides through modified dissipative properties and altered resonance/back-effect conditions due to changing geometries of Antarctica's sub-shelf cavities (Arbic et al., 2009a; Arbic and Garrett, 2010; Wilmes and Green, 2014). Sensitivity experiments (e.g., Rosier et al., 2014; Wilmes et al., 2017) have revealed the relevance of changes in ice shelf cavity geometry as a driver for regional and potentially global changes in

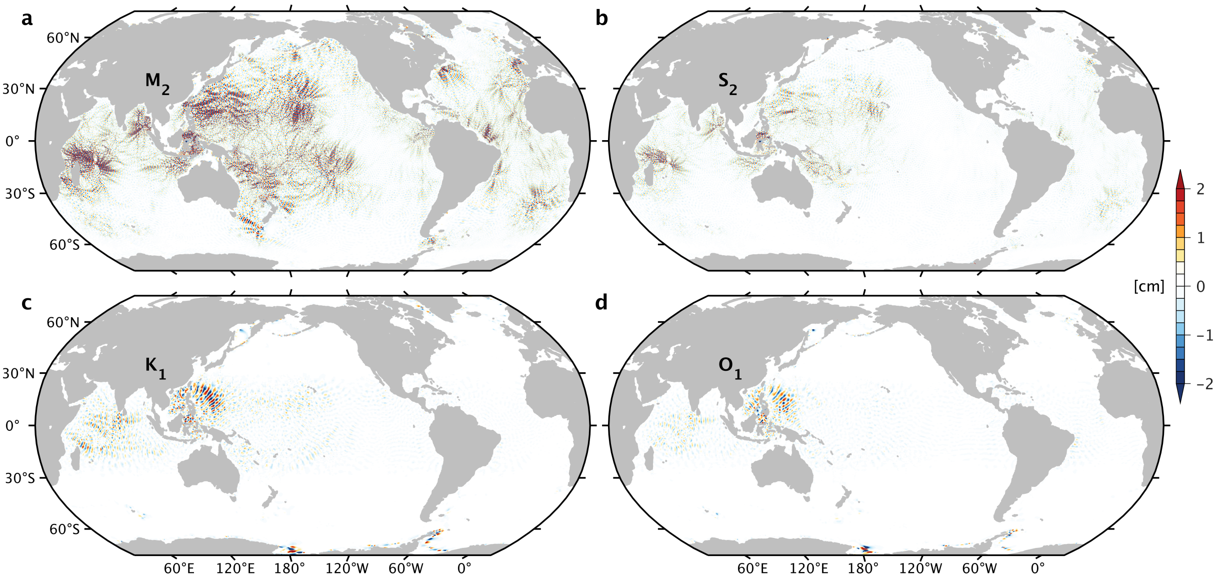

Figure 7.3: Baroclinic amplitude of M_2 **a**, S_2 **b**, K_1 **c**, and O_1 **d** in 2100 relative to 2000, under RCP8.5 assumptions.

tides. The approaches to modeling relative sea level rise and ice shelf cavity effects are described briefly in Section 4.4 and in more detail in Opel et al. (2025).

All three adopted drivers of future tidal changes induce appreciable modulations in the barotropic M_2 amplitude, but their relative importance changes with time and location (Figure 7.5). In particular, deep and shallow ocean regions are affected by different physical mechanisms. Stratification and ice shelf melt dominate the tidal changes in the open ocean on basin scales, irrespective of the time window. However, the ratio of impact between stratification and ice shelf melt differs in 2060 and 2100, as is evident from Figure 7.5a/b and e/f. Although stratification is the main driver for open-ocean barotropic M_2 amplitude change in 2060 (consistent with present-day findings in Opel et al., 2024), the impact of the melting ice shelves is strongly enhanced until the end of the century in 2100, where it evokes the largest tidal response among the three drivers. Under RCP8.5, the impact of ice shelf cavity changes on M_2 in the deep ocean exceeds the impact of stratification changes by 2090.

In contrast to modulations on basin scales, tidal changes related to sea level rise are mainly concentrated in coastal and shelf areas, visible in Figure 7.5c/d. The open ocean is affected on a broader scale only in the North Atlantic, likely due to tidal resonance and coupled oscillation between shelf and deep-ocean regions, which increases the sensitivity of the semidiurnal tide to changes in local water depth (Arbic et al., 2009a). The M_2 modulation due to sea level rise in the Atlantic also includes a tidal response to a pronounced GIA signal (Schindelegger et al., 2018). Besides the broader response in the Atlantic, relative sea level rise only accounts for small M_2 amplitude changes on basin and sub-basin scales. In general, the tidal changes in 2100 are approximately doubled relative to those of 2060, and therefore scale almost linear with time. Implied M_2 amplitude changes in 2100 (2060) are in the order of a few centimeters, e.g., for the Gulf of Maine $\sim$3 cm ($\sim$1.5 cm), the Mid Atlantic Bight ~ -3 cm (~ -1.5 cm), or the German Bight $\sim$10 cm ($\sim$5 cm).

Ice shelf melt exerts limited impact on the global M_2 tide in 2060, as illustrated in Figure 7.5a. The response is mostly restricted to regions in the Weddell Sea around the Filchner-Ronne ice

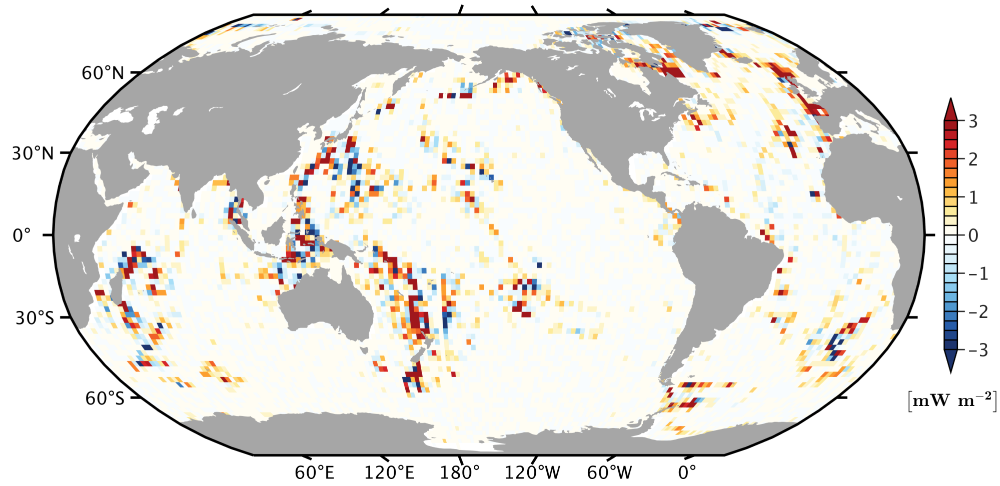

Figure 7.4: Modeled, area-averaged (2°×2°) tidal conversion in the year 2100 relative to the year 2000 (mW m^{-2}).

shelf (FRIS) (∼±4 cm) and the Argentine Sea (up to ∼2 cm). By 2100, the cavity-induced M_2 perturbations strongly increase and develop into a global phenomenon under RCP8.5 (Figure 7.5b). The tidal impact is largest around Antarctica, e.g., at the FRIS (∼−20 cm), at the Thwaites glacier ∼−6 cm, or at the tip of Antarctica Peninsula (∼6 cm). Further afield, the modulations in 2100 reach ∼3.5 cm around New Zealand, ∼6–17 cm in the Argentine Sea, ∼−2 cm around South Africa, ∼−3 cm at the West European Shelf, or ∼−6 cm off southern Brasil.

The global impact from expanding ice shelf cavities, is due to strong back-effects onto the open ocean associated with altered resonance properties of the basins and their adjacent wider shelves (Arbic et al., 2009a; Arbic and Garrett, 2010; Wilmes and Green, 2014). Especially the FRIS and the Atlantic are close to tidal resonance, which creates strongest back-effects from damped shelf tides on open ocean tides (Arbic and Garrett, 2010). In general, the patterns seen in Figure 7.5b, can in large parts be attributed to the thinning of FRIS rather than to grounding line changes (Opel et al., 2025). Regarding the global sensitivity of the M_2 amplitude to geometry changes of the FRIS, the theory by Platzman et al. (1981) reveals the 12.8-hour normal mode as the dominant contribution to M_2, with peak energy densities in the South Atlantic and the Weddell Sea. Consequently, changes in the geometry of these regions can have substantial impacts on global scales. In addition to changes in tidal amplitude, altered dissipation beneath FRIS causes northward shifts of the M_2 amphidromic points in and around the South Atlantic due to modified tidal energy flux, see for detailed interpretation Opel et al. (2025).

Considering future changes of the global S_2 tide, Figure 7.6a/c/e reveals ice shelf cavity changes as the forcing factor under RCP8.5. As for M_2, the spatial patterns are structured along normal mode features in Figure 7.6a (Platzman et al., 1981). Differences to M_2 (Figure 7.5b) occur for instance south of New Zealand with a switch in sign, at the US East coast with strong amplitude increases (especially in the Gulf of Maine), or on the European Shelf where changes in S_2 are fairly small. The impact of sea level rise in Figure 7.6c remains limited to smaller coastal regions. Similarities to M_2 are also apparent for changes in stratification (Figure 7.6e) with predominantly negative amplitude changes that are amplified at Northwest Australia, off the FRIS, in the Mozambique Channel, on the European Shelf, and in the Labrador Sea.

Considering the amplitude changes for K_1, illustrated in Figure 7.6b/d/f, ice shelf cavity changes effectively dampen the K_1 Antarctic Kelvin wave around the continent (Cartwright and Ray,

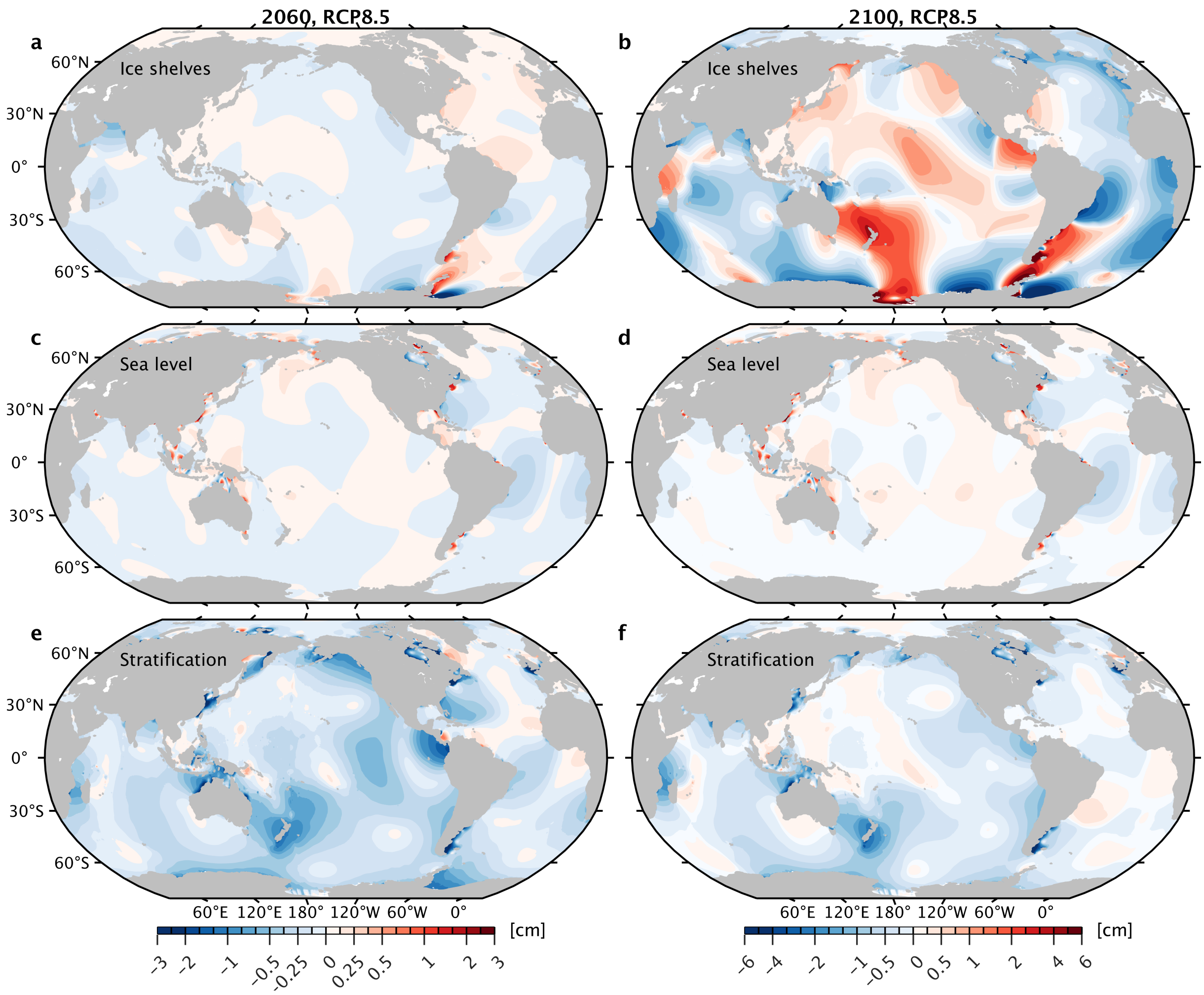

Figure 7.5: Simulated changes in the barotropic M_2 amplitude (cm) under RCP8.5 at 2060 (left column) and 2100 (right column), relative to the year 2000, in response to projected (a, b) Antarctic ice shelf cavity geometry changes, (c, d) relative sea level rise, and (e, f) strengthening of ocean stratification. Note the non-linear color scale. The Figure is taken from Opel et al. (2025).

1991; Ray and Egbert, 2004), especially close to the FRIS and the Ross Ice Shelf. Additionally, (mostly small) back-effects on the open ocean are present, mainly in the Atlantic, for instance in the form of an increase west and southeast of Africa ($\sim$0.3 cm), or at the European Shelf (reaching $\sim$0.6 cm at the UK East coast). Sea level rise induces spatially limited coastal K_1 changes in both positive and negative sign, located in the Persian Gulf, the Indonesian Seas, and in the Gulf of Carpentaria (Figure 7.6d). The effect of strengthened stratification on K_1, illustrated in Figure 7.6f, differs from the predominantly negative change of M_2 and S_2. In detail, the Antarctic Kelvin mode is dampened (as by ice shelf cavity changes), while reduced amplitudes are also seen in limited regions north of Australia. Enhanced K_1 amplitudes are present north of Antarctica Peninsula ($\sim$1.4 cm), at the West European Shelf (especially in the Irish Sea, $\sim$1.7 cm), and in the Yellow and East China Sea ($\sim$0.5 to 2 cm). The altered barotropic K_1 amplitude could potentially point to changing energy transfer to K_1 internal tides (as is evident for M_2, e.g., Zhao, 2023; Opel et al., 2024), even poleward of the K_1 critical latitude where bottom-trapped internal tides exist (Li et al., 2017).

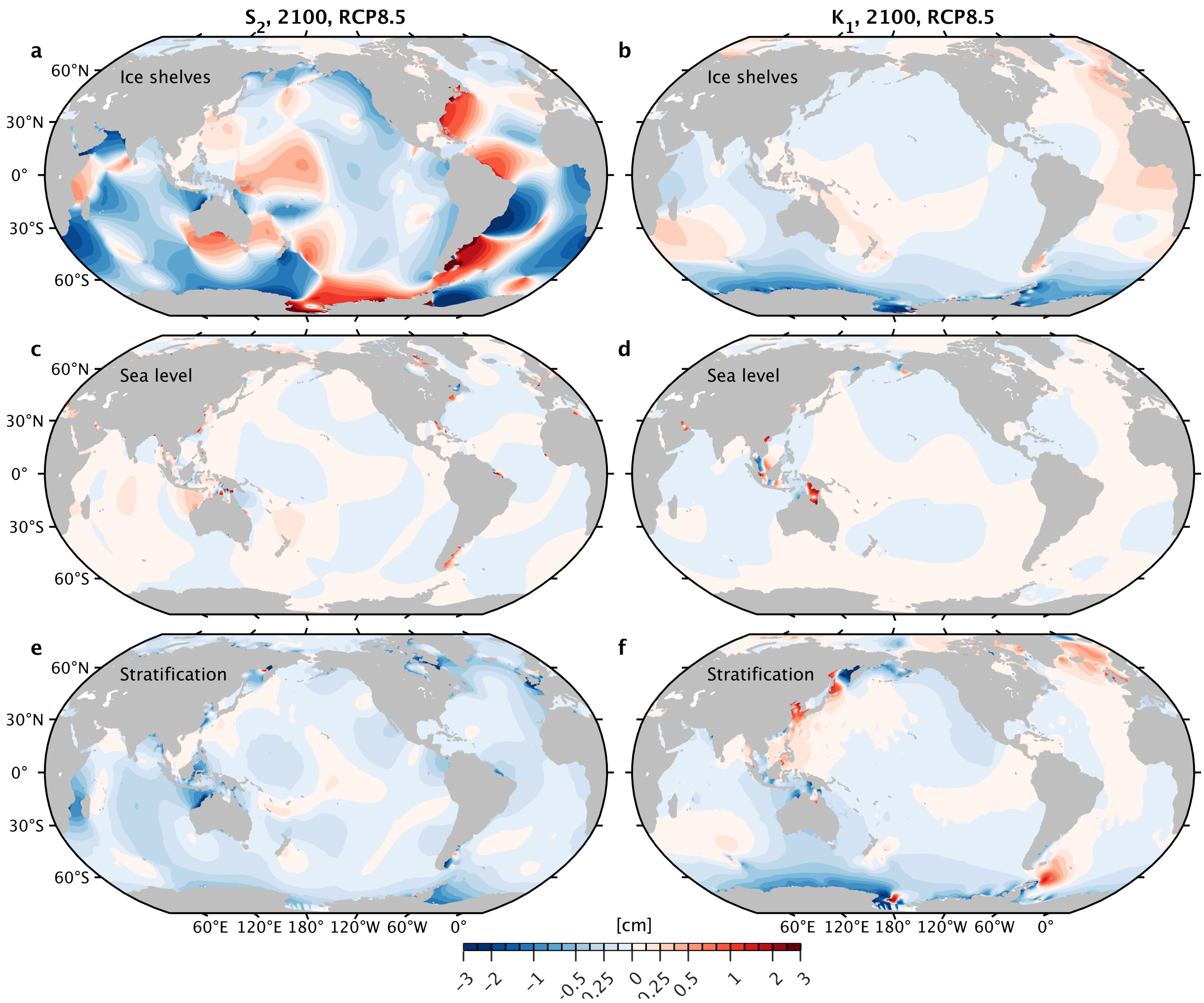

Figure 7.6: As in Figure 7.5, but for S_2 (left column) and K_1 (right column) changes by 2100 under RCP8.5 assumptions. The Figure is taken from Opel et al. (2025).

The findings in Figure 7.5 are based on the high greenhouse gas emission scenario RCP8.5, representing an upper bound estimate for the involved magnitudes. Figure 7.7 illustrates the M_2 amplitude change in 2100 under the RCP4.5 scenario (cf. Section 3.2.2), which yields lower bound estimates. As both scenarios are projections into the future, the truth may be located somewhere in between both scenarios. With RCP4.5, the year 2100 reveals similar impact among the three drivers, as all open-ocean signals in Figure 7.7 range in the same magnitude. In 2100 under RCP4.5, tidal changes due to altered ice shelf cavities are largely comparable to those of RCP8.5 in 2060, regarding both structure and magnitude. The same holds for the spatial pattern of tidal changes due to sea level rise, although there is a tendency toward smaller patterns of alternating increases and decreases at the coast. The magnitude of local sea level rise-driven changes at the coast are comparable for RCP4.5 and RCP8.5 with an approximate ratio of 1:2 between the scenarios. The predominant M_2 decrease due to strengthened stratification is also present in Figure 7.7c, although less pronounced in the open ocean in comparison to RCP8.5 in 2060. Additionally, some signals are more regionally limited than for RCP8.5, e.g., around New Zealand. The RCP4.5 major open-ocean amplitude decrease in Figure 7.7c, is ∼30–50 % relative to RCP8.5 in 2100 (Figure 7.5f). The changes of S_2, K_1, and O_1 amplitudes with RCP4.5 and due to strengthened stratification are small, as visible in Figure D.14b–d.

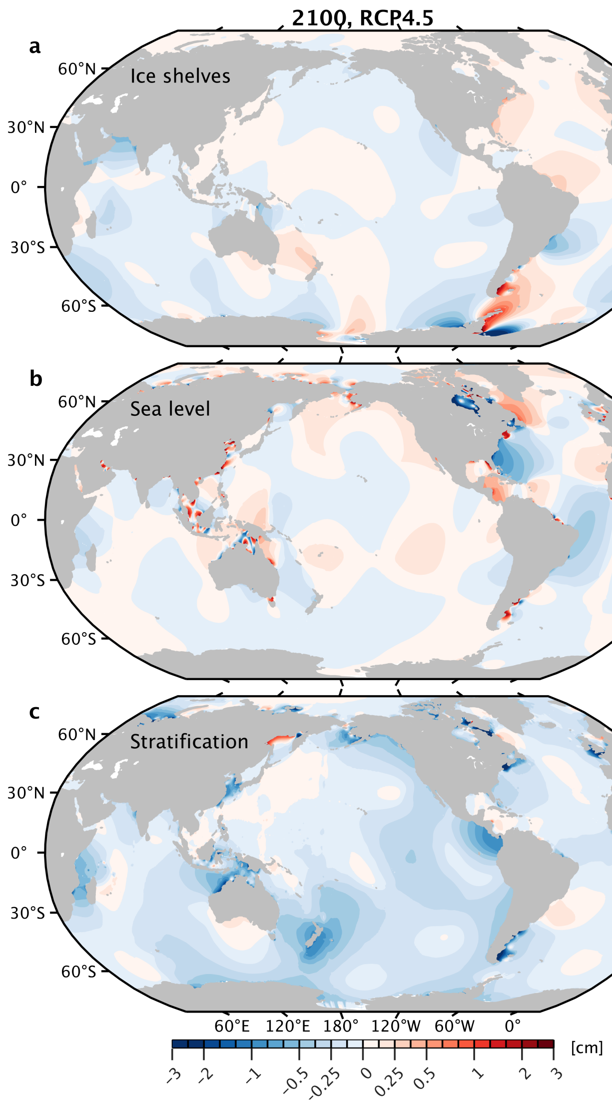

Figure 7.7: As in Figure 7.5, but under RCP4.5 assumption by 2100. The Figure is taken from Opel et al. (2025).

To shed more light onto changes of the barotropic tide at the coast, Figure 7.8 illustrates the M_2 amplitude changes induced by the three driving mechanisms along the world's coastlines in the year 2100. Focus is put on interpretation in terms of spatial coherent signals rather than on changes at individual cities, as this allows for more meaningful interpretation (difficulties of interpreting tidal changes at individual locations are discussed throughout Chapter 5). It is clear from a glance to Figure 7.8, that under RCP4.5, geometry changes of ice shelves play only a limited to negligible role in the variability of the coastal M_2 amplitude. The only region worth noting is the Patagonian Shelf with an M_2 amplitude increase < 4 cm. In contrast, the impact of sea level rise is clearly evident globally around the world's coastlines (cf. Figure 7.8c). The appreciable impact of sea level rise on coastal tides is based on the sensitivity of tides in shallow water to changes in water depth. Thus, sea level rise modulates tides in shallow coastal regions through modified bottom friction, wave propagation, or resonance characteristics. Under RCP4.5, sea level rise exerts major control onto the coastal M_2 changes amongst the three drivers, mainly causing increasing M_2 amplitudes, e.g., along the coasts of Asia, at the Amazon Shelf, on the Northwest European Shelf, or in the Gulf of Mexico. Future stratification changes cause

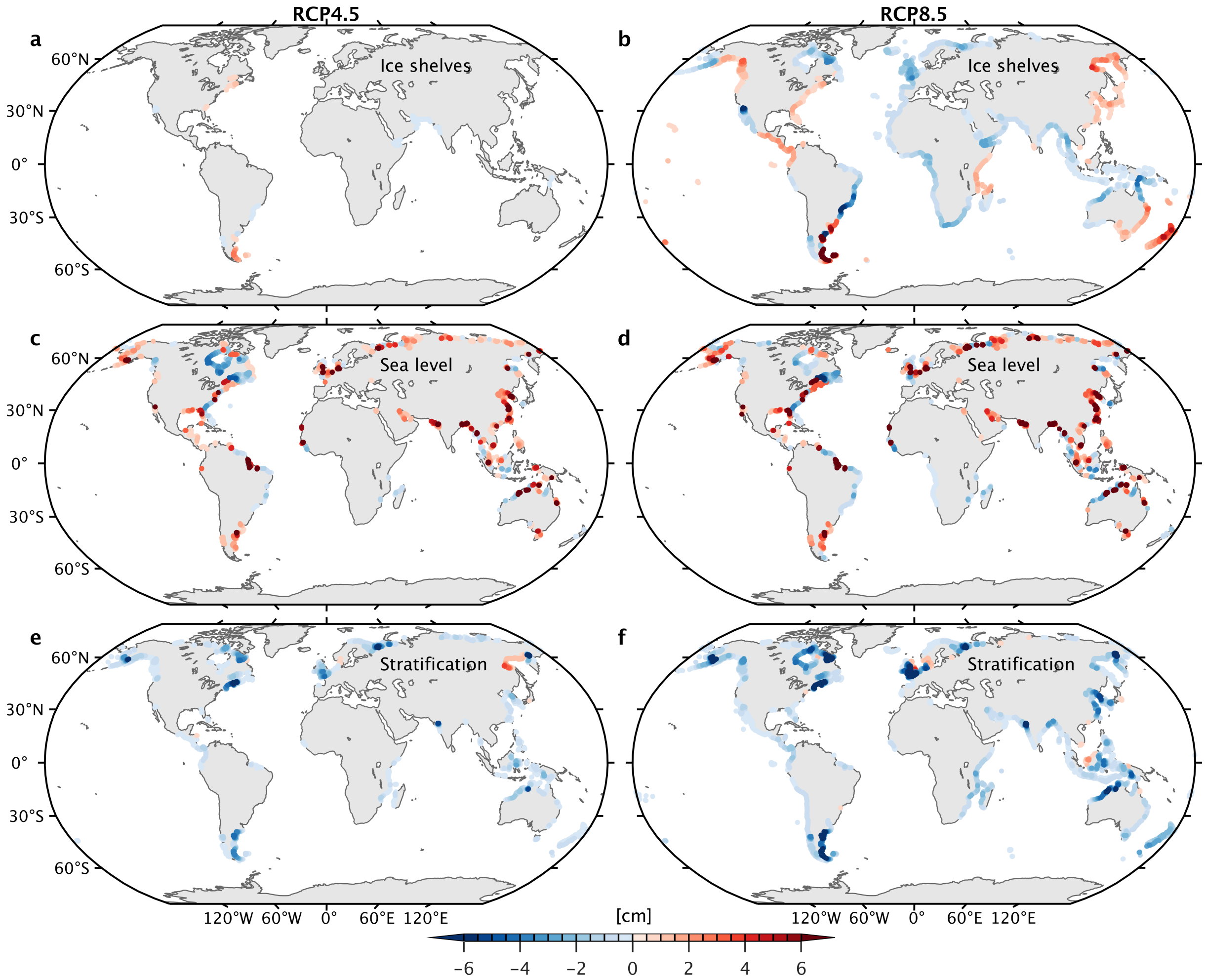

Figure 7.8: Barotropic M_2 amplitude changes in 2100 around the world's coastlines. The coastline locations are taken from Vousdoukas et al. (2018). Only data points with magnitudes larger than ± 0.5 cm are shown.

decreasing coastal M_2 amplitudes ranging in numerous locations up to -2 cm (cf. Figure 7.8e). Regions with stronger decreases are, e.g., the Gulf of Maine, the Patagonian Shelf, or parts of the Northwest European Shelf.

Under the assumption of RCP8.5, the spatial structure of M_2 amplitude changes caused by future stratification is very similar to RCP4.5 (cf. Figures 7.8e–f). In general, the coastal decreases are stronger in magnitude, especially on the Patagonian Shelf, the European Shelf, in Northwest Australia, or in the Yellow and East China Seas. The decrease is opposite to the overall increase of M_2 amplitude due to sea level rise. In some of these regions, where the amplitude decrease due to stratification is strong, the impact of sea level rise is strongly modulated or even overprinted. Those regions aside, sea level rise is the major contributor to coastal M_2 changes under RCP8.5. Albeit regions in the vicinity of the Southern Ocean, where significant amplitude increases due to ice shelf cavity changes are present (cf. Figure 7.8b), the magnitude of sea level rise-driven M_2 changes is almost everywhere more pronounced than that of changing cavity geometry. A comparison of Figures 7.8b/d/f also highlights the different spatial scales that the driving mechanisms are acting on. Given the peak magnitudes of M_2 amplitude changes at the end of the 21st century ± 6 cm (or more in some locations), implications for coastal risk assessments arise, as tides modulate the baseline for floods and storm surges.

Overall, the tidal changes simulated for the three driving mechanisms show a clear dependence on the assumed future climate forcing scenario. This dependence is particularly evident for tidal changes caused by altered ice shelf geometry. Which driver dominates the tidal modification further depends on the location, specifically whether we consider the open-ocean or coastal regions. As for coastlines, relative sea level rise is an important driver for tidal change, even being the main mechanism in many locations. The impact of sea level rise on coastal tides mainly manifests as localized responses, reflecting the influence of water depth changes, resonance conditions, friction, and wave characteristics. Besides sea level rise the impact of the other two drivers is generally characterized by larger spatial scales and dominating in the open ocean. Stratification impacts the global open-ocean tides with spatial changes being structured along normal mode features (Platzman et al., 1981). Under RCP8.5, strengthening ocean stratification dominates the changes of M_2 amplitude until 2090, before being exceeded by the effects of ice shelf melt.

8 Conclusions

8.1 Summary of Main Results

In this thesis, I have quantified the impact of changes in ocean stratification on the global amplitudes of the primary tidal constituents M_2, S_2, K_1, and O_1, using a global 3D setup of the MITgcm (Marshall et al., 1997). The modeling approach consists of simulations in annual time slices over a nominal time span of 1993–2020. Besides simulations for past decades, the model configuration has also been employed to map tidal changes due to future increases in ocean stratification through to the end of the 21st century. From a technical point of view, the main challenges persist in the requirements on the model's horizontal and vertical resolution, since both oceanic large-scale and small-scale processes need to be resolved at once.

The modeled tidal harmonics have been first subjected to an analysis on interannual time scales. Comparisons with tide gauge time series reveal correlations and show that tidal changes due to strengthened ocean stratification can explain observed amplitude variations to a high degree in certain locations, despite complications due to local (mostly unknown) factors at tide gauges. Secondly, the simulations suggest small yet statistically significant tidal trends, which are largely commensurate with observations by satellite altimetry in the open ocean and tide gauges at the coast. Detailed analyses of the dynamics and energetics of the M_2 tide point to enhanced barotropic-to-baroclinic energy conversion over the analysis time span 1993–2020 as the key process behind most signals seen in the model and observations. The thesis thus highlights the role of ocean stratification changes as the major present-day driver for tidal change in the deep ocean and provides the first global model-based quantification of the impact of changes in the ocean's density structure on both the barotropic and baroclinic surface tide.

The findings of this thesis contribute to a better understanding of the observed worldwide tidal changes and their physical driving mechanisms. The novel insights into the impact of changing ocean stratification on the global tides is scientifically important, for instance, in the context of the global ocean circulation or the processing of space-geodetic satellite data. More generally, better understanding of present-day tidal changes is crucial for accurate future coastal flood risk assessments and efficient use of tides as renewable energy source, and particularly lays the groundwork for more robust and complete projections of tidal changes in the coming decades.

3D Modeling of Tides

The first main objective has been to set up an adequate 3D MITgcm configuration, with the goal to accurately model the global primary tidal constituents (M_2, S_2, K_1, O_1). Therefore, I tested sensitivities of the model setup to different parameters and vertical model domain discretizations, and assessed the realism of the simulated barotropic and baroclinic tides. The key component of the individual time slice simulations, that is, the annually changing density stratification, needs to be included with the aid of a nudging scheme, as there is no external atmosphere forcing to set the stratification and thus the initial density structure has to be maintained during the model run. Moreover, I have adapted the model configuration to run crash-free on a parallel supercomputer.

Upon completion of the runs and subsequent post-processing, the annually modeled tidal harmonics were validated against independent tidal estimates from observations. The validation was conducted separately for the barotropic and the baroclinic tide, split by a specially designed smoothing technique for each tidal constituent. Afterwards, the barotropic tide was validated against the TPXO9 atlas (updated version of Egbert and Erofeeva, 2002), while the baroclinic tide was compared to the internal tide model of Zaron (2019). Both the barotropic and the baroclinic tide were deemed sufficiently accurate in the comparison to observations and literature (Stammer et al., 2014; Jeon et al., 2019), although the MITgcm solutions in shallow water are not as accurate as solutions from one-layer ocean models and typically overestimate tidal amplitudes at the coast.

Present-day Tidal Changes on Interannual Timescales

The modeled interannual variability of the four primary tidal constituents from 1993 to 2020 has been analyzed and compared to observations from tide gauges. In general, the global barotropic M_2 tide is characterized by enhanced variability in shallow waters (e.g., the Indonesian Seas), with year-to-year fluctuations amounting to $\sim$1 % in magnitude of the mean amplitude itself. The M_2 baroclinic (surface) component behaves somewhat differently, as it yields enhanced interannual variability in the deep ocean, especially in the western Pacific. The regions with high interannual baroclinic variability are known hot spots of tidal conversion. The magnitude of the variability of the baroclinic tide is $\sim$10 % of the tidal mean amplitude itself.

Tide gauges are located at coastlines often on wide continental shelves (regions of enhanced interannual variability of the barotropic tide), as well as on small islands (partly regions of enhanced interannual variability of the baroclinic tide). Despite their sparse distribution, regionally coherent agreement between neighboring stations is evident for, e.g., the western Pacific, the coasts of Northwest Australia, or the Gulf of Mexico. The tidal variability in these three regions is correlated with the modeled time series and contains signals from leading natural climate modes (e.g., ENSO), that are present in the ocean's density structure. The agreement between the simulated and observed tidal variability highlights stratification as an important driver for tidal changes at present day. Mapping interannual tidal variability over almost three decades and on a global scale, as done here with a 3D ocean model, has not been achieved before and is therefore a major advance on the specific topic.

Present-day Tidal Trends

Least-squares analysis of the modeled yearly tidal harmonics reveals large-scale statistically significant, linear trends of the barotropic tide in the major ocean basins, particularly for M_2 in the order of $\sim -0.1\,\mathrm{mm\,year^{-1}}$ (1993–2020). The comparison to global and independent trend estimates from satellite altimetry yields agreement in terms of structure and sign of the barotropic trend patterns in the open ocean. Regionally coherent M_2 trends are present in the tropical Indian Ocean, at the US West and East coast, in North Australia, and on the Northwest European Shelf. The barotropic M_2 amplitude is characterized by a widespread decrease due to enhanced energy transfer to the baroclinic tide, which exhibits mainly increasing surface amplitudes in the same time span. The corresponding increase in M_2 conversion of $\sim 0.56\,\%\,\mathrm{decade}^{-1}$ provides a consistent physical explanation for the modeled (and observed) tidal trends. Within this thesis, I have highlighted the role of strengthened ocean stratification on global tidal changes and found that stratification changes are responsible for present-day large-scale trends in the open-ocean, especially for M_2 (Opel et al., 2024). Moreover, the open-ocean tidal trends caused by changing stratification contribute much more to the globally observed tidal changes than present-day relative sea level rise does. To expand the analysis focus from the deep to the shallow ocean, tidal trends have also been estimated from tide gauge time series around the world's coastlines. The analysis in coastal regions is more involved due to the influence of local (usually anthropogenic) factors, but nevertheless reveals spatial coherent trends for individual regions, reflected both in the observed and the modeled trends.

Tidal Changes Toward the End of the 21st Century

Understanding the processes causing past and present-day tidal changes is an essential step toward projecting these changes into the future. With ocean stratification being projected to strengthen further in the future due to climate change, especially in the upper ocean, its role in modulating tides of the future needs to be examined and quantified. From the 3D numerical simulations conducted in this work, stratification-driven changes of the global tides up to the year 2100 are evident from deep to shallow ocean regions, featuring in particular decreasing barotropic amplitudes of semidiurnal constituents. The energy loss of the semi diurnal barotropic tide is accompanied by an increase in tidal conversion and in turn, by an increase of surface signatures of baroclinic tides. The general physical process is consistent with findings at present day (Opel et al., 2024), despite not scaling linearly with time until the end of the 21st century.

Comparisons to tidal changes caused by future sea level rise and ice shelf cavity geometry changes highlight the dependence of the modeled signals on the assumed climate forcing scenario, especially in the case of the latter driver. In the open ocean, the impact of stratification is appreciable and structured mainly along normal mode features (Platzman et al., 1981) for all four simulated constituents. Under the assumption of RCP8.5, stratification is the main driver of tidal open-ocean trends, approximately until the year 2090 where it is surpassed in magnitude by effects of changing ice shelf cavity geometries. Toward shallow ocean regions, the impact of relative sea level rise gains in importance and becomes the main driver for tidal changes in numerous coastal regions. Being highly sensitive to water depth changes, tides in shallow waters respond to sea level rise at relatively small spatial scales. By contrast, coastal tidal impacts due to strengthened stratification and altered ice shelf cavities attain much larger spatial scales and therefore induce regionally coherent amplitude changes. In many locations, the joint effect of all three drivers appears to be large enough ($\gtrsim$ 3–5 cm relative to year-2000 conditions) to warrant consideration in flood risk assessments and related coastal engineering measures. Within this work, the role of future stratification changes on the global tides is revealed for the first time and set into context to the effects of other potential driving mechanisms. Thus, this work contributes fundamentally to a global quantification of what future modifications in surface tidal elevations are to be anticipated, depending on time, location, and expected climate policies.

8.2 Recommendations

This thesis has revealed that strengthening ocean stratification is an important driver in the context of globally changing ocean tides. Despite the advances, several refinements and extensions are worth considering. Below, I provide suggestions to improve both the numerical modeling and data analysis aspects beyond what was presented in this thesis. Benefits would exist, e.g., in geodetic Earth monitoring applications or the prediction of future changes in the ocean state and its impact on society, especially with regard to future flood risk assessment.

Improvement of the Model Setup

Besides the advances in customizing the MITgcm for tidal simulations on the LLC1080 grid, the setup is limited in a few points. The LLC1080 grid spacing in the tropics is about 9 km, which is too coarse by a factor of two for accurate resolution of small-scale tidal phenomena, e.g., the complex baroclinic tide field in the Indonesian Seas (Ray et al., 2005; Robertson and Ffield, 2008). Errors in resolving the full and correct baroclinic tide field could possibly cause feedback errors to the barotropic tide. Another factor that limits the models capability to map the tidal properties is the vertical domain discretization. The vertical spacing of 6 m near the ocean's surface is relatively coarse in comparison to changes in the vertical eddy viscosity profile or very shallow water processes, occurring, e.g., in the German Bight. The vertical spacing can lead to imperfect representation of these processes and overestimation of tidal amplitudes, particularly in shallow waters. Another factor that potentially limits the setup would be the stratification data used as model input, but inaccuracies in these 3D fields are hard to quantify, since suitable validation data are sparse. In general, further tests with different (horizontal and vertical) domain discretization and different stratification data could particularly improve quantification of tidal changes in coastal and shelf areas.

Correction of Residual Sea Level Changes

The correction of residual sea level changes, necessary for the tidal trend estimates, is based on an additional simulation with the MITgcm (cf. Section 4.3.2). It is realized through an adaption of the bathymetry, meaning a change in water depth. In the 3D configuration of the MITgcm, the change in water depth alters the hFacs that are used for discretizing the ocean bottom (cf. Figure 3.1). A change in the discrete hFacs can lead to nonphysical jumps in the bottom discretization, when a critical value is exceeded for, e.g., the minimum height of the hFacs. The opposite effect is also possible, i.e., a change in water depth which is not represented by the hFacs. Such non-physical effects could impact the modeled tide. Especially tidal trends in regions that are sensitive to the correction, like the US East coast, the Amazon shelf, North Australia, or the Celtic and Irish Sea, could reveal differences in the tidal trends. A possibility to overcome such limitations is the estimation of the correction with a barotropic (2D) numerical model. Supplementary simulations (conducted outside this thesis) have revealed that use of a 2D instead of a 3D model for the sea level effect correction can indeed alter the inferred trends in certain regions, e.g., at the European Shelf. Further investigation and modeling work would help clarify which approach is to be preferred for modeling long-term changes in tides with a volume-conserving general circulation model.

Tide Gauge Analysis

Tide gauges represent an important data source for validating the modeled tidal harmonics and their temporal changes, particularly in coastal regions where the uncertainty of satellite altimetry observations strongly increases. Although some regionally coherent results were obtained within this thesis, the sparse global tide gauge network generally limits the identification of a spatially coherent mode of variability. In addition, tide gauge time series are often subject to unknown local factors (like dredging) and contain data gaps, which further complicates the analysis. In the context of a tidal connection to climate modes, detecting the modeled spatial patterns of variability in tide gauge observations would strengthen the case for such a link and provide further insight into the fidelity of the simulations (cf. Section 5.2). Therefore, year-by-year examination of the tide gauge time series at hand and addition of more records, e.g., from efforts of data archeology, would be of importance.

Treatment of Ocean Tides in Satellite Data Processing

The findings of this thesis raise questions as to the current treatment of global ocean tides in the processing of satellite gravimetry, as well as altimetry data. If the aim of the satellite data analysis is to reveal small scale signals of the ocean and its movements, tidal amplitudes and phases should not be assumed as constant and invariable in time. On small scales, tides are definitely far from constant, as I have illustrated on interannual and long-term timescales. Known components of tidal variability need to be corrected to recover and assess non-tidal signals of interest in the ocean or the adjacent land and ice masses. Otherwise the uncorrected tidal variability contributes to the uncertainty and systematic or random errors, particularly in the form of spatio-temporal aliasing.

Tidal Variability in Projections of the Future Ocean State

In projections of future sea level, tides are often assumed to be stationary, or any changes in them are modeled as a function of relative sea level rise alone. The findings of this thesis clearly highlight the importance of variable ocean stratification as a driving mechanism for present-day tidal changes on inter-annual and multi-decadal timescales. In the future, tides are assumed to be altered not only by relative sea level rise and strengthening stratification, but also by changes of Antarctic ice shelf cavity geometries. Which driver dominates the tidal changes depends on location and climate forcing scenario, as discussed through Chapter 7. While increased stratification and thinning ice shelves cause global changes of tides in the open ocean, impacts due to sea level rise are concentrated locally in shallow coastal regions. Therefore, including simulated tidal changes under diverse forcing factors and feeding them into projections of future sea level would increase the realism of such projections and yield useful insight for protecting (populated) coastal areas. Additionally, employing the modeling framework to quantify future changes in the vertical structure of internal tides and diapycnal mixing could provide useful insight into future changes of tidal energy dissipation. As internal tides are essential for sustaining the overturning circulation of the global oceans, modeling their expected changes would help clarify impacts on the future strength of the overturning circulation.

A Least-Squares Adjustment

The basic concept of the least-squares adjustment will be briefly described here and follows Koch (1999). In general, a linear Gauß-Markoff model forms the functional relation, as follows

$$\mathbf{l} + \mathbf{e} = \mathbf{A}\mathbf{x}. \tag{A.1}$$

Here $\mathbf{l}$ are the observations, that can also be described through the unknown parameters $\mathbf{x}$, the design matrix $\mathbf{A}$ and residuals of the observations $\mathbf{e}$. The observational stochastic model

$$\boldsymbol{\Sigma}_{\mathbf{ll}} = \sigma_0 \mathbf{P}^{-1} \tag{A.2}$$

represents the variance-covariance matrix of the observations Σ_{ll} and contains a variance factor σ_0 and the weight matrix $\mathbf{P}$. Through the estimation, the weighted sum of the squared residuals is minimized, which leads to the Best Linear Unbiased Estimator (BLUE)

$$\mathbf{e}^T \mathbf{P} \mathbf{e} \rightarrow minimum. \tag{A.3}$$

Therefore, the normal equations with the normal equation matrix

$$\mathbf{N} = \mathbf{A}^T {\boldsymbol{\Sigma}_{\mathbf{ll}}}^{-1} \mathbf{A} \tag{A.4}$$

and the normal equation vector

$$\mathbf{n} = \mathbf{A}^T {\boldsymbol{\Sigma}_{\mathbf{ll}}}^{-1} \mathbf{l} \tag{A.5}$$

are computed. The unknown parameters $\hat{\mathbf{x}}$ are estimated by solving the linear equation

$$\mathbf{N}\hat{\mathbf{x}} = \mathbf{n} \tag{A.6}$$

The estimated observations are computed as

$$\widetilde{\mathbf{l}} = \mathbf{A}\hat{\mathbf{x}} \tag{A.7}$$

and used to compute the residuals of the observations $\mathbf{e}$

$$\widetilde{\mathbf{e}} = \widetilde{\mathbf{l}} - \mathbf{l}. \tag{A.8}$$

To obtain the variance-covariance matrix of the parameters, the a posteriori variance factor $\widetilde{s}_0^2$ is estimated

$$\widetilde{s}_0^2 = \frac{\mathbf{v}^T \mathbf{P} \mathbf{v}}{n_o - n_p}, \tag{A.9}$$

where n_o is the number of observations and n_p is the number of parameters. Hence, the nominator describes the degrees of freedom of the overdetermined system. As a last step, the variance-covariance matrix $\Sigma_{\widetilde{x}\widetilde{x}}$ of the parameters is derived from

$$\mathbf{\Sigma}_{\widetilde{\mathbf{x}}\widetilde{\mathbf{x}}} = \widetilde{s}_0^2 \mathbf{N}^{-1}. \tag{A.10}$$

B Vertical Discretization of the Model

Table B.1: Layer thickness for vertical discretization of the model.

layer number	ocean depth (m)	layer thickness (m)
1	−6	6
2	−12	6
3	−18	6
4	−24.03	6.03
5	−30.15	6.12
6	−36.45	6.30
7	−43.07	6.62
8	−50.15	7.08
9	−57.87	7.72
10	−66.25	8.38
11	−75.30	9.05
12	−84.98	9.68
13	−95.37	10.39
14	−106.47	11.10
15	−118.36	11.89
16	−131.23	12.87
17	−145.26	14.03
18	−160.69	15.43
19	−177.82	17.13
20	−197.01	19.19
21	−218.5	21.49
22	−242.35	23.85
23	−268.59	26.24
24	−297.19	28.60
25	−328.36	31.17
26	−362.34	33.98
27	−399.38	37.04
28	−439.75	40.37
29	−483.75	44.00
30	−531.71	47.96
31	−583.99	52.28
32	−640.98	56.99
33	−702.81	61.83
34	−769.59	66.78
35	−841.38	71.79
36	−918.20	76.82
37	−999.63	81.43
38	−1085.95	86.32
39	−1177.45	91.50

40	−1273.53	96.08
41	−1373.93	100.40
42	−1479.35	105.42
43	−1592.15	112.80
44	−1716.15	124.00
45	−1859.58	143.43
46	−2031.70	172.12
47	−2239.97	208.27
48	−2484.55	244.58
49	−2770.71	286.16
50	−3096.93	326.22
51	−3462.30	365.37
52	−3864.20	401.90
53	−4298.25	434.05
54	−4754.00	455.75
55	−5218.87	464.87
56	−5690.41	471.54
57	−6165.96	475.50
58	−6645.52	479.56
59	−7129.09	483.57

C Tide Gauges

Table C.1: Secular trends in M_2 amplitude η_{M_2} at GESLA-3 tide gauges used in this work (cf. Section 4.2.1). 68% confidence intervals, time span, and number of full calendar years are also given.

GESLA-3 name	$\dot{\eta}_{M_2}$ (mm year^{-1})		Time span	No. years
aberdeen-abe-gbr-cmems	−0.03	±0.07	1995–2019	19
akune-gs15-jpn-jodc_giaj	−0.67	±0.07	1993–2019	27
alicante_i-ali-esp-da_mm	0.03	±0.01	2001–2018	17
andenes-anx-nor-nhs	0.09	±0.02	1993–2020	28
antofagasta-080a-chl-uhslc	0.10	±0.09	1994–2018	23
apalachicola-8728690-usa-noaa	0.59	±0.09	1993–2020	26
arena_cove-9416841-usa-noaa	−0.08	±0.04	1993–2020	28
argentia-835-can-meds	−0.11	±0.03	1993–2020	23
atlantic_city-8534720-usa-noaa	−0.16	±0.07	1993–2020	25
ballen-bal-dnk-cmems	0.40	±0.10	1994–2020	24
baltra-003b-ecu-uhslc	0.03	±0.07	1993–2018	18
bamfield_bc-8545-can-meds	−0.48	±0.07	1993–2020	28
barcelona-bar-esp-cmems	−0.08	±0.01	1993–2020	24
bermagui-219470-aus-bom	0.11	±0.05	1993–2019	23
bilbao-bil-esp-cmems	0.08	±0.04	1993–2020	28
bob_hall_pier-8775870-usa-noaa	0.03	±0.02	1994–2020	27
bodo-boo-nor-nhs	0.02	±0.03	1993–2020	27
boston-8443970-usa-noaa	0.03	±0.19	1993–2020	28
botany_bay-60390-aus-bom	0.07	±0.07	1993–2019	23
bowen-59320-aus-bom	0.28	±0.09	1993–2019	25
brisbane_bar-59980-aus-bom	0.66	±0.11	1993–2019	26
broome-62650-aus-bom	−0.67	±0.14	1993–2019	27
bundaberg-332a-aus-uhslc	−0.04	±0.08	1993–2018	26
cairns-59060-aus-bom	0.36	±0.15	1993–2019	26
callao-093b-per-uhslc	−0.17	±0.07	1993–2014	19
cape_may-8536110-usa-noaa	−0.33	±0.12	1993–2019	25
cedar_key-8727520-usa-noaa	0.61	±0.27	1993–2020	21
cendering-320a-mys-uhslc	0.11	±0.13	1993–2014	18
ceuta-207a-esp-uhslc	0.12	±0.08	1993–2017	23
cherbourg_60minute-che-fra-cmems	0.45	±0.13	1993–2019	26
christmas-011b-aus-uhslc	0.63	±0.11	1993–2018	19
cocos-171a-aus-uhslc	−0.09	±0.09	1993–2017	22
corpus_cristi_tx-770a-usa-uhslc	−0.02	±0.01	1993–2018	23
coruna-cor-esp-cmems	0.39	±0.11	1993–2020	25
crescent_city-9419750-usa-noaa	−0.04	±0.04	1993–2020	26
cuxhaven-825a-deu-uhslc	−0.92	±0.43	1993–2018	26
darwin-168a-aus-uhslc	−0.42	±0.18	1993–2018	25
degerby-deg-fin-cmems	0.01	±0.01	1993–2018	26
dover-dov-gbr-bodc	1.11	±0.26	1993–2009	14
drogden-dro-dnk-cmems	−0.04	±0.03	1993–2020	22
duck_pier_nc-260a-usa-uhslc	−0.18	±0.05	1993–2018	23
dunkerque_60minute-dun-fra-cmems	−0.01	±0.35	1998–2019	22
dutch_harbor_ak-041b-usa-uhslc	−0.23	±0.04	1993–2018	26
eastport-8410140-usa-noaa	0.41	±0.42	1993–2020	24

esperance-62080-aus-bom	0.02	±0.02	1993–2018	25
exmouth-62435-aus-bom	0.26	±0.11	1998–2017	19
fishguard-fis-gbr-cmems	−0.97	±0.07	1993–2019	19
foglo_degerby-134252-fin-fmi	0.01	±0.01	1993–2020	28
forsmark-for-swe-cmems	0.01	±0.01	1993–2020	28
fort_pulaski-8670870-usa-noaa	−0.16	±0.17	1993–2020	27
galets_60minute-gal-fra-cmems	−0.10	±0.16	1997–2018	19
galveston_pleasure_pier-8771510-usa-noaa	−0.14	±0.08	1993–2010	18
gan-109a-mdv-uhslc	−0.09	±0.04	1993–2018	26
gedser-837a-dnk-uhslc	0.18	±0.08	1993–2012	19
geraldton-62290-aus-bom	0.03	±0.02	1993–2019	26
geting-326a-mys-uhslc	0.49	±0.14	1993–2015	20
grand_isle-8761724-usa-noaa	0.11	±0.02	1993–2020	26
grena-gre-dnk-cmems	−0.34	±0.07	1993–2020	25
hanko_pikku_kolalahti-134253-fin-fmi	0.13	±0.03	1993–2020	28
harstad-har-nor-nhs	0.36	±0.03	1993–2020	27
helgeroa-hro-nor-nhs	0.22	±0.05	1993–2020	28
helsinki-hel-fin-cmems	0.01	±0.01	1993–2018	26
home_island-46280-aus-bom	−0.01	±0.07	1993–2019	24
honiara-56670-slb-bom	−0.11	±0.14	1995–2019	23
honningsvag-hvg-nor-nhs	0.15	±0.09	1993–2020	27
honolulu-1612340-usa-noaa	0.23	±0.16	1993–2020	28
hornbaek-hor-dnk-dmi	0.12	±0.04	1994–2019	24
hosojima-gs02-jpn-jodc_giaj	0.27	±0.15	1993–2019	25
huibertgat-huibgt-nld-rws	−0.82	±0.15	1993–2017	24
humboldt_bay_ca-576a-usa-uhslc	0.00	±0.05	1993–2018	24
ilfracombe-ilf-gbr-cmems	−0.41	±0.22	1993–2018	18
kabelvag-kab-nor-nhs	0.34	±0.04	1993–2020	27
kahului-059a-usa-uhslc	−0.04	±0.07	1993–2018	26
kalixstoron-kal-swe-cmems	0.03	±0.01	1993–2020	27
kanton-013b-kir-uhslc	0.45	±0.08	1993–2018	16
kapingamarangi-029a-fsm-uhslc	−0.01	±0.10	1993–2016	17
karumba-63580-aus-bom	0.26	±0.12	1994–2019	25
kashimako-0101-jpn-jodc_pahb	0.01	±0.10	2001–2019	16
kawaihae-1617433-usa-noaa	0.06	±0.16	1994–2020	23
kelang-140a-mys-uhslc	−0.27	±0.26	1993–2012	16
key_west-8724580-usa-noaa	0.10	±0.02	1993–2020	27
kushimoto-353a-jpn-uhslc	0.17	±0.11	1993–2018	26
kushiro-350a-jpn-uhslc	0.26	±0.03	1993–2018	25
kwajalein-1820000-usa-noaa	−0.19	±0.07	1993–2020	25
la_coruna-830a-esp-uhslc	0.46	±0.14	1993–2016	17
la_jolla-9410230-usa-noaa	0.08	±0.05	1993–2020	27
laspalmas-las-esp-cmems	−0.83	±0.09	1993–2020	23
leconquet_60minute-lec-fra-cmems	−0.53	±0.16	1993–2019	22
lehavre_60minute-leh-fra-cmems	−0.24	±0.21	1994–2019	24
lerwick-293a-gbr-uhslc	0.01	±0.04	1993–2015	16
lessablesdolonne_60minute-les-fra-cmems	−0.45	±0.13	1994–2019	19
lewes-8557380-usa-noaa	−0.39	±0.06	1993–2020	28
lime_tree_bay-9751401-usa-noaa	0.12	±0.04	1994–2020	24
liverpool-liv-gbr-cmems	−0.31	±0.12	1993–2020	15
lobos_de_afuera-084a-per-uhslc	−0.34	±0.13	1993–2016	17
lord_howe_island-57720-aus-bom	−0.39	±0.07	1995–2019	21
los_angeles-9410660-usa-noaa	−0.08	±0.04	1993–2020	28
lowestoft-low-gbr-cmems	−0.07	±0.11	1993–2019	25
lumut-143a-mys-uhslc	−0.21	±0.10	1995–2014	15
manila-370a-phl-uhslc	0.12	±0.07	1993–2014	15
marseille_60minute-mar-fra-cmems	0.20	±0.09	1999–2016	14
marviken-mar-swe-cmems	0.12	±0.03	1993–2018	25
milford-mil-gbr-cmems	−0.27	±0.15	1993–2019	15
miyako-ma09-jpn-jodc_jma	0.04	±0.02	1993–2019	22
mokuoloe-1612480-usa-noaa	−0.40	±0.13	1993–2020	27

monaco_fontvieille-22-fra-refmar	0.08	±0.01	2001–2020	18
murotomisaki-ma37-jpn-jodc_jma	−0.12	±0.04	1993–2019	25
naha-355a-jpn-uhslc	−0.01	±0.06	1993–2018	26
nantucket_ma-743a-usa-uhslc	0.37	±0.11	1993–2018	23
napier-668a-nzl-uhslc	−0.07	±0.09	1993–2018	21
neah_bay-9443090-usa-noaa	−0.24	±0.06	1993–2020	28
newcastle-60310-aus-bom	−0.14	±0.08	1993–2019	27
newhaven-new-gbr-cmems	−0.24	±0.12	1993–2020	22
newlyn_cornwall-294a-gbr-uhslc	−0.22	±0.11	1993–2016	19
nishinoomote-363a-jpn-uhslc	−0.01	±0.06	1993–2018	25
nome-9468756-usa-noaa	−0.28	±0.07	1993–2020	23
north_spit-9418767-usa-noaa	0.03	±0.04	1993–2020	27
noumea-019a-fra-uhslc	0.32	±0.09	1993–2018	24
ny_alesund-nya-nor-nhs	0.07	±0.02	1993–2020	28
nylesund-823a-nor-uhslc	0.12	±0.01	1993–2018	26
odomari-hd20-jpn-jodc_jcg	−0.03	±0.12	1993–2019	24
ofunato-351a-jpn-uhslc	0.02	±0.02	1993–2018	24
okinawa-gs21-jpn-jodc_giaj	0.16	±0.06	1993–2019	27
oskarshamn-osk-swe-cmems	0.05	±0.02	1993–2020	28
panama_city-8729108-usa-noaa	0.13	±0.02	1993–2019	22
papeete-015b-fra-uhslc	0.11	±0.18	1993–2018	24
penang-144a-mys-uhslc	−0.69	±0.19	1994–2014	19
penrhyn-024a-cok-uhslc	0.02	±0.06	1993–2018	23
pensacola-8729840-usa-noaa	−0.16	±0.02	1993–2020	25
pietarsaari-pie-fin-cmems	0.01	±0.01	1993–2018	26
point_reyes-9415020-usa-noaa	−0.13	±0.03	1993–2020	27
pointe_des_galets-110-fra-refmar	−0.06	±0.12	1997–2020	21
port_alma-59690-aus-bom	0.44	±0.11	1993–2019	25
port_hardy_bc-8408-can-meds	−0.60	±0.09	1994–2020	25
port_hedland-169a-aus-uhslc	−0.31	±0.09	1993–2018	25
port_kembla-60420-aus-bom	0.23	±0.07	1993–2019	27
port_louis-103c-mus-uhslc	0.46	±0.17	1993–2018	25
portpatrick-por-gbr-cmems	0.20	±0.06	1993–2020	20
port_san_luis-9412110-usa-noaa	−0.03	±0.03	1993–2020	27
port_tudy-71-fra-refmar	0.30	±0.18	1993–2019	23
portland-8418150-usa-noaa	0.21	±0.21	1994–2020	27
portsmouth-ptm-gbr-bodc	0.09	±0.08	1993–2020	22
porttudy_60minute-por-fra-cmems	0.31	±0.20	1993–2019	23
prudhoe_bay-9497645-usa-noaa	0.08	±0.03	1994–2020	27
queen_charlotte_city-9850-can-meds	−1.20	±0.15	1997–2020	24
rauma-rau-fin-cmems	0.01	±0.01	1993–2018	26
reunion-164a-fra-uhslc	−0.12	±0.15	1997–2018	19
reykjavik-reyk-isl-icg	−0.17	±0.03	1994–2020	26
rikitea-016a-fra-uhslc	−0.34	±0.12	1993–2018	21
ringhals-rin-swe-cmems	0.78	±0.21	1993–2020	24
rockport-8774770-usa-noaa	−0.01	±0.01	1993–2020	26
rodvig-rod-dnk-cmems	−0.00	±0.03	1993–2020	23
rorvik-803a-nor-uhslc	1.67	±0.10	1993–2018	26
roscoff_60minute-ros-fra-cmems	−0.11	±0.11	1993–2019	23
san_juan_pr-245a-usa-uhslc	0.01	±0.06	1993–2018	24
sandy_hook-8531680-usa-noaa	−0.14	±0.07	1993–2020	27
santa_cruz-030a-ecu-uhslc	−0.06	±0.05	1993–2018	24
santa_monica-9410840-usa-noaa	−0.15	±0.04	1995–2020	25
santander-san-esp-cmems	0.06	±0.06	1993–2020	26
sedili-324a-mys-uhslc	−0.29	±0.20	1993–2014	19
shute_harbour-59410-aus-bom	0.44	±0.11	1994–2017	22
sitka-9451600-usa-noaa	−0.14	±0.05	1993–2020	28
skagsudde-2321-swe-smhi	0.09	±0.04	1994–2017	21
skanor-ska-swe-cmems	0.08	±0.04	1993–2020	27
smogen-smo-swe-cmems	0.45	±0.07	1993–2020	28
south_beach-9435380-usa-noaa	−0.27	±0.04	1993–2020	28

spring_bay-61170-aus-bom	−0.64	±0.09	1993–2019	27
springmaid_pier-8661070-usa-noaa	−0.07	±0.07	1993–2020	24
st_helier_jersey-jer-gbr-bodc	−0.91	±0.21	1993–2015	22
st_johns-276b-can-uhslc	−0.15	±0.04	1993–2018	23
st_petersburg-8726520-usa-noaa	0.29	±0.10	1993–2019	27
stavanger-svg-nor-nhs	−0.13	±0.02	1993–2020	28
sthelier-sth-gbr-cmems	−0.59	±0.16	1993–2020	25
syowa_antarctica-127a-ata-uhslc	0.02	±0.06	1993–2015	21
tanjong_pagar-699a-sgp-uhslc	−0.15	±0.13	1993–2018	22
tarifa-tari-esp-ieo	0.17	±0.16	1994–2015	21
tauranga-073a-nzl-uhslc	−0.05	±0.16	1993–2018	21
tenerife-ten-esp-cmems	−0.18	±0.07	1994–2019	25
thevenard-62000-aus-bom	−0.06	±0.04	1993–2018	25
tioman-323a-mys-uhslc	0.15	±0.21	1993–2015	19
tofino_bc-8615-can-meds	−0.27	±0.04	1997–2020	24
tosashimizu-ma39-jpn-jodc_jma	−0.22	±0.05	1993–2019	27
unalaska-9462620-usa-noaa	−0.21	±0.04	1993–2020	25
urangan-59850-aus-bom	0.08	±0.08	1995–2019	21
vaca_key-8723970-usa-noaa	0.45	±0.12	1994–2020	24
valencia-val-esp-cmems	−0.01	±0.01	1993–2020	26
valparaiso-081a-chl-uhslc	−0.28	±0.14	1993–2018	23
vardo-805a-nor-uhslc	1.47	±0.15	1993–2018	25
venezia-vene-ita-cv	−0.74	±0.05	1993–2020	28
victor_harbor-61490-aus-bom	0.05	±0.03	1993–2019	23
wake_island-1890000-usa-noaa	−0.28	±0.11	1993–2020	26
wallaroo-61780-aus-bom	−0.21	±0.04	1993–2019	24
weymouth-wey-gbr-cmems	−0.13	±0.06	1993–2020	21
whitby-whi-gbr-cmems	−0.13	±0.12	1993–2019	20
wick-wic-gbr-cmems	0.01	±0.05	1993–2019	21
wierumergronden-wiermgdn-nld-rws	−0.66	±0.17	1993–2017	25
winter_harbour_bc-8735-can-meds	−0.45	±0.08	1998–2020	23
wyndham-165a-aus-uhslc	−2.03	±0.59	1994–2018	23
workington-wor-gbr-cmems	0.07	±0.14	1993–2020	21
yakutat-9453220-usa-noaa	−0.06	±0.06	1994–2019	24
zanzibar-151a-tza-uhslc	−0.35	±0.05	1993–2018	22

Table C.2: As Table C.1, but only those tide gauges considered for spatial averaging, see Figure 6.6.

GESLA-3 name	$\dot{\zeta}$ (mm year^{-1})		Time span	No. years
Gulf of Alaska, British Columbia				
dutch_harbor_ak-041b-usa-uhslc	−0.23	±0.04	1993–2018	26
unalaska-9462620-usa-noaa	−0.21	±0.04	1993–2020	25
yakutat-9453220-usa-noaa	−0.06	±0.06	1994–2019	24
sitka-9451600-usa-noaa	−0.14	±0.05	1993–2020	28
queen_charlotte_city-9850-can-meds	−1.20	±0.15	1997–2020	24
port_hardy_bc-8408-can-meds	−0.60	±0.09	1994–2020	25
winter_harbour_bc-8735-can-meds	−0.45	±0.08	1998–2020	23
tofino_bc-8615-can-meds	−0.27	±0.04	1997–2020	24
bamfield_bc-8545-can-meds	−0.48	±0.07	1993–2020	28
neah_bay-9443090-usa-noaa	−0.24	±0.06	1993–2020	28
US West Coast				
arena_cove-9416841-usa-noaa	−0.08	±0.04	1993–2020	28
crescent_city-9419750-usa-noaa	−0.04	±0.04	1993–2020	26
humboldt_bay_ca-576a-usa-uhslc	0.00	±0.05	1993–2018	24
la_jolla-9410230-usa-noaa	0.08	±0.05	1993–2020	27
los_angeles-9410660-usa-noaa	−0.08	±0.04	1993–2020	28
north_spit-9418767-usa-noaa	0.03	±0.04	1993–2020	27
point_reyes-9415020-usa-noaa	−0.13	±0.03	1993–2020	27
port_san_luis-9412110-usa-noaa	−0.03	±0.03	1993–2020	27
santa_monica-9410840-usa-noaa	−0.15	±0.04	1995–2020	25
south_beach-9435380-usa-noaa	−0.27	±0.04	1993–2020	28
West Florida Shelf				
apalachicola-8728690-usa-noaa	0.59	±0.09	1993–2020	26
cedar_key-8727520-usa-noaa	0.61	±0.27	1993–2020	21
key_west-8724580-usa-noaa	0.10	±0.02	1993–2020	27
panama_city-8729108-usa-noaa	0.13	±0.02	1993–2019	22
st_petersburg-8726520-usa-noaa	0.29	±0.10	1993–2019	27
vaca_key-8723970-usa-noaa	0.45	±0.12	1994–2020	24
Mid-Atlantic Bight				
atlantic_city-8534720-usa-noaa	−0.16	±0.07	1993–2020	25
cape_may-8536110-usa-noaa	−0.33	±0.12	1993–2019	25
duck_pier_nc-260a-usa-uhslc	−0.18	±0.05	1993–2018	23
lewes-8557380-usa-noaa	−0.39	±0.06	1993–2020	28
sandy_hook-8531680-usa-noaa	−0.14	±0.07	1993–2020	27
springmaid_pier-8661070-usa-noaa	−0.07	±0.07	1993–2020	24
Northwest European Shelf				
cherbourg_60minute-che-fra-cmems	0.45	±0.13	1993–2019	26
leconquet_60minute-lec-fra-cmems	−0.53	±0.16	1993–2019	22
newlyn_cornwall-294a-gbr-uhslc	−0.22	±0.11	1993–2016	19
portsmouth-ptm-gbr-bodc	0.09	±0.08	1993–2020	22
roscoff_60minute-ros-fra-cmems	−0.11	±0.11	1993–2019	23
st_helier_jersey-jer-gbr-bodc	−0.91	±0.21	1993–2015	22
sthelier-sth-gbr-cmems	−0.59	±0.16	1993–2020	25
weymouth-wey-gbr-cmems	−0.13	±0.06	1993–2020	21
workington-wor-gbr-cmems	0.07	±0.14	1993–2020	21
ilfracombe-ilf-gbr-cmems	−0.41	±0.22	1993–2018	18
milford-mil-gbr-cmems	−0.27	±0.15	1993–2019	15
fishguard-fis-gbr-cmems	−0.97	±0.07	1993–2019	19
liverpool-liv-gbr-cmems	−0.31	±0.12	1993–2020	15
portpatrick-por-gbr-cmems	0.20	±0.06	1993–2020	20
German Bight				
cuxhaven-825a-deu-uhslc	−0.92	±0.43	1993–2018	26
huibertgat-huibgt-nld-rws	−0.82	±0.15	1993–2017	24
wierumergronden-wiermgdn-nld-rws	−0.66	±0.17	1993–2017	25

Northwest Australia				
port_hedland-169a-aus-uhslc	−0.31	±0.09	1993–2018	25
broome-62650-aus-bom	−0.67	±0.14	1993–2019	27
wyndham-165a-aus-uhslc	−2.03	±0.59	1994–2018	23
darwin-168a-aus-uhslc	−0.42	±0.18	1993–2018	25
Northeast Australia				
bowen-59320-aus-bom	0.28	±0.09	1993–2019	25
brisbane_bar-59980-aus-bom	0.66	±0.11	1993–2019	26
bundaberg-332a-aus-uhslc	−0.04	±0.08	1993–2018	26
cairns-59060-aus-bom	0.36	±0.15	1993–2019	26
port_alma-59690-aus-bom	0.44	±0.11	1993–2019	25
shute_harbour-59410-aus-bom	0.44	±0.11	1994–2017	22
urangan-59850-aus-bom	0.08	±0.08	1995–2019	21
Southeast Australia, New Zealand				
bermagui-219470-aus-bom	0.11	±0.05	1993–2019	23
botany_bay-60390-aus-bom	0.07	±0.07	1993–2019	23
lord_howe_island-57720-aus-bom	−0.39	±0.07	1995–2019	21
napier-668a-nzl-uhslc	−0.07	±0.09	1993–2018	21
newcastle-60310-aus-bom	−0.14	±0.08	1993–2019	27
port_kembla-60420-aus-bom	0.23	±0.07	1993–2019	27
spring_bay-61170-aus-bom	−0.64	±0.09	1993–2019	27
tauranga-073a-nzl-uhslc	−0.05	±0.16	1993–2018	21
Malaysian West Coast				
kelang-140a-mys-uhslc	−0.27	±0.26	1993–2012	16
lumut-143a-mys-uhslc	−0.21	±0.10	1995–2014	15
penang-144a-mys-uhslc	−0.69	±0.19	1994–2014	19

D Additional Figures

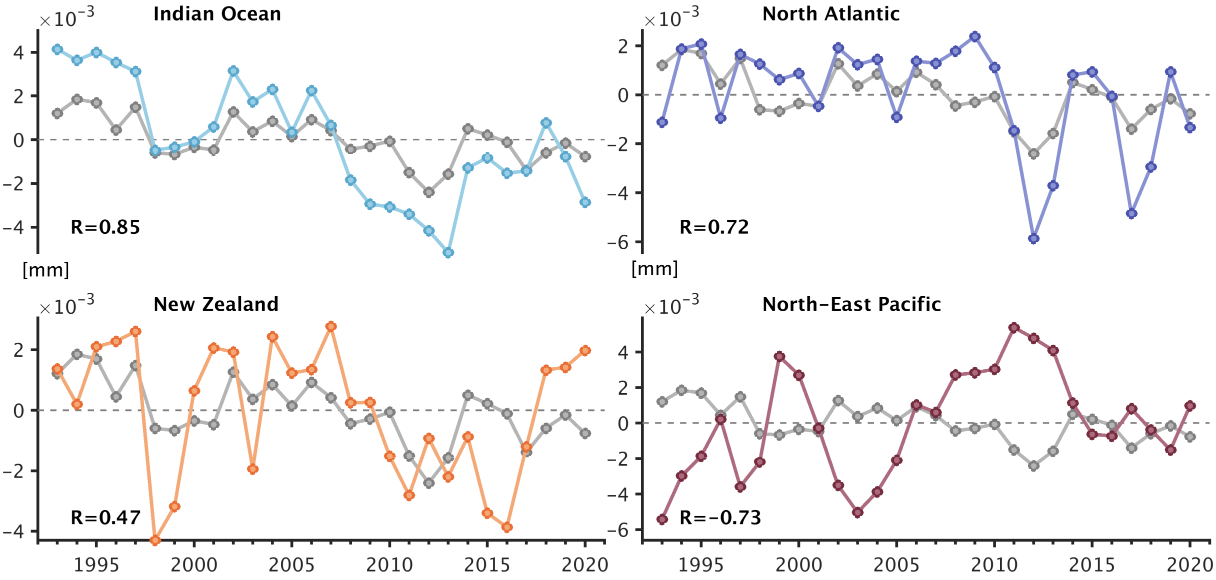

Figure D.1: As in Figure 5.3, but for S_2.

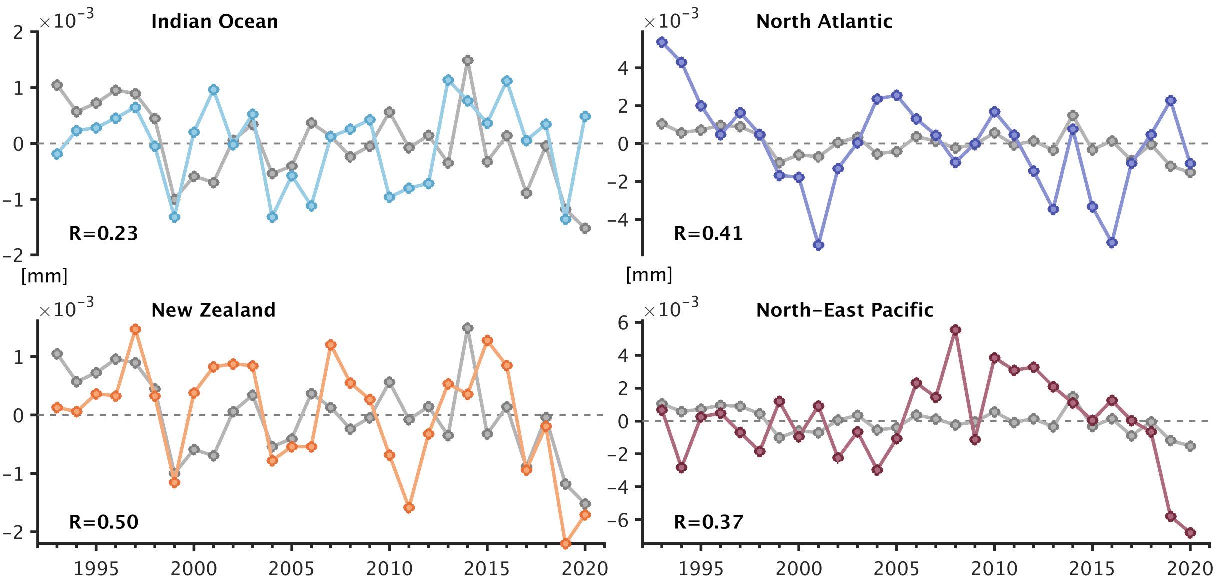

Figure D.2: As in Figure 5.3, but for K_1.

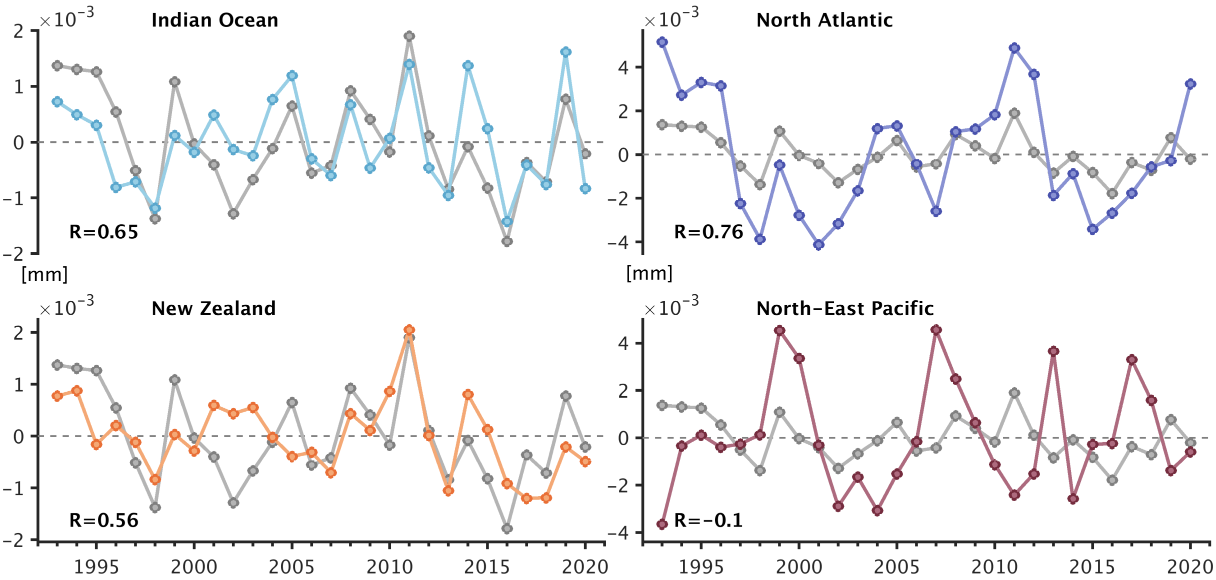

Figure D.3: As in Figure 5.3, but for O_1.

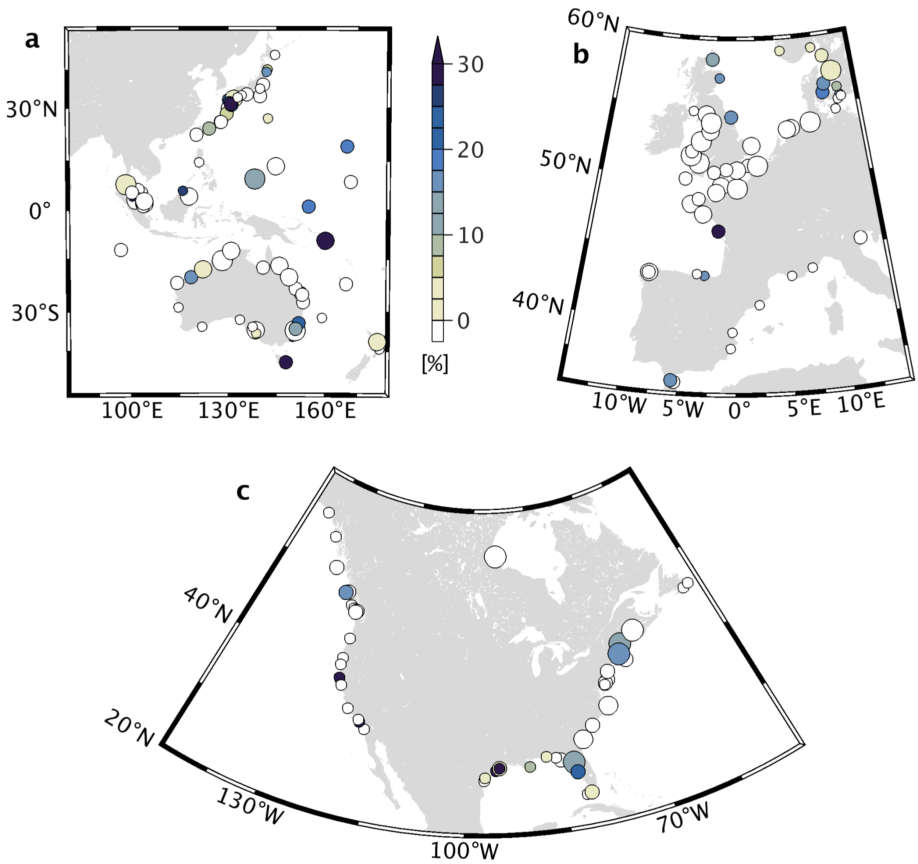

Figure D.4: As Figures 5.4c, 5.5c, and 5.6c, but with the modeled amplitude changes being scaled by the ratio of the observed total M_2 amplitude relative to the simulated total M_2 amplitude.

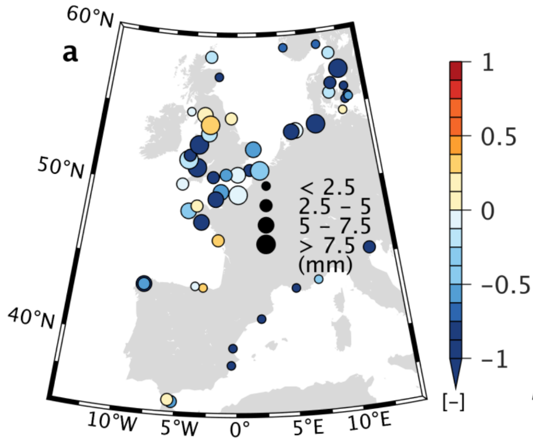

Figure D.5: Observed and modeled M_2 amplitude changes for Europe (1993–2020), compared using the KGE metric. Panel **a** is based on the full surface tide (sum of barotropic and baroclinic tide) and **b** is based on the baroclinic tide. The marker size is related to the standard deviation (mm) of tide gauge observations as explained in the legend in panel **a**.

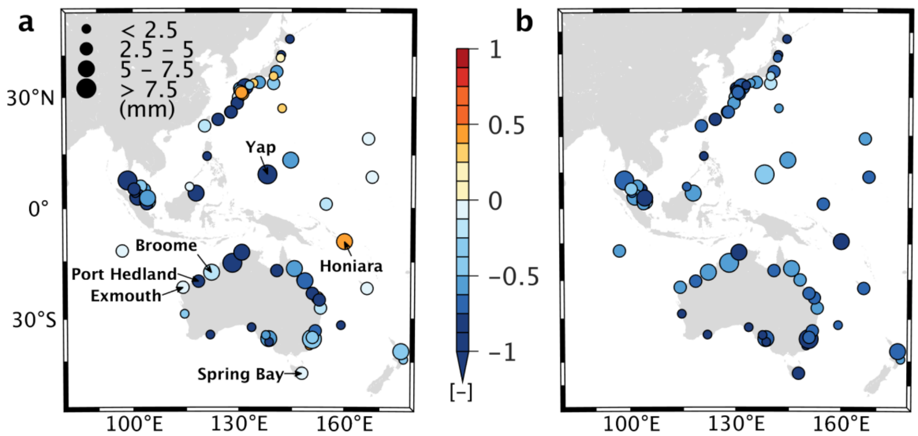

Figure D.6: As Figure D.5, but for the equatorial region of Australia and the Western Pacific.

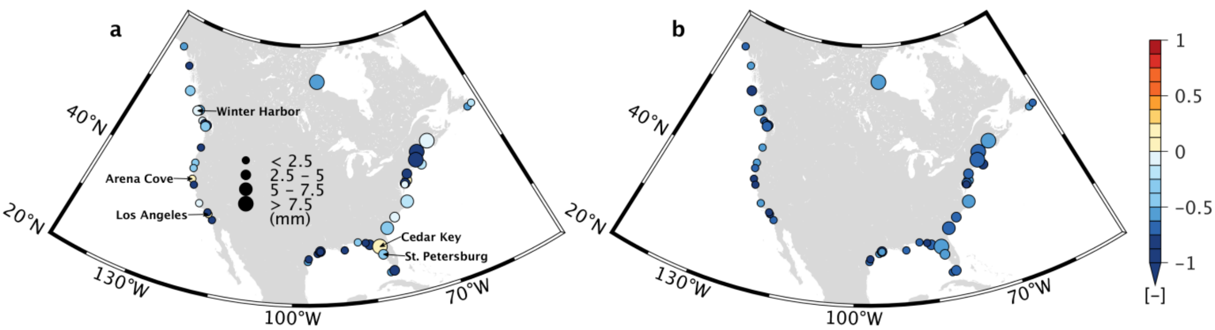

Figure D.7: As Figure D.5, but for both North American coasts.

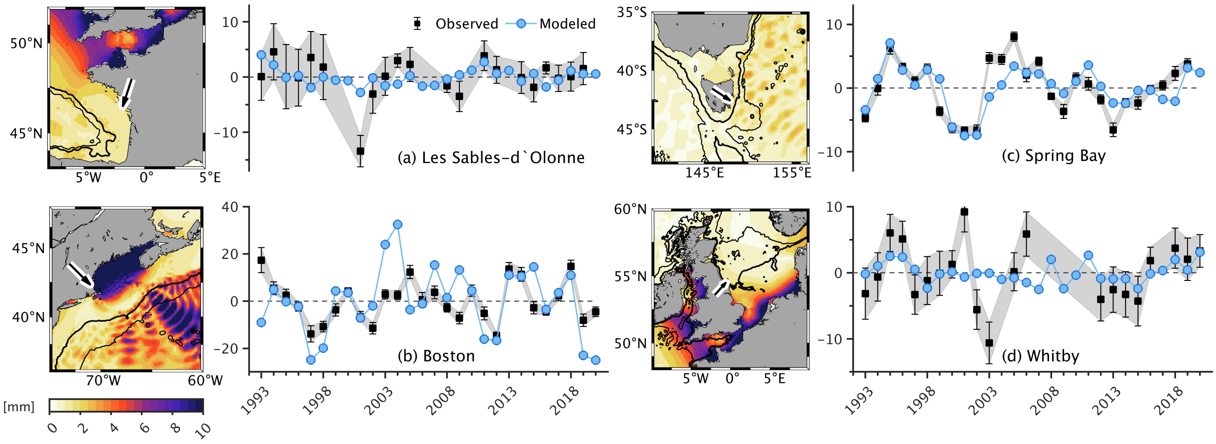

Figure D.8: As in Figure 5.7, but for four different tide gauges. Isobaths are marked as black contours, with thicker lines for shallower water drawn at (a–c) 2000 m and (d) 50 m. Lines correspond to the (a–c) 4000 m and (d) 100 m isobaths.

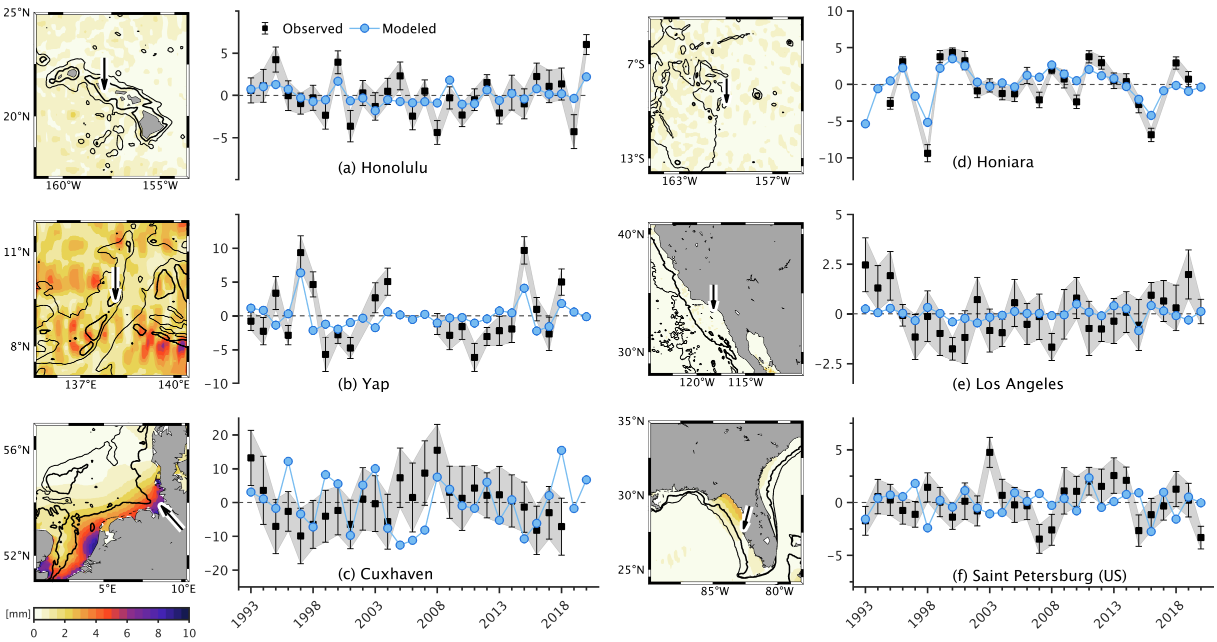

Figure D.9: As in Figure 5.7, but for S_2.

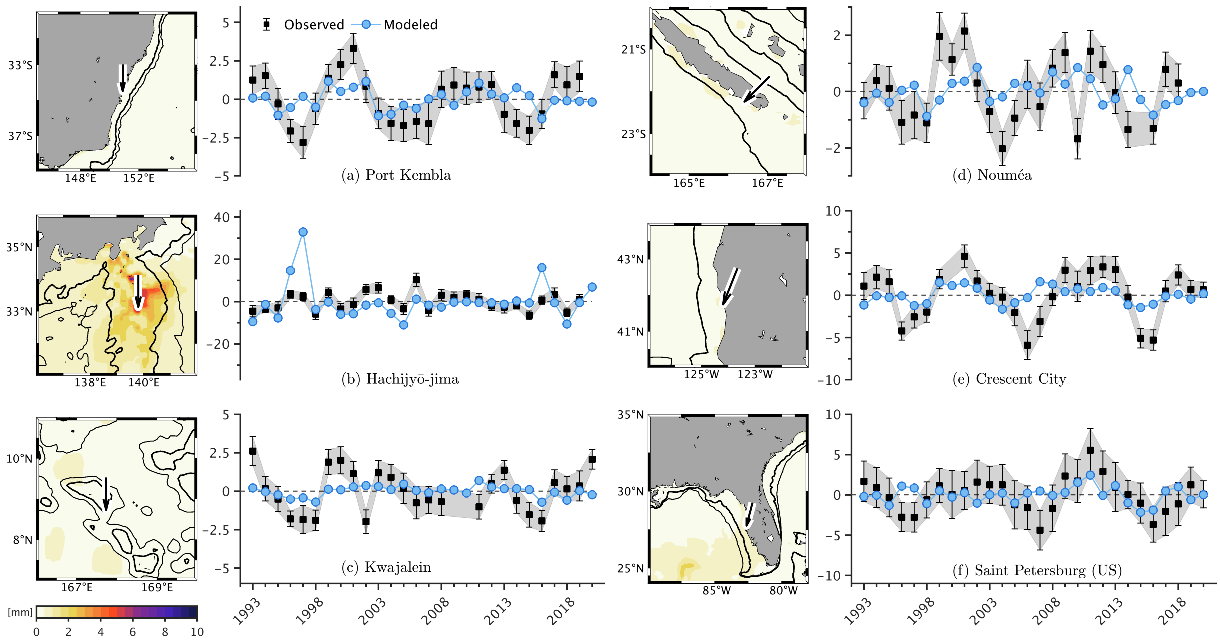

Figure D.10: As in Figure 5.8, but for O_1.

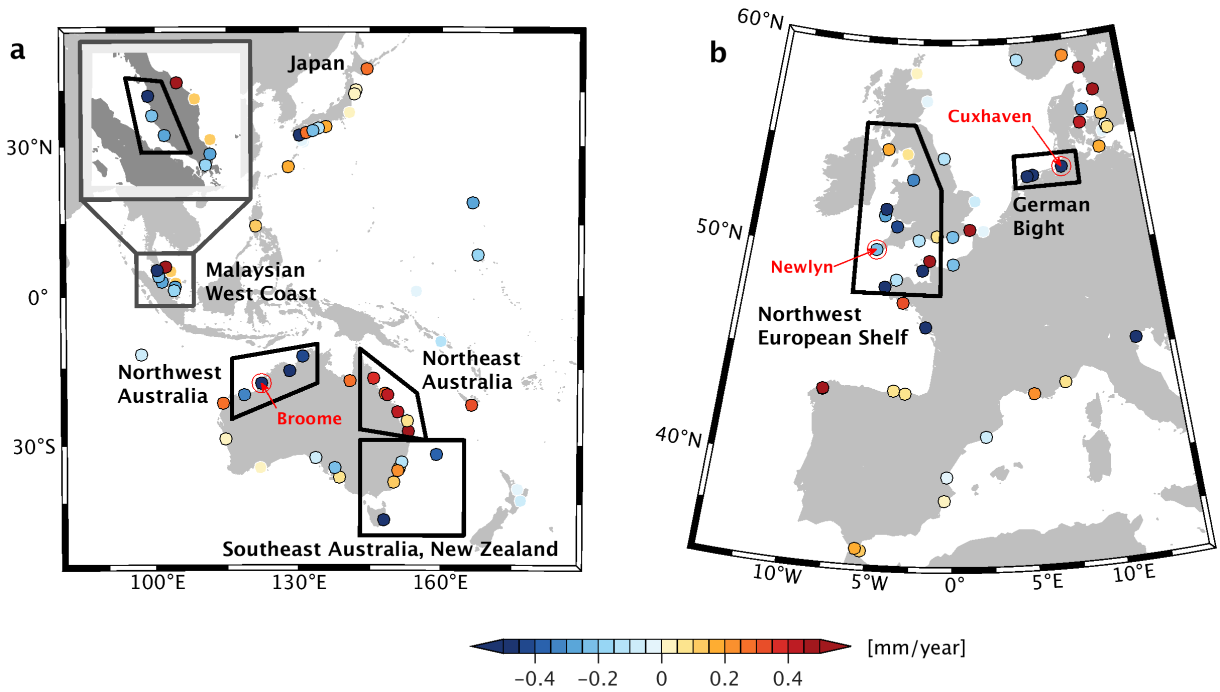

Figure D.11: Tide gauge estimates of M_2 amplitude trends (mm year^{-1}) around Australia/Southeast Asia and Europe. Markers are highlighted with black (or respectively white) edges wherever fitted rates are statistically significant (insignificant) at the 68 % confidence level. Polygons with black outline indicate the averaging regions underlying Figure 6.6. The tide gauge stations from Figure 6.7 are marked in red color.

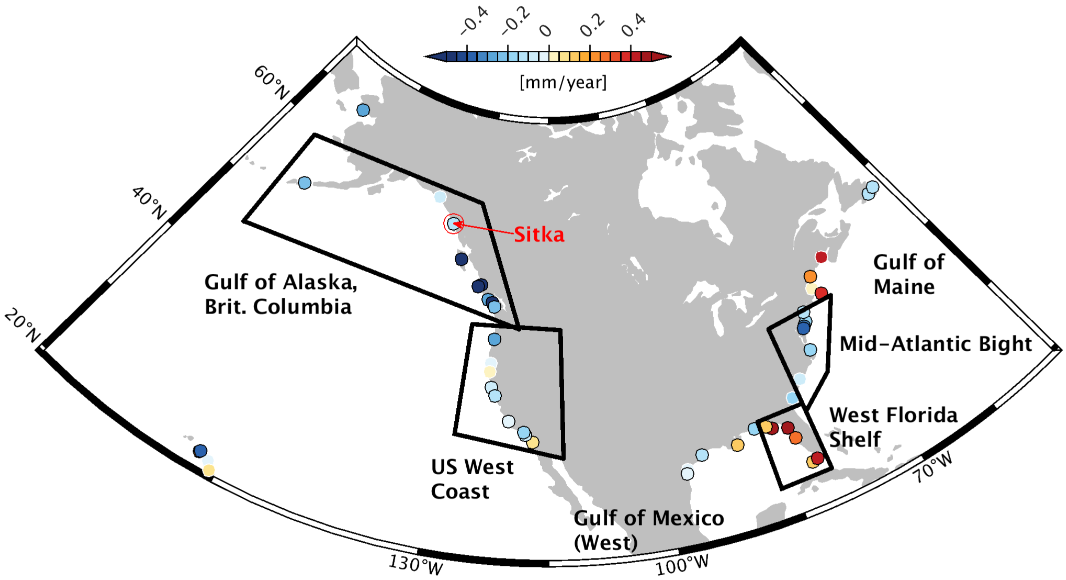

Figure D.12: As in Figure D.11, but for the ocean and marginal seas encasing North America.

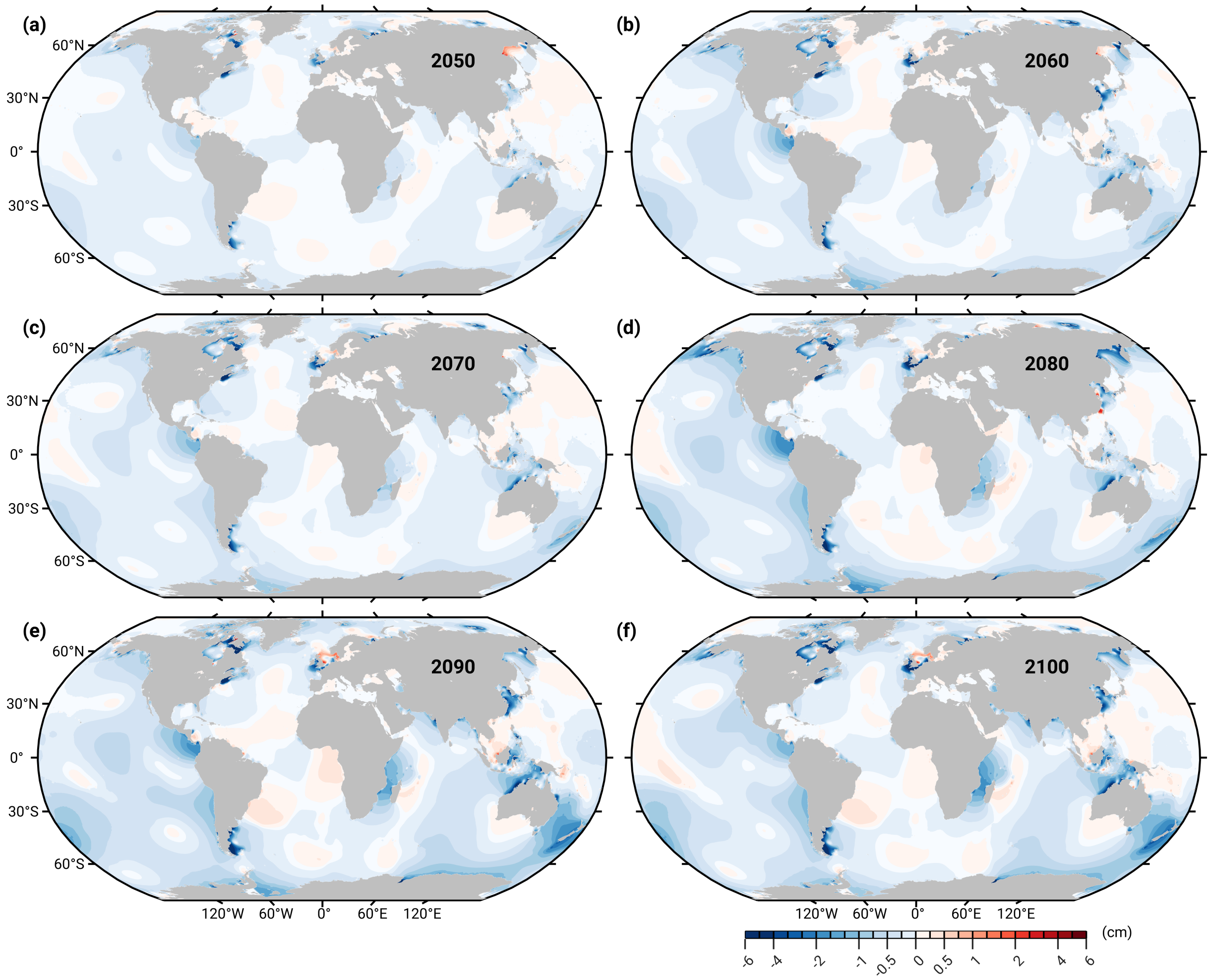

Figure D.13: Simulated barotropic M_2 amplitude changes (cm) over the time period 2050–2100 in response to changes in stratification as given by the EC-Earth3P scenario simulation under RCP8.5. Differences are relative to the year 2000 and shown in decadal steps. Note the non-linear color scale.

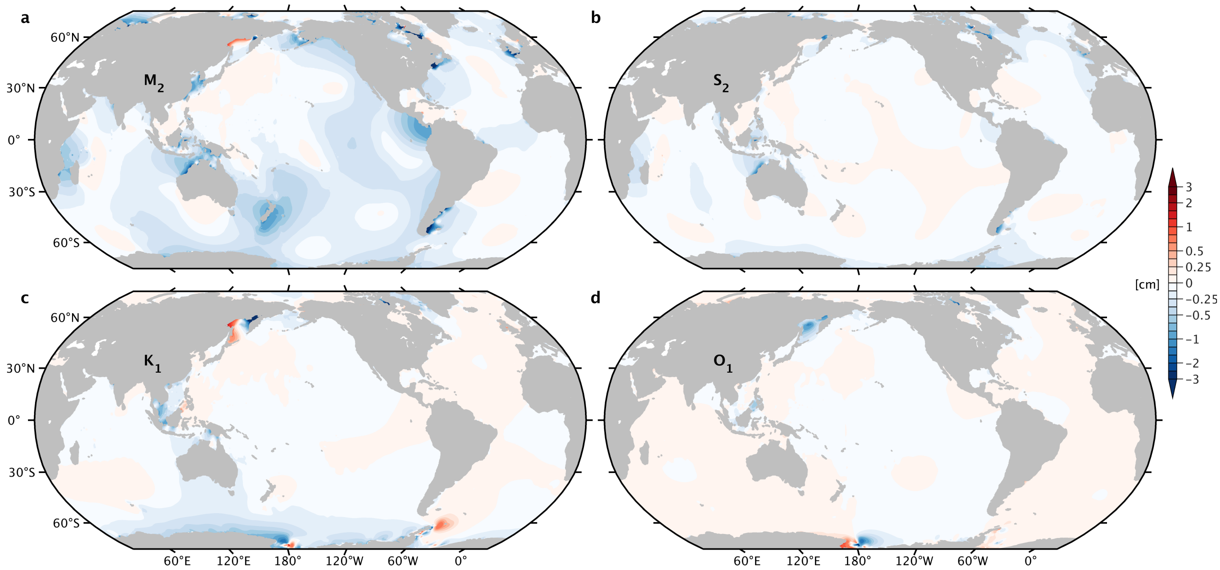

Figure D.14: Amplitude of M_2 **a**, S_2 **b**, K_1 **c** and O_1 **d** in 2100 relative to 2000, scaled to RCP4.5 assumption.

E Glossary

a	Earth radius (m)
d	Declination (°)
$\mathcal{F}$	Forcing term for momentum (kg m s^{-1})
f	Coriolis parameter (rad s^{-1})
G	Universal gravitational constant (m^3 kg^{-1} s^{-2})
g	Gravitational acceleration (m s^{-2})
H	Water depth (m)
k'_n,h'_n	Load Love numbers of degree n (–)
m	Mass of a (celestial) body (kg)
∇_h	Nabla operator in horizontal direction (–)
∇H	Gradients of bathymetry (–)
ω	Angular frequency (rad s^{-1})
R	Pearson correlation coefficient (–)
r	Distance (m)
t	Time (in general)

Ocean Physics

A_h	Horizontal eddy viscosity coefficient (kg m^{-1} s^{-1})
A_z	Vertical eddy viscosity coefficient (kg m^{-1} s^{-1})
$\mathcal{K}_h$	Horizontal eddy diffusion coefficient (m^2 s^{-1})
$\mathcal{K}_z$	Vertical eddy diffusion coefficient (m^2 s^{-1})
N^2	Brunt-Väsälä Frequency (rad^2 s^{-2})
p	Hydrostatic sea pressure (Pa)
ϕ	Potential energy anomaly (J m^{-3})
ρ	In-situ density (kg m^{-3})
ρ_θ	Potential density (kg m^{-3})
S	Ocean practical salinity (PSU)
T	In-situ ocean temperature (°C)
θ	Potential ocean temperature (°C)

Wave Characteristics

c	Propagation speed of a surface shallow water wave (m s^{-1})
L	Wavelength (m)
T	Wave's period (s)
$\mathbf{U} = \begin{bmatrix} U & V & W \end{bmatrix}^T$	Flow velocity (m s^{-1})
u_{max}	Maximum current speed of a wave (m s^{-1})

Ocean Tides

C	Barotropic-to-baroclinic energy conversion rate ($\mathrm{W\,m^{-2}}$)
D	Tidal dissipation rate ($\mathrm{W\,m^{-2}}$)
D^{+}_{nm}	Amplitude of degree-n, order-m prograde components of the ocean tide (m)
η	Tidal ocean surface deflection / Tidal amplitude (m)
η_{EQ}	Free surface height of the equilibrium tide (m)
η_{SAL}	Free surface height of the SAL tide (m)
η'	Surface signal of internal tides (m)
η_{COS}	Tidal cosine amplitude (in-phase, m)
η_{SIN}	Tidal sine amplitude (quadrature, m)
$\mathbf{F}_h$	Horizontal tidal forcing (N)
$\mathbf{P}$	Net input flux of tidal energy ($\mathrm{W\,m^{-1}}$)
Φ	Tidal phase lag (°)
Φ_{EQ}	Equilibrium tidal phase (°)
p_b	Bottom pressure ($\mathrm{m^2\,s^{-2}}$)
$p'_b(z,t)$	Baroclinic bottom pressure anomaly ($\mathrm{m^2\,s^{-2}}$)
ψ^{+}_{nm}	Phase lags of degree-n, order-m prograde components of the ocean tide (°)
$\mathbf{u} = \begin{bmatrix} u & v \end{bmatrix}^T$	Barotropic (depth-averaged) velocity ($\mathrm{m\,s^{-1}}$)
$\mathbf{V}$	Volume transport ($\mathrm{m^3\,s^{-1}}$)
W	Work done by the tide generating force ($\mathrm{W\,m^{-2}}$)

F Acronyms

AMO	Atlantic Multidecadal Oscillation
CMIP6	Coupled Model Intercomparison Project Phase 6 (Haarsma et al., 2016)
DAC	Dyanmic Atmosphere Correction
ENSO	El-Niño Southern Oscillation
EOF	Empirical Orthogonal Function
EQ	Equilibrium Tide
FRIS	Filchner-Ronne Ice Shelf
GESLA-3	Global Extreme Sea level Analysis Version 3 (Haigh et al., 2022; Woodworth et al., 2016; Caldwell et al., 2015)
GIA	Glacial Isostatic Adjustment
GLORYS12V1	Global Ocean Physics Reanalysis Version 1 (Lellouche et al., 2018)
HPC	High Performance Computing
IPCC	Intergovernmental Panel on Climate Change
KGE	Kling-Gupta-Efficiency (Gupta et al., 2009)
KPP	K-Profile-Parameterization (Large et al., 1994)
LAT	Lowest Astronomical Tide
LLC	Latitude–Longitude–Cap grid (see Forget et al., 2015)
MITgcm	Massachusetts Institute of Technology general circulation model (Marshall et al., 1997)
NAO	North Atlantic Oscillation
NOAA	National Oceanic and Atmospheric Administration (US)
RADS	Radar Altimeter Database System (Scharroo et al., 2013)
PC	Principal Component
PDO	Pacific Decadal Oscillation
PVE	Percentage of Variance Explained
RBCS	Restoring Boundary Conditions Package (MITgcm)
RCP	Representative Concentration Pathway
RMS	Root Mean Square
SAL	Self-Attraction and Loading Tide
SLR	Sea Level Rise
SOI	Southern Oscillation Index
SROCC	Specific Report on the Ocean and Cryosphere in a Changing Climate
SSP	Shared Socioeconomic Pathway
SWOT	Surface Water and Ocean Topography (radar altimeter satellite)
TEOS-10	Thermodynamic Equation of Seawater 2010
TGF	Tide Generating Force
TGP	Tide Generating Potential
T/P	Topex/Poseidon (radar altimeter satellite)
TPXO9	Tidal Atlas of Egbert and Erofeeva (2002) (updated version)
WOA	World Ocean Atlas

List of Figures

List of Tables

Bibliography

Adcroft, A. and Campin, J.-M. (2004). Rescaled height coordinates for accurate representation of free-surface flows in ocean circulation models. *Ocean Modelling*, 7(3):269–284.

Adcroft, A., Campin, J.-M., Doddridge, E., Dutkiewicz, S., Evangelinos, C., et al. (2024). MITgcm's user manual. Available at `https://mitgcm.readthedocs.io/en/latest/` (last accessed 28 October 2024).

Adcroft, A., Hill, C., and Marshall, J. (1997). Representation of Topography by Shaved Cells in a Height Coordinate Ocean Model. *Monthly Weather Review*, 125(9):2293–2315.

Albrecht, N., Vennell, R., Williams, M., Stevens, C., Langhorne, P., Leonard, G., and Haskell, T. (2006). Observation of sub-inertial internal tides in McMurdo Sound, Antarctica. *Geophysical Research Letters*, 33(24):L24606.

Alford, M. H. (2003). Redistribution of energy available for ocean mixing by long-range propagation of internal waves. *Nature*, 423(6936):159–162.

Arakawa, A. and Lamb, V. R. (1977). Computational Design of the Basic Dynamical Processes of the UCLA General Circulation Model. In Chang, J., editor, *General Circulation Models of the Atmosphere*, volume 17 of *Methods in Computational Physics: Advances in Research and Applications*, pages 173–265. Elsevier.

Arbic, B. K. (2005). Atmospheric forcing of the oceanic semidiurnal tide. *Geophysical Research Letters*, 32(2):L02610.

Arbic, B. K., Alford, M. H., Ansong, J. K., Buijsman, M. C., Ciotti, R. B., Farrar, J. T., et al. (2018). A Primer On Global Internal Tide And Internal Gravity Wave Continuum Modeling In Hycom And Mitgcm. In Chassignet, E., Pascual, A., Tintoré, J., and Verron, J., editors, *New Frontiers In Operational Oceanography*, Methods in Computational Physics: Advances in Research and Applications, pages 307–392. GODAE OceanView.

Arbic, B. K., Garner, S. T., Hallberg, R. W., and Simmons, H. L. (2004). The accuracy of surface elevations in forward global barotropic and baroclinic tide models. *Deep Sea Research Part II: Topical Studies in Oceanography*, 51(25):3069–3101.

Arbic, B. K. and Garrett, C. (2010). A coupled oscillator model of shelf and ocean tides. *Continental Shelf Research*, 30(6):564–574.

Arbic, B. K., Karsten, R. H., and Garrett, C. (2009a). On tidal resonance in the global ocean and the back-effect of coastal tides upon open-ocean tides. *Atmosphere-Ocean*, 47(4):239–266.

Arbic, B. K., Lyard, F., Ponte, A., Ray, R. D., Richman, J. G., Shriver, J. F., Zaron, E., and Zhao, Z. (2015). Tides and the SWOT mission: Transition from Science Definition Team to Science Team. Technical Report 336, Civil and Environmental Engineering Faculty Publications and Presentations.

Arbic, B. K., Richman, J. G., Shriver, J. F., Timko, P. G., Metzger, E. J., and Wallcraft, A. J. (2012). Global Modeling of Internal Tides: Within an Eddying Ocean General Circulation Model. *Oceanography*, 25(2):20–29.

Arbic, B. K., Shriver, J. F., Hogan, P. J., Hurlburt, H. E., McClean, J. L., Metzger, E. J., et al. (2009b). Estimates of bottom flows and bottom boundary layer dissipation of the oceanic general circulation from global high-resolution models. *Journal of Geophysical Research: Oceans*, 114(C2):C02024.

Arbic, B. K., Wallcraft, A. J., and Metzger, E. J. (2010). Concurrent simulation of the eddying general circulation and tides in a global ocean model. *Ocean Modelling*, 32:175–187.

Arns, A., Wahl, T., Dangendorf, S., and Jensen, J. (2015). The impact of sea level rise on storm surge water levels in the northern part of the German Bight. *Coastal Engineering*, 96:118–131.

Arns, A., Wahl, T., Haigh, I., Jensen, J., and Pattiaratchi, C. (2013). Estimating extreme water level probabilities: A comparison of the direct methods and recommendations for best practise. *Coastal Engineering*, 81:51–66.

Arns, A., Wahl, T., Wolff, C., Vafeidis, A. T., Haigh, I. D., Woodworth, P., et al. (2020). Nonlinear interaction modulates global extreme sea levels, coastal flood exposure, and impacts. *Nature Communications*, 11(1):1918.

Baines, P. (1982). On internal tide generation models. *Deep Sea Research Part A. Oceanographic Research Papers*, 29(3):307–338.

Barbot, S., Lagarde, M., Lyard, F., Marsaleix, P., Lherminier, P., and Jeandel, C. (2022). Internal tides responsible for lithogenic inputs along the Iberian continental slope. *Journal of Geophysical Research: Oceans*, 127(10):e2022JC018816.

Barbot, S., Lyard, F., Tchilibou, M., and Carrere, L. (2021). Background stratification impacts on internal tide generation and abyssal propagation in the western equatorial Atlantic and the Bay of Biscay. *Ocean Science*, 17(6):1563–1583.

Benninghoff, M. and Winter, C. (2019). Recent morphologic evolution of the German Wadden Sea. *Scientific Reports*, 9:9293.

Bij de Vaate, I., Slobbe, D. C., and Verlaan, M. (2022). Secular trends in global tides derived from satellite radar altimetry. *Journal of Geophysical Research: Oceans*, 127(10):e2022JC018845.

Bij de Vaate, I., Vasulkar, A. N., Slobbe, D. C., and Verlaan, M. (2021). The Influence of Arctic Landfast Ice on Seasonal Modulation of the M_2 Tide. *Journal of Geophysical Research: Oceans*, 126(5):e2020JC016630.

Blackledge, B. W., Green, J. A. M., Barnes, R., and Way, M. J. (2020). Tides on Other Earths: Implications for Exoplanet and Palaeo-Tidal Simulations. *Geophysical Research Letters*, 47(12):e2019GL085746.

Blakely, C. P., Ling, G., Pringle, W. J., Contreras, M. T., Wirasaet, D., Westerink, J. J., et al. (2022). Dissipation and Bathymetric Sensitivities in an Unstructured Mesh Global Tidal Model. *Journal of Geophysical Research: Oceans*, 127(5):e2021JC018178.

Buijsman, M. C., Arbic, B. K., Green, J. A. M., Helber, R. W., Richman, J. G., Shriver, J. F., et al. (2015). Optimizing internal wave drag in a forward barotropic model with semidiurnal tides. *Ocean Modelling*, 85:42–55.

Buijsman, M. C., Arbic, B. K., Richman, J. G., Shriver, J. F., Wallcraft, A. J., and Zamudio, L. (2017). Semidiurnal internal tide incoherence in the equatorial Pacific. *Journal of Geophysical Research: Oceans*, 122(7):5286–5305.

Buijsman, M. C., Legg, S., and Klymak, J. (2012). Double-ridge internal tide interference and its effect on dissipation in Luzon Strait. *Journal of Physical Oceanography*, 42(8):1337–1356.

Caldwell, P. C., Merrifield, M. A., and Thompson, P. R. (2015). Sea level measured by tide gauges from global oceans – the Joint Archive for Sea Level holdings (NCEI Accession 0019568), Version 5.5. *NOAA National Centers for Environmental Information.*

Capotondi, A., Alexander, M. A., Bond, N. A., Curchitser, E. N., and Scott, J. D. (2012). Enhanced upper ocean stratification with climate change in the CMIP3 models. *Journal of Geophysical Research: Oceans*, 117(C4):C04031.

Carrère, L., Arbic, B. K., Dushaw, B., Egbert, G., Erofeeva, S., Lyard, F., Ray, R. D., et al. (2021). Accuracy assessment of global internal-tide models using satellite altimetry. *Ocean Science*, 17(1):147–180.

Carrère, L. and Lyard, F. (2003). Modeling the barotropic response of the global ocean to atmospheric wind and pressure forcing – comparisons with observations. *Geophysical Research Letters*, 30(6):1275.

Carter, G. S., Fringer, O. B., and Zaron, E. D. (2012). Regional Models of Internal Tides. *Oceanography*, 25(2):56–65.

Cartwright, D. E. (1999). *Tides: A Scientific History.* Cambridge University Press.

Cartwright, D. E. and Edden, A. C. (1973). Corrected Tables of Tidal Harmonics. *Geophysical Journal International*, 33(3):253–264.

Cartwright, D. E. and Ray, R. D. (1991). Energetics of global ocean tides from Geosat altimetry. *Journal of Geophysical Research: Oceans*, 96(C9):16897–16912.

Challis, J., Idier, D., Wöppelmann, G., and André, G. (2023). Atmospheric Wind and Pressure-Driven Changes in Tidal Characteristics over the Northwestern European Shelf. *Journal of Marine Science and Engineering*, 11(9):1701.

Chen, G., Peng, L., and Ma, C. (2018). Climatology and seasonality of upper ocean salinity: a three-dimensional view from argo floats. *Climate Dynamics*, 50(5):2169–2182.

Cheng, L., von Schuckmann, K., Abraham, J. P., Trenberth, K. E., Mann, M. E., Zanna, L., et al. (2022). Past and future ocean warming. *Nature Reviews Earth & Environment*, 3(11):776–794.

Codiga, D. L. (2011). Unified tidal analysis and prediction using the UTide Matlab functions. Technical Report 2011-01, Graduate School of Oceanography, University of Rhode Island Narragansett, RI.

Colosi, J. A. and Munk, W. (2006). Tales of the Venerable Honolulu Tide Gauge. *Journal of Physical Oceanography*, 36(6):967–996.

Crank, J. and Nicolson, P. (1947). A practical method for numerical evaluation of solutions of partial differential equations of the heat-conduction type. *Mathematical Proceedings of the Cambridge Philosophical Society*, 43(1):50–67.

de Lavergne, C., Vic, C., Madec, G., Roquet, F., Waterhouse, A. F., Whalen, C. B., et al. (2020). A Parameterization of Local and Remote Tidal Mixing. *Journal of Advances in Modeling Earth Systems*, 12(5):e2020MS002065.

Deepa, J. and Gnanaseelan, C. (2021). The decadal sea level variability observed in the Indian Ocean tide gauge records and its association with global climate modes. *Global and Planetary Change*, 198:103427.

Dematteis, G., Le Boyer, A., Pollmann, F., Polzin, K. L., Alford, M. H., Whalen, C. B., and Lvov, Y. V. (2024). Interacting internal waves explain global patterns of interior ocean mixing. *Nature Communications*, 15(1):7468.

Dengler, L. and Uslu, B. (2011). Effects of harbor modification on Crescent City, California's tsunami vulnerability. *Pure and Applied Geophysics*, 168:1175–1185.

Desai, S. D. and Ray, R. D. (2014). Consideration of tidal variations in the geocenter for satellite altimeter observations of ocean tides. *Geophysical Research Letters*, 89:2454–2459.

Devlin, A. T., Jay, D. A., Talke, S. A., and Zaron, E. (2014). Can tidal perturbations associated with sea level variations in the western Pacific Ocean be used to understand future effects of tidal evolution? *Ocean Dynamics*, 64:1093–1120.

Devlin, A. T., Thompson, P. R., Jay, D. A., and Zaron, E. D. (2025). Variable Tidal Amplitude in Hawai'i and the Connection to Pacific Decadal Climate Variability. *Journal of Geophysical Research: Oceans*, 130(2):e2024JC021646.

Devlin, A. T., Zaron, E. D., Jay, D. A., Talke, S. A., and Pan, J. (2018). Seasonality of tides in Southeast Asian waters. *Journal of Physical Oceanography*, 48(5):1169–1190.

Doodson, A. T. and Lamb, H. (1921). The harmonic development of the tide-generating potential. *Proceedings of the Royal Society of London. Series A, Containing Papers of a Mathematical and Physical Character*, 100(704):305–329.

Durran, D. R. (1991). The Third-Order Adams-Bashforth Method: An Attractive Alternative to Leapfrog Time Differencing. *Monthly Weather Review*, 119(3):702–720.

Dushaw, B. D., Howe, B. M., Cornuelle, B. D., Worcester, P. F., and Luther, D. S. (1995). Barotropic and baroclinic tides in the central North Pacific Ocean determined from long-range reciprocal acoustic transmissions. *Journal of Physical Oceanography*, 25:631–647.

Dushaw, B. D. and Menemenlis, D. (2023). Resonant Diurnal Internal Tides in the North Atlantic: 2. Modeling. *Geophysical Research Letters*, 50(3):e2022GL101193.

Egbert, G. D. and Erofeeva, S. Y. (2002). Efficient Inverse Modeling of Barotropic Ocean Tides. *Journal of Atmospheric and Oceanic Technology*, 19(2):183–204.

Egbert, G. D. and Ray, R. D. (2000). Significant dissipation of tidal energy in the deep ocean inferred from satellite altimeter data. *Nature*, 405(6788):775–778.

Egbert, G. D. and Ray, R. D. (2001). Estimates of M_2 tidal energy dissipation from TOPEX/Poseidon altimeter data. *Journal of Geophysical Research: Oceans*, 106(C10):22475–22502.

Egbert, G. D. and Ray, R. D. (2003). Semi-diurnal and diurnal tidal dissipation from TOPEX/Poseidon altimetry. *Geophysical Research Letters*, 30(17):1907.

Egbert, G. D., Ray, R. D., and Bills, B. G. (2004). Numerical modeling of the global semidiurnal tide in the present day and in the last glacial maximum. *Journal of Geophysical Research: Oceans*, 109(C3):C03003.

Einšpigel, D. and Martinec, Z. (2017). Time-domain modeling of global ocean tides generated by the full lunisolar potential. *Ocean Dynamics*, 67:165–189.

Eyring, V., Bony, S., Meehl, G. A., Senior, C. A., Stevens, B., Stouffer, R. J., and Taylor, K. E. (2016). Overview of the Coupled Model Intercomparison Project Phase 6 (CMIP6) experimental design and organization. *Geoscientific Model Development*, 9(5):1937–1958.

Falahat, S., Nycander, J., Roquet, F., and Zarroug, M. (2014). Global Calculation of Tidal Energy Conversion into Vertical Normal Modes. *Journal of Physical Oceanography*, 44(12):3225–3244.

Farhat, M., Auclair-Desrotour, P., Boué, G., and Laskar, J. (2022). The resonant tidal evolution of the Earth-Moon distance. *Astronomy & Astrophysics*, 665:L1.

Feistel, R. (2003). A new extended Gibbs thermodynamic potential of seawater. *Progress in Oceanography*, 58(1):43–114.

Feistel, R. (2008). A Gibbs function for seawater thermodynamics for -6 to 80°C and salinity up to 120g/kg. *Deep Sea Research Part I: Oceanographic Research Papers*, 55(12):1639–1671.

Feng, X., Tsimplis, M. N., and Woodworth, P. L. (2015). Nodal variations and long-term changes in the main tides on the coasts of China. *Journal of Geophysical Research: Oceans*, 120(2):1215–1232.

Flechtner, F., Neumayer, K.-H., Dahle, C., Dobslaw, H., Fagiolini, E., Raimondo, J.-C., and Güntner, A. (2016). What can be expected from the GRACE-FO laser ranging interferometer for Earth science applications? *Surveys in Geophysics*, 37:453–470.

Flick, R. E., Murray, J. F., and Ewing, L. C. (2003). Trends in United States tidal datum statistics and tide range. *Journal of Waterway, Port, Coastal, and Ocean Engineering*, 129(4):155–164.

Forget, G., Campin, J.-M., Heimbach, P., Hill, C. N., Ponte, R. M., and Wunsch, C. (2015). ECCO version 4: an integrated framework for non-linear inverse modeling and global ocean state estimation. *Geoscientific Model Development*, 8(10):3071–3104.

Fox-Kemper, B., Hewitt, H. T., Xiao, C., Adalgeirsdóttir, G., Drijfhout, S. S., Edwards, T. L., et al. (2021). Ocean, Cryosphere and Sea Level Change. In Masson-Delmotte, V., Zhai, P., Pirani, A., Connors, S. L., Péan, C., Berger, S., et al., editors, *Climate Change 2021: The Physical Science Basis. Contribution of Working Group I to the Sixth Assessment Report of the Intergovernmental Panel on Climate Change*, pages 1211–1362. Cambridge University Press, Cambridge, United Kingdom and New York, NY, USA.

Fu, L.-L., Pavelsky, T., Cretaux, J.-F., Morrow, R., Farrar, J. T., Vaze, P., et al. (2024). The surface water and ocean topography mission: A breakthrough in radar remote sensing of the ocean and land surface water. *Geophysical Research Letters*, 51(4):e2023GL107652.

Fu, W., Randerson, J. T., and Moore, J. K. (2016). Climate change impacts on net primary production (NPP) and export production (EP) regulated by increasing stratification and phytoplankton community structure in the CMIP5 models. *Biogeosciences*, 13(18):5151–5170.

Garrett, C. (2003). Internal tides and ocean mixing. *Science*, 301(5641):1858–1859.

Gerkema, T., Staquet, C., and Bouruet-Aubertot, P. (2006). Non-linear effects in internal-tide beams, and mixing. *Ocean Modelling*, 12(3):302–318.

Gerkema, T. and van Haren, H. (2007). Internal tides and energy fluxes over Great Meteor Seamount. *Ocean Science*, 3(3):441–449.

Golledge, N. R., Keller, E. D., Gomez, N., Naughten, K. A., Bernales, J., Trusel, L. D., and Edwards, T. L. (2019). Global environmental consequences of twenty-first-century ice-sheet melt. *Nature*, 566:65–72.

Gong, Y., Chen, Z., Xu, J., Yao, Y., Wang, C., and Cai, S. (2025). Accelerated internal tides in a warming climate. *Science Advances*, 11(8):eadq4577.

Greatbatch, R. J. (1994). A note on the representation of steric sea level in models that conserve volume rather than mass. *Journal of Geophysical Research: Oceans*, 99(C6):12767–12771.

Green, J. A. M. (2010). Ocean tides and resonance. *Ocean Dynamics*, 60(5):1243–1253.

Green, J. A. M. and Nycander, J. (2013). A Comparison of Tidal Conversion Parameterizations for Tidal Models. *Journal of Physical Oceanography*, 43(1):104–119.

Greenberg, D. A., Blanchard, W., Smith, B., and Barrow, E. (2012). Climate Change, Mean Sea Level and High Tides in the Bay of Fundy. *Atmosphere-Ocean*, 50(3):261–276.

Guo, Z., Wang, S., Cao, A., Chen, X., Song, J., and Guo, X. (2024). Variability of the M_2 internal tides in the Luzon Strait under climate change. *Climate Dynamics*, 62(6):5019–5028.

Gupta, H. V., Kling, H., Yilmaz, K. K., and Martinez, G. F. (2009). Decomposition of the mean squared error and NSE performance criteria: Implications for improving hydrological modelling. *Journal of Hydrology*, 377(1):80–91.

Haarsma, R. J., Acosta, M., Bakhshi, R., Bretonnière, P.-A., Caron, L.-P., Castrillo, M., et al. (2020). HighResMIP versions of EC-Earth: EC-Earth3P and EC-Earth3P-HR – description, model computational performance and basic validation. *Geoscientific Model Development*, 13(8):3507–3527.

Haarsma, R. J., Roberts, M. J., Vidale, P. L., Senior, C. A., Bellucci, A., Bao, Q., et al. (2016). High Resolution Model Intercomparison Project (HighResMIP v1.0) for CMIP6. *Geoscientific Model Development*, 9(11):4185–4208.

Haigh, I. D., Marcos, M., Talke, S. A., Woodworth, P. L., Hunter, J. R., Hague, B. S., et al. (2022). GESLA Version 3: A major update to the global higher-frequency sea-level dataset. *Geoscience Data Journal*, 00:1–22.

Haigh, I. D., Pickering, M. D., Green, J. A. M., Arbic, B. K., Arns, A., Dangendorf, S., et al. (2020). The Tides They Are A-Changin': A Comprehensive Review of Past and Future Nonastronomical Changes in Tides, Their Driving Mechanisms, and Future Implications. *Reviews of Geophysics*, 58(1):e2018RG000636.

Hartmann, T. and Wenzel, H.-G. (1995). The HW95 tidal potential catalogue. *Geophysical Research Letters*, 22(24):3553–3556.

He, R. and Weisberg, R. H. (2002). Tides on the West Florida Shelf. *Journal of Physical Oceanography*, 32(12):3455–3473.

Hendershott, M. C. (1972). The Effects of Solid Earth Deformation on Global Ocean Tides. *Geophysical Journal International*, 29(4):389–402.

Hurrell, J. W., Kushnir, Y., Ottersen, G., and Visbeck, M. (2003). An overview of the North Atlantic oscillation. *Geophysical Monograph-American Geophysical Union*, 134:1–36.

Hurrell, J. W., Phillips, A., and National Center for Atmospheric Research Staff (Eds) (2018). The Climate Data Guide: Hurrell North Atlantic Oscillation (NAO) Index (PC-based). `https://climatedataguide.ucar.edu/climate-data/hurrell-north-atlantic-oscillation-nao-index-pc-based`. last access: 31-07-2024.

Huss, M. and Hock, R. (2015). A new model for global glacier change and sea-level rise. *Frontiers in Earth Science*, 3:54.

Idier, D., Paris, F., Le Cozannet, G., Boulahya, F., and Dumas, F. (2017). Sea-level rise impacts on the tides of the European Shelf. *Continental Shelf Research*, 137:56–71.

Jackson, L. P. and Jevrejeva, S. (2016). A probabilistic approach to 21st century regional sea-level projections using RCP and high-end scenarios. *Global Planetary Change*, 146:179–189.

Jan, S., Chern, C.-S., Wang, J., and Chao, S.-Y. (2007). Generation of diurnal K_1 internal tide in the Luzon Strait and its influence on surface tide in the South China Sea. *Journal of Geophysical Research: Oceans*, 112(C6):C06019.

Japan Meteorological Agency (2024). PDO index. `https://ds.data.jma.go.jp/tcc/tcc/products/elnino/decadal/pdo.html`. last access: 26-06-2024.

Jay, D. A. (2009). Evolution of tidal amplitudes in the eastern Pacific Ocean. *Geophysical Research Letters*, 36(4).

Jeon, C.-H., Buijsman, M. C., Wallcraft, A. J., Shriver, J. F., Arbic, B. K., Richman, J. G., and Hogan, P. J. (2019). Improving surface tidal accuracy through two-way nesting in a global ocean model. *Ocean Modelling*, 137:98–113.

Jiang, L., Lu, X., Xu, W., Yao, P., and Cheng, X. (2022). Uncertainties associated with simulating regional sea surface height and tides: A case study of the East China seas. *Frontiers in Marine Science*, 9.

Jithin, A. K., Francis, P. A., Unnikrishnan, A. S., and Ramakrishna, S. S. V. S. (2020a). Energetics and spatio-temporal variability of semidiurnal internal tides in the Bay of Bengal and Andaman Sea. *Progress in Oceanography*, 189:102444.

Jithin, A. K., Subeesh, M. P., Francis, P. A., and Ramakrishna, S. S. V. S. (2020b). Intensification of tidally generated internal waves in the north-central Bay of Bengal. *Scientific Reports*, 10(1):6059.

Jo, A. R., Lee, J.-Y., Timmermann, A., Jin, F.-F., Yamaguchi, R., and Gallego, A. (2022). Future amplification of sea surface temperature seasonality due to enhanced ocean stratification. *Geophysical Research Letters*, 49(9):e2022GL098607.

Jutras, M., Dufour, C. O., Mucci, A., and Talbot, L. C. (2023). Large-scale control of the retroflection of the Labrador Current. *Nature Communications*, 14(1):2623.

Jänicke, L., Ebener, A., Dangendorf, S., Arns, A., Schindelegger, M., Niehüser, S., et al. (2021). Assessment of Tidal Range Changes in the North Sea From 1958 to 2014. *Journal of Geophysical Research: Oceans*, 126(1):e2020JC016456.

Kang, S. K., Foreman, M. G. G., Lie, H.-J., Lee, J.-H., Cherniawsky, J., and Yum, K.-D. (2002). Two-layer tidal modeling of the Yellow and East China Seas with application to seasonal variability of the M_2 tide. *Journal of Geophysical Research: Oceans*, 107(C3):6–1–6–18.

Katavouta, A., Thompson, K. R., Lu, Y., and Loder, J. W. (2016). Interaction between the tidal and seasonal variability of the Gulf of Maine and Scotian Shelf region. *Journal of Physical Oceanography*, 46(11):3279–3298.

Kemp, A. C., Hill, T. D., Vane, C. H., Cahill, N., Orton, P. M., Talke, S. A., et al. (2017). Relative sea-level trends in New York City during the past 1500 years. *The Holocene*, 27(8):1169–1186.

Kerry, C. G., Powell, B. S., and Carter, G. S. (2014). The impact of subtidal circulation on internal tide generation and propagation in the Philippine Sea. *Journal of Physical Oceanography*, 44(5):1386–1405.

Knauss, J. A. and Garfield, N. (2016). *Introduction to Physical Osceanography*. Waveland Press, Inc.

Koch, I., Duwe, M., and Flury, J. (2024). Residual and Unmodeled Ocean Tide Signal From 20+ Years of GRACE and GRACE-FO Global Gravity Field Models. *Journal of Geophysical Research: Solid Earth*, 129(9):e2024JB029345.

Koch, K.-R. (1999). *Parameter Estimation and Hypothesis Testing in Linear Models*. Springer Berlin, Heidelberg, 2 edition.

Kodaira, T., Bernier, N., and Thompson, K. R. (2019). Application of the spectral nudging on global tides towards a global total water level prediction system. *Proceedings of the ASME 2019 38th International Conference on Ocean, Offshore and Arctic Engineering - OMAE*, 9:V009T13A011.

Kopp, R. E., Gilmore, E. A., Little, C. M., Lorenzo-Trueba, J., Ramenzoni, V. C., and Sweet, W. V. (2019). Usable science for managing the risks of sea-level rise. *Earth's Future*, 7(12):1235–1269.

Large, W. G., McWilliams, J. C., and Doney, S. C. (1994). Oceanic vertical mixing: A review and a model with a nonlocal boundary layer parameterization. *Reviews of Geophysics*, 32(4):363–403.

Lau, H. C. and Schindelegger, M. (2023). Chapter 15 — Solid Earth tides. In Green, M. and Duarte, J. C., editors, *A Journey Through Tides*, pages 365–387. Elsevier.

Leith, C. E. (1996). Stochastic models of chaotic systems. *Physica D: Nonlinear Phenomena*, 98(2):481–491.

Lellouche, J.-M., Greiner, E., Bourdallé-Badie, R., Garric, G., Melet, A., Drévillon, M., et al. (2021). The Copernicus Global 1/12° Oceanic and Sea Ice GLORYS12 Reanalysis. *Frontiers in Earth Science*, 9.

Lellouche, J.-M., Greiner, E., Le Galloudec, O., Garric, G., Regnier, C., Drevillon, M., et al. (2018). Recent updates to the Copernicus Marine Service global ocean monitoring and forecasting real-time 1/12° high-resolution system. *Ocean Science*, 14(5):1093–1126.

Li, G., Cheng, L., Zhu, J., Trenberth, K. E., Mann, M. E., and Abraham, J. P. (2020). Increasing ocean stratification over the past half-century. *Nature Climate Change*, 10:1116–1123.

Li, Z., von Storch, J.-S., and Müller, M. (2017). The K_1 internal tide simulated by a 1/10° OGCM. *Ocean Modelling*, 113:145–156.

Liu, Y., Cheng, L., Pan, Y., Abraham, J., Zhang, B., Zhu, J., and Song, J. (2022a). Climatological seasonal variation of the upper ocean salinity. *International Journal of Climatology*, 42(6):3477–3498.

Liu, Z., Zhang, W. G., and Helfrich, K. R. (2022b). Vertical Structure of Barotropic-to-Baroclinic Tidal Energy Conversion on a Continental Slope. *Journal of Geophysical Research: Oceans*, 127(9):e2022JC019130.

Mantua, N. J., Hare, S. R., Zhang, Y., Wallace, J. M., and Francis, R. C. (1997). A Pacific Interdecadal Climate Oscillation with Impacts on Salmon Production. *Bulletin of the American Meteorological Society*, 78(6):1069–1080.

Marshall, J., Adcroft, A., Hill, C., Perelman, L., and Heisey, C. (1997). A finite-volume, incompressible Navier Stokes model for studies of the ocean on parallel computers. *Journal of Geophysical Research: Oceans*, 102(C3):5753–5766.

Mawdsley, R. J., Haigh, I. D., and Wells, N. C. (2014). Global changes in mean tidal high water, low water and range. *Journal of Coastal Research*, (70):343–348.

Mawdsley, R. J., Haigh, I. D., and Wells, N. C. (2015). Global secular changes in different tidal high water, low water and range levels. *Earth's Future*, 3(2):66–81.

McPhaden, M. (2015). Playing hide and seek with El Niño. *Nature Climate Change*, 5(9):791–795.

Millero, F. J., Feistel, R., Wright, D. G., and McDougall, T. J. (2008). The composition of Standard Seawater and the definition of the Reference-Composition Salinity Scale. *Deep Sea Research Part I: Oceanographic Research Papers*, 55(1):50–72.

Morrow, R., Fu, L.-L., Rio, M.-H., Ray, R., Prandi, P., Le Traon, P.-Y., and Benveniste, J. (2023). Ocean circulation from space. *Surveys in Geophysics*, 44(5):1243–1286.

Munk, W. H. (1966). Abyssal recipes. *Deep Sea Research and Oceanographic Abstracts*, 13(4):707–730.

Munk, W. H. (1981). Internal waves and small-scale processes. *Evolution of physical oceanography.*

Munk, W. H. and MacDonald, G. J. F. (1960). Continentality and the gravitational field of the Earth. *Journal of Geophysical Research (1896–1977)*, 65(7):2169–2172.

Munk, W. H. and Wunsch, C. (1998). Abyssal recipes II: energetics of tidal and wind mixing. *Deep Sea Research Part I: Oceanographic Research Papers*, 45(12):1977–2010.

Müller, M. (2011). Rapid change in semi-diurnal tides in the North Atlantic since 1980. *Geophysical Research Letters*, 38(11):L11602.

Müller, M. (2012). The influence of changing stratification conditions on barotropic tidal transport and its implications for seasonal and secular changes of tides. *Continental Shelf Research*, 47:107–118.

Müller, M. (2013). On the space- and time-dependence of barotropic-to-baroclinic tidal energy conversion. *Ocean Modelling*, 72:242–252.

Müller, M., Arbic, B. K., and Mitrovica, J. X. (2011). Secular trends in ocean tides: Observations and model results. *Journal of Geophysical Research: Oceans*, 116:C05013.

Müller, M., Cherniawsky, J. Y., Foreman, M. G. G., and von Storch, J.-S. (2012). Global M_2 internal tide and its seasonal variability from high resolution ocean circulation and tide modeling. *Geophysical Research Letters*, 39(19):L19607.

Müller, M., Cherniawsky, J. Y., Foreman, M. G. G., and von Storch, J.-S. (2014). Seasonal variation of the M_2 tide. *Ocean Dynamics*, 64:159–177.

Nash, J. D., Alford, M. H., and Kunze, E. (2005). Estimating Internal Wave Energy Fluxes in the Ocean. *Journal of Atmospheric and Oceanic Technology*, 22(10):1551–1570.

NOAA (2024a). ENSO index. `https://psl.noaa.gov/data/correlation/oni.data0`. last access: 26-07-2024.

NOAA (2024b). NAO index. `https://www.ncei.noaa.gov/access/monitoring/nao/`. last access: 31-07-2024.

Nycander, J. (2005). Generation of internal waves in the deep ocean by tides. *Journal of Geophysical Research: Oceans*, 110(C10):C10028.

O'Neill, B. C., Tebaldi, C., Van Vuuren, D. P., Eyring, V., Friedlingstein, P., et al. (2016). The Scenario Model Intercomparison Project (ScenarioMIP) for CMIP6. *Geoscientific Model Development*, 9(9):3461–3482.

Opel, L., Schindelegger, M., MacPherson, L. R., Vafeidis, A. T., Green, J. A. M., Rietbroek, R., et al. (2025). Three Drivers of 21st-Century Changes in Ocean Tides. *ESS Open Archive*. April 14, 2025. DOI: 10.22541/essoar.174461421.17562797/v1.

Opel, L., Schindelegger, M., and Ray, R. D. (2024). A likely role for stratification in long-term changes of the global ocean tides. *Communications Earth & Environment*, 5(1):261.

Pan, H., Xu, T., and Wei, Z. (2025). Observing ENSO-modulated tides from space. *Progress in Oceanography*, 231:103410.

Pelling, H. E., Green, J. M., and Ward, S. L. (2013). Modelling tides and sea-level rise: To flood or not to flood. *Ocean Modelling*, 63:21–29.

Pickering, M. D., Horsburgh, K. J., Blundell, J. R., Hirschi, J. J.-M., Nicholls, R. J., Verlaan, M., and Wells, N. C. (2017). The impact of future sea-level rise on the global tides. *Continental Shelf Research*, 142:50–68.

Pickering, M. D., Wells, N. C., Horsburgh, K. J., and Green, J. A. M. (2012). The impact of future sea-level rise on the European Shelf tides. *Continental Shelf Research*, 35:1–15.

Pineau-Guillou, L., Lazure, P., and Wöppelmann, G. (2021). Large-scale changes of the semidiurnal tide along North Atlantic coasts from 1846 to 2018. *Ocean Science*, 17(1):17–34.

Platzman, G. W. (1984). Planetary energy balance for tidal dissipation. *Reviews of Geophysics*, 22(1):73–84.

Platzman, G. W., Curtis, G. A., Hansen, K. S., and Slater, R. D. (1981). Normal modes of the world ocean. Part II: Description of modes in the period range 8 to 80 hours. *Journal of Physical Oceanography*, 11(5):579–603.

Ponte, A. L. and Cornuelle, B. D. (2013). Coastal numerical modelling of tides: Sensitivity to domain size and remotely generated internal tide. *Ocean Modelling*, 62:17–26.

Pugh, D. and Woodworth, P. (2014). *Sea-Level Science — Understanding Tides, Surges, Tsnunamis, Mean Sea-Level Changes*. Cambridge University Press.

Qiu, B., Chen, S., Wang, J., and Fu, L.-L. (2024). Seasonal and Fortnight Variations in Internal Solitary Waves in the Indonesian Seas From the SWOT Measurements. *Journal of Geophysical Research: Oceans*, 129(7):e2024JC021086.

Rainville, L. and Pinkel, R. (2006). Propagation of Low-Mode Internal Waves through the Ocean. *Journal of Physical Oceanography*, 36(6):1220–1236.

Ray, R. D. (1998). Ocean self-attraction and loading in numerical tidal models. *Marine Geodesy*, 21(3):181–192.

Ray, R. D. (2006). Secular changes of the M_2 tide in the Gulf of Maine. *Continental Shelf Research*, 26(3):422–427.

Ray, R. D. (2009). Secular changes in the solar semidiurnal tide of the western North Atlantic Ocean. *Geophysical Research Letters*, 36(19).

Ray, R. D. (2013). Precise comparisons of bottom-pressure and altimetric ocean tides. *Journal of Geophysical Research: Oceans*, 118(9):4570–4584.

Ray, R. D. and Egbert, G. D. (2004). The Global S_1 Tide. *Journal of Physical Oceanography*, 34(8):1922–1935.

Ray, R. D. and Egbert, G. D. (2017). Tides and Satellite Altimetry. In Stammer, D. and Cazenave, A., editors, *Satellite Altimetry Over Oceans and Land Surfaces*, pages 427–458. CRC Press.

Ray, R. D., Egbert, G. D., and Erofeeva, S. Y. (2005). A brief overview of tides in the Indonesian Seas. *Oceanography*, 18(4).

Ray, R. D. and Mitchum, G. T. (1996). Surface manifestation of internal tides generated near Hawaii. *Geophysical Research Letters*, 23:2101–2104.

Ray, R. D. and Mitchum, G. T. (1997). Surface manifestation of internal tides in the deep ocean: Observations from altimetry and island gauges. *Progress in Oceanography*, 40:135–162.

Ray, R. D. and Schindelegger, M. (2025). Trends in the M_2 ocean tide observed by satellite altimetry in the presence of systematic errors. *Journal of Geodesy*, 99(2):11.

Ray, R. D. and Talke, S. A. (2019). Nineteenth-century tides in the Gulf of Maine and implications for secular trends. *Journal of Geophysical Research: Oceans*, 124(10):7046–7067.

Ray, R. D., Widlansky, M. J., Genz, A. S., and Thompson, P. R. (2023). Offsets in tide-gauge reference levels detected by satellite altimetry: ten case studies. *Journal of Geodesy*, 97(12):110.

Rienecker, M. M. and Teubner, M. D. (1980). A note on frictional effects in Taylor's problem. *Journal of Marine Research*, 38(2):183–191.

Robertson, R. and Ffield, A. (2008). Baroclinic tides in the Indonesian seas: Tidal fields and comparisons to observations. *Journal of Geophysical Research: Oceans*, 113(C7).

Rocha, C. B., Gille, S. T., Chereskin, T. K., and Menemenlis, D. (2016). Seasonality of submesoscale dynamics in the Kuroshio Extension. *Geophysical Research Letters*, 43(21):11,304–11,311.

Rose, L., Rohith, B., and Bhaskaran, P. K. (2022). Amplification of regional tides in response to sea level. *Ocean Engineering*, 266:112691.

Rosier, S. H. R., Green, J. A. M., Scourse, J. D., and Winkelmann, R. (2014). Modeling Antarctic tides in response to ice shelf thinning and retreat. *Journal of Geophysical Research: Oceans*, 119:87–97.

Ross, A. C., Najjar, R. G., Li, M., Lee, S. B., Zhang, F., and Liu, W. (2017). Fingerprints of Sea Level Rise on Changing Tides in the Chesapeake and Delaware Bays. *Journal of Geophysical Research: Oceans*, 122(10):8102–8125.

Sallée, J.-B., Pellichero, V., Akhoudas, C., Pauthenet, E., Vignes, L., Schmidtko, S., et al. (2021). Summertime increases in upper-ocean stratification and mixed-layer depth. *Nature*, 591:592–598.

Santamaria-Aguilar, S., Schuerch, M., Vafeidis, A. T., and Carretero, S. C. (2017). Long-term trends and variability of water levels and tides in Buenos Aires and Mar del Plata, Argentina. *Frontiers in Marine Science*, 4.

Savage, A. C., Arbic, B. K., Alford, M. H., Ansong, J. K., Farrar, J. T., Menemenlis, D., et al. (2017). Spectral decomposition of internal gravity wave sea surface height in global models. *Journal of Geophysical Research: Oceans*, 122(10):7803–7821.

Schaffer, J., Timmermann, R., Arndt, J. E., Kristensen, S. S., Mayer, C., Morlighem, M., and Steinhage, D. (2016). A global, high-resolution data set of ice sheet topography, cavity geometry, and ocean bathymetry. *Earth System Science Data*, 8(2):543–557.

Scharroo, R., Leuliette, E. W., Lillibridge, J. L., Byrne, D., Naeije, M. C., and Mitchum, G. T. (2013). RADS: Consistent multi-mission products. In *Proc. Symposium on 20 Years of Progress in Radar Altimetry*. European Space Agency. Spec. Publ. SP-710.

Schindelegger, M., Einšpigel, D., Salstein, D., and Böhm, J. (2016). The global S_1 tide in Earth's nutation. *Surveys in Geophysics*, 37(3):643–680.

Schindelegger, M., Green, J. A. M., Wilmes, S.-B., and Haigh, I. D. (2018). Can We Model the Effect of Observed Sea Level Rise on Tides? *Journal of Geophysical Research: Oceans*, 123(7):4593–4609.

Schindelegger, M., Kotzian, D. P., Ray, R. D., Green, J. A. M., and Stolzenberger, S. (2022). Interannual Changes in Tidal Conversion Modulate M_2 Amplitudes in the Gulf of Maine. *Geophysical Research Letters*, 49(24).

Schrama, E. J. O. and Ray, R. D. (1994). A preliminary tidal analysis of TOPEX/Poseidon altimetry. *Journal of Geophysical Research*, 99:24799–24808.

Sen Gupta, A., Jourdain, N. C., Brown, J. N., and Monselesan, D. (2013). Climate Drift in the CMIP5 Models. *Journal of Climate*, 26(21):8597–8615.

Shriver, J. F., Arbic, B. K., Richman, J. G., Ray, R. D., Metzger, E. J., Wallcraft, A. J., and Timko, P. G. (2012). An evaluation of the barotropic and internal tides in a high-resolution global ocean circulation model. *Journal of Geophysical Research: Oceans*, 117(C10).

Simpson, J. H., Crisp, D. J., Hearn, C., Swallow, J. C., Currie, R. I., and Gill, A. E. (1981). The shelf-sea fronts: implications of their existence and behaviour. *Philosophical Transactions of the Royal Society of London. Series A, Mathematical and Physical Sciences*, 302(1472):531–546.

Stammer, D., Ray, R. D., Andersen, O. B., Arbic, B. K., Bosch, W., Carrère, L., et al. (2014). Accuracy assessment of global barotropic ocean tide models. *Reviews of Geophysics*, 52(3):243–282.

Stepanov, V. N. and Hughes, C. W. (2004). Parameterization of ocean self-attraction and loading in numerical models of the ocean circulation. *Journal of Geophysical Research: Oceans*, 109(C3):C03037.

Su, M., Yao, P., Wang, Z. B., Zhang, C. K., and Stive, M. J. F. (2015). Tidal wave propagation in the Yellow Sea. *Coastal Engineering Journal*, 57(3):1550008–1–1550008–29.

Sulzbach, R., Klemann, V., Knorr, G., Dobslaw, H., Dümpelmann, H., Lohmann, G., and Thomas, M. (2023). Evolution of Global Ocean Tide Levels Since the Last Glacial Maximum. *Paleoceanography and Paleoclimatology*, 38(5):e2022PA004556.

Taburet, G., Sanchez-Roman, A., Ballarotta, M., Pujol, M.-I., Legeais, J.-F., Fournier, F., et al. (2019). DUACS DT2018: 25 years of reprocessed sea level altimetry products. *Ocean Science*, 15:1207–1224.

Talke, S. A. and Jay, D. A. (2020). Changing Tides: The Role of Natural and Anthropogenic Factors. *Annual Review of Marine Science*, 12:121–151.

Tamisiea, M. E. and Mitrovica, J. X. (2011). The Moving Boundaries of Sea Level Change: Understanding the Origins of Geographic Variability. *Oceanography*, 2:24–39.

Taylor, G. I. (1920). I. Tidal friction in the Irish Sea. *Philosophical Transactions of the Royal Society of London. Series A, Containing Papers of a Mathematical or Physical Character*, 220(571-581):1–33.

Tchilibou, M., Carrere, L., Lyard, F., Ubelmann, C., Dibarboure, G., Zaron, E. D., and Arbic, B. K. (2024). Internal tides off the Amazon shelf in the western tropical Atlantic: Analysis of SWOT Cal/Val Mission Data. *EGUsphere [preprint]*, 2024:1–23.

Tchilibou, M., Koch-Larrouy, A., Barbot, S., Lyard, F., Morel, Y., Jouanno, J., and Morrow, R. (2022). Internal tides off the Amazon shelf during two contrasted seasons: interactions with background circulation and SSH imprints. *Ocean Science*, 18(6):1591–1618.

Thomson, W. (1863). XXVII. On the rigidity of the earth. *Philosophical Transactions of the Royal Society of London*, 153:573–582.

Verezemskaya, P., Barnier, B., Gulev, S. K., Gladyshev, S., Molines, J.-M., Gladyshev, V., Lellouche, J.-M., and Gavrikov, A. (2021). Assessing Eddying (1/12°) Ocean Reanalysis GLORYS12 Using the 14-yr Instrumental Record From 59.5°N Section in the Atlantic. *Journal of Geophysical Research: Oceans*, 126(6):e2020JC016317.

Vic, C., Naveira Garabato, A. C., Green, J. A. M., Spingys, C., Forryan, A., Zhao, Z., and Sharples, J. (2018). The Lifecycle of Semidiurnal Internal Tides over the Northern Mid-Atlantic Ridge. *Journal of Physical Oceanography*, 48(1):61–80.

Vic, C., Naveira Garabato, A. C., Green, J. A. M., Waterhouse, A. F., Zhao, Z., Melet, A., et al. (2019). Deep-ocean mixing driven by small-scale internal tides. *Nature Communications*, 10(1):2099.

Vinogradov, S. V. and Ponte, R. M. (2011). Low-frequency variability in coastal sea level from tide gauges and altimetry. *Journal of Geophysical Research: Oceans*, 116(C7):C07006.

Viola, C. N., Verdon-Kidd, D. C., and Power, H. E. (2024). Spatially varying impacts of pacific and southern ocean climate modes on tidal residuals in New South Wales, Australia. *Estuarine, Coastal and Shelf Science*, 305:108869.

Vousdoukas, M. I., Mentaschi, L., Voukouvalas, E., Verlaan, M., Jevrejeva, S., et al. (2018). Global probabilistic projections of extreme sea levels show intensification of coastal flood hazard. *Nature Communications*, 9:2360.

Vreugdenhil, C. B. (2013). *Numerical methods for shallow-water flow*, volume 13. Springer Science & Business Media.

Wang, G. and Schimel, D. (2003). Climate Change, Climate Modes, and Climate Impacts. *Annual Review of Environment and Resources*, 28:1–28.

Wang, H., Li, M., Wei, N., Han, S.-C., and Zhao, Q. (2024). Improved estimation of ocean tide loading displacements using multi-GNSS kinematic and static precise point positioning. *GPS Solutions*, 28:27.

Wang, X., Peng, S., Liu, Z., Huang, R. X., Qian, Y.-K., and Li, Y. (2016). Tidal mixing in the South China Sea: An estimate based on the internal tide energetics. *Journal of Physical Oceanography*, 46(1):107–124.

Wang, Y., Xu, Z., Li, Q., Chen, Z., You, J., Yin, B., and Robertson, R. (2023). Observed internal tides in the deep northwestern Pacific by Argo floats. *Deep Sea Research Part II: Topical Studies in Oceanography*, 207:105248.

Ward, S., Bowers, D., Green, M., and Wilmes, S.-B. (2023). Chapter 4 — Why is there a tide? In *A Journey Through Tides*, pages 81–113. Elsevier.

Weis, P., Thomas, M., and Sündermann, J. (2008). Broad frequency tidal dynamics simulated by a high-resolution global ocean tide model forced by ephemerides. *Journal of Geophysical Research: Oceans*, 113:C10029.

White, N. J., Haigh, I. D., Church, J. A., Koen, T., Watson, C. S., Pritchard, T. R., et al. (2014). Australian sea levels—Trends, regional variability and influencing factors. *Earth-Science Reviews*, 136:155–174.

Wilmes, S.-B. and Green, J. A. M. (2014). The evolution of tides and tidal dissipation over the past 21,000 years. *Journal of Geophysical Research: Oceans*, 119(7):4083–4100.

Wilmes, S.-B., Green, J. A. M., Gomez, N., Rippeth, T. P., and Lau, H. (2017). Global tidal impacts of large-scale ice-sheet collapses. *Journal of Geophysical Research: Oceans*, 122:8354–8370.

Woodworth, P. L. (2010). A survey of recent changes in the main components of the ocean tide. *Continental Shelf Research*, 30(15):1680–1691.

Woodworth, P. L., Hunter, J. R., Marcos, M., Caldwell, P., Menéndez, M., and Haigh, I. (2016). Towards a global higher-frequency sea level dataset. *Geoscience Data Journal*, (2):50–59.

Woodworth, P. L., Shaw, S. M., and Blackman, D. L. (1991). Secular trends in mean tidal range around the British Isles and along the adjacent European coastline. *Geophysical Journal International*, 104(3):593–609.

Wunsch, C. (1975). Internal tides in the ocean. *Reviews of Geophysics*, 13(1):167–182.

Wunsch, C. and Ferrari, R. (2004). Vertical mixing, energy, and the general circulation of the oceans. *Annual Review of Fluid Mechanics*, 36(Volume 36, 2004):281–314.

Wunsch, C. and Stammer, D. (1998). SATELLITE ALTIMETRY, THE MARINE GEOID, AND THE OCEANIC GENERAL CIRCULATION. *Annual Review of Earth and Planetary Sciences*, 26:219–253.

Yadidya, B. and Rao, A. (2022). Interannual variability of internal tides in the Andaman Sea: an effect of Indian Ocean Dipole. *Scientific Reports*, 12(1):11104.

Yamaguchi, R. and Suga, T. (2019). Trend and Variability in Global Upper-Ocean Stratification Since the 1960s. *Journal of Geophysical Research: Oceans*, 124(12):8933–8948.

Yang, Z., Jing, Z., Zhai, X., Vic, C., Sun, H., de Lavergne, C., and Yuan, M. (2024). Enhanced generation of internal tides under global warming. *Nature Communications*, 15(1):7657.

Zaron, E. D. (2017). Mapping the nonstationary internal tide with satellite altimetry. *Journal of Geophysical Research: Oceans*, 122(1):539–554.

Zaron, E. D. (2019). Baroclinic Tidal Sea Level from Exact-Repeat Mission Altimetry. *Journal of Physical Oceanography*, 49(1):193–210.

Zaron, E. D. and Egbert, G. D. (2014). Time-Variable Refraction of the Internal Tide at the Hawaiian Ridge. *Journal of Physical Oceanography*, 44(2):538–557.

Zaron, E. D. and Jay, D. A. (2014). An analysis of secular change in tides at open-ocean sites in the Pacific. *Journal of Physical Oceanography*, 44(7):1704–1726.

Zaron, E. D. and Ray, R. D. (2018). Aliased tidal variability in mesoscale sea level anomaly maps. *Journal of Atmospheric and Oceanic Technology*, 35:2421–2435.

Zeng, Z., Brandt, P., Lamb, K. G., Greatbatch, R. J., Dengler, M., Claus, M., and Chen, X. (2021). Three-Dimensional Numerical Simulations of Internal Tides in the Angolan Upwelling Region. *Journal of Geophysical Research: Oceans*, 126(2):e2020JC016460.

Zhang, H., Qian, Y.-K., Wen, X., and Peng, S. (2023). Energetics of semidiurnal internal tides near Madagascar in the Southwest Indian Ocean. *Progress in Oceanography*, 211:102972.

Zhang, Z., Chen, X., and Pohlmann, T. (2021). The Impact of Fortnightly Stratification Variability on the Generation of Baroclinic Tides in the Luzon Strait. *Journal of Marine Science and Engineering*, 9(7).

Zhao, Z. (2014). Internal tide radiation from the Luzon Strait. *Journal of Geophysical Research: Oceans*, 119(8):5434–5448.

Zhao, Z. (2017). Propagation of the Semidiurnal Internal Tide: Phase Velocity Versus Group Velocity. *Geophysical Research Letters*, 44(23):11,942–11,950.

Zhao, Z. (2018). The Global Mode-2 M_2 Internal Tide. *Journal of Geophysical Research: Oceans*, 123(11):7725–7746.

Zhao, Z. (2023). Satellite evidence for strengthened M_2 internal tides in the past 30 years. *Geophysical Research Letters*, 50(24):e2023GL105764.

Zhao, Z. (2024). Internal Tides From SWOT: A 75-Day Instantaneous Mode-1 Internal Tide Model. *Journal of Geophysical Research: Oceans*, 129(12):e2024JC021174.

Zhao, Z., Alford, M. H., and Girton, J. B. (2012). Mapping Low-Mode Internal Tides from Multisatellite Altimetry. *Oceanography*, 25(2):42–51.

Zhao, Z., Alford, M. H., Girton, J. B., Rainville, L., and Simmons, H. L. (2016). Global Observations of Open-Ocean Mode-1 M_2 Internal Tides. *Journal of Physical Oceanography*, 46(6):1657–1684.

Zilberman, N. V., Becker, J. M., Merrifield, M. A., and Carter, G. S. (2009). Model Estimates of M_2 Internal Tide Generation over Mid-Atlantic Ridge Topography. *Journal of Physical Oceanography*, 39(10):2635–2651.